University of Glasgow

METABOLOMIC SENSING SYSTEM FOR PERSONALISED MEDICINE USING AN INTEGRATED CMOS SENSOR ARRAY TECHNOLOGY

Boon Chong Cheah

A Thesis submitted to
School of Engineering
at the University of Glasgow
in fulfilment of the requirements for the degree of
Doctor of Philosophy

July 2016

Abstract

Precision healthcare, also known as personalised medicine, is based on our understanding of the fundamental building blocks of biological systems, with the ultimate aim to clinically identify the best therapeutic strategy for each individual. Genomics and sequencing technologies have brought this to the foreground by enabling an individual's entire genome to be mapped for less than a thousand dollar in just one day. Recently, metabolomics, the quantitative measurement of small molecules, has emerged as a field to understand an individual's molecular profile in terms of both genetics and environmental factors. This is crucial because a genome could only indicate an individual's susceptibility to a particular disease, whereas a metabolome provides an immediate measurement of body function, enabling a means of diagnosis. However, the current approach of measurements depends on large-scale and expensive equipment such as mass spectroscopy and NMR instrumentation, which does not offer a single analytical platform to detect the entire metabolome.

This thesis describes the development of an integrated CMOS sensor array technology as a single platform to quantify different metabolites using specific enzymes. The key stages in the work were: to construct instrumentation systems to perform enzyme assays on the CMOS sensor array; to establish techniques to package the CMOS sensor array for an aqueous environment; to implement and develop a room temperature Ta_2O_5 sputtering process on CMOS sensor array for hydrogen ion detection; to collaborate with a chemist and investigate an inorganic layer on top of the CMOS ISFET sensor to show an improvement of sensitivity towards potassium ion; to test several different enzyme assays electrochemically and optically and show the functionalities of the sensors; to devise microfluidic channels for segregation of the sensor array into different compartments and perform enzyme immobilisation techniques on CMOS chips; and integrate the packaged chip with microfluidic channels and enzyme immobilisation using 2D inkjet printer into a complete system that has the potential to be used as a multi-enzyme platform for detection of different metabolites.

Two CMOS sensor array chips (1) a 256×256-pixel ISFET array chip and (2) a 16×16-pixel Multi-Corder chip were fully understood. Therefore, a high-speed instrumentation system was constructed for the ISFET array chip with a maximum readout speed of 500 frames per second, with 2D and 3D imaging capability, as well as single pixel analysis. Follow by that, a miniaturised measurement platform was implemented for the Multi-Corder chip that has three different sensor arrays, which are ISFET, PD and SPAD. All the sensor arrays can be operated independently or together (ionic sensor and one of the optical sensors).

Several post-processing steps were investigated to allow suitable fabrication process on small 4×4 mm^2 CMOS chips. Post-processing of the CMOS chips was first established using room temperature sputtering process for Ta_2O_5 layer, achieving Ta:O ratio of 1:1.77 and a surface roughness of 0.42 nm. This Ta_2O_5 layer was then fabricated on top of CMOS ISFETs, which improves the ISFET pH sensitivity to 45 mV/pH, with an average drift of 6.5 ± 8.6 mV/hour from chip to chip and a working pH range of 2 to 12. Furthermore, a layer of POMs was drop casted on top of Ta_2O_5 ISFET to make ISFET sensitive to potassium ions. This was investigated in terms of potassium ions sensitivity, hydrogen ions sensitivity and sodium ions as interfering background ions. The POMs Ta_2O_5 ISFET was found to have a net potassium sensitivity of 75 mV/pK, with a linear range between pH 1.5 to 3. Moreover, the POMs ISFET has -5 mV/pH in pH sensitivity, showing that it is selectivity towards potassium ions and not hydrogen ions. However, sodium ions were found to produce a large interference towards the pK sensitivity of POMs ISFET and reduced the pK sensitivity of POMs ISFET. Hence, further work is still required to modify POMs layer for better selectivity and sensitivity. Besides that, microfluidic channels were fabricated on top of the CMOS chips that could provide segregation for multiple enzyme assays on a single chip. In addition, a PDMS and a manual dam and fill method were developed to encapsulate the CMOS chips for wet biochemistry measurements.

The CMOS sensor array was found to have the ensemble averaging capability to reduce noise as a function of $\sqrt{N}$, where N is the number of sensors used for averaging. Several enzyme assays that include: hexokinase, lactate dehydrogenase, urease and lipase were tested on the ISFET sensor array.

Moreover, using an optical sensor array, namely a PD on the Multi-Corder chip and using LED illumination, quantification of cholesterol levels in human blood serum was demonstrated. Enzyme kinetics calculations were performed for hexokinase and cholesterol oxidase assays and the results were comparable to that obtained from a bench top spectrophotometer. This shows the CMOS sensor array can be used as a low cost portable diagnostic device.

Several enzyme immobilisation techniques were explored but were unsuccessful. Alginate enzyme gel immobilisation with a 2D inkjet printer was found to be the best candidate to bio-functionalise the CMOS sensor array. The packaged chip was integrated with microfluidic channels and alginate enzyme gel immobilisation into a complete system, in order to perform an enzyme assay with its control experiments simultaneously on a single chip. As a proof-of-concept, this complete system has the potential to be used as a multiple metabolite quantification platform.

Acknowledgements

This thesis would not have been possible without the constant support from a numerous people whom I am very grateful to. First and foremost, I would like to thank my supervisor, David Cumming, for offering me the opportunity to work on this futuristic, challenging and exciting PhD project, and to be part of the Multicorder vision for bringing *Star Trek* Tricorder to reality. Like the famous lines from *Star Trek*, "To Boldly Go Where No Man Has Gone Before". For the past four years, David has been constantly supporting me technically, pointing me to the correct path and also teaching me a great deal of proper English in scientific writing, which ensures my success in the PhD research. Special thanks also go to my second supervisor, Mike Barrett, for giving me inspirations and ideas on metabolomics that led to my first publication. Also, I enjoyed my random locations scientific chat, i.e. in NHS clinic. I would also like to thank Alasdair MacDonald for teaching me all that he knows about enzymes and all sorts of biochemistry, and also his wonderful chats about life. He could be quite pessimistic but a lot of fun working with him for my whole PhD. I am extremely thankful to the Lord Kelvin Adam Smith Sensor Studentship for funding my PhD studies. Special thanks to my internal examiner, Manuel Salmeron-Sanchez for all his help with the thesis corrections and PhD viva.

I would also like to extend my thanks to all members in the Microsystem Technology Group. Particularly, James Grant for all the technical help and cleanroom training that he has given me. He has devoted a lot of his time listening to my problems and giving me a great deal of advices (sometimes in the gym's changing room too!), when he is not even involved in my project. I would like to thank him for reviewing almost 60% of my Thesis. A lot of thanks also go to Chris Martin for all his random jokes, football chats and technical advices that helped me to stay on track. I am also extremely grateful to Mohammed Al-Rawhani who taught me all his electronics knowledge without holding anything back and was the person who guided me through my first year. I would also like to thank my flatmate Christos Giagkoulovits who is sincere and nice to me, but sometimes his tiring chats drove me nuts. Also thanks to Nadia Pinton and Ivonne Hernandez for their constant support, listening to my "complaints" and always

be there as my friends. Especially Ivonne, who always cheers me up, gives me spiritual guidance and introduces me to new friends. Also thanks to my office buddy Iain McCrindle, Mohsin Aziz and Chunxiao Hu. Lastly, thank you to all staff members of James Watt Nanofabrication Centre. None of my work would have been possible without their hard work in maintaining the facility.

Beyond University work colleagues, I am grateful to all my friends in Malaysia that supported me, especially Ka Yian Then, Jee Sien Hee and Wei Lun Oo who talks rubbish in my Skype chat. Also, thanks to Kah Wai Cham for his rude and gay chats from time to time. Special thanks to Yen-Chun Fu and Nina Chang who always spend time with me to go for foods or movies, they are one of my best friends in Glasgow. I would also like to thank all my usual friends whom I hang out with, Sankar Peralagu, Irene Suárez Marina, Sergio Martín Martí, Sala Sharabi and Kirsty Walls. Also thank you Sweeting Ooi, my Yorkhill flatmate, who made my life in Glasgow so exciting with a lot of amazing activities such as skydiving, zip wire adventures and crazy 24-hour hiking (I won Silver and Bronze medals!!!). Thanks to all my friends during my lunch hour with all those amazing chats.

Lastly, I would like to thank my girlfriend, Lourdes Ferre Llin for her constant support and encouragement throughout my journey to obtain the PhD. A lot of “quality” time with her in the gym to gain my six packs that kept me healthy and sane. Also, appreciation to all her efforts to constantly listen to my complaints and metabolome chats. Thank you for cheering me up and lending me a shoulder to cry on whenever I was weak. Thank you for cooking all those Spanish food for me too (too much salt sometimes)! Amazing partner (except for the impatience and the crazy grumpiness sometimes)! I would also like to thank her family members for welcoming me during festive or holiday periods when I am so far away from home. Finally, thank you to my Mummy and Daddy for their weekly Skype call with me that kept me in check, and also supported and encouraged me in all aspects since the day I was born. I am also blessed to have my brother, sister-in-law, sister, brother-in-law and my two nephews, Ethan and Kah Jun in my life. I hope you are all proud of what I have achieved thus far.

Publications

Journal Papers

1. M. A. Al-Rawhani, B. C. Cheah, A. I. MacDonald, C. Martin, C. Hu, J. Beeley, L. Gouveia, J. P. Grant, G. Campbell, M. P. Barrett, and D. R. S. Cumming, "A colorimetric CMOS-based platform for rapid total serum cholesterol quantification", *IEEE Sensors Journal*, vol 17, no.2, pp. 240–247, 2017.

2. A. Shakoor, B. C. Cheah, D. Hao, M. A. Al-Rawhani, B. Nagy, J. P. Grant, C. Dale, N. Keegan, C. McNeil, and D. R. S. Cumming, "Plasmonic sensor monolithically integrated with a CMOS photodiode", *ACS Photonics*, vol. 3, no. 10, pp. 1936-1933, 2016.

3. B. C. Cheah, A. I. MacDonald, C. Martin, A. J. Streklas, G. Campbell, M. A. Al-Rawhani, B. Nemeth, J. P. Grant, M. P. Barrett, and D. R. S. Cumming, "An integrated circuit for chip-based analysis of enzyme kinetics and metabolite quantification", *IEEE Transactions on Biomedical Circuits and Systems*, vol. 10, no. 3, pp. 721-730, 2016.

Conference Paper

1. A. Shakoor, B. C. Cheah, D. Hao, M. A. Al-Rawhani, B. Nagy, J. P. Grant, C. Dale, N. Keegan, C. McNeil, and D. R. S. Cumming, "Monolithic integration of a plasmonic sensor with CMOS technology", *Proc. SPIE 10107,* Smart Photonic and Optoelectronic Integrated Circuits XIX, 101070F, 2017.

2. B. C. Cheah, A. I. MacDonald, M. P. Barrett, and D. R. S. Cumming, "Metabolomics on integrated circuit", *Biosensors*, 2016.

Oral Presentations

1. B. C. Cheah, "Fabrication on CMOS ISFET chip", *James Watt Nanofabrication Centre (JWNC) user meeting*, 2014.

Poster Presentations

1. B. C. Cheah, A. I. MacDonald, C. Martin, S. Velugotla, M. A. Al-Rawhani, M. P. Barrett, and D. R. S. Cumming, “Personal metabolome machine for precision healthcare”, *SET for BRITAIN*, 2016.

2. B. C. Cheah, A. I. MacDonald, C. Martin, S. Velugotla, M. A. Al-Rawhani, M. P. Barrett, and D. R. S. Cumming, “Personal metabolome machine for precision healthcare”, *Multicorder IAB Meeting*, 2016.

3. B. C. Cheah, A. I. MacDonald, M. P. Barrett, and D. R. S. Cumming, “CMOS based 256×256-pixel ISFET sensor array for enzyme kinetics applications”, *Multicorder IAB Meeting*, 2015.

4. B. C. Cheah and D. R. S. Cumming, “CMOS based 256×256-pixel ISFET sensor array for electrochemical applications”, *Multicorder IAB Meeting*, 2014.

5. B. C. Cheah, M. A. Al-Rawhani, J. Beeley, B. Nemeth, and D. R. S. Cumming, “CMOS based 256×256-pixel ISFET sensor array for electrochemical applications”, *Kelvin Smith Scholar Event*, 2013.

Content

List of Figures

List of Tables

List of Acronyms

Acronym	Meaning
2D	Two Dimension
3D	Three Dimension
6-PG	6-phospho-d-gluconate
A	adenine
ADC	analogue-to-digital converter
ADP	adenosine diphosphate
AFM	atomic force microscopy
AMS	*austriamicrosystems*
ASCII	American Standard Code for Information Interchange
ASIC	application-specific integrated circuit
ATP	adenosine triphosphate
BSA	bovine serum albumin
C	cytosine
cat	catalytic
CMOS	complementary metal oxide semiconductor
CPGA	ceramic pin grid array
DI	deionised
DMA	direct memory access
DNA	deoxyribonucleic acid
E	enzyme
EIS	electrolyte-insulator-semiconductor
ENFET	enzyme field effect transistor
EP	enzyme-product
ES	enzyme-substrate
G	guanine
G6PDH	glucose-6-phosphate-dehydrogenase
GC-MS	gas chromatography mass spectroscopy
GDH	glucose-1-dehydrogenase
Gox	glucose oxidase
HCl	hydrochloric acid

continued on next page

continued from previous page

Acronym	Meaning
HDL	high-density lipoproteins
I/O	input-output
IC	integrated circuit
IBM	International Business Machines
IHP	inner Helmholtz plane
IMEC	Interuniversity MicroElectronics Center
ISFET	ion sensitive field effect transistor
JWNC	James Watt Nanofabrication Centre
LabVIEW	Laboratory Virtual Instrument Engineering Workbench
LCECA	liquid chromatography electrochemistry array
LC-MS	liquid chromatography mass spectroscopy
LDH	lactate dehydrogenase
LDL	low-density lipoproteins
LED	light emitting diode
LPCVD	low pressure chemical vapour deposition
LSB	least significant bit
MCU	microcontroller unit
MEDLINE	Medical Literature Analysis and Retrieval System Online
MEMS	microelectromechanical systems
MES	morpholineethanesulfonic
MetaChip	metabolic enzyme microarray
MOS	metal oxide semiconductor
MOSFET	MOS field effect transistor
MS	mean squared
MSB	most significant bit
MST	Microsystem Technology
MTMOS	methyltrimethoxysilane
NADP	nicotinamide adenine dinucleotide phosphate
NADPH	nicotinamide adenine dinucleotide phosphate (reduced)
NI	National Instruments
nMOS	n-channel MOS
NMR	nuclear magnetic resonance

continued on next page

continued from previous page

Acronym	**Meaning**
OCP	open-circuit potential
OHP	outer Helmholtz plane
P	product
PC	personal computer
PCB	printed circuit board
PCR	polymerase chain reaction
PDMS	polydimethylsiloxane
PISA	protein in situ array
pMOS	p-channel MOS
POC	point-of-care
polysilicon	polycrystalline silicon
POMs	polyoxometalates
pzc	point of zero charge
REF	reference
RF	radio frequency
S	substrate
SCE	saturated calomel electrode
SEM	scanning electron microscopy
SNP	single nucleotide polymorphism
SOL	solution
SPAD	single photon avalanche diode
SRAM	static random access memory
SSD	solid-state drive
T	thymine
TBA	tetrabutylammonium
TDMS	test data exchange stream
USB	Universal Serial Bus
UV	ultraviolet
VLDL	very low-density lipoproteins
XPS	x-ray photoelectron spectroscopy

Symbol Definitions

Symbol	Meaning	Units	Value
$	US dollar	/	
$[A]$	concentration of substrate A	M	
$[E]$	enzyme concentration	M	
$[X]$	ion concentration of species X	mol	
A	total surface area of IHP and OHP	m^2	
C	capacitance per unit area	$F\ m^{-2}$	
c	total ionic concentration	M	
d	distance between IHP and OHP	m	
E	electrode potential	V	
F	Faraday constant	$C\ mol^{-1}$	96.5×10^3
G	free energy	$kJ\ mol^{-1}$	
ΔG_{act}	free energy of activation	$kJ\ mol^{-1}$	
i	Current density	$A\ m^{-2}$	
k	(a) rate constant	s^{-1}	
	(b) Boltzmann constant	$J\ K^{-1}$	1.38×10^{-23}
K_m	Michaelis-Menten constant	M	
K_S	"True" dissociation constant	M	
N_X	Density of surface sites of type X	m^{-2}	
Q	charge density	$C\ m^{-2}$	
q	electronic charge	C	1.6×10^{-19}
R	molar gas constant	$J\ mol^{-1}\ K^{-1}$	8.31
T	temperature	K	
t	time	s	
V	voltage	V	
ν	velocity	$M\ s^{-1}$	
z	formal ionic charge	/	
ε	permittivity	$F\ m^{-1}$	
ς	symmetry coefficient	/	
σ	surface charge density	$C\ m^{-2}$	
ϕ	surface potential	V	

continued on next page

continued from previous page			
Symbol	**Meaning**	**Units**	**Value**
$\Delta\phi$	Potential difference across an interface	V	
Φ	work function	eV	
χ	(a) surface dipole potential	V	
	(b) normalised net charge	m^{-2}	

Chapter 1 : Introduction to the Research

1.1 Introduction

This chapter describes the motivation of the research in terms of applications and technology. The aim and objectives of the work are identified and an outline of the thesis is provided.

1.2 Motivation

Modern biomedical and life sciences are predicated on our understanding of the fundamental building blocks that underpin biological systems. This knowledge will lead us to personalised healthcare, whereby individualised therapy or drugs that are best suited for an individual can be selected based on their clinical profile. It all began with the coining of the phrase “genomics” in 1986 and the sequencing of the human genome soon after, which brought the practice of medicine to enter the era of understanding an individual’s genome to determine optimal healthcare [1, Ch. 1]. Therefore, a low cost, rapid and portable medical device for routine testing is required. This will allow physician to tailor diagnosis, prevention and treatment based on an individual’s genetic makeup. However, sequencing 3-billion base pairs of DNA found in the human genome is very time consuming and expensive, thus various technologies have been established to reduce the cost of sequencing with a goal of reaching $1,000 per genome [2].

Common practice of DNA sequencing is limited by imaging technology, electromagnetic intermediates such as X-rays or light and specialised reagents or preparations [3]. In order to overcome this limitation, a non-optical sequencing technology using integrated circuits has been pursued. The microelectronics industry is dominated by complementary metal oxide semiconductor (CMOS) technology with its scalability, mass-manufacturing and low cost production.

More importantly, CMOS has the ability to facilitate an array of sensors into a small space and incorporate high quality standard electronics into one single integrated platform. CMOS has brought success to modern computing, communication and sensing technology by creating ubiquitous computers, mobile phones and digital cameras. Recently, Ion Torrent (Thermo Fisher Scientific) has brought the price of genome sequencing to the foreground, by inventing a personal genome machine on CMOS technology – the world's first optics free sequencing system [4].

Personalised medicine has been focussing on the understanding of an individual's genetic makeup to provide precision healthcare. However, a genome could only indicate an individual's susceptibility to a particular disease. Moreover, most diseases are very complex and involve the interaction between genetics and environmental factors [5]. Therefore, studying the molecular makeup of an individual is very important for the advancement of personalised medicine. Various other "omics" groups such as transcriptomics (RNA), proteomics (proteins) and metabolomics (metabolome) have been spawned after genomics to better understand an individual's clinical profile. Metabolomics is particularly well suited for this approach since the metabolome is the ensemble of all the tiny molecules, or metabolites of life, which reflects an individual's health at a given period of time in one's lifespan that is affected by both genetics and lifestyle, hence allowing immediate diagnosis.

To date, metabolome detection relies on expensive, large-scale equipment such as mass spectroscopy and nuclear magnetic resonance (NMR) instrumentation and the required special skillsets to operate them [6]. More importantly, this equipment does not provide a single platform to detect the entire metabolome. In the same way that pioneering research in sequencing technologies unravelled the personal genome and reduced the genome cost, thus the pursuit of a technology is required to give everyone near instant access to their own metabolome for the advancement of personalised medicine.

In this study, an integrated CMOS sensor array technology is developed as a single platform to quantify different metabolites using specific enzymes. Furthermore, using this platform, in tandem with microfluidics to segregate the sensor array into different sections, together with different enzyme

functionalisation, allows detection of multiple metabolites simultaneously. Finally, this sensor array can be integrated into a portable device, leading to a handheld diagnostic tool as a personal metabolome machine, revolutionising healthcare provision worldwide.

1.3 Aim and Objectives

The research work presented in this thesis is part of *The Multicorder* project that has a larger vision of using microelectronics technology to create the world's first broad spectrum sensor technology for diagnostics, chemical synthesis and biotechnology. The main objective of this project is to develop a personal metabolome machine for precision healthcare, which is the primary aim of this thesis. *The Multicorder* is supported by the UK Engineering and Physical Sciences Research Council, with Professor David Cumming as the head of project. The project co-investigators are the School of Chemistry, Institute of Infection, Immunity and Inflammation (Wellcome Trust Centre for Molecular Parasitology) and the University of Newcastle.

Dr. Balazs Nemeth, previously a research assistant in the microsystem technology (MST) group designed the 256×256-pixel ISFET array chip. The second CMOS chip studied in this work is the 16×16-pixel Multi-Corder chip designed by Dr. Mohammed Al-Rawhani, who is a research associate in the MST group. Moreover, Christoph Busche, a research fellow in the School of Chemistry, was responsible for synthesising the polyoxometalates (POMs) and worked with myself and Dr. Srinivas Velugotla, a research associate in the MST group, to enhance the sensitivity of the ISFET towards potassium ions with POMs. Furthermore, Dr. Alasdair MacDonald, a research associate at Institute of Infection, Immunity and Inflammation, prepared all the required enzyme assays reagents to be performed on top of the CMOS sensor array. Therefore, it has to be pointed out that all the CMOS chips are designed and enzyme assays are prepared by the individuals mentioned above. In spite of that, the designs of the CMOS chips have to be well understood to construct a complete instrumentation system for two different CMOS chips and the preparation of the reagents had to be fully comprehended to be able to produce proper measurements on the CMOS

chips. All this work is included in the thesis to provide a better understanding of the thesis.

My activity in this project consisted in measuring and analysing different enzyme assays on two different CMOS chips using ISFET and PD sensors. At the same time, integrating SU-8 microfluidic channels with alginate entrapment of enzyme that was printed by a 2D inkjet printer, to produce a multi-enzyme platform for simultaneous measurements of different metabolites. Furthermore, part of my time was also devoted to improving the performance of ISFET towards hydrogen ions and potassium ions, using Ta_2O_5 thin film and POMs inorganic layer respectively. The specific objectives of this research work are detailed as follows:

- To understand the design of both chips, (1) 256×256-pixel ISFET array chip and (2) 16×16-pixel Multi-Corder chip and develop two separate instrumentation systems for both chips, in terms of hardware and software.

- To develop a robust and stable packaging technique, in order to produce a waterproof CMOS chip that could perform chemical and biological experiments.

- To develop a fabrication process of Ta_2O_5 film on top of CMOS ISFETs using room temperature sputtering process and characterise it for its sensing performance, which includes sensitivity towards hydrogen ion concentration, drift and robustness.

- To comprehend all the enzyme assays reagents preparation by the biologist, in order to measure and analyse all the enzyme assays on top of the CMOS chips. At the same time, learn how to prepare enzyme assays in order to be become independent.

- To fabricate and test the SU-8 microfluidic channels on the CMOS chips.

- To develop an enzyme immobilisation technique using a 2D inkjet printer that is measureable using the CMOS chips.

- To integrate the SU-8 microfluidic channels with enzyme immobilisation using 2D inkjet printing to create a complete system, which has the potential to perform multiple enzyme assays for simultaneous detection of different metabolites.

1.4 Thesis Outline

The subsequent chapters of this thesis are divided into seven chapters and a brief description of each chapter is provided as follows:

Chapter 2 is a review of the literature relevant to the development of a personal metabolome machine for precision healthcare using CMOS sensor array technology.

Chapter 3 presents the fundamental theory of enzymes to quantify metabolites using enzyme kinetics and describes how these enzyme assays can be detected optically and electrochemically. Finally, the theory of pH measurement using a conventional glass electrode in the context of an ISFET is provided.

Chapter 4 describes the two different chips, 256×256-pixel ISFET array chip and 16×16-pixel Multi-Corder chip, focussing on the understanding of the designs of both chips, to construct two separate instrumentation platforms.

Chapter 5 discusses the post-processing that is required to improve the sensitivity of the ISFET towards hydrogen ions and potassium ions. In addition, a discussion on the fabrication of microfluidic channels on CMOS chips for multiple metabolite detection. Finally, the packaging technique is described for chemical and biological experiments in aqueous solution.

Chapter 6 provides details of the measurements of different metabolites using both chips, including results and discussion.

Chapter 7 describes the enzyme functionalisation technique on CMOS chips and how to integrate it into a complete system together with microfluidics to perform multiple metabolites with specific enzymes, including results and discussion.

Chapter 8 summarises the conclusion of this research work and discusses potential future work.

1.5 Summary

The motivation of this project was provided by describing the limitations of current approaches and proposed a better technology to overcome them with the potential of achieving greater goals. Furthermore, the aim and objectives of the research work were identified and an outline of the thesis was provided. The next chapter will be a review of the literature relevant to this project.

Chapter 2 : Literature Review

2.1 Introduction

This chapter presents a review of the literature relevant to the development of a sensor system on chip, specifically focussing on the advancements towards personalised medicine via genomics and metabolomics. A brief history of personalised medicine is first given along with a chronological description of the technology and strategies employed in genomics and metabolomics. Next, the various methods employed in microarray technologies that are commonly used for genomics research that could apply to metabolomics are discussed. This chapter further discusses low cost CMOS technology for the adaption of various different chemical sensors that can be integrated on a single chip. Finally the ion sensitive field effect transistor (ISFET) is introduced and adapted to CMOS technology, which opened up to various biosensing applications.

2.2 Personalised Medicine

The wellbeing of human health has always been a driving force for scientists to strive for the development of a better healthcare. Most of the current strategies of illness treatment and drug development are based on the efficacy towards a large population of people. These methods provide the same treatment to all patients with the same diagnosis of a certain disease, a conventional concept of “one-drug-fits-all” [1, Ch. 1]. These methods of medical treatment are based on the hypothesis that all diseases affect each patient in the same way however the same medical treatment could lead to different responses for each patient. Although the genetic makeup of mankind is 99.1% identical, a small inter-individual genetic variation of 0.9% accounts for the huge variability that exists in human beings [1, Ch. 1], [5].

The medical community has long recognised each patient has unique inherent traits, which may be evidenced by the ubiquity of certain diseases within families or ethnicities, variations in response to treatment and different manifestations of a single pathology [5]. In spite of these observations, medical

practice still uses a standard treatment for a heterogeneous population. With the advancement of scientific knowledge over the years, medical practice has underwent a paradigm shift towards tailoring medical treatment to best suit an individual's needs taking into consideration both genetic and environmental factors, which is known as personalised medicine [1, Ch. 1], [7]. Figure 2.1 shows the difference between present conventional medicine and personalised medicine.

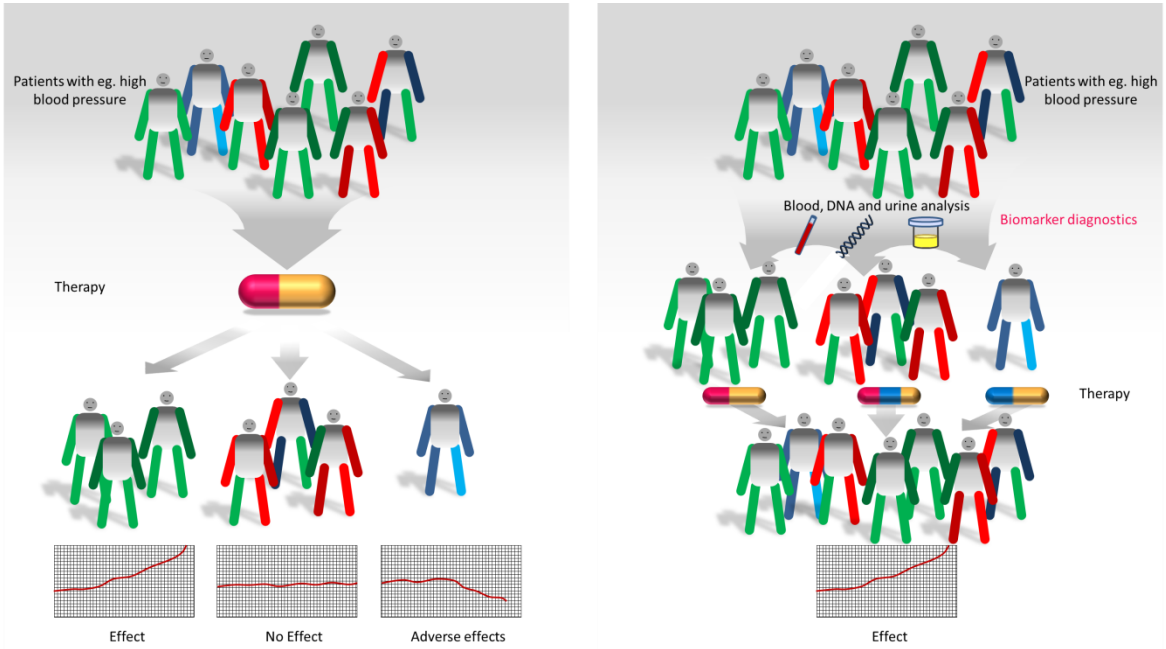

a) Medicine of the present: one treatment fits all

b) Medicine of the future: more personalised diagnostics

Figure 2.1 – Difference between conventional medicine and personalised medicine. Reproduced from [8].

2.2.1 History of Personalised Medicine

The term personalised medicine was first used as a title in a monograph in 1998 and followed by subsequent publications in MEDLINE in 1999 [1, Ch. 1]. However, the first concept of individualised healthcare was actually dated back to 4000 BC and the ancient medical system of India known as Ayurveda, where therapy is customised to the individual's constitution (Prakriti) [9]. In addition, traditional Chinese medicine [10] and traditional Korean medicine (Sasang typology) [11] also provide treatments according to the needs and personality of the patient. Each of these traditional medicines has their specific methods to classify an individual's constitution. For example, Ayurvedic practices use the tridosha theory to identify principles of motion (vata), metabolism (pitta) and structure

(kapha) to classify individual Prakriti subtype [9]. These ancient healthcare systems survive to the present day and are still practiced.

From the late 19th century onwards, it is the beginning of modern medicine with the use of scientific knowledge to better understand diseases and enable accurate classification of patients. A lot of advances occurred during this period, from which genetic medicine started with the observation by Garrod [12] in 1931 that inter-individual variation to drugs is due to differences in each person's genetic constitution. The completion of Human Genome Project [13] in 2000 has hugely impacted scientists understanding of individuals and also brought personalised medicine a step closer to reality. The primary advancement in genetics technologies that enabled significant progress within the field of personalised medicine are single nucleotide polymorphism (SNP) genotyping [14] and microarrays/biochips [1, Ch. 2], [15]. Figure 2.2 illustrates the definition of the SNP biomarker and an example of the usage of a microarray for deoxyribonucleic acid (DNA) sequencing.

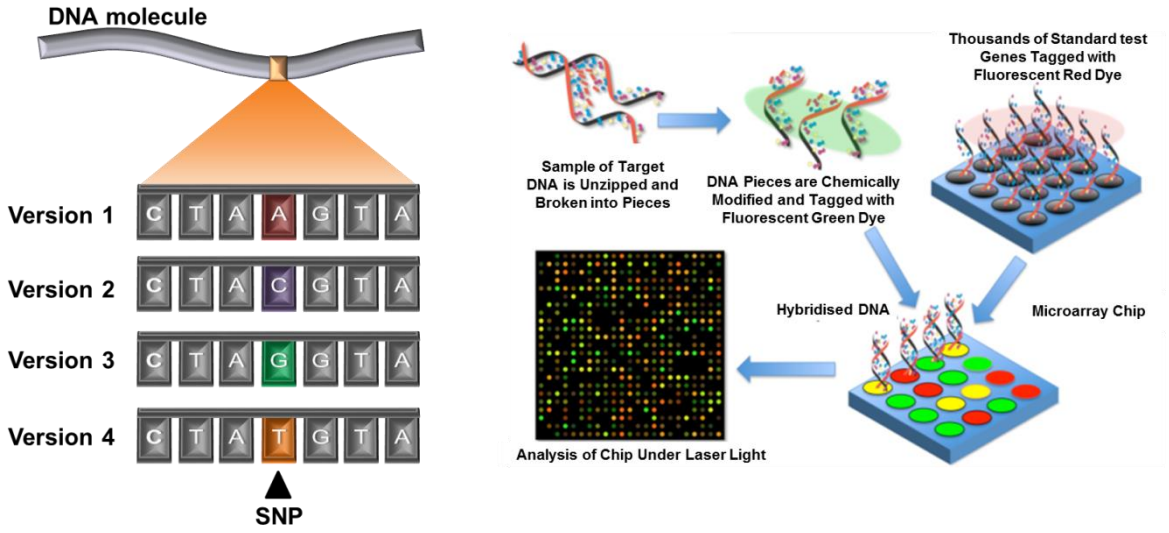

a) Four different versions of SNP **b) DNA microarray testing process**

Figure 2.2 – The two most significant advancements for personalised medicine. Reproduced from [16], [17].

The discovery of SNP – the single-nucleotide (base) substitution in the (DNA) sequence of the general population (at least 1%) explains most of the inter-individual genetic variability [5]. The ability to identify SNPs is very important as it helps to link an individual's susceptibility to certain diseases and also response

to medications. Through a lot of clinical studies and trials, researchers have proven that SNPs can be used as invaluable markers for segregating individuals.

The invention of the efficient and cost effective microarray biochip has revolutionised the field of personalised medicine, with the capability to store and rapidly analyse the entire human genome of a patient. Microarray technology allows researchers and clinicians to conduct SNP genotyping efficiently and rapidly, enabling early detection of disease and prediction of drug response [14]. Ultimately, this will offer the possibility of analysing the entire proteome or metabolome, leading to protein-based diagnostics and therapeutics which could potentially provide point-of-care (POC) diagnosis.

2.2.2 Genomics

DNA is the chemical compound that carries the genetic information of an organism [18, Ch. 1]. DNA is made up of four different chemical units, called nucleotide bases: adenine (A), guanine (G), cytosine (C) and thymine (T). It is the sequence or the order of these bases that determines the encoded information in the DNA. All the bases tend to form base pairs, A with T and C with G, and creates two long DNA strands that twist into a spiral called a double helix. The complete DNA sequence of all these nucleotides is the total genetic material of an organism, called its genome. A human genome is very complex and contains approximately 3-billion DNA base pairs [19]. It is located in every single cell nucleus of the human body as 23 pairs of chromosomes. In these chromosomes, there are units of DNA called genes that carry the information to produce proteins, which are the main macromolecules of an organism and are used to build body structures such as organs. Figure 2.3 illustrates a graphical explanation of a genome. Currently, the Human Genome Project holds an estimation of the total number of genes in the human genome to be around 20,500 [20].

In 1860, Gregor Mendel experimented with pea plants and developed the fundamental principles of genetics, which is the study of singles genes and their functions [21]. Genetic research has pushed scientists to investigate the molecular makeup of a gene until in 1953 Watson and Crick [22] solved the puzzle of the DNA molecule. In 1960, Brenner described the correlation between

DNA and proteins and led to the identification of the first gene-disease association known as Huntington's disease [5], [23]. This is a genetic disease caused by alterations in a single gene. However, many common human diseases are caused by the interaction between genes and their environments, which is called multifactorial or complex diseases. In contrast to a single gene disorder, they are caused by the defects in multiple genes with the effect from the environment.

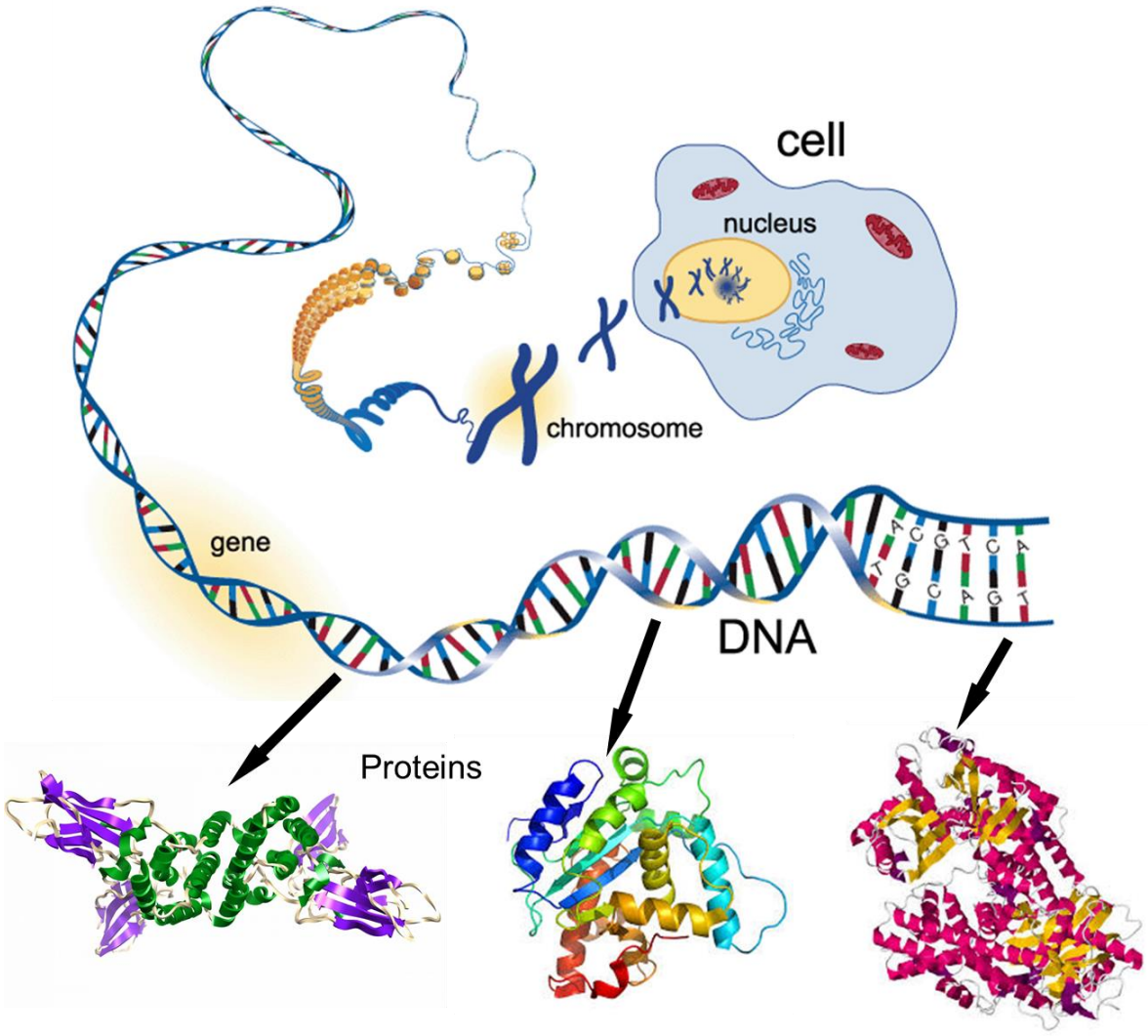

Figure 2.3 – Graphical explanation of a genome, from the cellular level to the formation of complex proteins that could be used for organ construction. Reproduced from [24].

Therefore, determining the complete base sequence of a DNA segment is crucial to understand genes and their effects. This led to the development of Sanger Sequencing, first demonstrated by Frederick Sanger [25] in 1977, which has become the basis for modern sequencing techniques [26], [27]. In order to study large pieces of DNA such as a gene, scientists have to sequence small sections of

DNA and assemble them into a larger sequence. Overlapping segments of DNA sequences between these short segments have to be read multiple times to ensure fidelity. This led to the introduction of polymerase chain reaction (PCR), a commonly used method to amplify DNA rapidly, by Karry B. Mullis [28] in 1987. With the need to understand the entire human genome, various next generation sequencing technologies have been developed to allow high-throughput sequencing and reduce the costs. With the advancement in genome sequencing, SNPs are identified by scientists when DNA samples were sequenced from multiple people. SNPs are the best markers for explaining most of the inter-individual variations in general population [29]. Large scale genotyping of SNPs at thousands of genes in a human genome can establish an individual's susceptibility to a disease and drugs response. Genomics technology has formed the basis for personalised medicine.

2.2.3 Metabolomics

Genomics alone is inadequate to describe an individual's susceptibility to a certain disease or response to a drug with absolute certainty. To better comprehend the reason genomics technology is insufficient to represent personalised medicine, it is crucial to define the principal terms: genotype and phenotype. Genotype is the complete genomic sequence of an individual, while phenotype is the individual observable differences that generates from the complex interaction between genotype and environment [5]. Figure 2.4 illustrates that metabolomics have the closest link to an individual's phenotype. These environmental causes include diet, lifestyle, nutrition, medications and age [30]. Similar with the discussion in genomics, almost all common diseases have a multifactorial pathogenesis, which have genetic and environmental causes. Therefore, genotypic makeup of an individual is not enough to paint a clear picture to one's risk of developing a disease or response to drugs.

Metabolomics is a study of the metabolome, which is the total collection of small molecules known as metabolites in a human cell, body fluids, tissue or organ involved in the primary and intermediary metabolism [1, Ch. 7]. Metabolome is affected by both genetic and environmental factors, where the quantifiable metabolites at a given time will provide the closest link between

genotype and phenotype. Hence, it is the biological end point that commences from DNA and provides useful information about an individual phenotype, while genomics is just a prediction of the potential cause for a phenotypic response. This could provide useful information for an individual's physiological status at a given time in life and assist early identification of diseases. Similar to single gene detection, the detection of a single metabolite can only provide crude diagnosis to an individual's health, thus metabolome detection is required to provide an overall understanding of the metabolism of an individual [31]. Metabolomics was first demonstrated in the late 1960s and it was not until 1971 that it was described by Pauling *et al.* in his publication [30]. They investigated several metabolites in body fluids that reflect certain diseases. After approximately 20 years, metabolomics started to blossom in 1990 with the first publication on metabolome and the Human Metabolome Project provided the first draft of human metabolome by 2007 [32]. Currently, the Human Metabolome database holds data on over 40,000 metabolites [33].

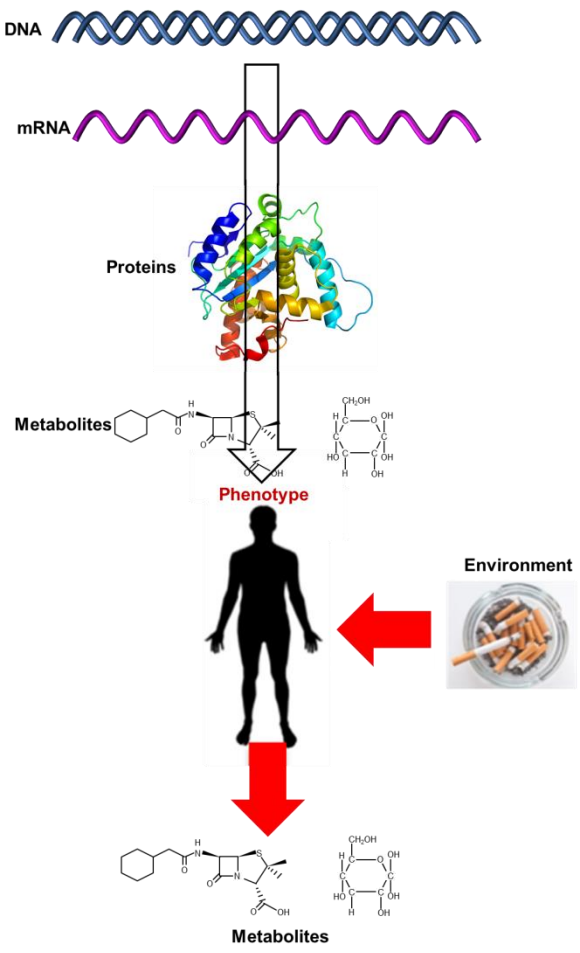

Figure 2.4 – Flow chart of an individual's phenotypic profile, from DNA to metabolites. Reproduced from [34].

The common method to study metabolomics is by collecting samples of interest, such as blood plasma and cerebral spinal fluids, and using different analytical platforms for detection. Reviews have reported that there are several commonly used analytical platforms that are proven to identify metabolites: nuclear magnetic resonance (NMR) spectroscopy, gas chromatography mass spectroscopy (GC-MS), liquid chromatography mass spectroscopy (LC-MS) and liquid chromatography electrochemistry array (LCECA) [6], [35].

The choice of a metabolomic analytical instrument depends on their analytical goal [6], for instance:

- NMR has been very successful in toxicology studies.
- GC-MS is commonly used in lipidomics, mapping of lipid biochemical pathways.
- LC-MS can analyse most biochemical compounds, hence it is normally used to map the largest possible biochemical profile.
- LCECA is excellent at mapping neurotransmitter pathways and oxidative stress pathways.

All analytical platforms have their own strengths and limitations, as described in Table 2.1. Currently there is no single analytical platform that has the capability to detect the complete metabolome in one sample [6]. Moreover, all the analytical platforms are expensive and require special skillsets to operate them and understand the data. Metabolomics markers could provide early diagnosis of diseases and bring personalised medicine to the bedside of patients. With expensive and huge analytical platforms, POC diagnosis is not possible. Therefore, like genomics, metabolomics analytical platforms should be reduced in cost to the clinical medical range, and ideally there should be a single technology to detect whole human metabolome. Such a tool would revolutionise personalised medicine.

Table 2.1 – Comparison of different analytical platforms for metabolomics [6]

Analytical Platforms	Advantages	Disadvantages
NMR	• Structural analysis • High-sample-throughput • Universal detection • Excellent quantitative precision • Non-destructive processing	• Expensive (over one million dollars) • Poor sensitivity
GC-MS	• Structural analysis. • High-sample-throughput • Reasonable quantitative precision • Better sensitivity than NMR	• Only study molecules that can be readily volatilised. • Expensive (100 – 300 thousand dollars) • Destructive processing
LC-MS	• Can detect most compounds with different configurations	• Inconsistent quantitative precision • Expensive (100 thousand to one million dollars) • Destructive processing
LCECA	• Extremely sensitive, better than GC-MS • Lower cost (slightly below 100 thousand dollars)	• Detects only electrochemical active compounds • Lack of structural analysis • Low-sample-throughput

2.3 Microarray Technologies

Microarrays are multiplexing technologies that enable simultaneous assessments of multiple variables using a tiny amount of sample with one single experiment. A microarray contains microspots of probing molecules immobilised onto a solid surface in rows and columns. These microspots are exposed to corresponding target molecules for detection in a sample. Various detection methods can be used to readout the signal from the microarray, such as fluorescence, mass

spectrometry, electrochemistry, chemiluminescence, colorimetric or radioactivity [36].

The first implementation of microarray technology was in a multi-analyte immunoassay by Roger Ekins [37] in 1989. They demonstrated that microspot capture probes could be used to detect analyte concentration with high sensitivity and accuracy. However, microarray technology was not in demand during that period. Interest in microarray technology burgeoned with the advent of genome sequencing requiring simultaneous multi-gene analysis. Together with the high-throughput oligonucleotide synthesis using PCR amplification, microarray technology has created an array of oligonucleotide probes to sequence DNA samples via hybridisation. The 'DNA chip' became one of the greatest achievements in genomics. DNA is a uniform and stable molecule and its primary sequence binds with specific target DNA with good specificity using the complementary base-pair principle [38]. Hence, prediction of the DNA sequence of a target molecule can be easily determined. However, microarray technologies for complex molecules such as enzymes are not well established. Unlike DNA, enzymes are much more complex molecules. The primary amino acid sequence of an enzyme does not determine the affinity towards the target molecule. It also depends on the molecular structure of the enzyme and also a numerable of ways to interact with target molecules. Besides that, enzymes are not only specific to one target molecule but several of them. Enzymes will be discussed in more detail in Chapter 3. The following sections delineate the contemporary techniques to microarray technologies that are commonly used in creating planar DNA microarrays, which could be adopted for enzyme microarrays for metabolites detection on a CMOS platform, with the focus on printed microarrays.

2.3.1 Printed Microarrays

Printed microarrays were the first microarrays to be used in research laboratories. These microarrays have a lower density compared to in situ-synthesised microarrays and high-density bead arrays [39]. In printed microarray technology, the probe spots are normally deposited onto a solid surface using non-contact or contact printing. Non-contact printing uses technology such as

inkjet printing, where the print head disperses the solution with a gap above the surface, while in contact printing, the print head contacts the surface to deliver the solution. Figure 2.5 shows the difference between contact and non-contact printing. These microarrays are inexpensive and rather simple to make. In addition, they are very versatile in which they can be used to print different kinds of biological samples. However, cross-contamination is a very critical issue for printed microarrays – it is imperative to maintain the integrity of the biological sample being printed.

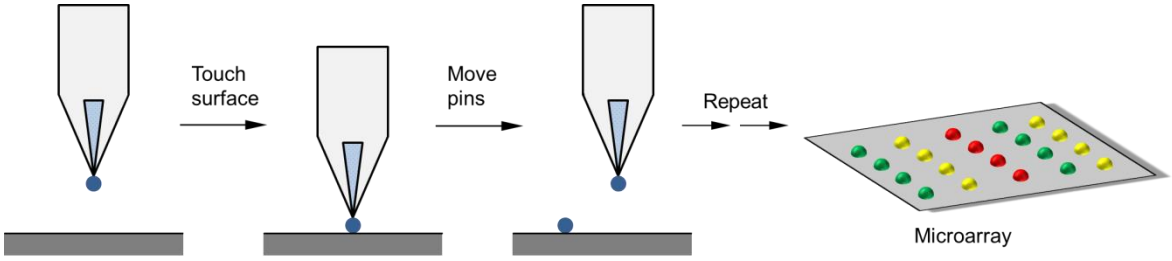

a) Contact mechanical microspotting

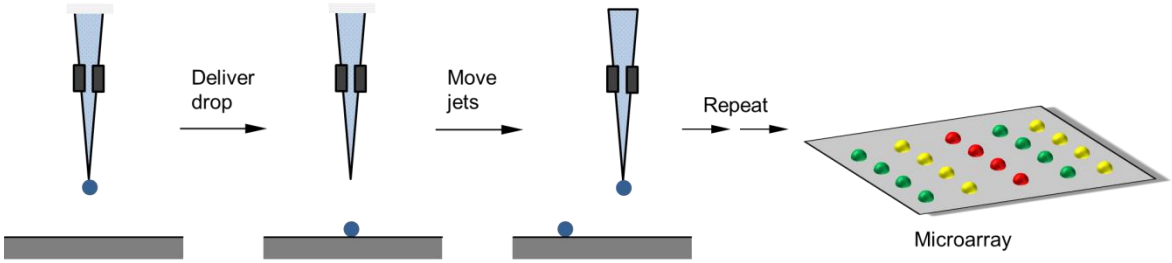

b) Non-contact inkjet printing

Figure 2.5 – Working mechanism of different printing techniques. Reproduced from [40].

Printed DNA microarrays normally use double-stranded DNA from a known genome sequence (denature to form single-stranded DNA after immobilisation) or chemically synthesised oligonucleotide. The desired DNA is first printed on the surface and it is then followed by the immobilisation of the DNA. The double-stranded DNA immobilisation can be done via electrostatic interaction between the negatively charges DNA and the positively charged coated surface, or via UV-cross-linked covalent bonds between thymidine bases in the DNA and the amine groups on the surface. On the other hand for oligonucleotide attachment on the surface, it is normally coupled on aldehyde treated surface.

In 2000, MacBeath *et al.* [41] demonstrated the first protein microarray using specific enzymes to detect small molecules. They used a high-precision contact-

printing robot to produce such a microarray. The enzymes solutions were printed in phosphate-buffered saline with 40% glycerol to prevent evaporation. Similar to the coupling of oligonucleotide to the surface, they used an aldehyde treated solid surface to react with amine groups in enzymes immobilised on the surface. Using this method, enzymes could be attached on the surface in a variety of orientations without impeding the ability of the enzymes to interact with small molecules. Bovine serum albumin (BSA) was also used to quench all the unreacted aldehyde surfaces to prevent unspecific binding.

The most recent invention, by Lee *et al.* [42] in 2004, is called the metabolic enzyme microarray (MetaChip). They developed an enzymatic microarray using a printing technique and also the immobilisation of enzymes on the surface using alginate gels [43, Ch. 14]. They used a solid surface coated with methyltrimethoxysilane (MTMOS) to produce hemispherical spots on the surface. The compounds required for enzyme reaction, barium chloride and poly-L-lysine ($BaCl_2$-PLL) solutions, were printed onto the MTMOS coated solid surface. They were left to dry for some time and alginate solutions containing specific enzyme were printed straight on top of the compound spots, causing almost instantaneous gelation of the alginate matrix to form enzyme microarrays. Figure 2.6 shows the process of alginate gel enzyme formation and also a micrograph of the gel microspot.

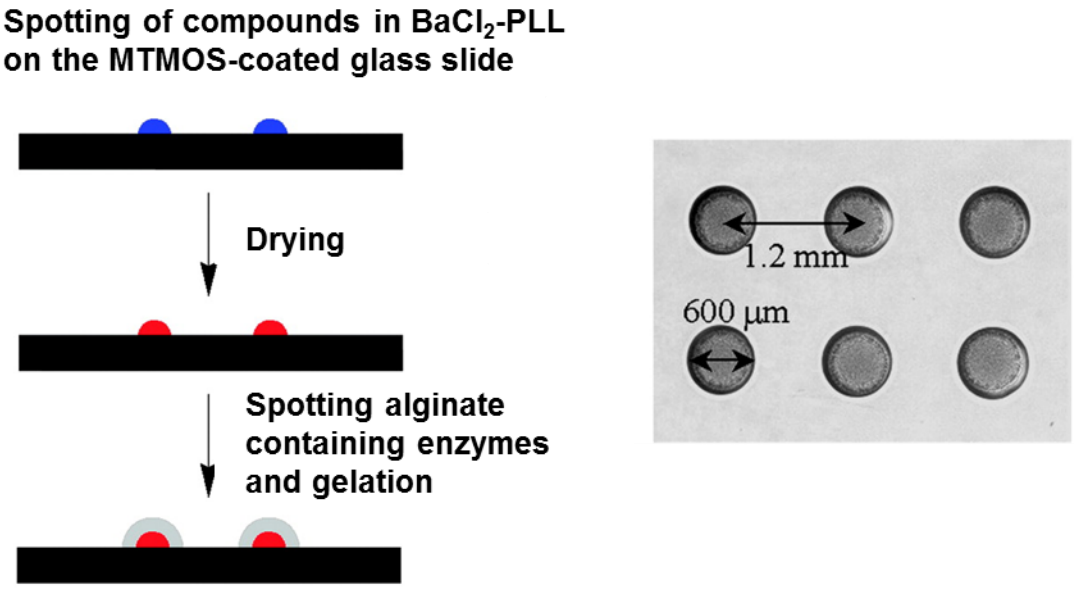

a) MetaChip process **b) Microscopic photograph of gel**

Figure 2.6 – Schematic and microscopic photograph of the gel microscpots on MetaChip [42].

2.3.2 In Situ-Synthesised Microarrays

In situ-synthesised microarrays are extremely high-density microarrays that were first developed and patented by Affymetrix and are now known as GeneChips [39]. Affymetrix GeneChip oligonucleotide microarrays are fabricated using photolithography technology used in the semiconductor industry and synthesised onto a quartz surface. The quartz surface is modified with a photochemical resist, and then it is followed by UV light exposure using a photolithographic mask on a specific area. On the unprotected regions of the surface, a specific nucleotide is added to grow the oligonucleotide. The process of cycling mask, UV light exposure, and the addition of A, C, T or G to grow the oligonucleotide creates GeneChip, shown in Figure 2.7.

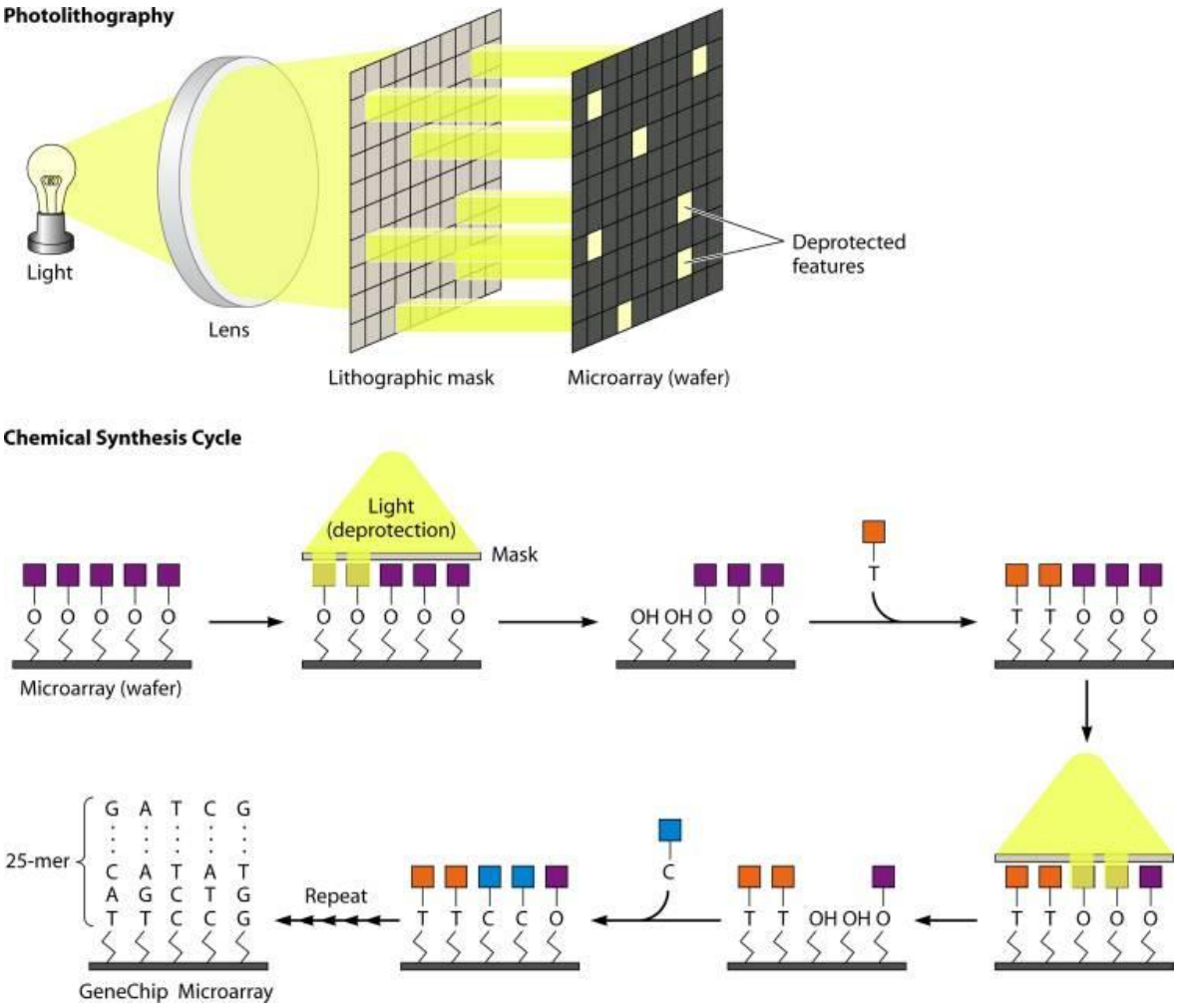

Figure 2.7 – Chemical synthesis cycle for GeneChip microarray using photolithography [39].

A later invention from Roche NimbleGen oligonucleotide microarrays used a digital mask to replace the photolithographic mask. This technology uses

programmable micromirrors for the UV light to create a pattern for the nucleotide addition. Further improvements by Agilent Technologies eliminated the need for photolithographic or digital mask. Their technology uses inkjet printing, adopted from printed microarrays, to deposit the 4 different nucleotide bases and stack them into oligonucleotide synthesised on a glass slide, as shown in Figure 2.8.

a) Inkjet printing of four different bases

b) Repeat base by base to reach required oligonucleotide length

Figure 2.8 – Agilent oligonucleotide microarray using non-contact inkjet printing [39].

In 2001, He *et al.* [44] adopted in situ-synthesised DNA microarray to form an enzyme (luciferase) microarray [45], termed PISA (protein in situ array), shown in Figure 2.9. The enzyme is synthesised from a specific DNA sequence and tagged with a DNA sequence. Then, the enzyme is attached onto the surface with another DNA tag sequence that is complementary to the one on the enzyme. However, these microarrays are expensive to customise for different enzymes and involve a lot of complex chemical synthesis.

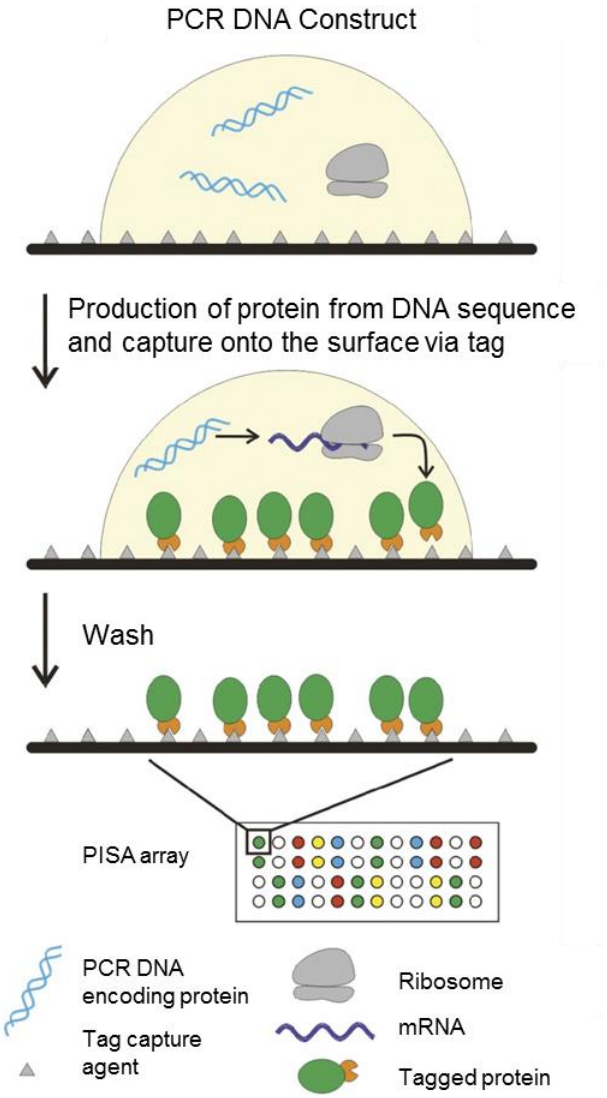

Figure 2.9 – The PISA procedure for protein microarray formation [45].

2.3.3 High-Density Bead Arrays

Bead arrays are highly packed microarray first developed by Illumina and named BeadArrays [39], shown in Figure 2.10. Unlike printed and in situ-synthesised microarrays described above, which immobilise probing molecules (DNA) directly onto a solid surface, bead arrays use different type of beads to attach the probing molecules. Illumina BeadArrays use fibre-optics bundles (an array of light-conducting fibres) or a well in silicon to accommodate the probing beads. To fabricate the well in the fibre core, a chemical etching technique is used. To form the silicon well, micro-electro-mechanical-systems technology is employed. In contrast to the known location on the surface using printed or in situ-synthesised microarrays, beads with different covalently bonded probing molecules are randomly arranged into each of the microwells. Hence, a technique to identify the location is important. Typically for DNA bead

microarrays, the location is identified with fluorescently labelled complementary base pairs through hybridisation. Each bead has a unique capture oligonucleotide to serve as an identifier, which is specifically avoided the human DNA sequence. Bead arrays have been successfully applied to semiconductor integrated circuits for genome sequencing by Life Technologies (now Thermo Fisher Scientific), called Ion Torrent [4]. They have demonstrated 1.2 million microwells of bead arrays for large scale and low cost genome sequencing. The technology will be further explained in Section 2.4.3.

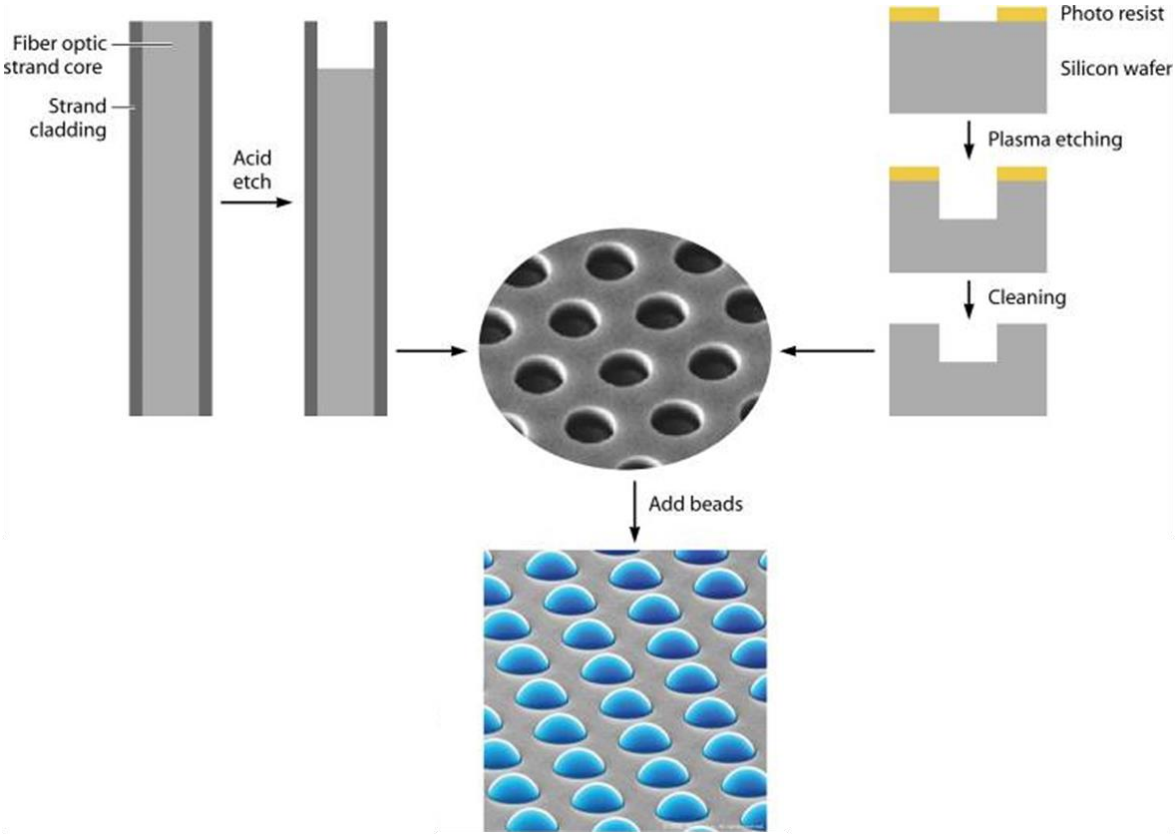

Figure 2.10 – Illumina BeadArray using fibre optics bundles (left) or silicon wafer (right) [39].

2.3.4 Electronic Microarrays

All the microarray technologies that are described above rely on the passive attachment of probing molecules onto the surface. Electronic microarrays provide an active attachment of probing molecules to a specific location using electric fields. Nanogen's "NanoChip" was the first electronic approach to create a DNA microarray [39]. It only has 400 spots of probing molecules. It uses a positive current to activate several specific sites on the microarray and allows formation of a binding agent on the surface. Negatively charged DNA probes are

attracted to the site and create a bond with the binding agent. The greatest advantage of this microarray is the ability to combine it with semiconductor technology to address the probing molecules locations. This would enable semiconductor technology to create a complete system for immobilisation of probing molecules to sensor system. However, electronic microarrays do not provide a high-throughput analysis for large scale genome sequencing compared to other microarray technologies. The Nanogen microarray technology was discontinued in 2007 due to lack of demand.

2.4 Sensor System on Chip

In the wake of the Human Genome Project that revolutionised healthcare, the cost of genome sequencing has been substantially reduced, with the goal of reaching the $1,000 genome [2]. With the demand of increasing number of genomes being sequenced per year, in order to transition sequencing instruments from small-scale biomedical research efforts to diagnostic in clinical laboratories, with the aim of one day reaching the hands of a physician, a repeatable large scale manufacturing process is needed.

In parallel to the development of personalised medicine, the electronics industry is also advancing, especially low cost, large scale and high quality manufacturing techniques for integrated circuits. The present dominant manufacturing technique is called complementary metal oxide semiconductor (CMOS) technology. CMOS has revolutionised modern computing, with the invention of digital logic chips such as microprocessors and memory. This can be seen from the transformation of the computer from as big as a room to current portable computing devices. A more recent advancement of CMOS has led to the commercialisation of digital camera and mobile phone communications using mixed digital-analogue signal chips. Mixed signal chips have enabled the possibility of creating a complete sensor system on chip. Using the analogue signal, electronic readout (voltage or current) from the sensor can be obtained, while the digital signal allows data processing and off-chip transmission. The advent of the digital camera has had an enormous impact on sensing technology. This can be observed in the evolution of the photography industry, with the displacement of chemical film technology to CMOS image sensor array chips. This

technological advancement has shown that it is important to embody a measuring device with a CMOS chip as a core component to enable large scale, high quality and low cost manufacturing. This will provide the necessary platform for both genomics and metabolomics development.

2.4.1 CMOS Technology

With the desire to miniaturise electronic systems, it was essential to replace the bulky, expensive and unreliable vacuum valve with a solid-state device [46]. The transistor, invented by Shockley, Bardeen and Brattain at Bell Laboratories [47], was the key technological breakthrough. For a decade, transistors were made individually from silicon and then assembled together to create electronic circuits. In 1976, Kilby [48] realised that this was a laborious and inefficient approach and prototyped the first integrated circuit on a single piece of silicon. The invention of the metal oxide semiconductor field effect transistor (MOSFET) enabled the first demonstration of a logic gate, presented by Wanlass and co-workers [49]. Their logic gate was built with two different transistors, nMOS and pMOS, using n-type and p-type dopants respectively; hence the name complementary metal oxide semiconductor (CMOS).

The CMOS process begins with a silicon wafer where it can be doped with an n-type impurity, doped with p-type impurity or left undoped, creating different types of silicon substrate. CMOS processes can be classified into an n-well process, p-well process or twin-well process. Figure 2.11 illustrates the common n-well CMOS process. An n-well in p-type substrate is required to create a pMOS transistor. To form an n-well on a p-type silicon substrate donor atoms such as phosphorus are implanted into the silicon substrate. Prior to ion implantation of phosphorus to form the n-well, the silicon substrate is coated with a layer of silicon dioxide for masking and an opening over the desired area is made for the n-well formation. A thin layer of silicon dioxide is then thermally grown on top of the silicon substrate, creating the gate oxide. With the same mask, a thin layer of silicon nitride is deposited to define the active region for each transistor (Figure 2.11a). When transistors are next to each other, they inadvertently will have leakage current in between them. To eliminate this, a thick field oxide is formed in the shallow trenches between the transistors, in a process called

shallow trench isolation. For even better transistor isolation, deep trench isolation can be formed as well. The silicon nitride on top of each active region is etched away and polycrystalline silicon (polysilicon) is deposited on the same location, creating the gates for each transistor (Figure 2.11b). After the formation of transistor gates, the source and drain regions are defined. For an nMOS transistor the source and drain regions are doped with donor atoms such as arsenic or phosphorus to form heavily doped n^+ diffusion regions. On the other hand for a pMOS transistor, the source and drain regions are doped with acceptor atoms such as boron to form heavily doped p^+ diffusion regions (Figure 2.11c). A thick silicon dioxide layer is deposited on top of the substrate and etched away at designated areas of the gate, source and drain, to deposit aluminium metal on top of them and introduce interconnects between devices (Figure 2.11d). Modern CMOS processes have multiple metal layers to create interconnects, with silicon dioxide layers in between each metal layer for isolation. After top metal layer is realised, a thick silicon dioxide layer is deposited as passivation to provide electrical, mechanical or chemical protection to the internal circuitry. A thin layer of silicon nitride is deposited on top of this for extra protection to liquids. Finally, the dielectric on top of the bond pads is etched away to enable wire bonding and allow connection to external circuitry.

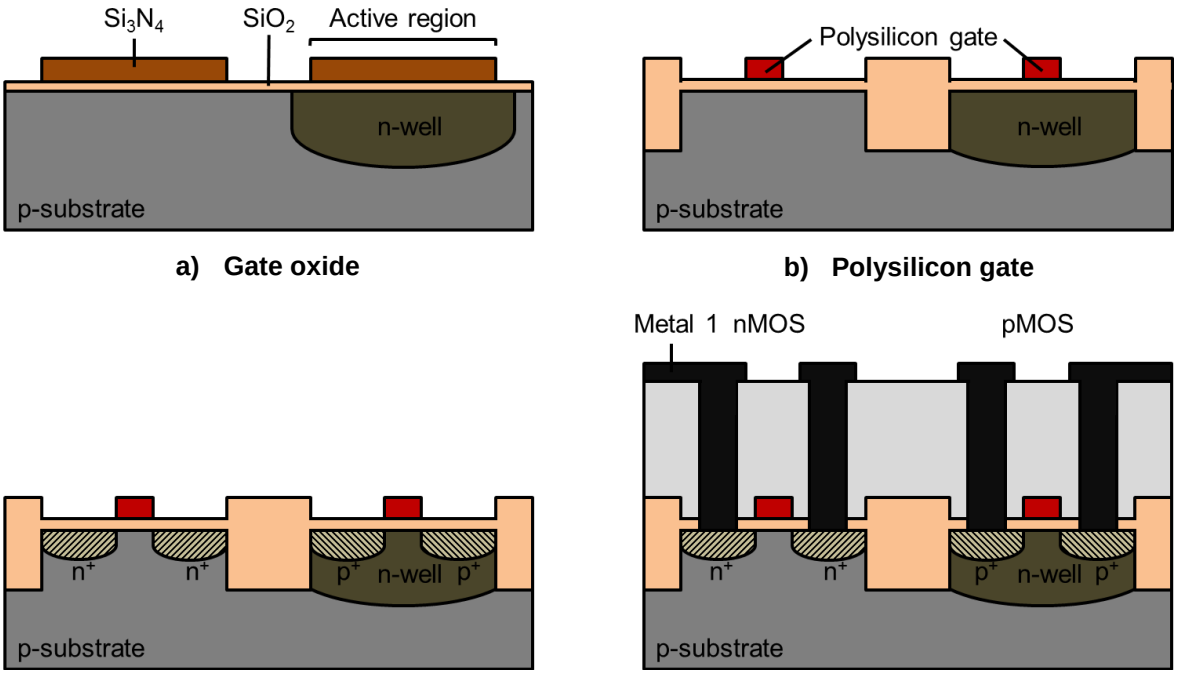

a) Gate oxide **b) Polysilicon gate**

c) Source and drain **d) Metallisation**

Figure 2.11 – Cross-section through an n-well CMOS process at various stages.

2.4.2 CMOS based Chemical Sensor System

With the rapid advancement of CMOS technology, various attempts have been made to fabricate chemical sensors on a silicon substrate [50]. Micro-electro-mechanical-systems (MEMS) have enabled the two-dimensional CMOS based chemical sensor integrated system to be extended to three dimensions by using micromachining techniques. Either bulk or surface micromachining is used. Bulk micromachining uses wet or dry etching to remove bulk silicon and create a sensing structure underneath the bulk silicon [51]. Surface micromachining keeps the silicon intact and uses a sacrificial layer that can be easily etched away to create three-dimensional sensing structures [52].

CMOS technology provides a platform for sensor integration with various attributes such as device miniaturisation capability, low power consumption, rapid response, high yield and low cost manufacturing [50]. As a consequence, various sensors with different physical characteristics have been implemented using CMOS technology.

- **Chemomechanical sensors** respond to the mass of species collected on the sensing layer. The mass can be detected through the deflection of a micromechanical structure or the frequency of a resonating structure or a travelling acoustic wave.

- **Thermal sensors** detect the change in temperature using a thermocouple as a sensing material. It can be measured either through the resistance of the thermocouple or the voltage difference of two different thermocouples.

- **Optical sensors** use silicon-based photodiodes or other semiconductor materials to detect the change in light intensity.

- **Electrochemical sensors** measure the voltage, current or resistance due to charge transfer from a chemical reaction.

The idea of building a complete computer using one single chip is called system-on-chip. This idea has inspired CMOS based sensors and readout circuitry to be integrated in one single chip rather than using printed circuit board.

One of the early works of a sensor system on chip was demonstrated by Yeow *et al.* [53] in 1997. The sensor system on chip consisted of a 15 × 16 array of pH-ISFET with integrated readout circuitry. However, this was not fully compatible to a standard CMOS process since four new masks and four extra processing steps were required to complete the device. A far more superior sensor system on chip was reported by Hagleitner *et al.* [54] in 2001. The sensor system had demonstrated the capability of a CMOS smart gas sensor using three different transducers: mass-sensitive cantilever, calorimetric sensor and temperature sensor, together with integrated readout and signal conditioning circuits. An analogue-to-digital converter (ADC) was incorporated to improve signal-to-noise ratio in order for a robust digital signal to send off-chip. The complete sensor system was fabricated using an unaltered CMOS process with a few micromachining steps for the cantilever and calorimetric sensor. Figure 2.12a illustrates the device.

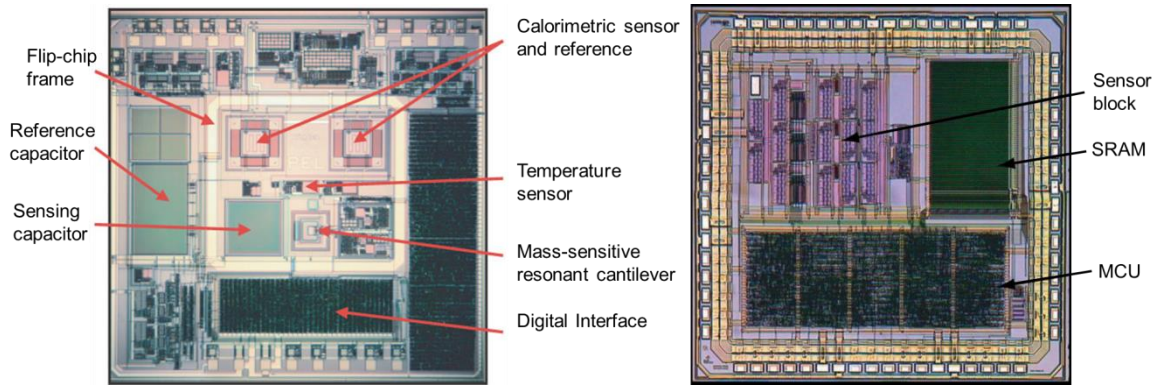

a) Gas sensor [54] **b) pH sensor** [55]

Figure 2.12 – Microphotograph of two sensor systems on CMOS chips.

In 2005, Hammond *et al.* [55] demonstrated that the system-on-chip could be developed into a capsule-based device using an ion sensitive field effect transistor for *in vivo* diagnostic applications. Figure 2.12b shows the device. An on-chip programmable microcontroller unit (MCU) was designed to control the whole system for collecting and processing pH data, which can be stored in static memory (SRAM) or transmitted to the outside world using an off-chip radio transmitter. The whole system was fabricated using an unmodified CMOS

process. A more recent system-on-chip approach in the biomedical field was presented by Huang *et al.* [56] for monitoring real-time multiple physiological parameters for the human body. The sensor system consisted of four different types of sensors: MEMS with modified hydrogel, nanowire, ISFET and bipolar junction transistor, to detect glucose, protein, pH and temperature respectively. The complete system had a digital processor to control almost all the functions including signal processing and additional circuitry including an ADC, signal amplification and a wireless transmitter to send to the outside world. This smart system was also self-powering with on-chip circuitry to receive two different off-chip harvesting energy capabilities: solar cell and RF coil. Figure 2.13 illustrates the overall system architecture.

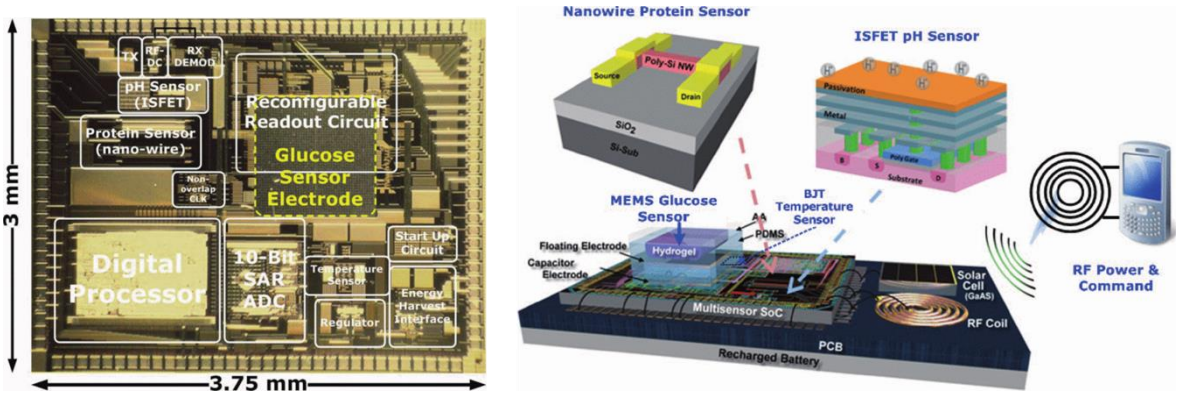

a) Chip microphotograph **b) Cross-section view of sensors**

Figure 2.13 – Microphotograph and overall system architecture of the most recent multiple sensor systems on a CMOS chip [56].

2.5 The Ion Sensitive Field Effect Transistors

The largest and oldest group of chemical sensors are electrochemical sensors, many of which are commercially available. Similar to the transistor replacing the vacuum valve, a solid-state device was required to replace the glass electrode as an electrochemical sensor. As a consequence, the ion sensitive field effect transistor (ISFET) was introduced by Bergveld [57] in 1970 as the first miniaturised silicon-based chemical sensor. The operation and physical characteristics of the ISFET are almost similar to the conventional MOSFET with the exception that the metal gate electrode is removed, exposing the gate oxide (Figure 2.14).

Bergveld initially carried out a simple experiment with an ISFET by applying a constant voltage across the source and drain, and exposing the native silicon dioxide (SiO_2) to an aqueous solution. In order for him to carry out ISFET experiments with aqueous solution, it is important that all the electrical contacts to source, drain and substrate are well insulated with epoxy resin. He found that the drain current of the device varied with the molarity of sodium chloride (NaCl) in the solution, with constant pH. Not long after, Bergveld reported that SiO_2, the ion sensing membrane, is sensitive to the molarity of both sodium (Na^+) ions and hydrogen (H^+) ions, but with different sensitivity [58]. In his publication, Bergveld also demonstrated the measurement of extracellular ion pulses with a guinea pig taenia coli, using an ISFET. Ever since its introduction, the ISFET has captured the interest of researchers towards various applications.

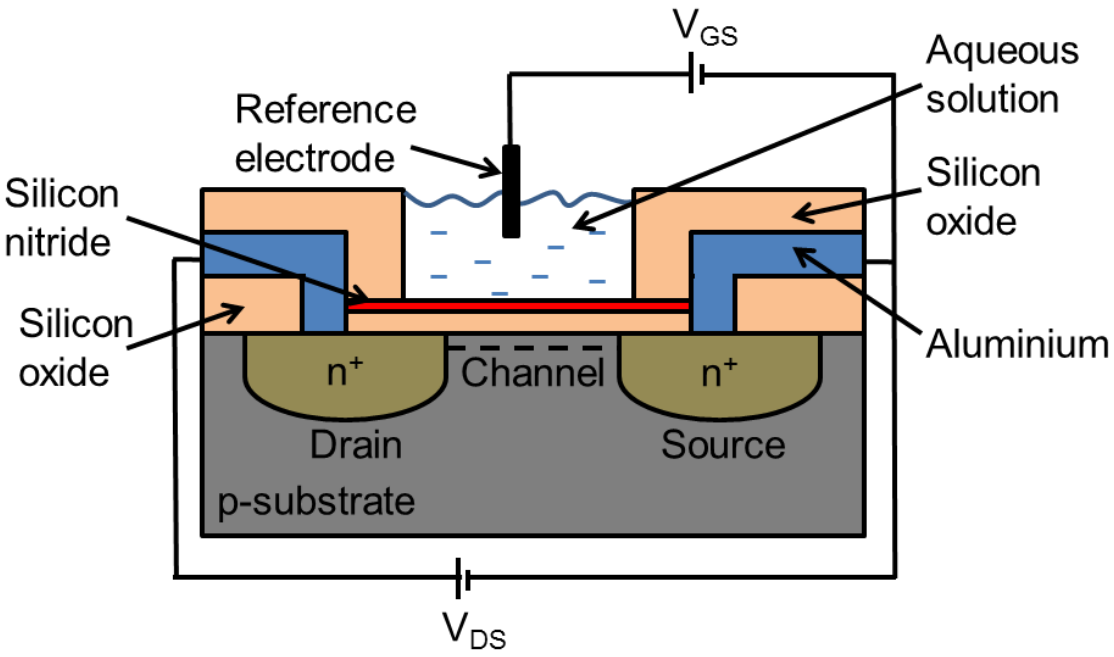

Figure 2.14 – Cross-section of an ISFET with silicon nitride as the sensing layer.

2.5.1 Fabrication Materials

The capability of ISFET to detect different ions species is dependent on the gate dielectric material. Moreover, this material acts as a protection for the ISFET's channel from aqueous solution. Therefore, it is very important to explore a good sensing dielectric material for ISFET. A few years after the first introduction of the ISFET, Matsuo and Wise [59] made an improvement of the measurement

configuration by using silicon nitride (Si_3N_4) as the ion sensing layer as it provided better stability as the gate dielectric. The device had two dielectric layers on top of the gate, which were thermally grown SiO_2 at the bottom and Si_3N_4 on top which was in direct contact with the aqueous solution. The ISFET was located at the tip of a probe structure with SiO_2 covering the whole device to insulate the underlying circuitry and the SiO_2 was selectively removed over the sensor area creating a cavity. In addition, the device was immersed in the solution together with a reference electrode to control the drain current. The results from the experiments had shown pH sensitivity that was similar to a conventional glass electrode but with slight sensitivity towards Na^+ and potassium (K^+) ions. Hence, this has fuelled the research towards using the ISFET as a miniaturised pH meter.

Table 2.2 – Chemical characteristics of various sensing layers on the gate of an ISFET [60]

Characteristics	**SiO_2**	**Si_3N_4**	**Al_2O_3**	**Ta_2O_5**
pH range tested	4 – 10	1 – 13	1 – 13	1 – 13
pH sensitivity (mV/pH)	25 - 35 (pH > 7) 37 – 48 (pH < 7)	46 – 56	53 – 57	56 – 57
Sensitivity (mV/pX) Na^+ K^+	 30 – 50 20 - 30	 5 – 20 5 - 25	 2 2	 < 1 < 1
Response time (95%) (s) (98%) (min)	 1 Undefinable	 < 0.1 4 – 10	 < 0.1 2	 < 0.1 1
Long term drift (mV/h, pH 7)	Unstable	1.0	0.1 – 0.2	0.1 – 0.2
Hysteresis	Unstable	3.0	0.8	0.2

Si_3N_4 fulfils the requirements as an ISFET gate oxide being waterproof, chemically inert and an excellent barrier for ion migration. However, the pH sensitivity of Si_3N_4 degrades with the increment of oxygen content in the film. As a consequence, this motivated Matsuo and Esashi [60] in 1981 to investigate several different kinds of dielectric material as ISFET sensing layer. These materials were SiO_2, Si_3N_4, aluminium oxide (Al_2O_3) and tantalum pentoxide

(Ta_2O_5). Their findings of these gate oxide materials are summarised in Table 2.2. In their investigation, they found that SiO_2 was the poorest material to be used as pH sensing layer, with a sensitivity of 25 – 48 mV/pH and nonlinear dependence to pH. Si_3N_4 gave an improvement in pH sensitivity, with a sensitivity of 46 – 56 mV/pH and a near linear response to pH. Due to the decrement of pH sensitivity with oxygen content in Si_3N_4, Al_2O_3 and Ta_2O_5 were studied as gate oxide sensing layers. Al_2O_3 showed a sensitivity of 53 – 57 mV/pH while Ta_2O_5 showed a sensitivity of 56 – 57 mV/pH, with both materials displaying a near linear response to pH. In addition, both Al_2O_3 and Ta_2O_5 have shown almost zero sensitivity towards Na^+ and K^+ ions. Hence, these two materials are very selective to H^+ ions and are excellent for pH sensing.

Table 2.3 – Different uncommon sensing layer that have been studied in the literature

Materials	pH range	Sensitivity (mV/pH)	Reference
Zirconium dioxide (ZrO_2)	1 - 10	56	[61]
Tin dioxide (SnO_2)	2 – 10	58	[62]
Silicon oxynitride (SiO_xN_y)	2 – 8.3	57 – 57.8	[63]
Iridium oxide (IrO_2)	1.5 - 12	51.1 – 51.7	[64]
Indium nitride (InN)	2 - 12	58.3	[65]
Indium tin oxide (ITO)	2 - 12	58	[66]
Praseodymium titanium oxide ($PrTiO_3$)	2 - 12	53.2 - 56.8	[67]
Ruthenium dioxide (RuO_2)	2 - 10	59.15	[68]
Holmium oxide (Ho_2O_3)	1 - 13	57	[69]
Erbium (III) oxide (Er_2O_3)	1 - 13	57.58	[70]
Borazon (BN)	1.8 – 10	50 – 59	[71]
Platinum (Pt)	1 - 5	25.1	[72]
Titanium nitride (TiN)	1.68 – 10.01	59	[73]

Various other materials have also been investigated for use as pH-ISFET dielectric sensing layers in order to increase the pH sensitivity e.g. zirconium dioxide (ZrO_2), tin dioxide (SnO_2), silicon oxynitride (SiO_xN_y), iridium oxide (IrO_2), indium nitride (InN), indium tin oxide (ITO), praseodymium titanium oxide

($PrTiO_3$), ruthenium dioxide (RuO_2), holmium oxide (Ho_2O_3), erbium (III) oxide (Er_2O_3) and borazon (BN). Some efforts have also been made to reduce the response time to ionic solution and improve long term stability with materials such as platinum (Pt), titanium nitride (TiN) and iridium oxide (IrO_2). The pH sensitivities for all the materials are presented in Table 2.3. Despite intense efforts at finding a material with high pH sensitivity, Si_3N_4 still remains the favourite choice among researchers since it is the default passivation layer for standard CMOS process. Besides that, various other materials have also been investigated to target different ionic species such as membranes containing valinomycin for K^+ ions [74], crown ethers for Na^+ ions [75] and tetracyano-quinodimethanecopper (TCNQ) for copper (Cu^{2+}) ions [76].

2.5.2 CMOS Integration

After Bergveld's description of using a solid-state device as a biosensor or chemical sensor, it has become a topic of interest to incorporate the device with integrated circuit technology into one single chip. CMOS technology is a standard process, which has been widely used for integrated circuit fabrication. Hence a great amount of interest is concentrated on utilising this technology to develop CMOS based ISFETs. However, the development of ISFET does not require polysilicon gate which acts like a mask to define self-aligned source and drain regions. Besides that, ISFET requires a chemical sensitive dielectric sensing layer which has to be deposited at a higher temperature than conventional metal layers. Consequently, the initial fabrication of CMOS based ISFET has been focussed on modifying or extending the standard CMOS process.

The early attempt from Bousse *et al*. [77] was concentrated on modifying the existing CMOS process to fabricate the ISFET. The standard n-well CMOS process was used and the processing steps remained the same throughout until the metallisation stage for interconnects. Tungsten silicide was used as the interconnect material instead of aluminium due to its resistance to high temperature in later processing steps. Silicon dioxide was deposited onto the metal interconnect and polysilicon which then followed by photolithography step to define the area above the polysilicon. The SiO_2 was etched away while retaining the polysilicon as a floating conductor in the insulator. The remaining

polysilicon did not affect the capacitance of the gate and had no negative effect to the ISFET sensitivity, while protecting the silicon substrate from ambient light. Si_3N_4 was deposited with low-pressure chemical vapour deposition (LPCVD) at 785°C across the whole surface and the opening window above the gate. The high temperature was not an issue as tungsten silicide has a high resistance towards high temperature. Therefore, the initial development of CMOS based ISFET required quite a lot of changes to the standard process.

Later, Wong and White [78] fabricated an ISFET using a standard CMOS process without any modification until just before the contact windows were to be opened. The polysilicon and the gate oxide were wet etched away and left with the bare silicon. After that, a thin oxide layer was regrown above the silicon and a chemically sensitive dielectric layer, Si_3N_4 and Ta_2O_5 deposited on top, one after another, using LPCVD and RF magnetron sputtering respectively. The standard CMOS process followed with the opening of contact windows and deposition of aluminium.

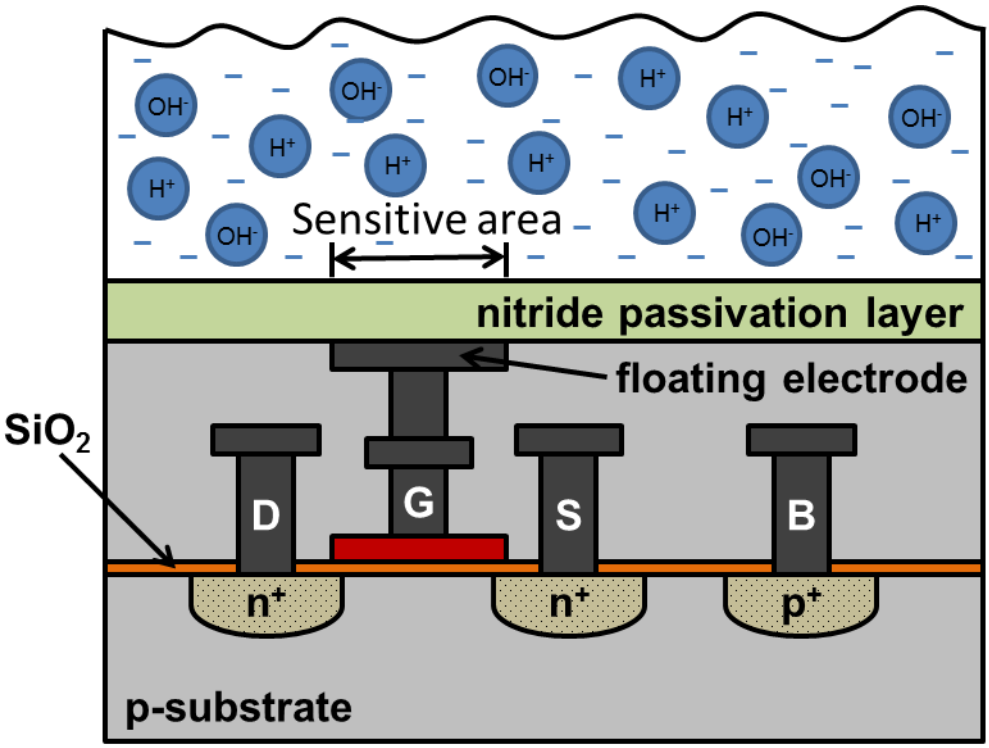

Figure 2.15 – Cross-section through an ISFET fabricated in an unmodified standard CMOS process.

Both processes had shown that a modified CMOS process was required to fabricate a CMOS based ISFET. This was the case until Bausells *et al.* [79]

demonstrated the capability of fabricating an ISFET with an unmodified two-metal CMOS process, shown in Figure 2.15. The device used silicon oxynitride (default passivation layer from foundry) as the ion sensing layer and also had an electrically-floating gate structure with polysilicon connected to two metal layers, similar to the structure proposed by Bousse and co-workers. The device had shown a sensitivity of 47 mV/pH. Using an unmodified commercial CMOS process to integrate the ISFET has simplified the circuit design and allowed the ability to use the tools and libraries provided by the foundry. This has led to the implementation of arrays of ISFET sensors with integrated readout circuits by Milgrew *et al.* [80] and Balazs *et al.* [81], [82], creating an ion imaging camera, illustrated in Figure 2.16.

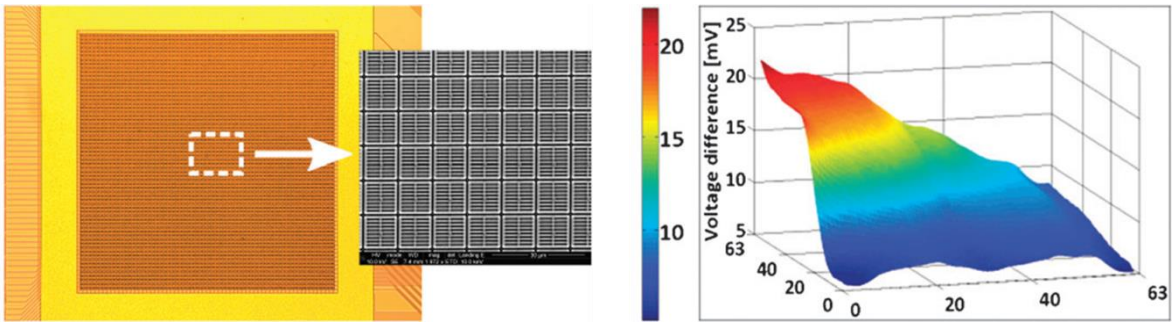

a) Chip microphotograph **b) pH fluctuation on chip**

Figure 2.16 – Arrays of ISFET sensors using an unmodified CMOS process as an ion camera [82].

2.5.3 Applications for ISFET Biosensors

The first demonstration by Bergveld that the ISFET could be used for extracellular detection led to the use of CMOS array ISFETs to monitor ion fluxes from both natural and artificial systems. However, ISFET capability is far more powerful and not just limited to extracellular imaging. A decade after the discovery of ISFET, Caras and Janata reported the first use of ISFET to detect penicillin directly via modification with an enzyme. This has created a basis for the ISFET to be used as a biosensor and numerous efforts have been made to incorporate different bio-recognition materials such as DNA and enzymes on ISFETs for biological detection, which could revolutionise the field of personalised medicine.

With the discovery of SNP genotyping, various attempts have been made to use the ISFET as a DNA sensing platform, which are normally performed with fluorescent nucleotides and detection following hybridisation, using optical imaging technology. The ISFET as a pH sensor normally measures the equilibrium of H^+ and OH^- ions in a solution that corresponds to the electrochemical double layer formed on top of gate insulator, which in turn affects the interface potential on the gate insulator. A detailed theoretical explanation is given in Chapter 3. Therefore, Estrela *et al*. [83] proposed that any immobilised bio-molecular interaction on top of the gate and electrolyte interface could change the potential across the double layer, which then modulates the potential applied to the gate of a field effect transistor. In their work, they immobilised single-stranded DNA on the surface of a metal, on top of an ISFET, and then the interaction of the complementary DNA gave a shift in voltage. They were able to detect a voltage shift with a DNA strand that had a mismatch of 3 nucleotide bases. This has presented a possibility of SNP detection. In 2006, Purushothaman *et al*. [84] demonstrated a much more sensitive procedure for single nucleotide mismatch detection using an ISFET. They immobilised single-stranded DNA on the sensing layer of the ISFET, then DNA polymerase and complementary nucleotides were added to give a potential shift. The incorporation of a nucleotide onto the single-stranded DNA would produce a proton, which acts as a marker. This technique was introduced by Sakurai and Husimi [85] in 1992 and showed the DNA polymerase incorporation reaction and subsequent hydrogen ion released could be sensed by an ISFET. However, this was only done in bulk reaction where all the nucleotides were incorporated completely to produce a potential change.

By using multiple ISFETs integrated in a CMOS process on a single chip and the capability of measuring SNP, in 2011 Ion Torrent (Thermo Fisher Scientific) [4] introduced the world's first non-optical genome sequencing, ion chip (Figure 2.17). Using the high-density bead array technology described earlier (Section 2.2.3), the ion chip has a microwell on top of each ISFET sensor, shown in Figure 2.17c and Figure 2.17d. It is formed by etching a dielectric layer on top of the sensor all the way down to the top metal layer. To increase the sensitivity of ion chip, a metal layer is deposited on top of the top metal layer and also the side walls of the microwell. Then, a layer of Ta_2O_5 is deposited everywhere to

provide a sensitivity of 58 mV/pH. Hence, the loss of hydrogen ions to the non-sensitive side wall would be prevented. The microwell is big enough to accommodate one magnetic bead that has hundreds or thousands of the same short DNA fragments together with DNA polymerase, to amplify the signal. They have demonstrated the genome sequencing of bacterial and human genome of G. Moore. This has brought the possibility of reaching the desirable $1,000 genome and provided one of the key ingredient, genomics, to realise personalised medicine.

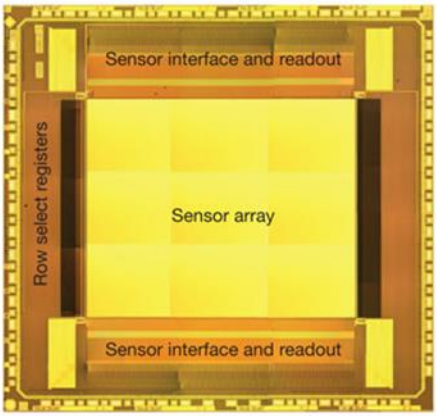

a) Chip microphotograph

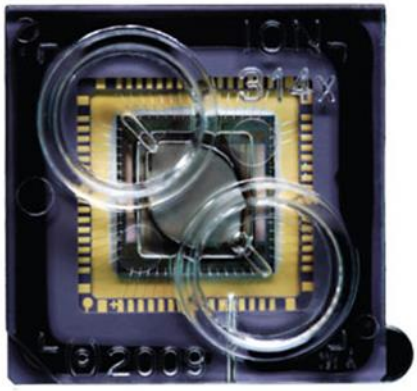

b) Full packaged chip with fluidics

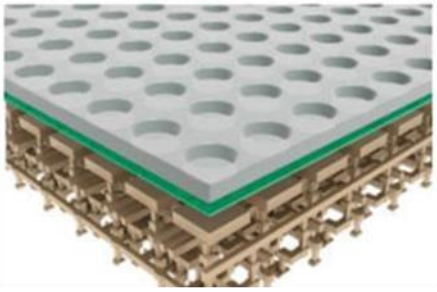

c) 3D cross-section of well

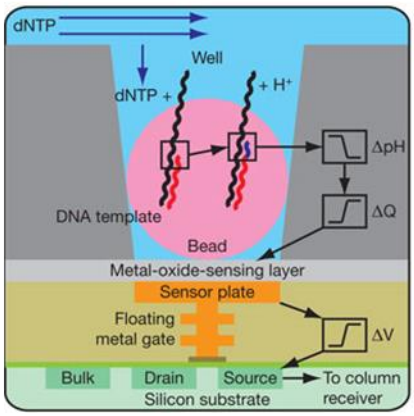

d) Sensor, well and chip operating system

Figure 2.17– Ion Torrent genome sequencing chip, packaging, well cross-section and working mechanism [4].

As previously discussed, the current methods for studying the metabolome rely on huge and expensive machinery, and more importantly there is no single apparatus or device that can detect the entire metabolome. Since the first use of an ISFET modified with an enzyme on top, called ENFET, for penicillin detection [86], a lot of effort has been made to use the enzyme ISFET for metabolite detection e.g. glucose [87], urea [88], creatinine [89], heparin [90],

acetylcholine [91], glutamate [92] and etc. In 1986, Hanazato *et al*. [93] demonstrated the first multi-enzyme ISFET using the enzymes glucose oxidase and urease for the detection of their corresponding metabolites, glucose and urea, respectively. As the discovery of ions chips brought genome sequencing to the foreground, the vision of this work is to integrate ISFET and other chemical sensors using CMOS technology to create a low cost multi-enzyme platform for metabolome detection.

2.6 Summary

In this chapter, personalised medicine was defined and a brief history outlined. The microarray technologies and SNPs genotyping from genomics that made personalised medicine a reality were introduced. The technological advancements in genomics which has formed a basis for personalised medicine were detailed. The limitations of using genomics for personalised medicine were described and act as motivation for studying metabolomics. Microarray technologies were described in detail, with an emphasis on how to adapt these technologies from genomics to metabolomics. Since the current instrumentations for metabolome detection are expensive, huge and require multiple tools, CMOS technology was introduced as the most established low cost and large scale manufacturing alternative. Also, further advancements in CMOS technology and MEMS were highlighted to show that various chemical sensors can be realised and integrated into one single CMOS chip. CMOS presents itself as the low cost single platform that could be implemented for metabolome detection. The ISFET was then described, along with details on how to integrate the sensor with CMOS technology. The development of CMOS based ISFET sensor array as a biosensor was provided, which led to the invention of the personal genome machine by Ion Torrent. The next chapter will present the theory of enzymes and ISFET.

Chapter 3 : Theory

3.1 Introduction

The previous chapter reviewed the background literature relevant to the development of an integrated CMOS sensor array technology, in order to advance personalised medicine specifically focussing on genomics and metabolomics. This chapter introduces enzymes and their fundamental theory to quantify metabolites using enzyme kinetics, and describes the different methods used for enzyme assays in this work. The chapter later presents the fundamental theory of pH measurement that initially required a conventional glass electrode and the need of a solid-state device, which sparked the development of the first miniaturised solid-state chemical sensor, the ISFET. The operating principle of ISFET is also explained, together with the mechanism known as the "site-binding model" to determine the pH response of the ISFET sensing material. In addition, the relationship between absorbance and concentration of absorbing substance in an aqueous solution is explained by Beer-Lambert Law.

3.2 Enzymes

All life-forms, from viruses to human beings, depend on a set of chemical reactions to sustain life, which is maintained by biological catalysts called enzymes [94, Ch. 1]. These chemical reactions involve building, breaking or modifying chemical compounds and enzymes are used to accelerate the rate of these reactions. Besides their ability to speed up chemical reactions, enzymes also possess a unique characteristic called specificity, where they are able to recognise specific chemical compounds or substrates to act on and ignore everything else. As described in Figure 3.1, these enzymatic processes actually act like a "lock and key" mechanism, where enzymes are biologically shaped as locks (active-sites) and only the correct keys (substrates) can trigger the chemical reaction [95, Ch. 7]. In addition, enzymes are not consumed in the reaction and can be used again after the chemical reaction. Figure 3.2 shows a pectinase enzyme in the process of catalysing a specific substrate.

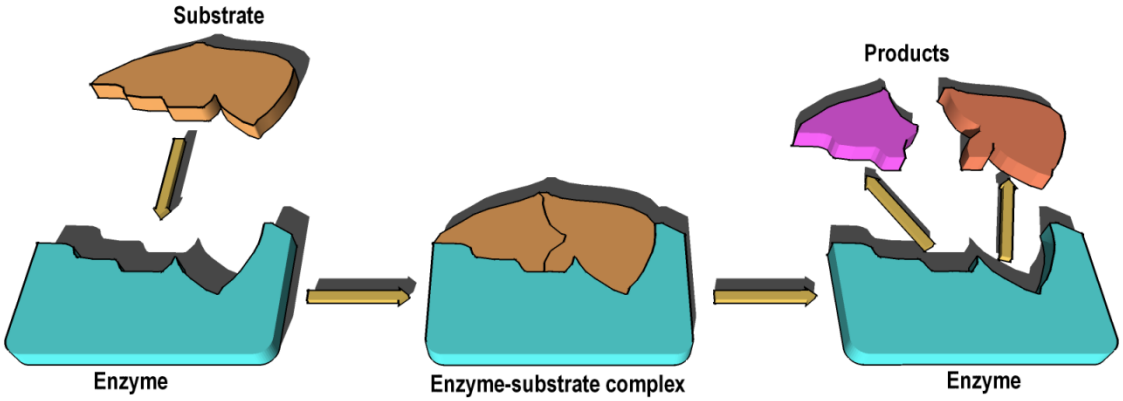

Figure 3.1 – The lock-and-key model for an enzyme reaction.

Since the discovery of enzymes, a lot of industries have been increasingly exploiting their potential in food [96], beverages [97] and detergents [98]. Due to enzymes' highly selective nature, they are also used in medical diagnostics as biomarkers to detect specific substrates [99], [100]. In an enzyme-catalysed reaction, the amount of substrate converted to product can be measured using different analytical methods such as spectrophotometry, electrochemistry, chemiluminescence or fluorescence [101, Ch. 1]. Hence, various diagnostic tools have been developed with specific enzyme to quantify metabolite from different biological analytes such as blood serums, urine, tears and sweat [102], [103, Ch. 2].

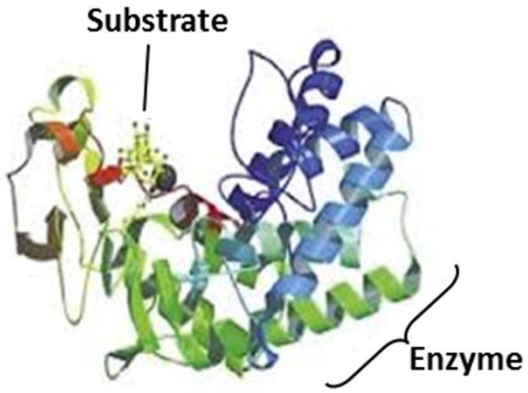

Figure 3.2 – A pectinase enzyme in the act of catalysis, where the substrate pectate (yellow) is diffusing into the active-site of the enzyme [104].

3.2.1 Enzyme Kinetics

To use enzyme as a biological sensor for detecting metabolite, the fundamental mechanism of enzymatic reaction has to be understood. In all types of chemical

reactions, both non-catalysed and catalysed, kinetic studies are used to understand them. In measuring the amount of substrate corresponding to the product of an enzyme-catalysed reaction, the most common question is the influence of time on both substrate and product. In every chemical reaction, the conversion of substrate to product undergoes a few states where some bonds are broken or formed, and the highest energy in between this transformation is called transition state. It is the limiting factor for a chemical reaction. Figure 3.3 illustrates the free energy of the substrate, transition state and product in a so called reaction coordinate diagram. The energy difference between the substrate and product shows which direction of the reaction is more thermodynamically favourable, and does not tell the reaction rate. The free energy between the substrate and transition state is called free energy of activation (ΔG_{act}), where the lower it is the faster the chemical reaction. In order to lower the activation energy and speed up reaction, enzyme acts as a catalyst to stabilise the transition state or find a lower energy pathway.

Figure 3.3 presents the coordinate diagram for both enzyme-catalysed and non-catalysed chemical reactions. An enzyme-catalysed reaction is a multi-step progression that involves several intermediates. At this point, it is important to differentiate between an intermediate and a transition state. An intermediate is a stable/semi-stable chemical species formed during a reaction, known as a local energy minimum, whereas a transition state known as a local energy maximum. For an enzyme to stabilise the transition state, the substrate and enzyme would come together and form a reversible enzyme-substrate complex, ES. This will lead to the formation of a stabilised enzyme-transition state complex ($ES^{\ddagger}$). During the transformation of substrate (ground state) to the transition state structure, the enzyme would provide functional groups in the active-site for necessary interactions to stabilise the transition state structure and bind it tighter than to the substrate [105, Ch. 3]. The more stable the ES complex, the lower the free energy for activation and increase of the reaction speed. Finally the formation of an enzyme-product complex, which can then be dissociate to product molecules and free enzyme for catalysis again. The enzymatic reaction is given below:

$$E + S \rightleftharpoons E \cdot S \rightleftharpoons E \cdot P \rightleftharpoons E + P \qquad 3.1$$

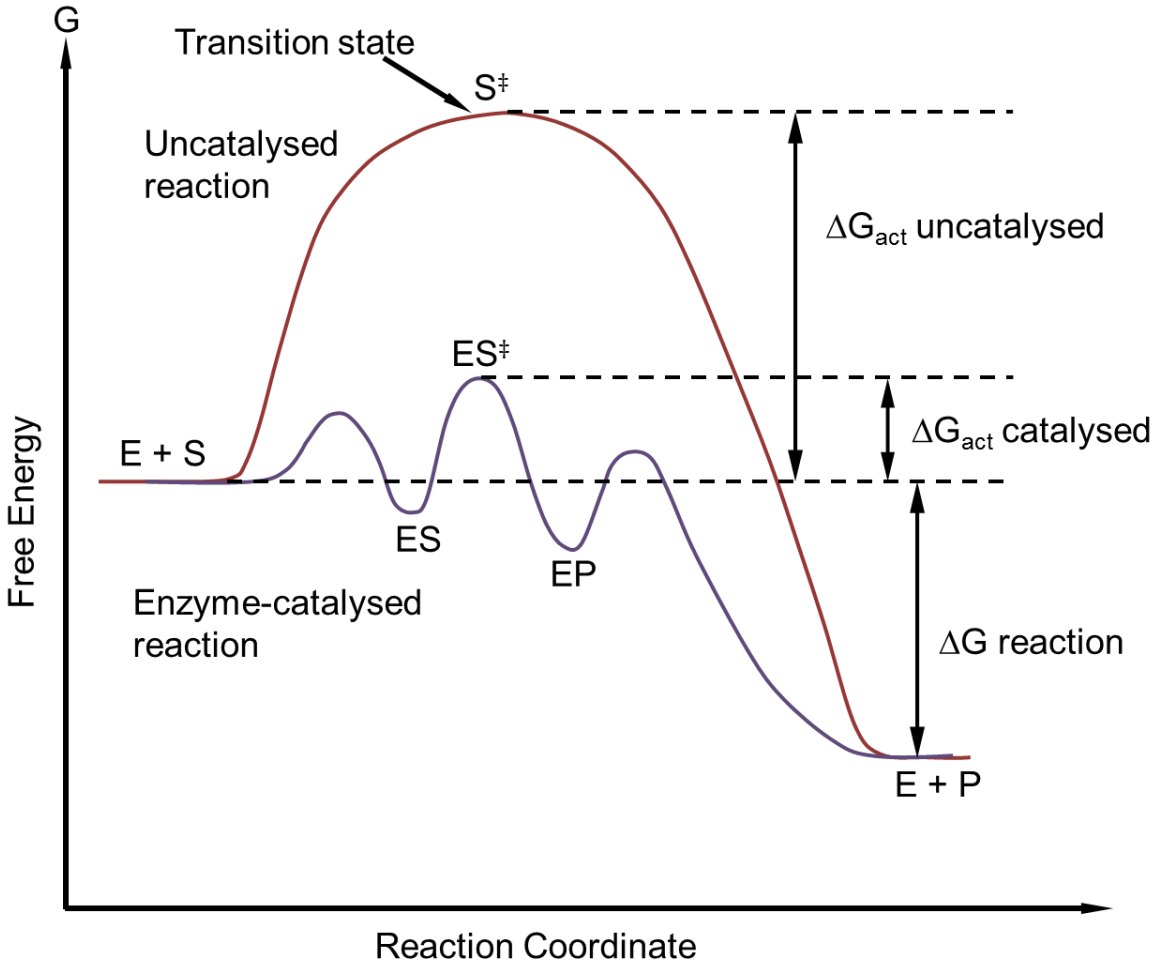

Figure 3.3 – Free energy profile of uncatalysed (red) and enzyme-catalysed reaction (purple) [105, Ch. 3].

As discussed above, an enzyme can accelerate a chemical reaction by lowering the activation energy. However, all enzymes have different catalytic power called the turnover number. It is defined as the maximum number of substrate molecules converted to product by one enzyme molecule per second, under conditions at which the concentration of all substrates is saturating. Hence, all enzymes will have different rate/velocity conversion of substrate to product.

In any chemical reaction, the rate/velocity of the chemical reaction is described by the rate constant *k*:

$$A \xrightarrow{k} B \qquad\qquad A + B \xrightarrow{k} C + D \qquad 3.2$$

In a non-catalysed chemical reaction, the reaction rate is proportional to single substrate, two substrates or independent of substrate concentration respectively, as described:

First order	Second order	Zero order	
$\nu = k \times [A]$	$\nu = k \times [A] \times [B]$	$\nu = k$	3.3

where the rate constant k has a unit of s^{-1} and ν is change of substrate concentration with time in second.

However an enzyme-catalysed chemical reaction is more complex; simple equations like those above are not adequate to fully described enzyme kinetics. In 1913, Michaelis and Menten [106] provided the mathematical model for the analysis of enzyme reactions mechanisms [107, Ch. 2], [108, Ch. 2]. There are a few assumptions in Michaelis-Menten kinetics [109, Ch. 4]:

- There is only one substrate change in the chemical reaction.
- The substrate concentration is a lot higher than enzyme concentration.
- The initial reaction rate is taken into account, where the product concentration is still very low.
- The course of chemical reaction observation is very short, where the change in substrate and product concentration is very little.

With these assumptions, not all enzyme reactions follow Michaelis-Menten model but it is a useful model to describe a wide range of enzymes [105, Ch. 3].

As described in Equation 3.1, there are three steps in an enzymatic reaction. At low product concentration in the initial state of the reaction, the reverse reactions of $E.S \rightleftharpoons E.P \rightleftharpoons E + P$ are neglected and yield:

$$E + S \underset{k_{-1}}{\overset{k_1}{\rightleftharpoons}} E \cdot S \xrightarrow{k_{cat}} E + P \qquad 3.4$$

Hence, Equation 3.4 gives the velocity of product formation, which can also be defined as the rate of the overall reaction:

$$\nu = k_{cat} \times [E \cdot S] \tag{3.5}$$

When the substrate concentration is a lot higher than enzyme concentration, the upper limit of ν will be achieved. Therefore, all enzyme molecules are present as ES complexes and Equation 3.5 can be redefined as:

$$\nu_{max} = k_{cat} \times [E_T] \tag{3.6}$$

where ν_{max} is the maximal reaction rate, k_{cat} is the enzyme turnover number and $[E_T]$ is the total enzyme concentration.

Besides the rate of product formation from Equation 3.4, the rate of formation of ES complex has to be defined as well. The ES complex could undergo decomposition into free enzyme and substrate with an equilibrium constant, known as the "true" dissociation constant:

$$K_S = \frac{[E] \times [S]}{[E \cdot S]} = \frac{k_{-1}}{k_1} \tag{3.7}$$

Most of the enzyme reactions occur when the ES complex concentration remains constant, known as steady state approximations. This was proposed by Briggs and Haldane [110] in 1925 to provide a more general description of the Michaelis-Menten approach. With the rate of formation of ES complex is to be equal to the sum of the rate of breakdown to free enzyme and substrate, and the rate of catalysis into product:

$$\underbrace{k_1 \times [E] \times [S]}_{\substack{Rate\ of\ formation \\ of\ E \cdot S}} = \underbrace{k_{-1} \times [E \cdot S]}_{\substack{Rate\ of\ dissociation \\ of\ E \cdot S\ to\ E+S}} + \underbrace{k_{cat} \times [E \cdot S]}_{\substack{Rate\ of\ product \\ formation}} \tag{3.8}$$

This gives:

$$k_1 \times [E] \times [S] = (k_{-1} + k_{cat}) \times [E \cdot S] \tag{3.9}$$

and,

$$\frac{[E] \times [S]}{[E \cdot S]} = \frac{k_{-1} + k_{cat}}{k_1} = K_m \quad 3.10$$

$$[E \cdot S] = [E] \times \frac{[S]}{K_m} \quad 3.11$$

Equation 3.10 gives the definition of the Michaelis-Menten constant, with the unit of mol l^{-1} or M. K_m is similar to the dissociation constant and normally used as a relative measure of substrate binding affinity. With rearrangement of Equation 3.10 to 3.11, it has become clear that when the substrate concentration [*S*] is equal to K_m, the free enzyme and ES complex matched up. This means that K_m is the substrate concentration at which the enzyme is half saturated with its substrate. From Equation 3.5, the reaction rate is proportional to the ES complex concentration. Hence, K_m also stands for the substrate concentration when the rate of reaction is at half maximal.

At the initial states of the reaction there is no other intermediates build-up, only ES complexes. Therefore, it can be assumed that the total amount of enzyme is:

$$[E_T] = [E] + [E \cdot S] \quad 3.12$$

From Equation 3.8, it can be further described as follows:

$$k_1[E_T][S] - k_1[E \cdot S][S] = k_{-1}[E \cdot S] + k_{cat}[E \cdot S] \quad 3.13$$

$$[E \cdot S] = \frac{k_1[E_T][S]}{k_1[S] + k_{cat} + k_{-1}} \quad 3.14$$

To obtain the Michaelis-Menten equation, Equation 3.5 is combined with 3.14 to become:

$$\nu = \frac{k_{cat}k_1[E_T][S]}{k_1[S] + k_{cat} + k_{-1}} = \frac{k_{cat}[E_T][S]}{\frac{k_{-1} + k_{cat}}{k_1} + [S]} = \frac{k_{cat}[E_T][S]}{K_m + [S]} \quad 3.15$$

Hence, the final Michaelis-Menten equation is given as:

$$\nu = \nu_{max} \frac{[S]}{K_m + [S]} \qquad 3.16$$

As shown in Figure 3.4, this equation can be represented graphically and can also be altered slightly to represent a Lineweaver-Burk plot, in order to determine ν_{max} and K_m.

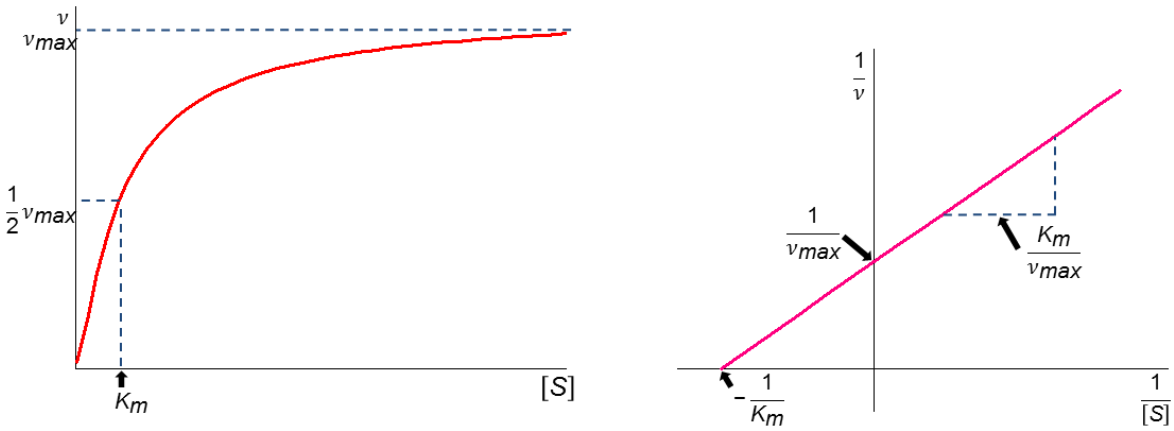

a) Typical enzymatic reaction plot **b) Lineweaver-Burk plot**

Figure 3.4 – Graphical representation of the relationship between reaction rate (v) and substrate concentration ([S]) in a typical enzymatic reaction [109, Ch. 4].

From the Michaelis-Menten equation measuring the reaction rate can be used to determine a range of different substrate concentrations. At zero substrate concentration, the velocity of the reaction is zero. When the substrate concentration doubles, the velocity doubles in proportion to the substrate concentration. When substrate concentration reaches K_m, the velocity is at half of the maximal velocity. At a high substrate concentration, where almost all the enzyme can find the substrate and react, the velocity will approach ν_{max}.

3.2.2 Enzyme Assays

Enzyme kinetics offers a wealth of information regarding enzyme-catalysed chemical reactions, providing the determination of K_m and k_{cat} from the initial velocity with different substrate concentration. In order to determine the substrate concentration, there are several different enzyme assays to measure these reactions. The following discussions will describe the types of enzyme assays that are used in this work.

3.2.2.1 Direct Assay

In an enzyme-catalysed reaction, any property change such as pH or absorbance on the substrates or products can be measured directly using detection techniques such as electrochemistry or spectrophotometry [101, Ch. 1]. Direct assay is always the most preferable method of measuring enzymatic reactions. The reasons are the simplicity of progression curve observation through time to minimise source of errors and allow a better interpretation of the initial rate of the reaction. The most common method is using a spectrophotometric assay where the light absorbance properties that occur from substrate depletion or product formation are measured. Besides that, a lot of enzyme reactions produce or consume hydrogen ions in their reaction pathway. Hence, this will induce a pH change in an unbuffered or weakly buffered enzyme solution, that can be measured directly using a glass or ion sensitive electrode, with a restriction that it does not exceed the pH range of tolerance for an enzyme activity.

3.2.2.2 Indirect Coupled Assay

However, not all enzymatic reactions produce detectable signal for convenient measurement. In these cases, an indirect approach has to be implemented where an additional chemical reaction has to be added to produce a measureable signal. The most commonly used indirect assay is a coupled assay [101, Ch. 1]. It involves pairing up other enzymatic reactions to yield a chemical compound that is conveniently detectable. Normally, the product of the enzyme reaction of interest is the substrate of the subsequent enzyme reactions. Coupled assays usually utilise the reduction of $NADP^+$ to NADPH that could be readily measured as light adsorption with spectrophotometry or production of hydrogen ion with a pH sensitive electrode. Figure 3.5 shows a simple example of a coupled assay to monitor the hexokinase reaction using the reduction of $NADP^+$. This reaction can be summarised as follows:

$$A \overset{\nu_1}{\rightarrow} B \overset{\nu_2}{\rightarrow} C \qquad 3.17$$

where *A* is substrate of interest, ν_1 is the velocity for the enzyme of interest, *B* is the product of first reaction and also substrate for the coupling enzyme, ν_2 is

the velocity for the coupling enzyme and *C* is the product from the coupling enzyme that can be measured easily.

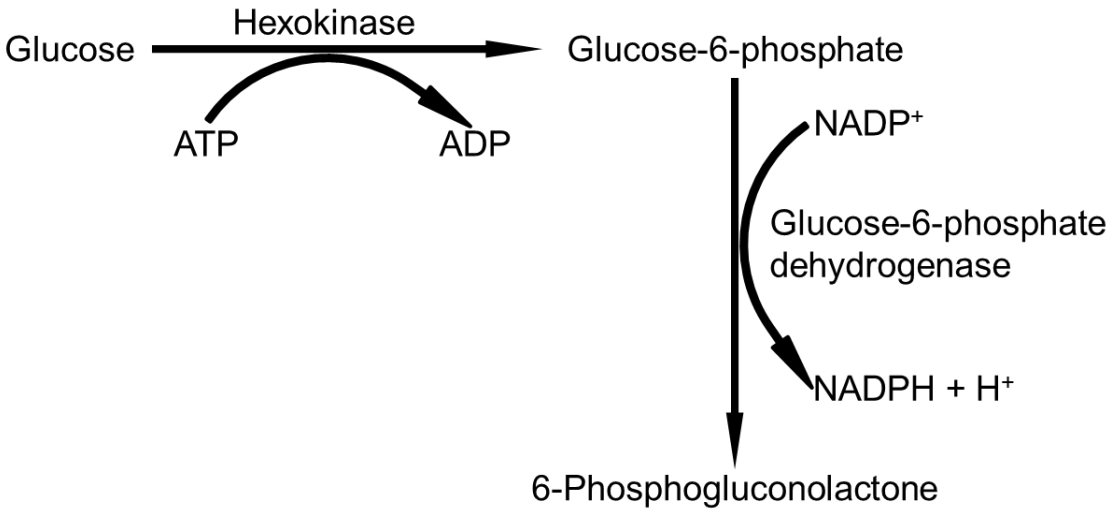

Figure 3.5 – A coupled assay for hexokinase enzyme reaction [101, Ch. 1].

Due to coupled assays using more enzyme reactions for measurement, they present some potential problems. To produce a meaningful study of v_1, it is important to make sure that the coupling enzyme does not become rate limiting ($v_1 << v_2$), where the conversion of *B* to *C* is almost instantaneous. The velocity of v_2 is dependent on the concentration of *B*. Hence, in the initial state of the measurement, there is a lag phase where v_2 is only a fraction of its maximum velocity until it reaches the velocity of the enzyme of interest or faster. This will impede the correct measurement of the initial velocity if the lag phase is too long, where the catalysing enzyme starts to slow down before the coupling enzyme reaches its steady state velocity. The following equation shows the time required for [*B*] to reach steady state level $[B]_{ss}$:

$$t_{99\%} = \frac{\phi K_{m_2}}{v_1} \qquad 3.18$$

where ϕ is the ratio of v_1/v_{max2}. Therefore, to minimise the lag phase, the K_m value of the coupling enzyme has to be low to be efficient at low substrate concentrations. As described previously in enzyme kinetics, v_{max2} is affected by the concentration of the enzyme. Increasing the concentration of the coupling enzyme can decrease the lag phase as well.

3.3 Measurement of pH

The measurement of hydrogen ions (H^+) concentration in an aqueous solution is introduced by Sørensen in 1909, which is known as pH [95, Ch. 23]. Hence, this concept gives the degree of acidity or alkalinity of a solution. The meaning of pH stands for "power of hydrogen" and it is defined as:

$$pH = -\log[H^+] = \log\frac{1}{[H^+]} \tag{3.19}$$

where [H^+] is the concentration of hydrogen ions/protons, with a unit of Molar (M).

3.3.1 Interface Charge Transfer

When measuring pH in an aqueous solution, an electrode is required to perform the measurement, which creates an electrolyte-electrode junction. Hence, it is important to understand the junction between them. When two chemical phases come together, for instance liquid-liquid or liquid-solid, there will be charge transfer across the interface creating a potential difference. At this boundary, electron transfer and a redistribution of charge species in the electrolyte creating an electrical double layer [111, Ch. 25] (discuss in detail in section 3.5) occurs, until the electrochemical potential of the charge carriers in both phases are in balance. Hence, it is vital to understand the interface charge transfer across different chemical environments.

The kinetics of the electronic charge transfer across an interface between two chemical phases can be described by the Butler-Volmer equation [112, Ch. 3]. Imagine the interface between a solid (β-phase) and a solution (α-phase). The net charge for a single ion species, p, that flows in between these two phases, i_p, is described as the difference of ion fluxes going outward from a solid ($\overrightarrow{\iota_p}$) and going into a solid ($\overleftarrow{\iota_p}$). Therefore, the net charge across the interface is, $i_p = \overrightarrow{\iota_p} - \overleftarrow{\iota_p}$ and is given in general by the Butler-Volmer equation:

$$i_p = z_p F\overrightarrow{k_p}\left[X_p\right]_\beta exp\left(\frac{z_p F \varsigma \Delta\phi}{RT}\right) - z_p F\overleftarrow{k_p}\left[X_p\right]_\alpha exp\left(\frac{-z_p F(1-\varsigma)\Delta\phi}{RT}\right) \quad 3.20$$

where i_p is described by the potential difference between the solid phase and solution phase ($\Delta\phi = \phi_\beta - \phi_\alpha$) and also the concentration of the ion species, *p*, in solid phase $\left[X_p\right]_\beta$ and solution phase $\left[X_p\right]_\alpha$. The term $\overrightarrow{k_p}$ and $\overleftarrow{k_p}$ are the heterogeneous rate constants of the forward and reverse flow of the ion fluxes across the interface. The component z_p is the formal charge of *p* and ς is the symmetry coefficient between the forward and reverse ion fluxes across the interface, which is in the range of 0 to 1 but is normally 0.5 [113]. T, F and R are the absolute temperature, Faraday constant and universal gas constant respectively. However, the general Butler-Volmer equation is not limited to describe the charge transfer across solid and liquid but it can be used for the interface between any chemical phases. Equation 3.20 has formed a foundation for describing a potential difference across an arbitrary interface between two distinct phases.

Normally, a chemical phase interface involves more than one ion species. Hence, the total charge across the interface is $i_{tot} = \sum_{p=1}^{m} i_p$ and governed by a single interfacial potential. However, in most cases, such as for an ion-selective electrode, it can be approximated that the interface potential is dominated by one single forward and reverse ion species, which is the fastest exchanging ions across the interface. Figure 3.6 describes the $i/\Delta\phi$ curves with respect to the most dominant ion species. Besides that, Figure 3.6 also shows the i_{tot} in dotted line. Also, the $\Delta\phi$ value when i_{tot} = 0 is the open-circuit potential (OCP) difference. Since there is only one ion species, OCP is also the equilibrium potential, $\Delta\phi_{p(eq)}$ with the forward and reverse ion fluxes are equal ($\overrightarrow{i_p} = \overleftarrow{i_p}$). Therefore i_{tot} = i_p, then Equation 3.20 can be solved for $\Delta\phi$, which will lead to the Nernst equation:

$$\Delta\phi = \frac{RT}{z_p F}\ln\frac{\overleftarrow{k_p}}{\overrightarrow{k_p}} + \frac{RT}{z_p F}\ln\frac{\left[X_p\right]_\alpha}{\left[X_p\right]_\beta} = \phi_k + \frac{RT}{z_p F}\ln\frac{\left[X_p\right]_\alpha}{\left[X_p\right]_\beta} \quad 3.21$$

For the condition where the concentration of the ion species in the solid phase remains constant, due to large capacity of ions, then the term $\left[X_p\right]_\beta$ can be included into ϕ_k to form a simplified version of the equation:

$$\Delta\phi = \phi_k' + \frac{RT}{z_p F}\ln\left[X_p\right]_\alpha = \phi_k' + 2.303\frac{RT}{z_p F}\log\left[X_p\right]_\alpha \qquad 3.22$$

From this equation, $\Delta\phi$ against $\log\left[X_p\right]_\alpha$ is a linear plot with a slope of 59.2 mV/decade for univalent ions (z_p = 1) at a temperature of 25°C. This is ideal response for an interface and also referred to the Nernstian response [112, Ch. 3]. For an electrochemical electrode that is selective to a single ion species, it is desirable to achieve such a response or at least as close to Nernstian.

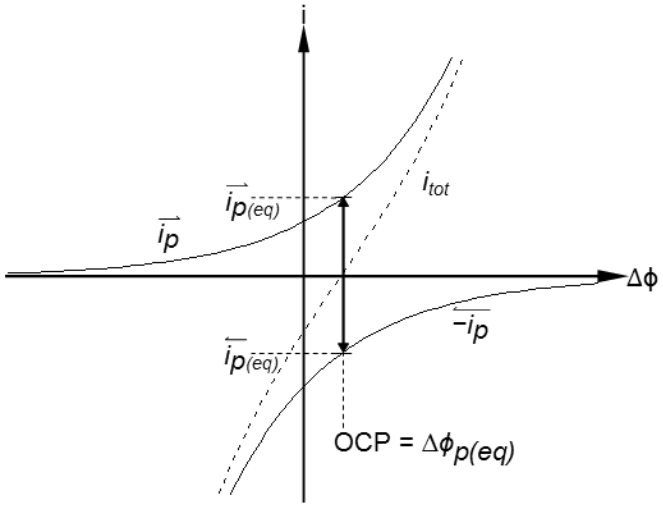

Figure 3.6 – Graph of the forward and reverse ion-exchange currents for the condition where the transport is dominated by a single ion species across the interface [113].

3.3.2 Glass Electrode

The most well recognised electrode/electrolyte interface is between glass and electrolyte interface. Hence in early twentieth century, the glass electrode was widely used for pH measurement [112, Ch. 2]. To use glass electrode for measurement, it is immersed into the test solution and the potential of the electrode is measured with respect to a reference electrode, for instance a saturated calomel electrode (SCE). The electrochemical cell of the system is described as [112, Ch. 2]:

$$\underbrace{Hg|Hg_2Cl_2|KCl(salt)}_{SCE}|Test\ solution|\underbrace{Glass\ membrane|\overbrace{HCl(0.1\ M)|AgCl|Ag}^{Internal\ reference}}_{Glass\ electrode}$$

where | represents the boundary with interface potential between two chemical phases.

From the electrochemical cell above, the properties of the test solution is governed by two interfaces which could influence the overall potential difference. The first one is the liquid junction between the test solution and the SCE, where the liquid junction is porous and allows ions to pass through easily. Thus, the potential at this interface is very minute and constant, which can be neglected. The second interface is between the test solution and the glass membrane. All other interfaces in the cell are constant composition, thus the interface between the glass membrane and test solution is the only variable that could affect the overall cell potential difference. If the glass electrode is only selective to an ion species *p*, following Equation 3.22, the cell potential *E* can be described as:

$$E = \overbrace{E_0}^{constant} + \frac{RT}{z_pF}\ln\left[X_p\right]_{SOL} = \overbrace{E_0}^{constant} + 2.303\frac{RT}{z_pF}\log\left[X_p\right]_{SOL} \qquad 3.23$$

where E_0 is the sum of all the potential differences at all the interfaces, including the interface between the test solution and SCE, which is all constant. E_0 can be measured with a known concentration of $\left[X_p\right]_{SOL}$ during calibration steps.

3.4 Ion Sensitive Field Effect Transistors

As described in Section 3.3, a glass electrode is an ideal sensor for detecting ionic concentration by measuring the interface potential. However, a glass electrode is not suitable for large scale integration with CMOS technology (described in Section 2.3.1), thus a solid-state device as a chemical sensor to measure interface potential is required. This has led to the implementation of the first miniaturised chemical sensor in 1970, known as the ISFET (described in Section 2.5). To understand the operating principle of an ISFET sensor, it is best

explained with the working mechanism of a MOSFET. Take an n-channel MOSFET, when a positive voltage is applied at the polysilicon (gate terminal) the electrons in the p-type silicon substrate are attracted towards the gate and accumulate underneath the gate oxide. When sufficient positive voltage is applied, known as the threshold voltage, the local change of the silicon substrate just beneath gate oxide will be inverted, from p-type to n-type material. Hence, this will create an n-type channel across the source and drain, which allows free electrons to move between them. To allow the formation of channel underneath the gate oxide, the surface potential has to be altered from its original negative value ($\phi_s = \phi_F$), through zero ($\phi_s = 0$) to a positive value ($\phi_s = -\phi_F$), where ϕ_F is the Fermi potential. The lowest required positive voltage to apply, the threshold voltage, in order to achieve a condition termed as "strong" inversion [114, Ch. 6], is given as:

$$V_T = V_{FB} - \frac{Q_B}{C_{OX}} + 2\phi_F \tag{3.24}$$

where V_{FB} is the flatband voltage, Q_B is the depletion charge in the silicon substrate and C_{OX} is the capacitance of the gate oxide. The flatband voltage can be further described as:

$$V_{FB} = \frac{\Phi_M - \Phi_S}{q} - \frac{Q_{SS} + Q_{OX}}{C_{OX}} \tag{3.25}$$

where $(\Phi_M - \Phi_S)$ is the work function between the gate metal (polysilicon) and the semiconductor (silicon substrate), q is the electron charge, Q_{SS} is the surface charge density at the silicon surface and Q_{OX} is the total fixed oxide charge. From Equation 3.24 and 3.25, it can be seen that the threshold voltage is affected by materials properties such as work function of the interface materials, the charge accumulation and also the material of the gate oxide that changes the gate oxide capacitance.

After understanding the fundamental working principle of a MOSFET, now consider a MOSFET with its gate metal removed, and replaced with a reference electrode that is immersed into an electrolyte. By doing this, the gate oxide will be in direct contact with the electrolyte. The gate voltage is the applied

potential at the reference electrode, which is normally a grounded reference electrode and remains constant. The modification of a MOSFET to an ISFET is shown in Figure 3.7. From Equation 3.25, this can be modified to describe the flatband voltage of an ISFET, which is dependent on the potential of the reference electrode (E_{REF}) and also the potential at the gate oxide/electrolyte interface ($\Delta\phi + \chi_{SOL}$). The term χ_{SOL} is the dipole potential of the electrolyte and is a constant, while $\Delta\phi$ is dependent on the concentration of the ion species in the electrolyte at the interface. Due to the replacement of the metal gate with the reference electrode, the associated work function ϕ_M is included in the term E_{REF}. Hence, the change is V_{FB} will affect the threshold voltage and the equation for V_{FB} is given as:

$$V_{FB} = E_{REF} - \Delta\phi + \chi_{SOL} - \frac{\Phi_S}{q} - \frac{Q_{SS} + Q_{OX}}{C_{OX}} \qquad 3.26$$

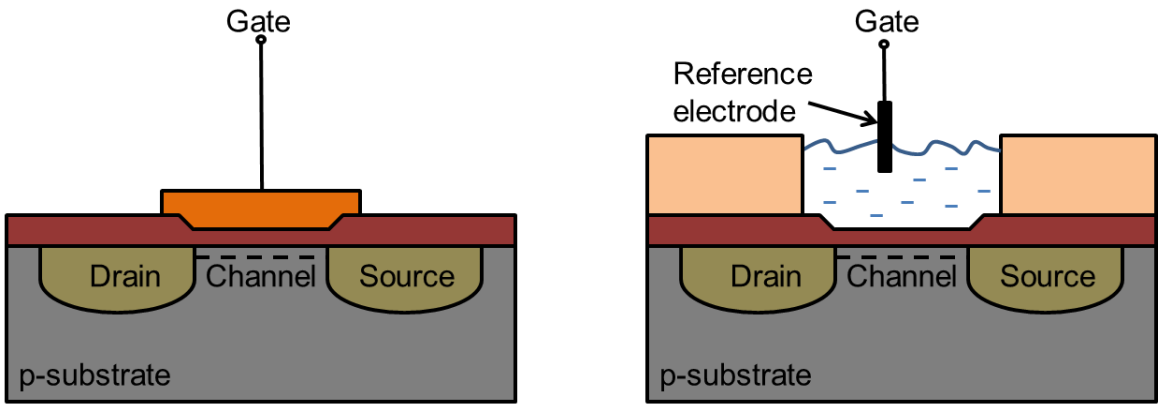

a) MOSFET b) ISFET

Figure 3.7 – Schematic view and physical structure of a MOSFET and an ISFET.

From Equation 3.26, it is clear that the only variable in the equation is the term $\Delta\phi$, where it changes according to the ionic concentration of the electrolyte. Therefore the ISFET is an ideal solid-state device that could replace glass electrode as an ionic sensor, for convenient implementation with CMOS technology. However, the ISFET sensing capability was found to have sub-Nernstian or non-linear characteristics that is not ideal for a transducer. This is due to the electrochemical interactions between the gate oxide and electrolyte. Therefore, it is vital to understand these electrochemical interactions to achieve a Nernstian response for the ISFET.

3.5 Electrolyte-Insulator-Semiconductor Interface

As discussed in Section 3.3.1, when two chemical phases come in contact with each other, a redistribution of charge and potential occurs at the interface, reaching an electrochemical equilibrium. At this equilibrium, charge carriers of both phases accumulated at the interface, creating an electrical double layer, develop an electrochemical potential by establishing an electric field across the interface. Previously the electrochemical reaction on the electrode is not considered. With the increasing usage of semiconductor electrode as chemical device (listed in Section 2.3.2), thus it is very important to understand the electrochemical properties of the electrolyte-insulator-semiconductor (EIS) interface.

As shown in Figure 3.8, the EIS interface consists of three layers and is analysed using a model proposed by Grahame [115]. The concept of the formation of an electrical double layer when an electrode is immersed into an electrolyte was first described by Helmhotz in the late 19th century. Consider an insulator-semiconductor electrode in contact with electrolyte. The solvent molecules in the electrolyte will adsorb onto the surface of the insulator electrostatically, creating a hydration sheath on the surface. At this monolayer, specific ion adsorption at the surface will occur within the hydration sheath as well. These unhydrated ions are absorbed onto the surface chemically and the electrostatic forces from the semiconductor have no effect on them. This locus of the electrical centres of the adsorbed ions is called inner Helmholtz plane (IHP) and the total charge density determined by these ions is termed σ_0. The next layer after the hydration sheath is populated by the hydrated ions. This is due to hydrated ions could not move to the surface as close as adsorbed ions, thus the locus of the closest approach of these hydrated ions is called outer Helmholtz plane (OHP). The interaction of these hydrated ions with the surface is purely electrostatic and has no effect on the chemical properties. According to the Helmholtz-Perin model [111, Ch. 25], the charge distribution on the surface forms a molecular capacitor, between the charge from the IHP and the opposing charge from the OHP. It is expressed as:

$$C_H = \frac{\varepsilon_0 \varepsilon_r A}{d} \qquad 3.27$$

where ε_0 and ε_r are the permittivity of free space and the electrolyte respectively, *A* is the total surface area of IHP and OHP, *d* is the distance between them.

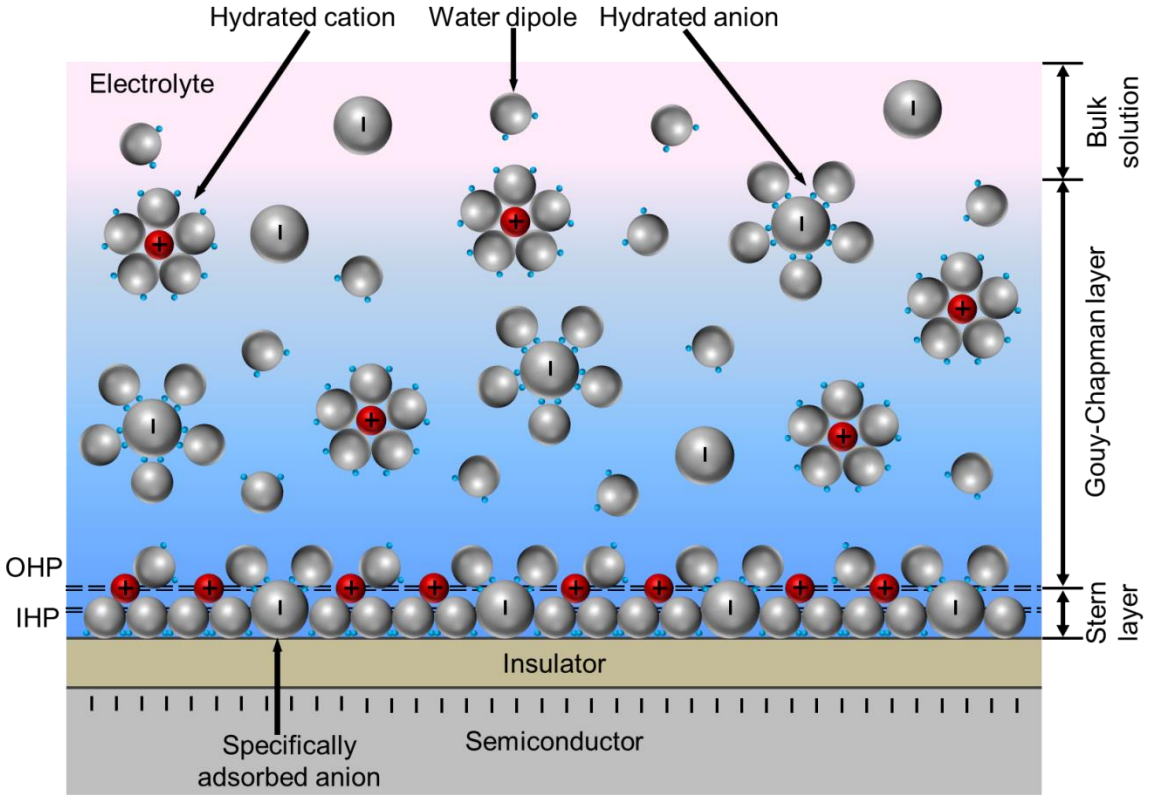

Figure 3.8 – The model of the electrical double layer for the EIS interface [115].

Stern later grouped IHP and OHP together as the Stern layer, which is also called the immobile layer [112, Ch. 13]. The OHP is the frontier between Stern layer and the third layer of the diffuse charge region, called Gouy-Chapman layer. This diffuse layer extends from OHP into the bulk electrolyte.

When an electrolyte and insulator come in contact, the insulator surface will be hydrolysed to form surface groups, which may have different states: positively charged, negatively charged or neutral. The charged states depend on the pH of the electrolyte. If the surface charge is zero with a certain pH value, it is defined as the pH of the point of zero charge "pH(pzc)". The positive (H^+) and negative (OH^-) ions from the electrolyte determine the surface charge on the insulator, thus they are called potential-determining ions. Hence, the charge

distribution and potential gradient of the EIS interface is dependent on the surface if it acquires negative charge or positive charge, as shown in Figure 3.9a and Figure 3.9b respectively.

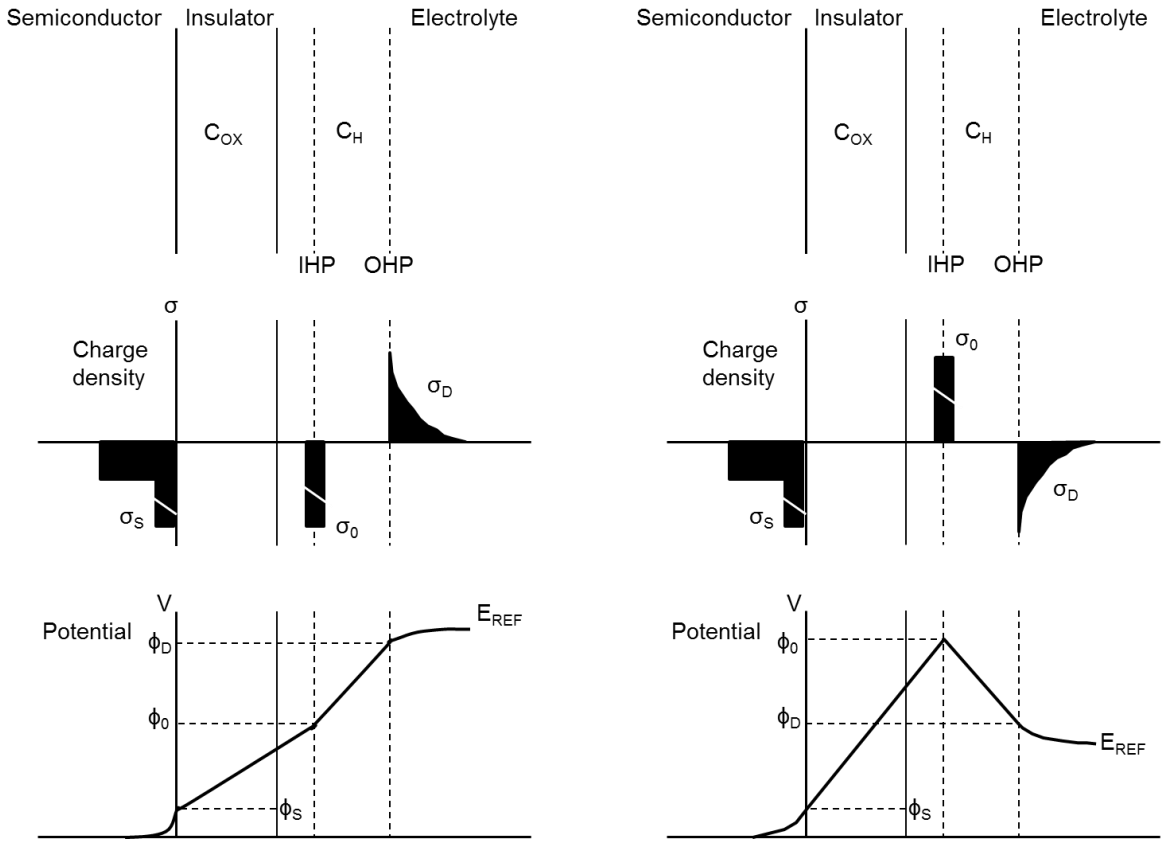

Figure 3.9 – Sketches of the charges and potentials distribution in the EIS interface [116].

The charge density σ_0 in the IHP is due to the ion adsorption on the surface and the excess charge density from Gouy-Chapman layer is σ_D, so the total charge density in the electrolyte is $\sigma_0 + \sigma_D$. The charge density in the solid phase (insulator-semiconductor) is in the semiconductor region σ_S. By applying the concept of charge neutrality:

$$\sigma_0 + \sigma_D + \sigma_S = 0 \qquad 3.28$$

The potential across the EIS interface has to be in continuity, hence:

$$E_{REF} + (\phi_D - E_{REF}) + (\phi_0 - \phi_D) + (\phi_S - \phi_0) - \phi_S = 0 \qquad 3.29$$

and,

$$(\phi_0 - \phi_S) = -\frac{\sigma_S}{C_{OX}} \tag{3.30}$$

$$(\phi_0 - \phi_D) = -\frac{\sigma_D}{C_H} \tag{3.31}$$

$$\phi_D - E_{REF} = -\frac{2kT}{q}\sinh^{-1}\left(\frac{\sigma_D}{\sqrt{8\varepsilon kTc}}\right) \tag{3.32}$$

where *k* is the Boltzmann's constant, ε is the electrolyte permittivity and *c* is the ionic concentration in the electrolyte. Equation 3.32 is the Gouy-Chapman model [112, Ch. 13] for the diffuse layer and by combining Equation 3.29 to 3.32, this will yield:

$$E_{REF} + \underbrace{\left[-\frac{2kT}{q}\sinh^{-1}\left(\frac{\sigma_D}{\sqrt{8\varepsilon kTc}}\right) - \frac{\sigma_D}{C_H}\right]}_{\phi_{EI}=-\Delta\phi} + \underbrace{\left[\frac{\sigma_S}{C_{OX}} - \phi_S\right]}_{\phi_{IS}} = 0 \tag{3.33}$$

The term E_{REF} is the external applied potential from a reference electrode in the electrolyte and ϕ_{EI} and ϕ_{IS} are the interface potentials at the electrolyte-insulator and insulator-semiconductor junction, respectively. This equation provides the relationship between interface potential difference $\Delta\phi$ and the charge density across the EIS interface.

3.6 Site Binding Model

As mentioned before, when an electrolyte and an insulator comes into contact, this can affect the insulator interface potential (Section 3.5) and modulate the ISFET's threshold voltage (Section 3.4). From Section 3.5, we also know that the insulator interface potential is affected by electrostatic potentials in the electrolyte and charge formation due to chemical reactions at the surface. Unlike electrostatic forces that are long ranged, these chemical reactions can only occur within the OHP. Only hydrogen and hydroxyl ions are small enough to penetrate the OHP to enable chemical reactions at the surface. Normally the surface would contain a large number of active-sites, which are amphoteric, basic and acidic. Amphoteric sites mean that they can act as proton donor or

receptor, while basic and acidic sites can only be proton acceptor and proton receptor respectively.

For an ideal unblocked interface between an electrolyte and an insulator, various ion species can exchange freely between the two phases (Section 3.3.1). Such condition can be achieved if the insulator is doped with impurity atoms to facilitate the ion exchange. On the contrary, a completely blocked interface will have no reactions between the insulator and electrolyte. The charge and potential distribution in such an EIS system will be purely electrostatic interaction. Moreover, the insulator has no specificity towards any ion species, thus the interface potential will be governed by the total ionic concentration of the electrolyte. In the general case, insulator exhibits neither ion exchange events nor is it completely inert. Therefore to better describe the interaction at a general oxide-electrolyte interface, Yates *et al.* [117] developed the site binding model in 1974. By adopting this model, the relationship of interface potential and pH, thus pH sensitivity, can be described.

The typical insulator materials used for ISFETs are oxides, such as SiO_2, Al_2O_3 and Ta_2O_5, where B will be used to represent Si, Al or Ta. When these oxides come in contact with an electrolyte, it will hydrolyse to form surface BOH groups, as shown in Figure 3.10. All of these oxides only have amphoteric sites, meaning they may be positively, negatively or neutral charged. The acidic and basic character of the neutral site BOH is described by the following reaction with two equilibrium constants K_{A1} and K_{A2} [118]:

$$BOH_2^+ \rightleftharpoons BOH + H^+ \quad K_{A1} = \frac{[BOH][H^+]_S}{[BOH_2^+]} \tag{3.34}$$

$$BOH \rightleftharpoons BO^- + H^+ \quad K_{A2} = \frac{[BO^-][H^+]_S}{[BOH]} \tag{3.35}$$

where $[H^+]_S$ indicates a surface concentration of H^+ ions, which can be related to the bulk H^+ ion concentration by Boltzmann statistics, under the condition of thermal mixing [117]:

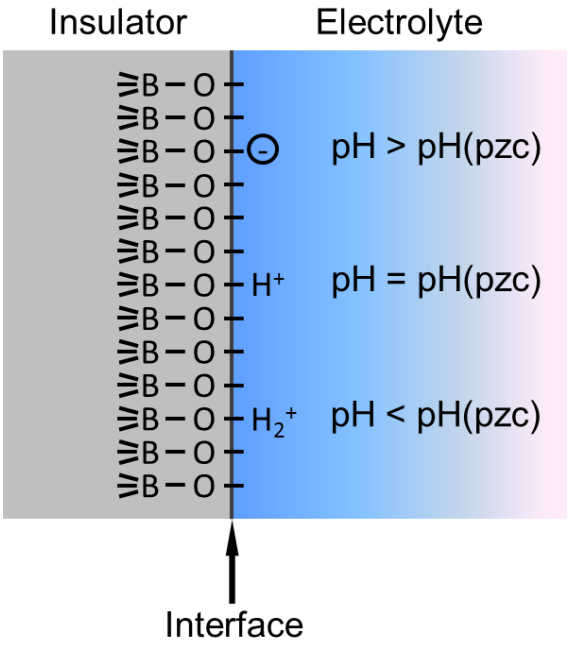

Figure 3.10 – Representation of surface sites and reactions for an oxide (BOH).

$$[H^+]_S = [H^+]exp\left(-\frac{q\Delta\phi}{kT}\right) \quad 3.36$$

The density of active-sites on the surface N_A and charge density per unit area σ_{0_A} are:

$$N_A = [BOH_2^+] + [BOH] + [BO^-] \quad 3.37$$

$$\sigma_{0_A} = q([BOH_2^+] - [BO^-]) \quad 3.38$$

By multiplying Equation 3.34 and 3.35, and replacing $[H^+]_S$ using Equation 3.36 gives:

$$[H^+] = \sqrt{K_{A1}K_{A2}}exp\left(\frac{q\Delta\phi}{kT}\right)\sqrt{\frac{[BOH_2^+]}{[BO^-]}} \quad 3.39$$

When $\Delta\phi$ = 0 and σ_{0_A} = 0 (i.e. $[BOH_2^+] = [BO^-]$), Equation 3.39 will be reduced to $[H^+] = \sqrt{K_{A1}K_{A2}}$. This is the amount of hydrogen ion concentration required in the solution to reach an electrically neutral insulator surface, which is known as the point of zero charge (pzc). The pH index for pzc is denoted as $pH(pzc)_A$ and Equation 3.39 can be expressed as:

$$2.303(pH(pzc)_A - pH) = \left(\frac{q\Delta\phi}{kT}\right) + \ln F_A \quad 3.40$$

This equation gives the relationship between charge, potential and pH, with a function:

$$F_A = \sqrt{[BOH_2^+]/[BO^-]} \quad 3.41$$

This function plays a vital role in the electrochemical response of the insulator's surface. In order to solve this function, the normalised net charge on the surface χ_A is defined as:

$$\chi_A = \frac{\sigma_{0_A}}{qN_A} = \frac{[BOH_2^+] - [BO^-]}{[BOH_2^+] + [BOH] + [BO^-]} \quad 3.42$$

χ_A can be expressed as a function of F_A, when Equation 3.42 is divided through by [BO^-]:

$$\chi_A = \frac{F_A^2 - 1}{F_A^2 + F_A\sqrt{K_{A1}/K_{A2}} + 1} \quad 3.43$$

This equation can be inverted by defining and substituting $\delta = 2\sqrt{K_{A2}/K_{A1}}$ and then taking the positive root of Equation 3.44 to give $F_A(\chi_A)$:

$$F_A^2(\chi_A - 1) + F_A\frac{2\chi_A}{\delta} + \chi_A + 1 = 0 \quad 3.44$$

$$F_A = \frac{\chi_A/\delta + \sqrt{(\chi_A/\delta)^2(1-\delta^2) + 1}}{1 - \chi_A} \quad 3.45$$

Using Equation 3.40 and 3.45, we can see that the pH of a solution is a function of both $\Delta\phi$ and σ_{0_A}, and a direct relationship of $\Delta\phi$ and σ_{0_A} can be found using Equation 3.33, which can be expressed as:

$$\Delta\phi = \frac{2kT}{q}\sinh^{-1}\left(\frac{\sigma_D}{\sqrt{8\varepsilon kTc}}\right) - \frac{\sigma_D}{C_H} \quad 3.46$$

Using charge neutrality through the EIS system:

$$\sigma_D + \sigma_{0_A} = \Delta\sigma = -\sigma_S \qquad 3.47$$

By assuming $\Delta\sigma_S$ = 0, which will give $\sigma_D = -\sigma_{0_A}$ [119], we could now use a parametric method to solve for $\Delta\phi/pH$. $\Delta\phi$ can be obtained from Equation 3.46 and F_A can be found using Equation 3.45, thus the pH of a solution can be obtained using these two parameters to solve Equation 3.40. Therefore, this procedure is used to generate $\Delta\phi/pH$ curves (pH sensitivity) for an insulator with single active-site in a straightforward manner.

3.7 Measurement of Light Absorbance

As mentioned previously, the concentration of metabolites in an enzyme assay is measured using light adsorption from spectrophotometer. For each wavelength of light passing through a solution that contains specific absorbing species, the intensity of the light, *I* is measured and this is neglecting the reflection of light off the vial that contains the solution. The Beer-Lambert Law [120] was discovered in the 19th century, which is used to relate the attenuation of a travelling beam of light through a sample, to the length of the path of the beam in the sample and to the concentration of the attenuating species in the sample. This simple event is presented in Figure 3.11.

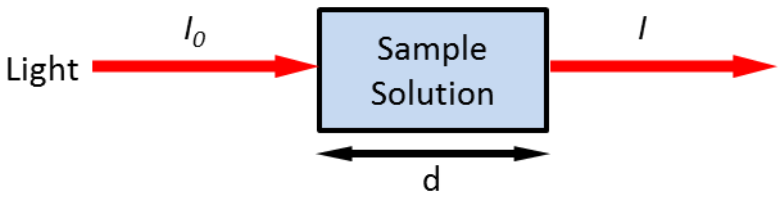

Figure 3.11 – Diagram of light absorbed by a sample solution with certain vial width.

The amount of light that is absorbed after passing through the solution is given as:

$$A = \log_{10}\frac{I_0}{I} \qquad 3.48$$

The absorbance, *A* is proportional to the concentration of the absorbing species in the sample, *c* and to the length of the light path in the sample, *d*. Hence, absorbance is given as:

$$A = kcd \tag{3.49}$$

where *k* is the molar absorptivity constant of the adsorbing species.

From Equation 3.48 and 3.49, it forms the common form of the Beer-Lambert Law, written as:

$$A = \log_{10} \frac{I_0}{I} = kcd \tag{3.50}$$

This formula gives a direct relationship between the absorbance and the concentration of the absorbing substance in the solution for an enzyme assay, which directly relates to the concentration of metabolites.

3.8 Summary

In this chapter, two unique abilities of enzymes were introduced; as a catalyst for increasing reaction rate and the “lock and key” specificity for specific substrate binding. This makes enzymes very useful for the application in metabolites quantification. Enzyme kinetics has also been presented to show how useful kinetic information can be obtained to understand metabolites quantification. Furthermore, two different enzymes assays, which are used in this work, have been introduced. These enzyme assays can be detected using spectrophotometric light absorbance and electrochemical pH sensing on CMOS ISFETs. Later in the chapter, the working mechanism of the ISFET was explained together with the insulator-electrolyte interface that demonstrates the theory behind the pH response of different insulator materials. Last but not least, the relationship of the absorbance and the absorbing substance in an aqueous solution was explained by Beer-Lambert Law, which relates to the concentration of metabolites in an enzyme assay. In the next chapter, the CMOS sensor array and sensor systems used in this work to demonstrate the enzyme assays will be discussed.

Chapter 4 : Sensors and Sensor Systems

4.1 Introduction

The previous chapter introduced the fundamental theory of enzyme kinetics and the description of enzyme assays that can be studied via hydrogen ion concentration or light absorbance changes. In addition, Chapter 3 also included an explanation on the working principles of ISFETs and the mathematical derivations of ISFETs' pH response. This chapter concentrates on the design descriptions of the CMOS sensor array chips and how to integrate into hardware and software system. The discussion for this chapter is separated into two distinct platforms: 256×256-pixel ISFET array chip and 16×16-pixel Multi-Corder chip. The ISFET array chip was designed by a former member of the Microsystem Technology (MST) group named Balazs Nemeth. The Multi-Corder chip was designed by Mohammed Al-Rawhani. He combined the circuitry of the ISFET (Balazs Nemeth), photodiode (Luiz Gouveia) and single photon avalanche diode (Mohammed Al-Rawhani) into one single chip. The chapter also emphasises the miniaturisation process from an expensive and bulky PXI platform to a low cost and small-scale ARM mbed platform measurement tool. This suited the idea of bringing the personal metabolome machine to the hands of a physician or patient as POC diagnostics.

4.2 256×256-Pixel ISFET Array Platform

The ability of using ISFET array CMOS chips for various applications, such as ionic imaging of fluids dynamics [121] and artificial [122] or natural systems [123] ion imaging, were demonstrated by the MST group at the University of Glasgow. This technology has been successfully implemented in genome sequencing as mentioned in Section 2.4.3, thus our vision is to further expand this technology for metabolome detection. The following sections will describe all the

components of the ISFET array chip (65,536 ISFET sensors) designed by our group along with the hardware and software system used for reading out the signals.

4.2.1 Foundry Technology

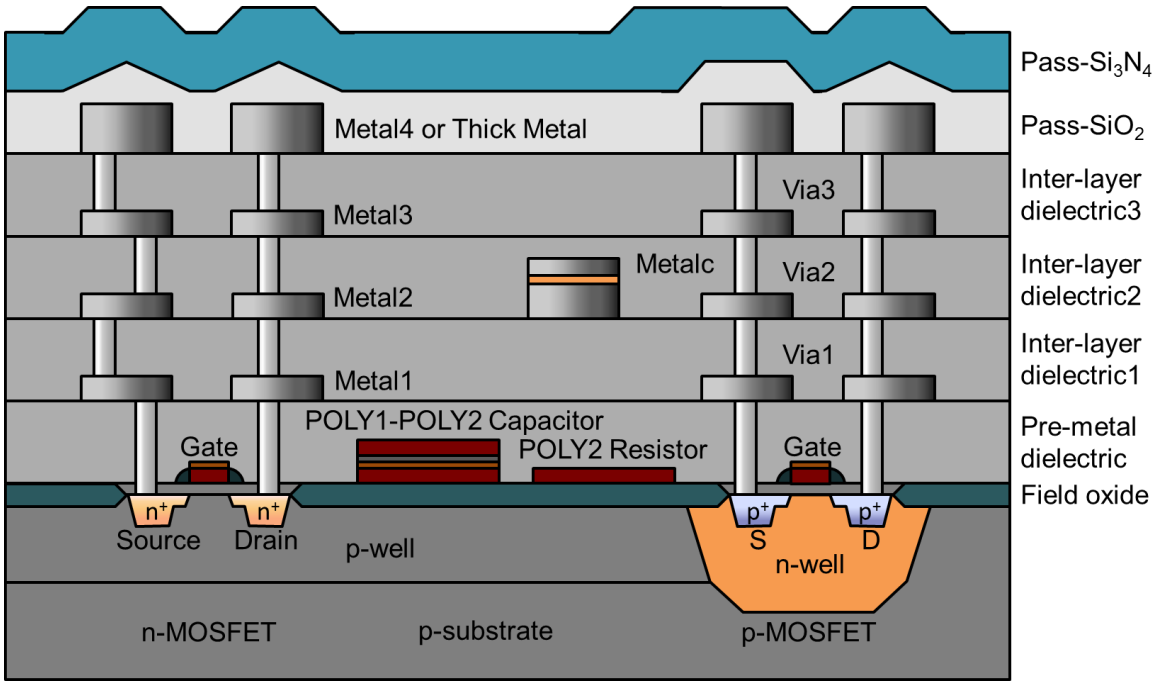

Figure 4.1 – Cross-sectional view of the 4 metal layer-0.35 μm AMS CMOS process [124].

The fabrication of the chip was outsourced to *austriamicrosystems* AG (AMS). They offer CMOS processes for ASIC (application-specific integrated circuit) systems and provide design kits to create integrated circuits [125]. The foundry technology is provided through the Europractice IC service [126]. This service is provided by IMEC and Fraunhofer which offer small volume and low cost ASIC prototyping through multi-project wafers. This service combines multiple designs from different customers on to a single wafer to reduce the cost of each ASIC design to approximately 5–10% of the full wafer cost. After the fabrication of the chips, Europractice also arranges the wafers to be diced, wire bonded and packaged into a standard chip carrier. However, in our case the CMOS chips have to be further post-processed to improve device sensitivity (a detailed discussion will be provided in Chapter 5), thus bare chips were requested and delivered to the University of Glasgow. The technology chosen for this project was the 'C35B4' 0.35 μm CMOS process which consists of four metal layers and an operating voltage of 3.3 V. This technology was selected in this work to design a

working ISFET array chip. The wafer cross-section of the C35B4 technology is shown in Figure 4.1.

4.2.2 ISFET Array Chip

The ISFET array is composed of multiple single ISFET sensor pixels in a configuration of 256 rows and 256 columns, providing a total number of 65,536 ISFET sensors. The circuit diagram and layout representation of a single ISFET pixel is shown in Figure 4.2. Each pixel circuit consists of four transistors (P1, P2, P3 and N1) as shown in Figure 4.2a. P2 is an ISFET pMOS transistor that is configured as a voltage-follower and used to measure the concentration of hydrogen ions in an aqueous solution. P1 is an in-pixel current source that acts as a load transistor, P3 and N1 form the transmission gate circuit used for individual pixel selection. In Figure 4.2b, it can be seen that the gate of the ISFET transistor is connected via POLY 1 to a central point of the pixel. Then it is connected to the top patterned Metal4 layer using intermediate vias and metal layers, creating a floating gate structure as an ISFET sensor (described in Section 2.4.2). The passivation layer on top of Metal4 acts as a sensing layer to detect hydrogen ion concentration. This detection is measured by the gate potential changes of P2. The transmission gate circuit is in between the source-follower circuit and the analogue output channel of the pixel, preventing from any charge sharing between pixels in the same output channel. The transmission gate circuit also known as a switch, is comprised of two complementary transistors that require opposite digital signals to open or close the switch. The digital signals are inputted from external digital pads to the gate of the complementary pMOS and nMOS transistors via $\overline{V_{col}}$ and V_{col} respectively.

Each individual pixel has a physical size of 10.2×10.2 μm^2 with 1 μm distance in between each adjacent pixel (11.2 μm pixel pitch size). The complete 256×256-pixel array occupies a total area of approximately 2.87×2.87 mm^2 in the middle of the chip and the total area of the chip is 4.6×4.7 mm^2. Figure 4.3a illustrates the optical micrograph of a 3×3-pixel array highlighting the dimensions of a single pixel. Figure 4.3b shows the whole chip including the 256×256-pixel ISFET array, the readout electronics (multiplexing systems and column decoders) and the input/output (I/O) pads.

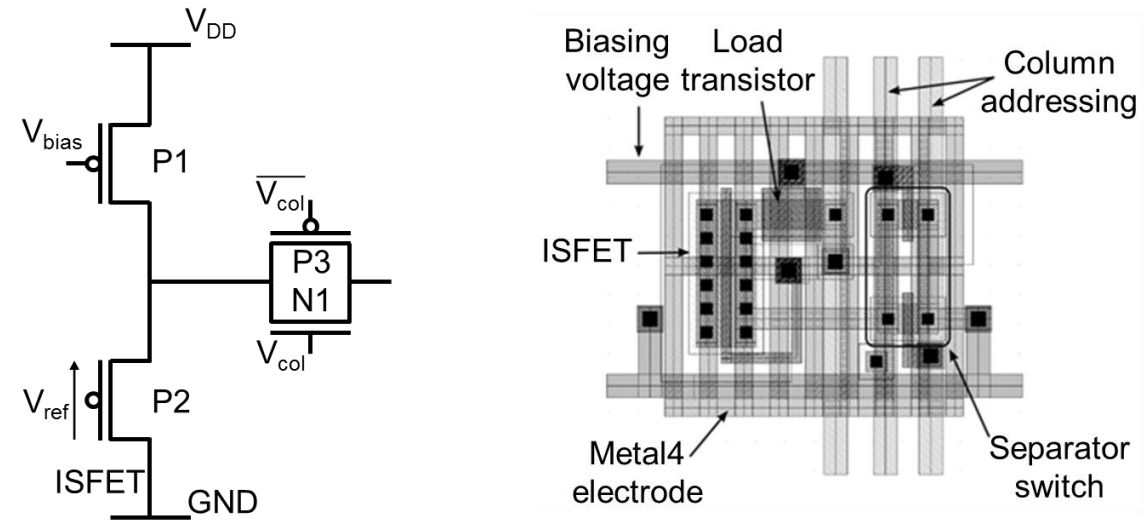

a) Schematic **b) Layout**

Figure 4.2 – A single pixel of the ISFET array chip.

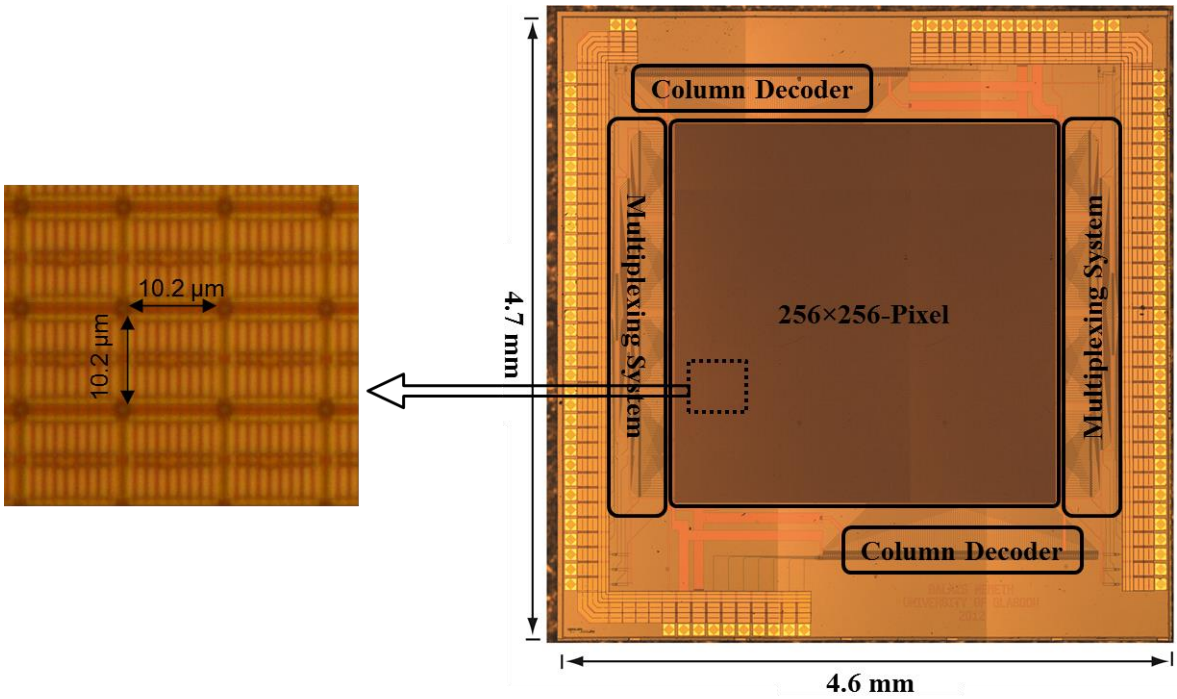

a) 3×3-pixel array **b) Whole chip**

Figure 4.3 – Optical micrograph of the ISFET array chip.

4.2.3 On-Chip Readout System

The ISFET sensor array is divided symmetrically into two halves; each half contains a pixel array of 256 rows and 128 columns. Figure 4.4 shows the symmetry of the 256×256-pixel array readout architecture, containing two identical row multiplexing systems and column decoders for both sides of the array. The bond pads are divided into two sides, each side contains individual

bond pads for each readout channel (32 channels per side), external digital addresses for the row multiplexers and column decoders, and global power supplies (V_{DD} and *GND*). All the digital addresses are inputted from an external source to the chip. To avoid confusion, all the external digital addresses for both sides of the array are obtained from the same source. A 7-bit column decoder is used to readout 128 pixels from one half of the array. The same digital addresses are used to read the remaining 128 pixels from the other half of the array. These digital addresses activate individual transmission gates for every pixel in the selected columns, where each pixel is selected by an individual digital word (e.g. 0000001). Both decoders are configured to operate in opposite phases, thus the array is read from the centre columns to the opposite sides of the array. The row multiplexing system at each side of the array contains seven pieces of 32/64 line selector blocks. Each block contains 32 single-pole-double-throw switches to enable the appropriate 32 channels selection (e.g. <0...31> or <32...63> lines) from 256 rows. The operating system of a single line selector block is shown in Figure 4.5. These blocks are configured in a 4-2-1 manner to function as a one from eight multiplexer. Blocks of 32 analogue signals are then readout sequentially from both sides of the array simultaneously.

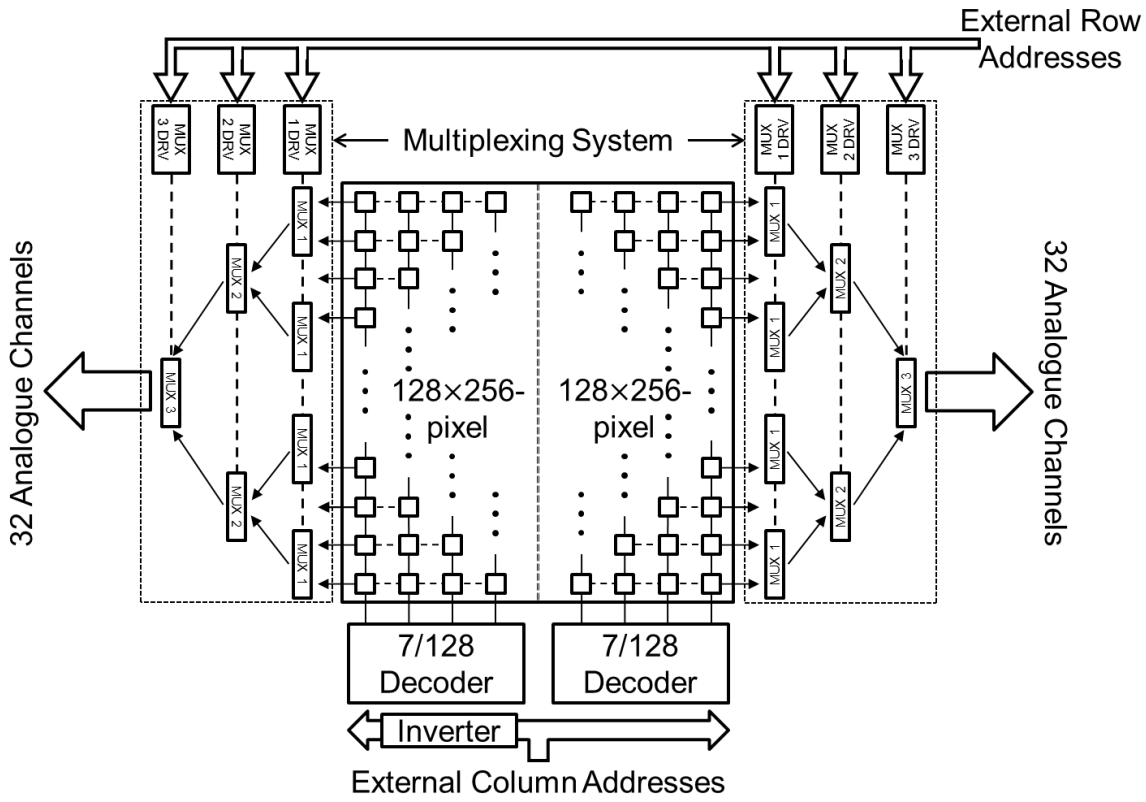

Figure 4.4 – A schematic diagram of the addressing architecture of the 256×256-pixel ISFET sensor array chip.

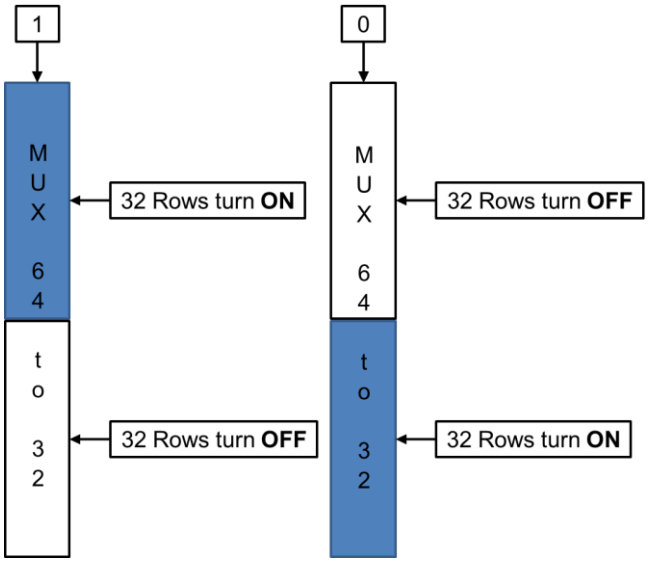

Figure 4.5 – Operation of the switches in the one from eight multiplexer selecting 32 rows of analogue output signals.

4.2.4 Off-Chip Instrumentation and Measurement System

In order to operate the ISFET sensor array chip, a high-speed instrumentation and measurement system was constructed to obtain the pixel output voltages and to provide digital addresses to the chip. The output voltages represent the local hydrogen ion concentration changes as explained in Section 3.4. The measurement tool designed for metabolites detection has a maximum speed capability of 2 μs/pixel, reading 64 analogue signals every 2 μs. Therefore, the maximum acquisition rate of the measurement unit can be translated into 2.048 ms/frame (reading all 65,536 pixels), which is equivalent to approximately 500 fps.

Figure 4.6 illustrates the operational flow of the instrumentation and measurement system. The system consists of a desktop computer, four PXI-Express-6538 X series acquisition cards placed in a PXI-Express-1073 chassis (National Instruments), a custom printed circuit board (Newbury Electronics) and a packaged ISFET array chip (the packaging process will be explained in Chapter 5). The chip was bonded to provide access to all the internal connections. In addition, a voltage source was connected to an Ag/AgCl quasi-reference electrode [127], which was immersed into the aqueous solution that was contained in the packaged chip. To form the Ag/AgCl quasi-reference electrode, an Ag wire was first immersed into 0.1 M KCl solution together with another inert electrode such as platinum and then biased to 1.3 V using a potentiostat

for 2 minutes. The purpose of the reference electrode is to set a reference potential to the floating gates of all the ISFET sensors in the array.

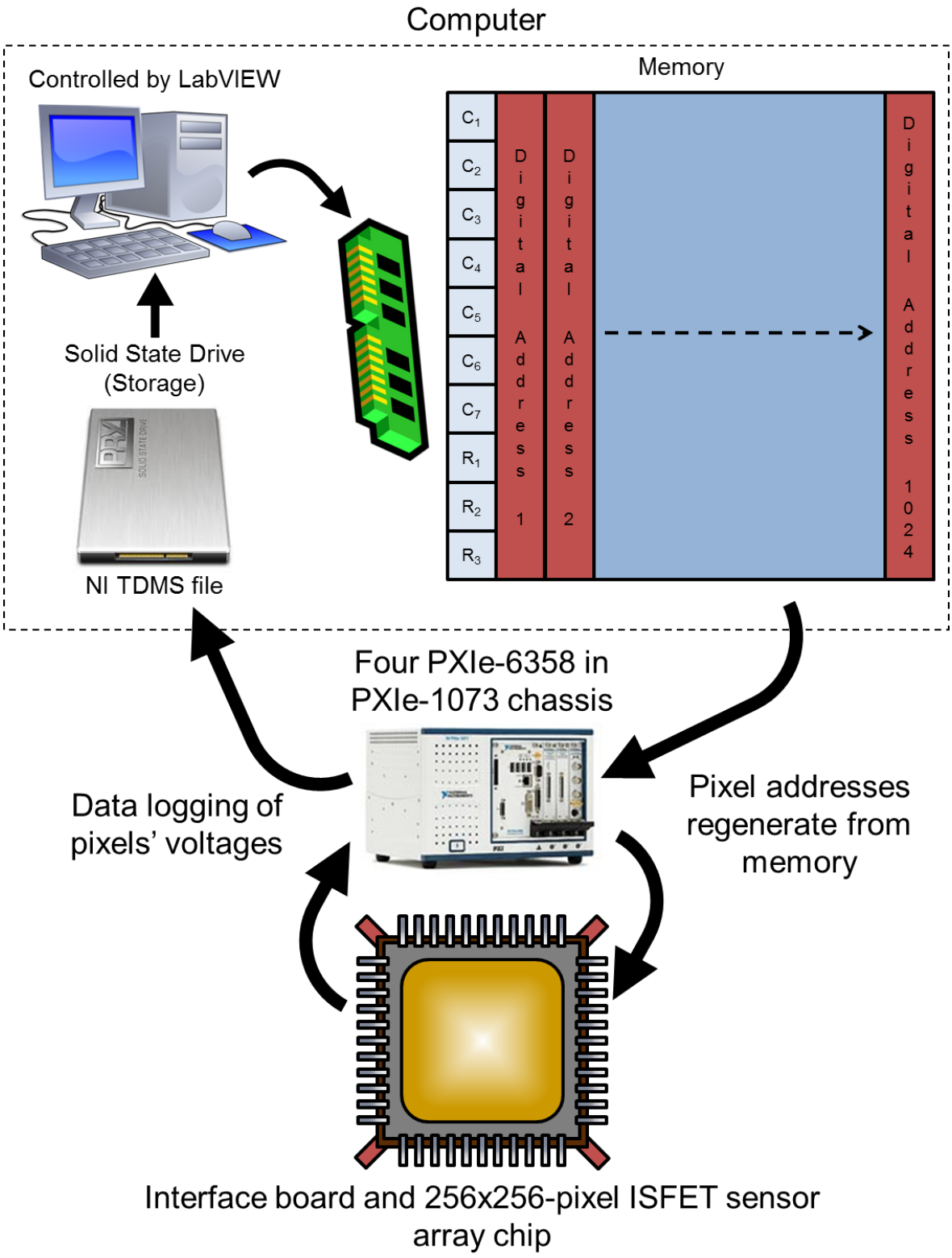

Figure 4.6 – The system-level description of the instrumentation system for 256×256-pixel ISFET array chip.

The PXI-Express chassis was connected to the desktop computer via a PCI-Express-8361 card, which was inserted in one of the PCI-Express slots in the computer. On the printed circuit board (PCB), a PGA ZIF 15×15 socket was used to house the packaged chip. The PCB was used to connect all the 64 analogue outputs from the chip to the 64 analogue inputs for each of the four PXI-Express acquisition cards (16 inputs per card). In addition, the PCB was used to connect the 10 digital outputs from one of the PXI-Express cards to all the respective digital inputs to the chip. However, all the digital outputs from the acquisition card have a voltage range of 0 – 5 V, which is not compatible to the operating voltage of the chip. Hence, two MAX 3001E voltage level shifters were used to lower the voltage of the digital outputs from the acquisition card to the electronics maximum output range of 0 – 3.3 V. The PCB also connected the gate of all the in-pixel load transistors (P1 in Figure 4.2a) to a 1 V voltage source.

The whole operation of the instrumentation and measurement system was controlled by the software package LabVIEW from National Instruments (NI). It was programmed to read all the 64 analogue outputs from the chip and send the 10-bit digital addresses to activate the pixels in the chip. Hence, it is very vital to synchronise the digital addressing and analogue data logging of the chip, in order to obtain the correct pixel voltage reading as a function of time. The PXI-Express reference clock in the chassis was used to synchronise both the analogue signals and digital addressing. This reference clock links all the four acquisition cards together. In order to make perfect sure that the correct pixel measurement was obtained, the analogue data was read at half the period of the sampling rate. A picture of the complete instrumentation and measurement system is shown in Figure 4.7.

The analogue input resolution of the acquisition cards is 16 bits for a single pixel voltage which means a frame will have 131.072 kB of data, thus the maximum transfer data rate from the chip to the computer is 64 MB/s. This is a significant amount of data that is difficult for a multi-tasking operating system such as Microsoft Windows to handle efficiently. Moreover, high-priority processes such as anti-virus or firewall could halt the measuring system, preventing a continuous process of sending digital addresses and receiving analogue signals.

To ensure high speed and continuous data transfer, the direct memory access (DMA) and data logging features of the PXI-Express-6358 X series acquisition cards were used in conjunction with a solid-state drive (SSD) of the PC. A total number of 1024 digital words made from 10-bit digital addresses were sent to the memory of the computer to extract a whole frame. The sending of digital addresses was also programmed to regenerate from memory after each frame to obtain continuous sampling. For high speed acquisition of analogue voltages, the data was transferred directly to the SSD as an NI standard TDMS file. Using this strategy, the system operated independently from the central processing unit and operating system of the computer, thus giving continuous addressing without interruptions and large volumes of data transfer.

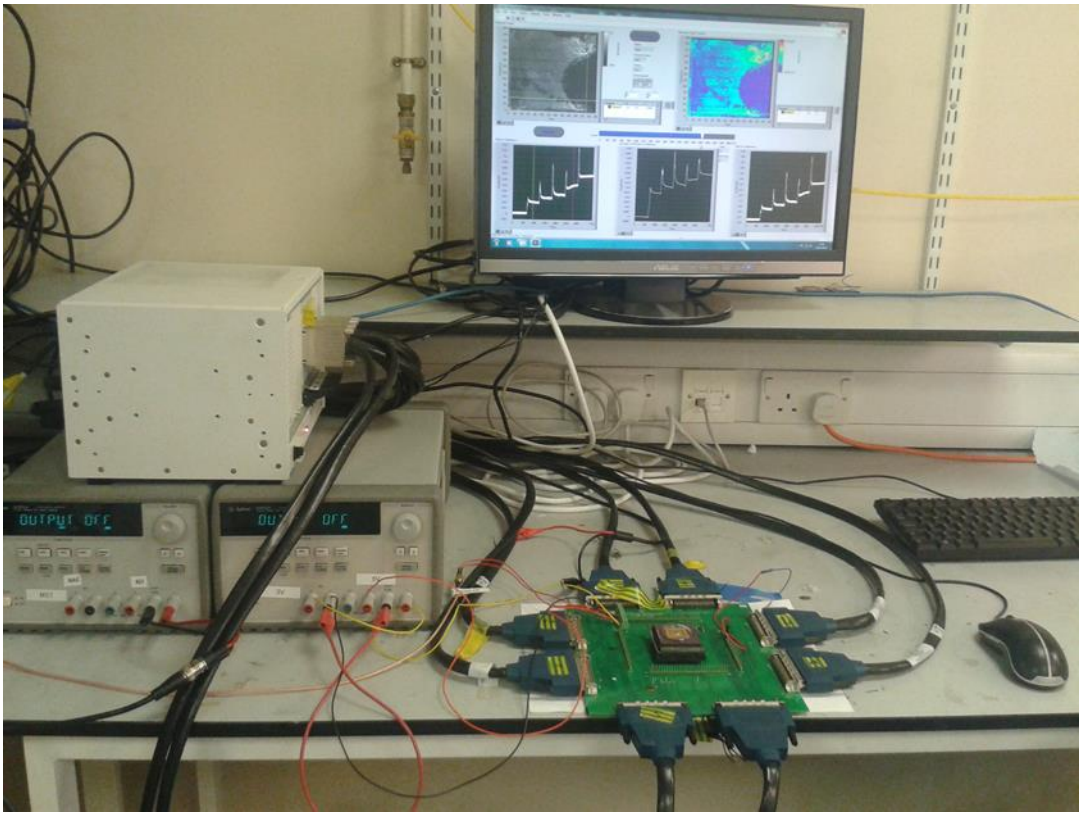

Figure 4.7 – Photograph of the instrumentation system for 256×256-pixel ISFET array platform.

4.2.5 Data Analysis

The raw data measurement from the acquisition system had to be extracted and analysed for the detection of hydrogen ion concentration in the aqueous solution on top of the chip. Figure 4.8 illustrates the data analysis procedure to visualise the hydrogen ion concentration. In order to do this, LabVIEW was again used to

arrange all the data into frames of 65,536 pixels. A reference frame was chosen manually prior to any chemical reaction. All the subsequent frames were then subtracted from the reference frame to take a differential measurement until the end of the desired length of the experiment. The results of each frame were then plotted to the appropriate LabVIEW graph to show 2D or 3D image representation, as well as the data analysis of individual pixels as a function of time. Furthermore, the average of all the pixels and the standard deviation between pixels can be obtained using the numerical operations in LabVIEW.

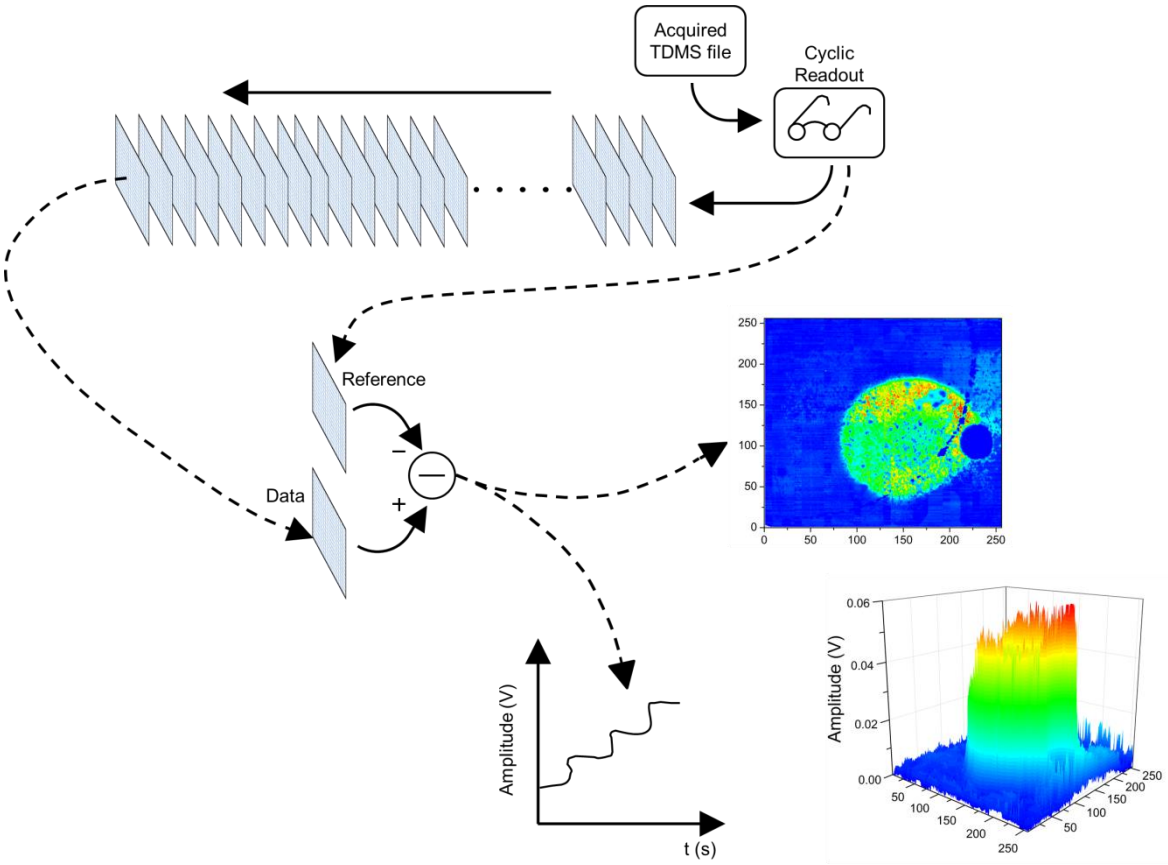

Figure 4.8 – Description of the data analysis from the chip.

4.3 16×16-Pixel Multi-Corder Array Platform

With the progression of the work, the 256×256-pixel ISFET array chip was found to lack certain characteristic required for metabolome detection such as measuring multiple metabolites. In order to achieve this, microfluidics (will be discussed in Chapter 5 and 7) were required to be post-processed on top of the chip, consequently increasing the fabrication complexity (will be explained in Section 4.3.2). Therefore, a new chip, 16×16-pixel Multi-Corder chip was

designed and fabricated to allow the addition of microfluidics on top of the chip with fewer complications. Furthermore, with the ability to measure enzyme assays by spectrophotometric means (see Section 3.2.2), the Multi-Corder chip was designed to include two different optical sensors into every pixel along with the ISFET circuitry. These two optical sensors are photodiode (PD) and single photo avalanche diode (SPAD). Hence, the Multi-Corder chip provided an improvement from the original ISFET array chip (single sensor) to a multiple modality platform for metabolome sensing using optical and ionic sensors. The following sections will describe the components of the Multi-Corder chip (256 pixels of three different sensors) as well as the new acquisition system to readout the signals from every sensor.

4.3.1 Foundry Technology

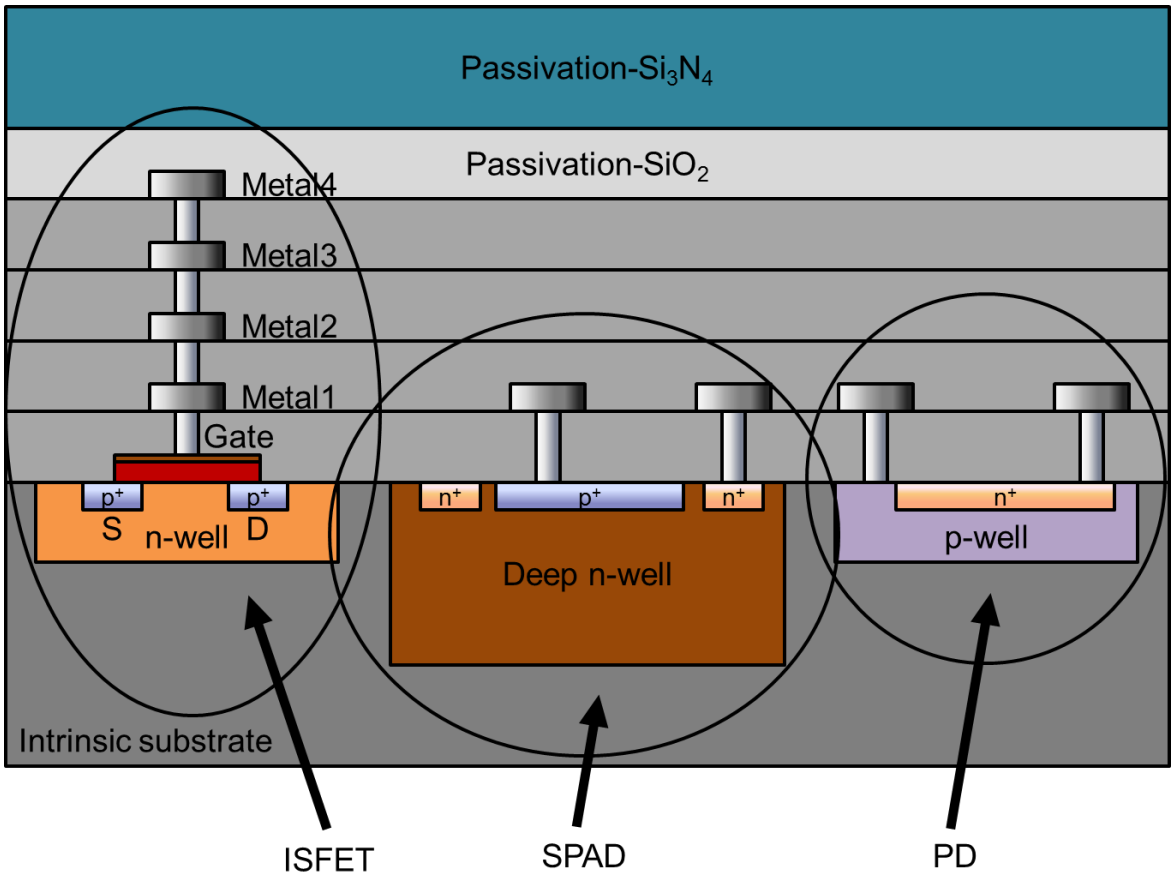

Figure 4.9 – Cross-sectional view of ISFET, PD and SPAD structures fabricated in H35B4 technology.

Similar to the 256×256-pixel ISFET array chip, the fabrication of the Multi-Corder chip was also outsourced to AMS. However, the CMOS process selected for the

16×16-pixel Multi-Corder chip was slightly different, which was the 0.35 μm high voltage (50 V) CMOS process with four metal layers (H35B4 technology). The reason behind the selection of a high voltage process was due to the requirements of SPADs to work at a high breakdown voltage. The CMOS H35B4 technology has a deep n-well that allows the SPADs to operate at a high breakdown voltage [128]. Figure 4.9 illustrates the cross-section of a cluster of ISFET, PD and SPAD using H35B4 technology.

4.3.2 Sensor Array Chip

The Multi-Corder array is composed of multiple single pixels containing a cluster of three different sensors, where an ISFET is integrated with a PD and a SPAD along with its corresponding sensing circuits. The three sensors with their sensing circuits are arranged in the order of 16 rows and 16 columns to provide a total number of 256 pixels. The ISFET pixel circuit is the same as the one previously explained in Section 4.2.2. The first optical sensor in the chip is a PD, its pixel circuit diagram and readout waveforms are shown in Figure 4.10. A PD is a p-n junction photosensitive detector and conventionally a single pixel of a CMOS PD imager incorporates a PD with three nMOS transistors to readout the photocurrent [129]. As can be seen in Figure 4.10a, the detected light generates a current, i_{ph}, that will discharge at V_d, node. The discharged voltage, V_d, is supplied to the gate of transistor M2 which is configured as a source-follower. As shown in the timing diagram of Figure 4.10b, each measurement cycle begins with $t = t_0$ when $V_{rst} = V_{DD}$. From t_0 to t_1, the PD is reset by transistor M1 to its original state, V_{DD} when a reset signal, V_{rst}, is provided to the gate of M1. At $t = t_1$, the circuit enters the integration phase. Depending on the integration time on the PD, a different i_{ph} leading to a corresponding rate of change of V_d, across the diode as the capacitance is discharged. At $t = t_2$, the PD voltage is buffered to the output voltage node, V_{out} when the gate of transistor M3 is provided with an external logical signal (sel). Hence, the amplitude of V_{out} is inversely proportional to the detected light intensity, as can be seen from traces labelled as V_{d1} and V_{d2} in Figure 4.10b. However, if the PD is saturated which is the trace labelled as V_{d3}, then PD will have completely discharged before $t = t_2$. In order to avoid this possibility, the measurement tool had to be designed to fix an integration period (t_1 – t_3) to 100 ms.

The second optical sensor in the chip is a SPAD, which is an avalanche photodiode that is reversed biased above the breakdown voltage to operate in Geiger mode [130]–[132]. High electric field within the active region of the SPAD will initiate an avalanche breakdown upon receiving a single photon. This will generate a large current pulse to be detected using a passive quenching circuit (SPAD connected in series with a load transistor). The reason two different optical sensors were used in this work was mainly to extend the dynamic range of the light intensity measurement, where high and low intensity light will be detected by PD and SPAD respectively.

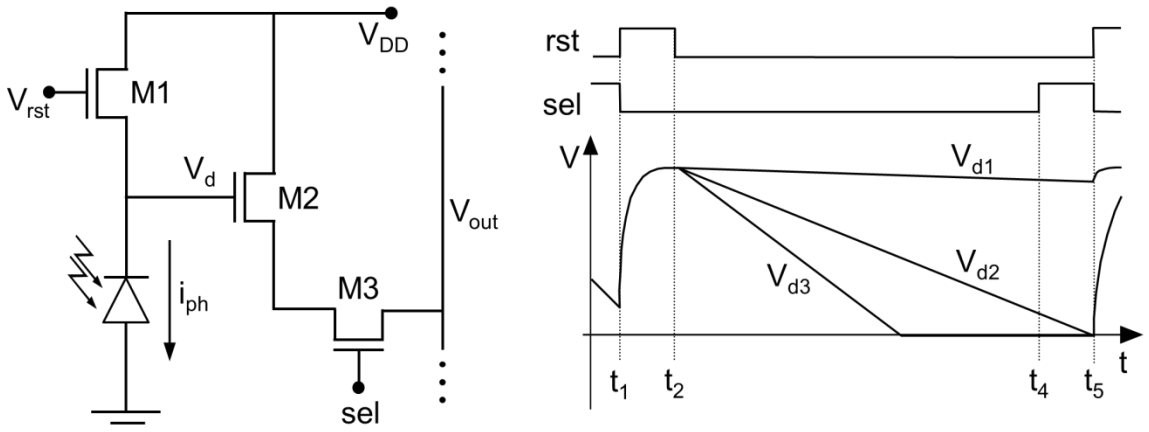

a) Circuit diagram **b) Operation waveform**

Figure 4.10 – Single PD pixel of the Multi-Corder chip array.

Figure 4.11 illustrates the optical micrograph of a single pixel containing its three sensors and the complete Multi-Corder chip. Each of these pixels has a physical size of 100×100 μm^2 and the entire array occupies a total area of approximately 1.6×1.6 mm^2 in the middle of the chip. As mentioned before, microfluidics are required for multiple metabolites detection, thus a continuous and smooth liquid flow of metabolites in the microfluidics is essential. However, the bond pads of the original ISFET array chip are at all four peripherals of the chip (see Figure 4.3b), which does not provide a good inlet and outlet port for the microfluidics. Hence, the Multi-Corder chip was designed to only have bond pads on opposite sides of the array as shown in Figure 4.11b. This allows a good inlet and outlet port for the microfluidics to be made for a continuous liquid flow across the array of the chip without any obstruction. In addition, each active pixel that is in line with the blank bond pads has a 50 μm gap in between

to allow microfluidics to be fabricated on top of the gap, without impeding the functionalities of the sensors.

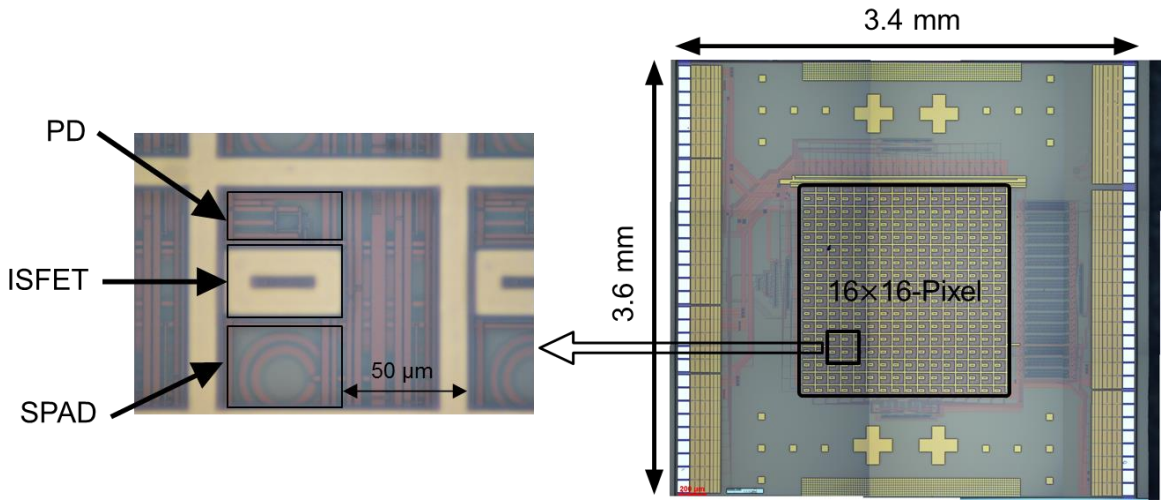

a) Single pixel **b) Whole chip**

Figure 4.11 – Optical micrograph of the Multi-Corder chip.

4.3.3 On-Chip Readout System

The on-chip readout system for the Multi-Corder chip is simpler than the one from the ISFET array chip. Each of the sensor array has its own corresponding addressing system and individual bond pads. Hence, each array can be acquired independently. Figure 4.12 illustrates the architecture of the readout system for all 16×16 pixels in the array. The ISFET readout system has a 4-bit decoder for column addressing and a one from eight multiplexer for row addressing, which require a total of 7-bit digital addresses. These digital addresses are supplied to the 4-bit decoder to readout one of the 16 columns of the array, which are used to activate the transmission gate of the ISFET pixel circuit in the selected column (see Section 4.2.3). The row data of the ISFET is divided into eight blocks of two analogue outputs which are read using a 3-bit digital address. These blocks of two analogue outputs are read out sequentially using a one from eight multiplexer.

As for the PD and SPAD readout system, each one has two 4-bit decoders for both row and column addressing. Unlike ISFET, PD only has one analogue signal to be readout at a time. For the PD readout system, global shutter readout scheme was used. When all the PDs are reset using transistor M1, the 4-bit column decoder selects a column and the 4-bit row decoder steps through each

of the 16 pixels across the column to provide a signal (sel) to the gate of transistor M3 (refer to Figure 4.10a). The digital addresses read through all 256 pixels when all of the PDs are active and discharging, before they are all reset again, thus the name global shutter readout scheme. On the other hand, SPAD readout system uses a rolling shutter readout scheme [132]. 16 SPAD array columns are powered up at a time via a 4-bit decoder. The output pulse from each SPAD in the selected column is counted by (16) 16-bit digital pulse counters. Each counter gate is opened using an external digital signal (gate) for a certain period of time, e.g. 10 ms, and counts the pulses of 16 SPADs from the selected column. After the pulse counting, a 4-bit row decoder selects and reads out serially from each of the 16 counters. To step through each of the 16-bit counters, an external digital signal (read) is used to read from most significant bit (MSB) to least significant bit (LSB), until all 16 counters are read. After the 16 counters of the selected column are readout, another external digital signal (clear) is provided to empty all the counters for the next column selection. Figure 4.13 shows the digital signals required for the SPAD array readout. The whole procedure is run through column-by-column, hence the name rolling shutter readout scheme.

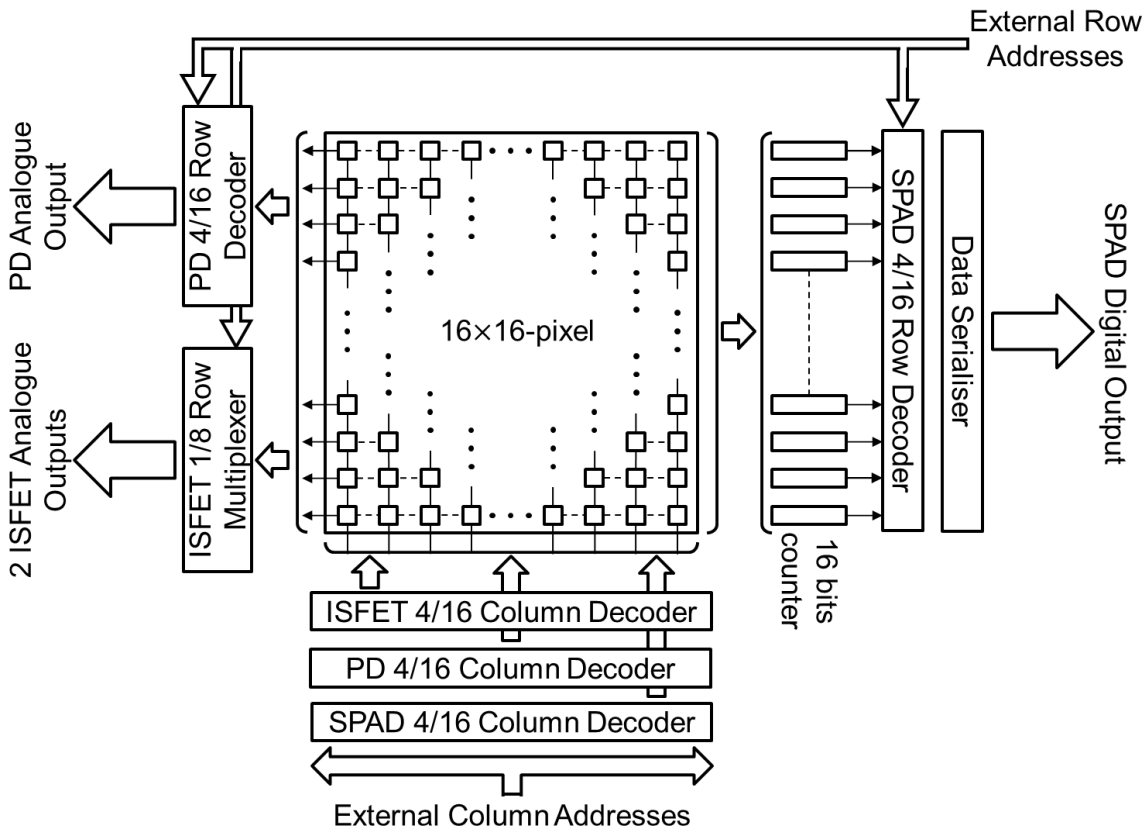

Figure 4.12 – A schematic diagram of the addressing and readout architecture of all three sensor arrays for 16×16-pixel Multi-Corder chip.

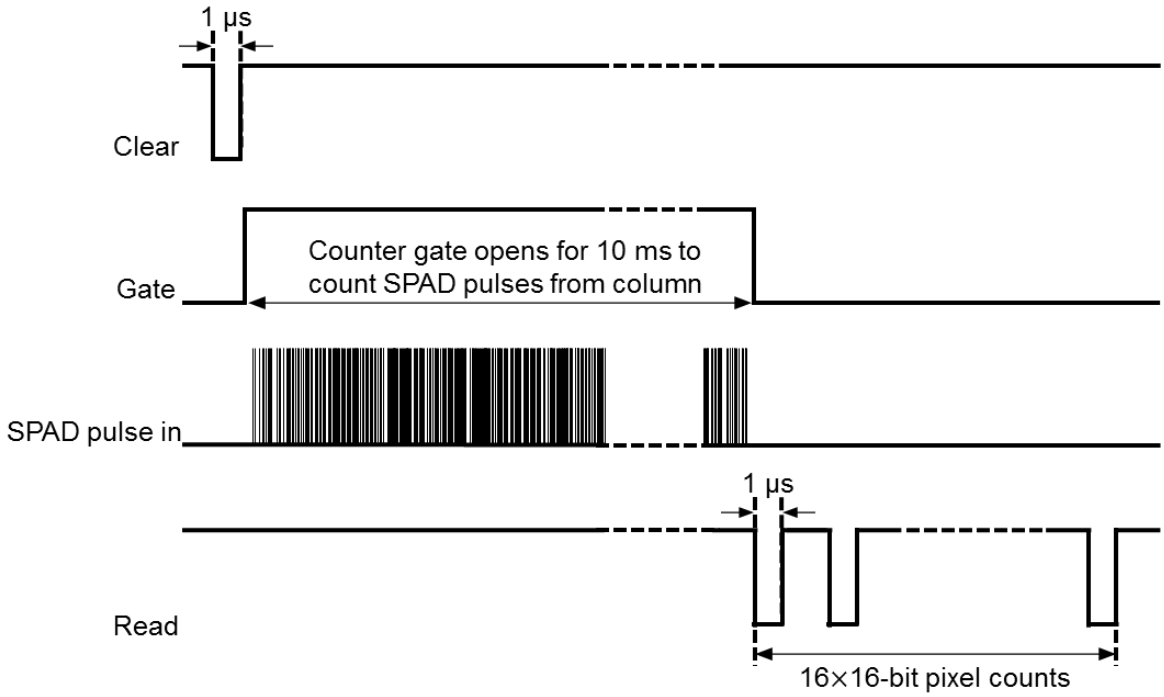

Figure 4.13 – SPAD array readout and communication protocol for Multi-Corder chip [132].

4.3.4 Off-Chip Instrumentation and Measurement System

In order to bring metabolome detection from the laboratory to the hands of a physician or patient, it is pivotal for the measurement tool to be compact and inexpensive. However, the instrumentation and measurement system that was constructed for the ISFET array chip was bulky and expensive, and was used mainly for laboratory experimentation. Moreover, the number of sensors pixels in the Multi-Corder chip is only 256, which is 256 times less than the number of pixels in the ISFET array chip. Hence a high-speed acquisition system was not required. Therefore, a low cost and miniaturised measurement tool was designed and constructed to demonstrate the ability of using the Multi-Corder chip to measure the concentration of hydrogen ions or spectrophotometric changes in an enzyme assay. The acquisition system was designed to acquire analogue signals (voltages) from the ISFET and PD sensors, obtain the digital signals from the counters of the SPAD sensors, and provide digital addresses to the chip. The system was designed to obtain the data from all three sensors independently, working with one sensor array at a time. However, this can be modified to acquire two sensor arrays at a time, which is either ISFET and PD or ISFET and SPAD, providing ionic and optical information simultaneously.

Figure 4.14 illustrates the flow of the instrumentation and measurement system for the Multi-Corder chip. The system comprises of a laptop, one ARM mbed Integrated Development Environment STM32 Nucleo-F334R8 board (STMicroelectronics), a custom PCB (Eurocircuits), and a packaged Multi-Corder chip. Similar to the ISFET array testing method, a quasi-reference electrode was used to set the floating gate potential for all the ISFET sensors in the array. In addition, a light source was required for the testing of spectrophotometric enzyme assays on the PD sensor array. An inexpensive and easy way of doing that was to use a standard green or blue LED shinning on top of the entire PD sensor array. To provide a more accurate measurement, a monochromator was used to transmit a narrow band wavelength from the light source and a lens was used to focus the light on top of the PD sensor array. SPAD is a highly sensitive optical sensor, thus it had to be operated in the dark. A black cardboard box was made to cover the whole measurement setup while realising SPAD-type experiments.

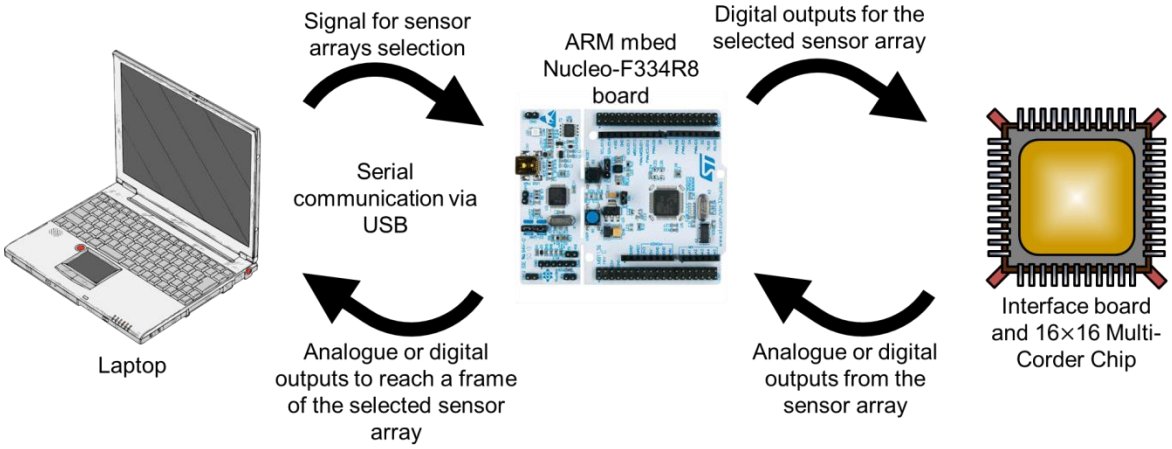

Figure 4.14 – System-level description of the measurement setup for the Multi-Corder chip.

Figure 4.15 shows the picture of the measurement setup. The mbed nucleo board (attached on to the PCB) was connected to the laptop via a standard USB (Universal Serial Bus) connection. On the PCB, a PGA ZIF 13×13 socket was used to house the packaged Multi-Corder chip. Furthermore, the PCB connected the two ISFET analogue outputs, one PD analogue output and one SPAD counters digital output from the chip to the mbed nucleo board. The PCB was also used to connect the 7-bit ISFET, 8-bit PD and 8-bit SPAD digital addresses that were provided from the mbed nucleo board to the chip. In addition, the digital signal of V_{rst} for PD and the other three digital signals for the SPAD (clear, gate and

read) were provided from the mbed nucleo board to the chip via the PCB. In addition, the PCB also connected a voltage source to all the in-pixel load transistor gates (exactly the same as the original ISFET array chip), a 22 V high voltage source to bias the SPAD and a 3.3 V power supply to power the chip.

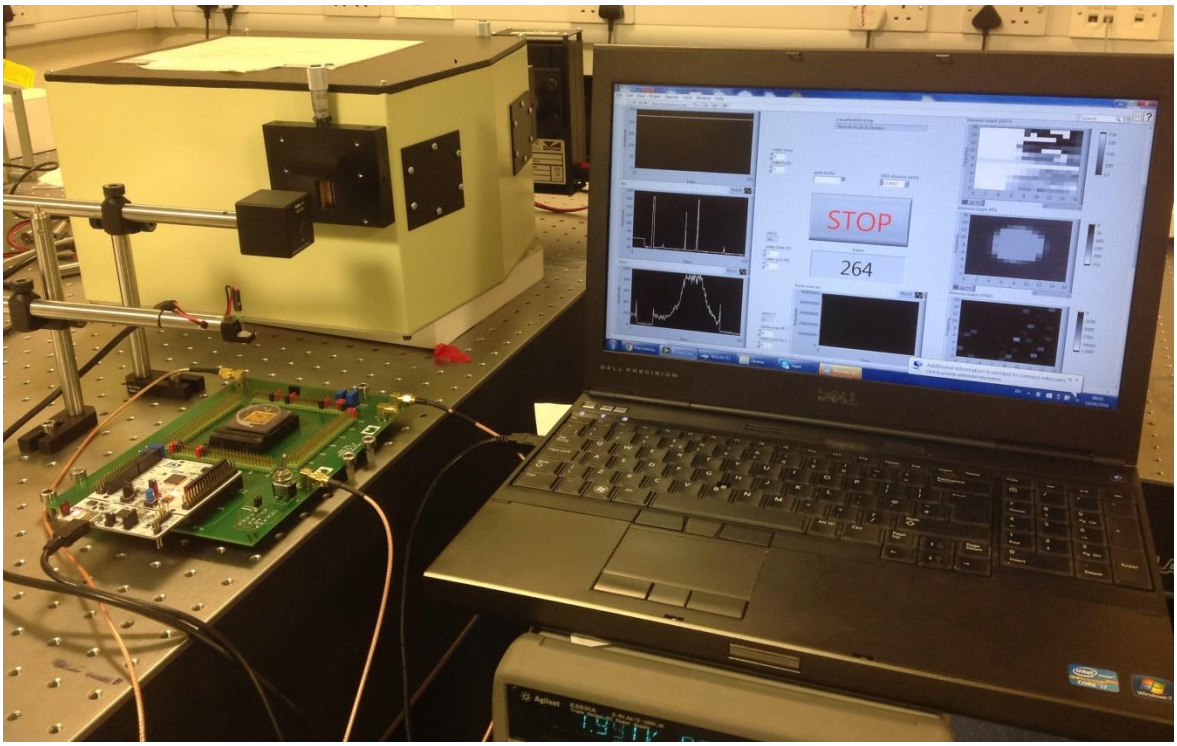

Figure 4.15 – Photograph of the measurement setup for the 16×16-pixel Multi-Corder chip.

The whole operation of the instrumentation system was controlled by LabVIEW using a laptop and the written program in the ARM mbed board. The mbed C++ program was written using mbed online compiler, which was downloaded into the microcontroller. The communication between the laptop and the ARM mbed board was through USB Serial port which uses a standard Serial interface. This is a generic protocol that is used by computers and electronic modules to transfer data in between each other [133]. It has two unidirectional channels to send and receive data through the Serial link. This link is asynchronous where both ends of the serial link have to be configured with the same settings such as baud rate, the rate of which data is transferred in a communication. Hence, the serial connection between the laptop and ARM mbed board was set to a baud rate (bits/s) of 115,200 at both ends. Moreover, the data transfer between them was designed to use the default 8-bit long data but can also be designed to a maximum of 12-bit long data.

Similar to the measurement tool for the original ISFET array chip, the digital signals for the addressing and readout signals for Multi-Corder chip had to be properly synchronised, this is very important to obtain the correct pixel measurements. Figure 4.16 is a flowchart showing how the synchronisation of the acquisition system works. A character (e.g. "A") was assigned for each sensor array. This character is recognised by the ARM mbed board program as an American Standard Code for Information Interchange (ASCII) code in decimal format (e.g. 65 for character "A"). This character was sent from the laptop using LabVIEW to the ARM mbed board program. When the ARM mbed board program receives the ASCII code, the program recognised which sensor array to activate and read from. The following steps describe the procedure for the three different sensor arrays:

1. If the ISFET sensor array is selected, the program will scan through 128 of 7-bit digital addresses to obtain two parallel analogue ISFET signals. These analogue signals will be sent through the USB Serial port to the laptop sequentially to form a 16×16 frame of data.

2. If the PD sensor array is selected, the program will send a digital signal (reset) to activate the gate of all the transistors M1 (Figure 4.10a) with V_{rst}. Then, the analogue signals from all the 256 sensors are readout using the 8-bit digital addresses. These analogue signals will be sent to the laptop serially to form a 16×16 frame of data.

3. If the SPAD sensor array is selected, the program will send the clear, gate and read digital signals to the chip, as described in Section 4.3.3. 256 of 7-bit digital addresses will be scanned through, until all the 16 counters for all 16 columns are read as 16-bit digital output signals from SPAD. These digital output signals will be sent to the laptop serially to form a 16×16 frame of data.

After one frame is obtained, another character is sent from the laptop to the ARM mbed board, in order to have a continuous flow of frames as a function of time. This summarises the synchronisation technique used to read out all the correct pixels. All of the above sensor array data were stored into a standard NI TDMS file.

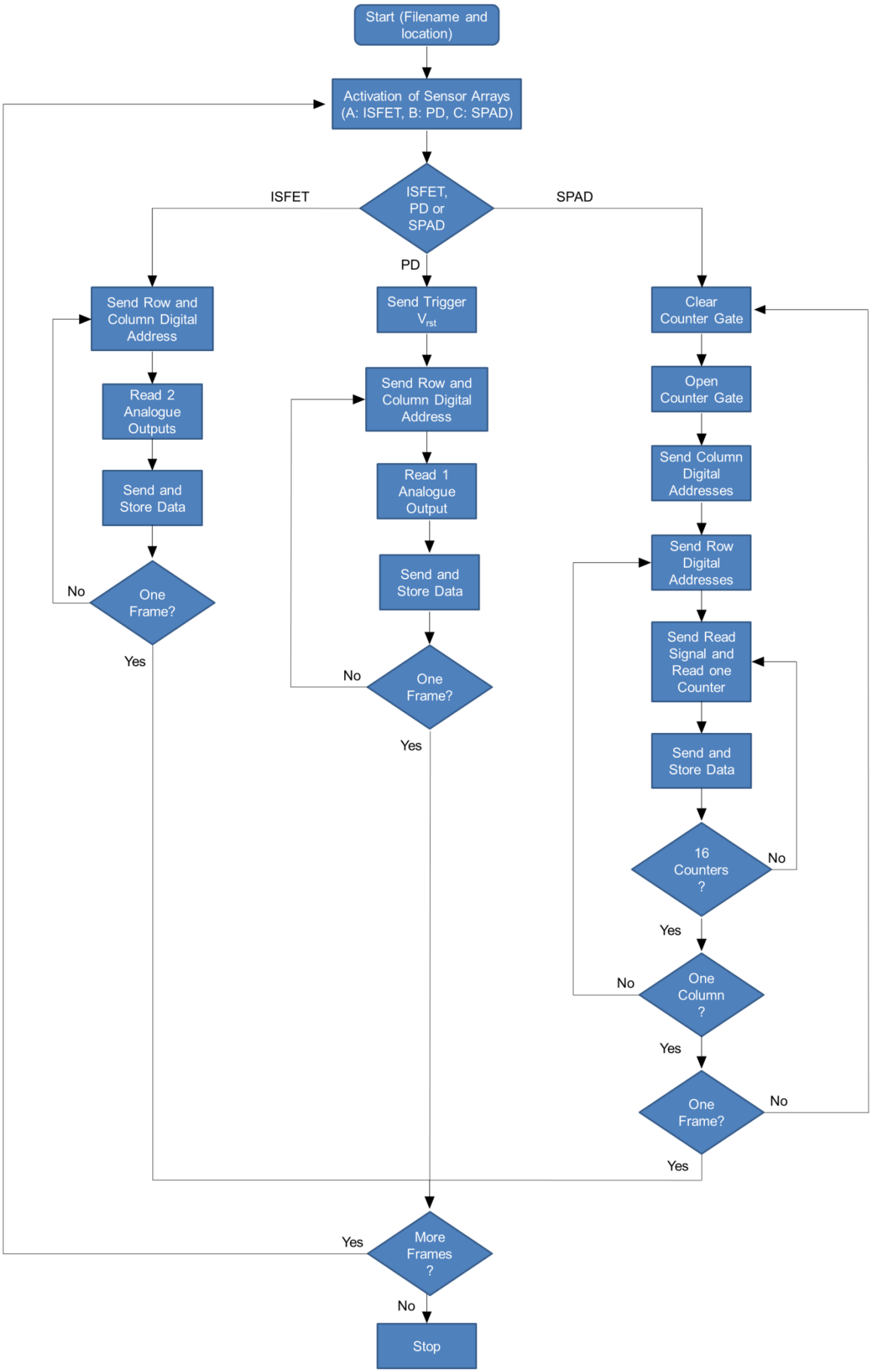

Figure 4.16 – Flow chart of the synchronisation architecture for the measurement setup used in the Multi-Corder platform.

4.3.5 Data Analysis

The raw data results from the acquisition system had to be extracted and analysed for both hydrogen ion concentration and spectrophotometric data. The acquired data was arranged into a 16×16 frame for each sensor array. Using the numerical functions in LabVIEW, a single pixel or an average of a certain area or the full array can be analysed as a function of time. Moreover, the visualisation of the 2D images for all the sensor arrays can be viewed across the complete duration of the experiment.

4.4 Summary

The design and fabrication of both chips, 256×256-pixel ISFET array and Multi-Corder, were described in detail. The ISFET array and Multi-Corder array designs were fabricated using AMS 'C35B4' 0.35 μm low voltage and AMS 'H35B4' 0.35 μm high voltage, four metal layer CMOS technology respectively. The readout architecture of both chips was discussed in detail, showing the interactions with the sensor pixel circuitry. Furthermore, a detail discussion was provided on developing a high-speed off-chip instrumentation system (PXI platform) to readout the analogue signals from all the sensors on the ISFET array chip by providing digital addresses to readout the selected pixels. Moreover, the chapter also emphasised on the use of CMOS chips for POC diagnostic applications. This led to the development of a low cost and miniaturised measurement tool (ARM mbed platform) for the Multi-Corder chip, where a detail discussion of the measurement tool was provided. Finally, the data of both chips was stored into a NI standard TDMS file and analysed using the NI software package LabVIEW. The next step will be to post-process the chips for sensitivity enhancement and microfluidics addition. The chips will be packaged with a suitable technique to be experimented with enzyme assays in wet environment.

Chapter 5 : Chip Post-Processing

5.1 Introduction

The previous chapter discussed two CMOS sensor array chips and also their instrumentation system. This chapter describes the post-processing of the CMOS ISFET to improve the sensitivity towards hydrogen and potassium ions. Furthermore, this chapter also discusses the microfluidics on top of a CMOS chip to provide multiple metabolites measurements. Finally, a discussion on packaging techniques that allow a CMOS chip to be used in a wet environment without compromising the electrical connections.

5.2 ISFET Sensitivity

On return from foundry, the CMOS chips normally cover with a layer of Si_3N_4 as passivation to protect the underlying embedded electronics. As mentioned in previous chapters, this passivation layer is in contact with the analyte solution and alters the electrical characteristics of the underlying ISFET through the metal stack, which can be detected by threshold voltage changes. Hence, the passivation layer may comprise of a variety of different materials to facilitate the sensitivity towards targeted ion sensitivity. Generally, Ta_2O_5 [134] is used to provide good sensitivity towards hydrogen ion concentration (pH) sensing while polyvinyl chloride membrane containing valinomycin [74], [135] provides good sensitivity to potassium ion concentration. The following sections will discuss about the material, method and characteristics for sensitivity towards both hydrogen and potassium ion concentration on a CMOS ISFET.

5.2.1 Tantalum Pentoxide

Since Matsuo and Esashi introduction of Ta_2O_5 as a sensing layer, it has been demonstrated that Ta_2O_5 presents better properties than Si_3N_4, which is the most commonly used pH-sensing layer, as mentioned in Section 2.4.1. These properties include better immunity to interference ions (selective to hydrogen

ions), higher sensitivity, lower drift, wider pH range and higher chemical resistance. Unlike Si_3N_4, Ta_2O_5 does not suffer from degradation of pH sensing characteristics from surface oxidation. Besides that, Si_3N_4 is known to show a sub-Nernstian response with a sensitivity of 46 mV/pH [60], whereas Ta_2O_5 has been shown to give a Nernstian response similar to glass electrode with a sensitivity of 58 mV/pH [134]. Hence, Ta_2O_5 is an ideal pH sensing layer to be used on top of a CMOS ISFET. Figure 5.1 shows the multi-layer metal structure CMOS ISFET with Ta_2O_5 exposed to the analyte solution.

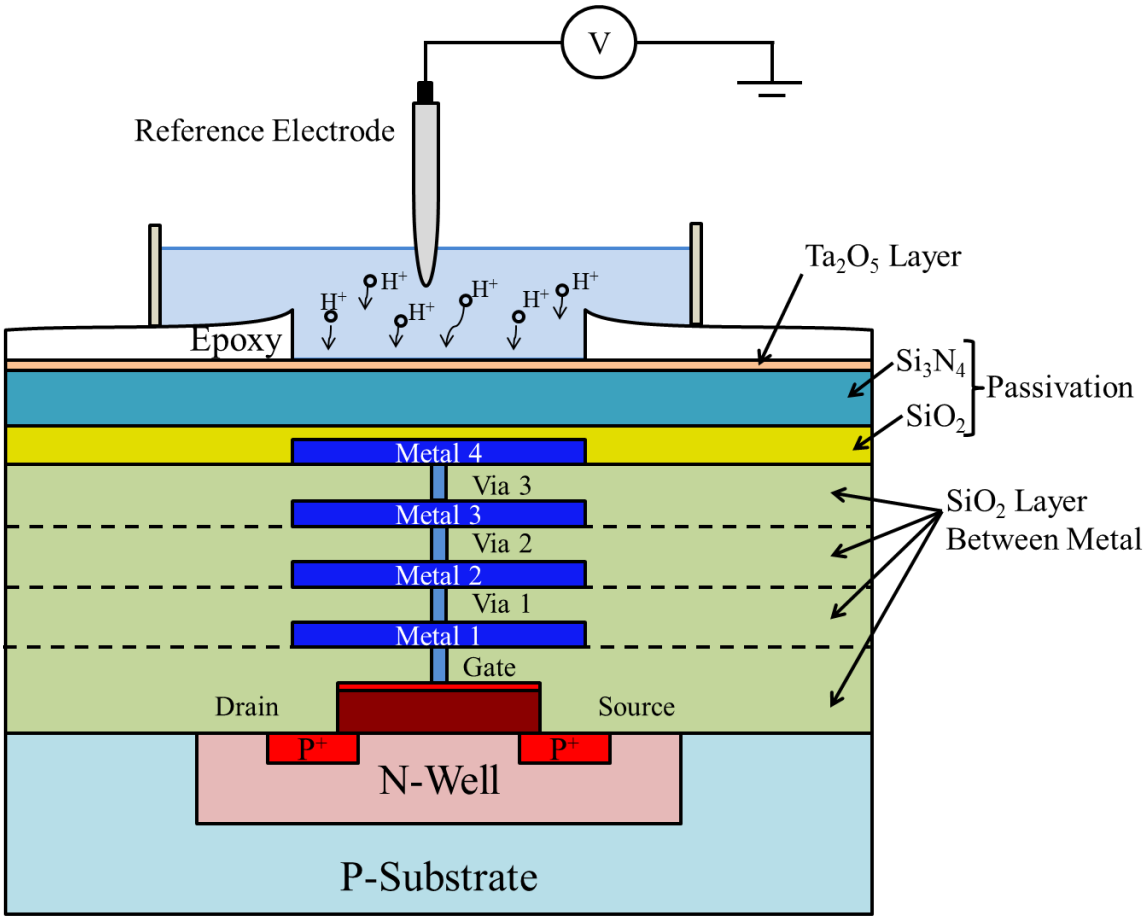

Figure 5.1 – A cross-sectional view of the CMOS ISFET structure with an additional Ta_2O_5 for pH sensitivity improvement.

5.2.1.1 Micro-Fabrication Process

In order to selectively deposit a layer of Ta_2O_5 on top of a CMOS chip, the facilities in the James Watt Nanofabrication Centre (JWNC) were used. A recipe to deposit Ta_2O_5 film with desired characteristics for ISFET was investigated in the course of this work. Furthermore, suitable processing steps had to be developed in order to fabricate on top of a small 4 by 4 mm^2 CMOS chip. Next,

the deposition steps are explained and followed by the characterisation procedures to obtain desired properties of Ta_2O_5 sensing layer, and also the fabrication steps taken to find an optimum recipe to selectively deposit this film on top of the chip.

Ta_2O_5 Deposition

For deposition of Ta_2O_5, the radio frequency (RF) sputtering tool was used. Sputtering is a physical thin film deposition technique that ejects target material from the surface when the surface is bombarded by sufficient energetic particles, normally inert gases such as argon. The target material is placed at the cathode while the substrate is placed at the anode. With high positive argon ions directed at the highly negative charged target, the target is struck by argon ions and the ejected atoms are transferred to the substrate. The atoms are condensed and formed a thin film. This technique provides uniform thickness and good adhesion of sputtered material across the surface of the substrate [136, Ch. 7]. Sputtering deposition technique can be reactive or non-reactive. Reactive sputtering is a process where a reactive gas is introduced to the target material to deposit compounds such as oxides, nitrides or carbides. While non-reactive sputtering is to deposit the target material as it is. In addition, the sputtering vacuum pressure, RF power and gas flow had to be investigated to obtain the desired characteristics for the Ta_2O_5 sensing layer.

For a good pH sensing Ta_2O_5 layer on ISFET, low drift and high sensitivity film is pivotal. The work from Chou and Hsiao [137] had demonstrated that the pH sensitivity of Ta_2O_5 varies with surface roughness. In their work, they used RF reactive sputtering system to deposit Ta_2O_5 and found that by changing the pressure in the chamber while sputtering had an effect on the surface roughness of the film. Hence, this had resulted in different pH sensitivity. Table 5.1 shows the effect of sputtering pressure towards surface roughness and pH sensitivity. Furthermore, Kwon *et al.* [138] demonstrated that the pH sensitivity of the Ta_2O_5 film was increased with the number of oxygen sites on the surface of the sensing membrane. Using RF reactive sputtering method and heating in O_2 ambient, they had deposited a Ta_2O_5 film with chemical atomic ratio (Ta:O) of 1:2.5, which is the ideal stoichiometric Ta_2O_5 film. With that, they had produced a Ta_2O_5 film with a high sensitivity of 58 – 59 mV/pH over with a wide pH range

of pH 2 – 12 and a low long term drift of 0.021 – 0.035 mV/hour. With this in mind, the Ta_2O_5 sputtering used in this work had to be developed to produce good surface roughness and chemical composition for good sensing characteristics.

Table 5.1 – Surface roughness and pH sensitivity for different sputtering pressures [137]

Variables	Pressure (mTorr)		
	5	15	25
Deposition rate (Å/min)	30.6	17.5	13.2
R_a (nm)	0.306	1.853	3.892
R_{max} (nm)	7.334	16.705	24.766
R_q (nm)	0.621	16.705	24.766
pH sensitivity (mV/pH)	55.2	48.2	46.8

Using reactive sputtering of Ta_2O_5 film discussed above, it requires Ta atoms to react with oxygen atoms at a proper ratio while having argon gas to bombard the target material and form a desired compound on a substrate. To reduce the complexity of reactive sputtering, a ceramic target (Ta_2O_5) with non-reactive sputtering was used in this work. According to Wu *et al*. [139] work, the Ta:O ratio of the ceramic target is close to the ideal stoichiometric ratio, thus only a small amount of oxygen atoms are required for ceramic target sputtering that is essential for the compensation of oxygen atoms lost during deposition process. They found that the deposited Ta_2O_5 film had to be annealed to a temperature of 400^{o}C to achieve surface roughness of 0.547 nm and Ta:O ratio of 1:2.5. Alternatively, they demonstrated that ceramic target can be deposited in pure oxygen atmosphere without any annealing to obtain the desired characteristics.

Since the RF sputtering tool and chamber in JWNC is different from the work described above, investigation had to be established. This includes working pressure, gas flow of Ar:O and RF power. The working pressure of almost all the JWNC processes used in the sputtering tool was 100 μbar. Therefore, the most sensible approach was to sputter Ta_2O_5 at this pressure to begin with. Later atomic force microscopic (AFM) measurement from the final sputtering conditions of Ta_2O_5 film deposition had shown an average surface roughness of 0.42 nm. This surface roughness agrees well with the earlier work described

previously. Hence, no further investigation of working pressures was required. Figure 5.2 illustrates the surface profile of the Ta_2O_5 layer using AFM.

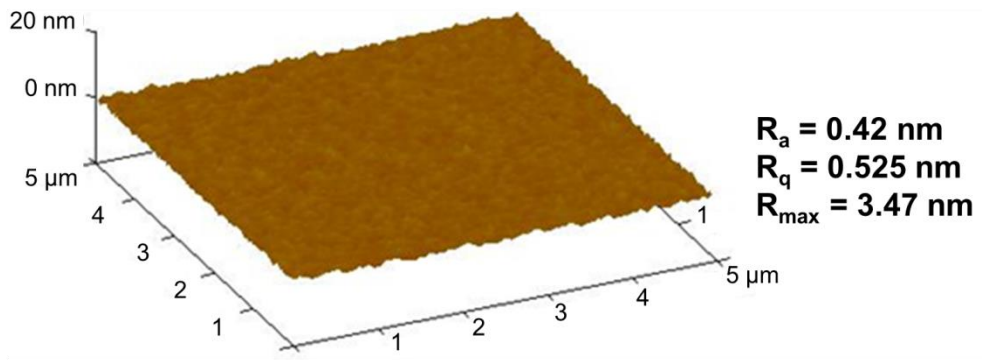

Figure 5.2 – The surface profile of the Ta_2O_5 film obtained from AFM, where R_a, R_q and R_{max} are average roughness, RMS roughness and maximum roughness, respectively.

Since the gas mixture ratio of Ar:O_2 is very important to form a good chemical composition of Ta:O for pH sensing, different gas mixture ratio was investigated using this sputtering tool. Using x-ray photoelectron spectroscopy (XPS) to analyse the surface chemistry of the Ta_2O_5 film, different chemical composition of Ta:O corresponded to different gas mixture of Ar:O_2 flow rate. Figure 5.3 shows the XPS spectrums obtained from the Ta_2O_5 films, which were sputtered with three different ratios of Ar:O_2. As can be seen in Figure 5.3, by increasing the gas mixture ratio of Ar:O_2 from 0% to 10% in O_2, this affected the Ta:O ratio of the surface from 1:1.51 to 1:1.77. These results were as expected from the previous work discussed above, thus ideally 100% oxygen sputtering is preferred to reach stoichiometric value of 1:2.5 for Ta_2O_5 film. However, it was noticed that as the oxygen content in the chamber increases, the temperature of the chamber during sputtering increases as well. High temperature sputtering was not good for later patterning process that involves photoresist. Moreover, high temperature will also compromise the structure integrity of the aluminium bond pads in the CMOS chips. Therefore, the gas mixture ratio of Ar:O_2 of 9:1 was chosen for this work. Even though the Ta:O ratio was only 1:1.77, a significant improvement in ISFET performance was obtained, which will be described later in Section 5.2.1.2.

Lastly, the thickness of the Ta_2O_5 film was affected by changing the RF power and duration of the sputtering. From various literatures, 50 to 120 nm thick layer of Ta_2O_5 was preferred for pH sensing [52], [134], [138]. Hence, the RF power

and duration of sputtering was varied to obtain a controllable thickness of 100 nm, under the sputtering conditions described above. In a nutshell, Table 5.2 shows the final sputtering conditions used to deposit a Ta_2O_5 film on a CMOS ISFET.

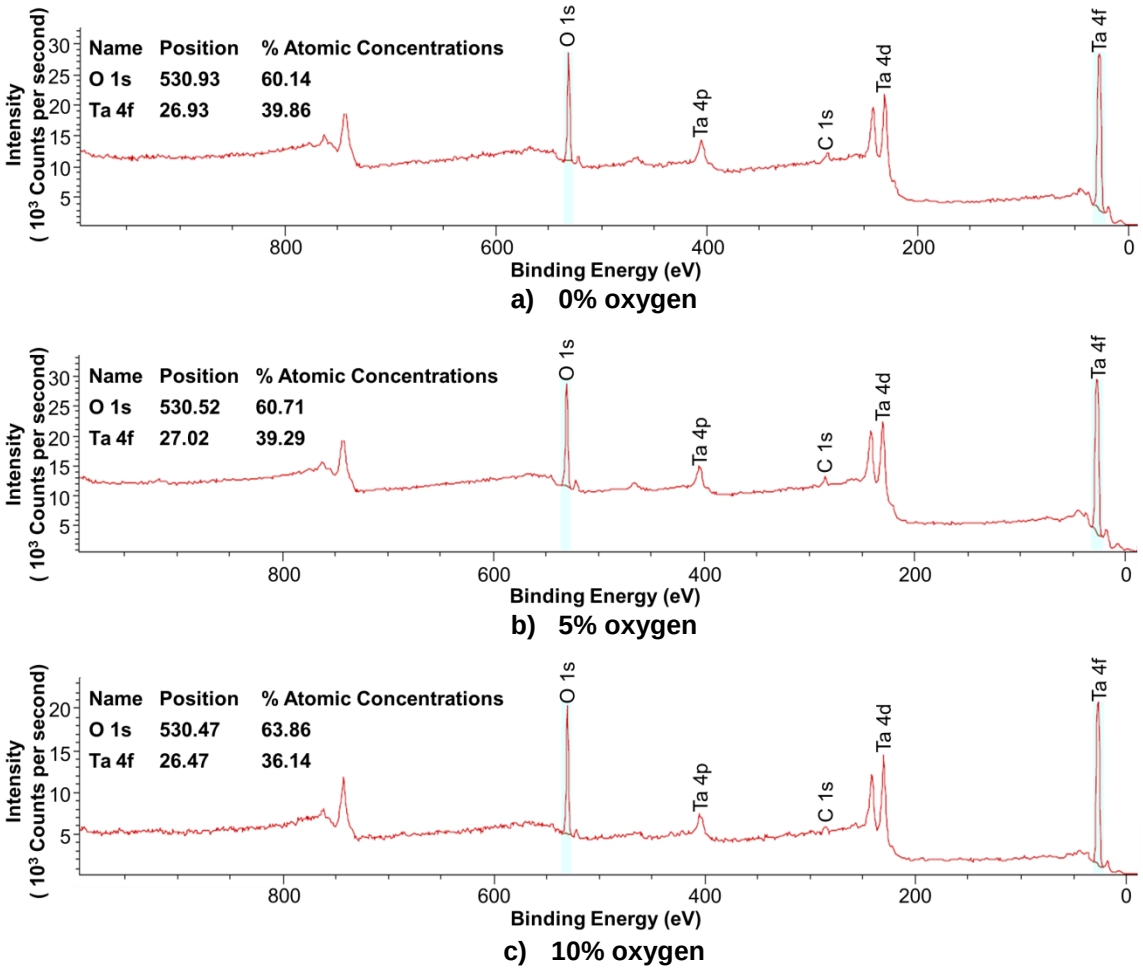

Figure 5.3 – XPS analysis of the chemical composition of the Ta_2O_5 film surface for various gas mixture ratio of $Ar:O_2$.

Table 5.2 – Sputtering conditions of Ta_2O_5 film deposition

RF power	300 W
Working pressure	100 μbar/75 mTorr
Gas mixture ratio	9:1 sccm ($Ar:O_2$)
Chamber and substrate temperature	Room temperature

Patterning Resist

The bond pads of the CMOS chip, which are made of aluminium (Al), had to be avoided from any Ta_2O_5 deposition, as they had to be wire bonded onto a chip carrier for electrical connections. Therefore, a patterning process had to be developed to deposit Ta_2O_5.

Two different methods could be used to selectively pattern a layer of Ta_2O_5. The first method consisted of sputtering a layer of Ta_2O_5 on top of the CMOS chip covering the full area, followed by a selective etching to release the Al bond pads. However, most of the dry/wet etches that could be used to etch Ta_2O_5 would strongly damage the Al bond pads, making the wire bonding almost impossible. In addition, a hard mask for the etching had to be investigated (most possible a metal mask), which would imply more steps on the fabrication process [140].

The second method consisted of a lift-off process. Lift-off process [141] was chosen to be the patterning process as this does not involve any etching process that will destroy the aluminium bond pads. Moreover, lift-off process has less processing steps compare to etching process, which is a lot more easy and simple for patterning. The only disadvantage of using lift-off process is that the processing temperature inside the deposition chamber could change the properties of the photoresist, as well as affecting the side wall profile of the photoresist. This was the reason why the temperature of the sputtering conditions had to be low, as mentioned previously. Furthermore, generally for a lift-off technique to work properly, a non-conformal deposition such as evaporation is preferred, which has poor step coverage. Nevertheless, lift-off technique still produced a good patterning Ta_2O_2 film on top a CMOS chip.

Figure 5.4 illustrates the lift-off technique for a Ta_2O_5 film. Photolithography was used to define a photoresist pattern on top of the CMOS chip, opening a window over the active area of the sensor array. The patterned resist created an undercut resist edge profile that will not provide a conformal coating and promote lift-off. Then, a Ta_2O_5 film was deposited all over the CMOS chip, covering the photoresist and also the areas where photoresist had been removed. Using wet chemical solvent to remove the photoresist underneath the

film and take the film as well, leaving the film on top of the CMOS chip with the desired pattern. Therefore, a suitable photoresist process had to be chosen to provide a good formation of Ta_2O_5 pattern on top of the CMOS chip.

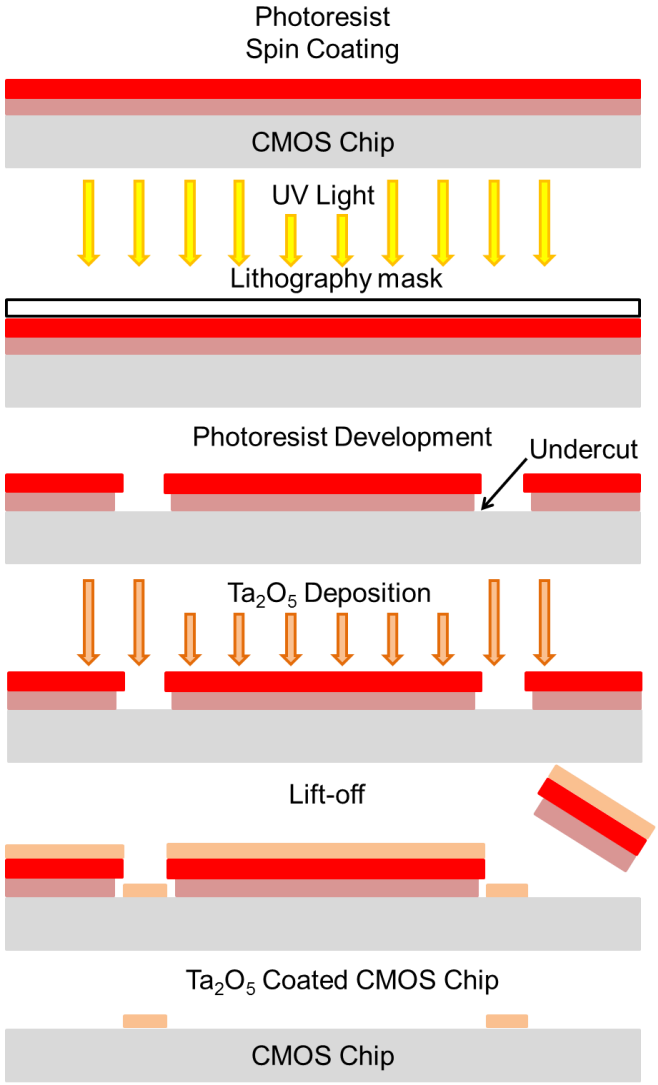

Figure 5.4 – Schematic diagram of the lift-off technique for Ta_2O_5 film on top of a CMOS chip.

Negative photoresists are generally the best choice of resists to be used for lift-off processes. A reproducible undercut can be obtained with negative photoresists which is ideal to perform a good lift-off. Besides that, a cross-linking step of negative photoresists helps to maintain the structure integrity of the resist when dealing with high temperature deposition. Hence, a process was developed using AZ2070, a negative photoresist with thickness of approximately 7 μm. The processing steps for depositing Ta_2O_5 film with AZ2070 [142] are given in Table 5.3. However, the lift-off process with AZ2070 was not lifting off after the sputtering. Figure 5.5 shows the evaluation of AZ2070, before and after

sputtering. Before sputtering, it had a very significant undercut, while after sputtering, the undercut profile was destroyed and the lift-off was not working. Hence, a new lift-off process was developed to replace AZ2070 process.

Table 5.3 – Lift-off process using AZ2070

Step	Details
Coat	1. Static dispense – covers approximately 80% of the surface with AZ2070. 2. Spin cycle – ramp up from 0 to 4000 rpm at 20000 rpm/s and hold for 60 seconds to obtain 7 μm resist layer thickness.
Soft bake	Bake at 110^{o}C on a hotplate for 1 minute and 30 seconds.
Photolithography	Expose on a standard mask aligner for 18 seconds.
Post bake	Bake at 110^{o}C on a hotplate for 1 minute.
Develop	1 minute and 20 seconds in MF-319 developer with continuous agitation.
Rinse and dry	Rinse in deionised (DI) water for at least 30 seconds and blow dry with a nitrogen gun.
Metallisation	Deposit Ta_2O_5 with RF non-reactive sputtering.
Lift-off	Immerse the sample in hot acetone after deposition that allows the acetone to attack the resist and lift-off the resist with Ta_2O_5.

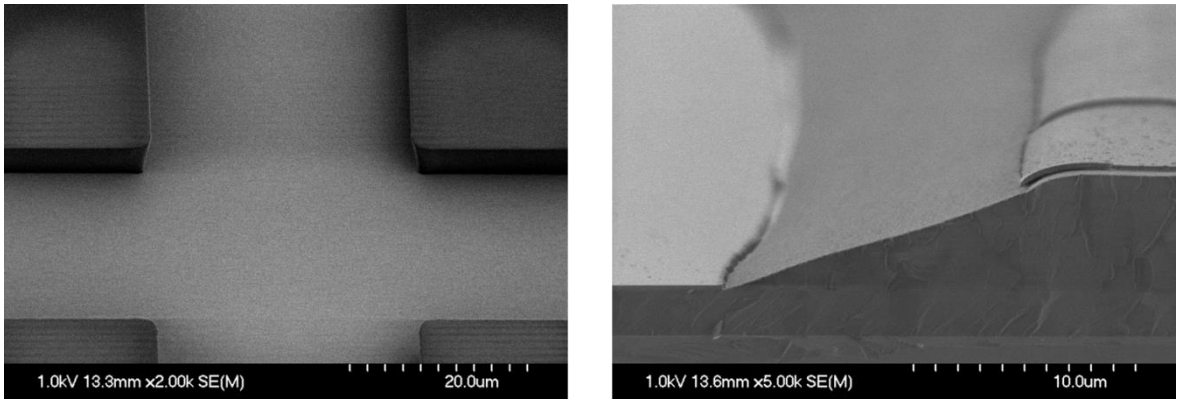

a) Before sputtering **b) After sputtering**

Figure 5.5 – SEM images of the lift-off from AZ2070 before and after deposition of Ta_2O_5.

This newly developed lift-off process used S1818 [143], a positive photoresist with a thickness of roughly 1.8 μm, together with LOR10A (lift-off resist) [144], a resist used to create undercut with a thickness of 1 μm. The first step was to spin-coat LOR10A at 6000 rpm for 30 seconds on to the sample. Then, the sample was baked on the hotplate at 150^{o}C for 2 minutes. Follow by, spin-coating of S1818 at 4000 rpm for 30 seconds and baking at 115^{o}C for 3 minutes. After the coating process, the sample was found to have large edge beads with bubbles at all the corners of the sample. The bubbles will compromise the bond pads during sputtering. Hence, a slight alteration to the coating process was done to remove the bubbles at the edge beads. This involved changing the speed and duration of the spinning of LOR10A. Figure 5.6 illustrates that the alteration of the coating process had removed the bubbles at the edge beads of the CMOS chip. Table 5.4 shows the working lift-off process for Ta_2O_5 that was carried out throughout this work.

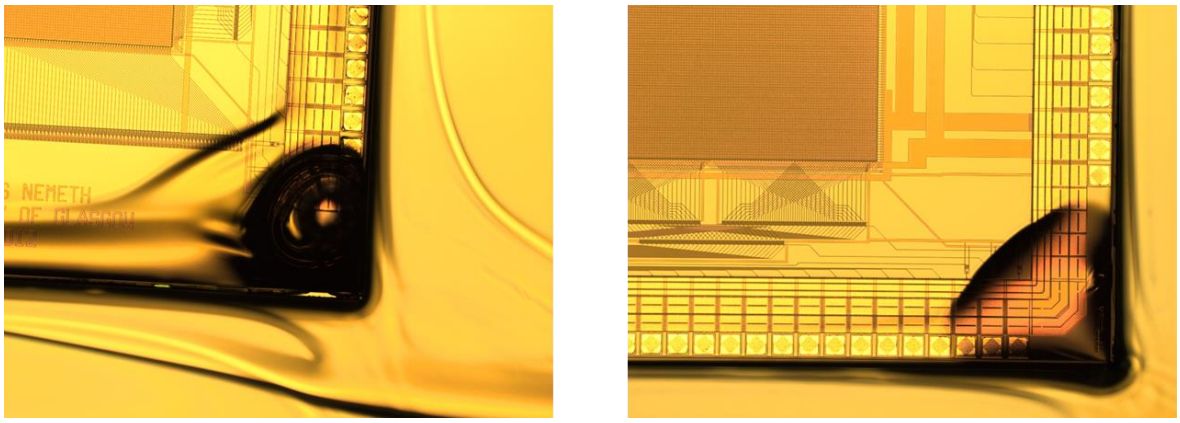

a) Before resist optimisation **b) After resist optimisation**

Figure 5.6 – Photo micrograph of the removal of bubbles from the edge bead of the resist S1818 and LOR10A.

With all the sputtering and patterning developed, Ta_2O_5 film was successfully fabricated on both ISFET array chip and Multi-Corder chip, as can be seen from Figure 5.7. Since ISFET array chip has only ISFET sensors, the entire array was covered with Ta_2O_5 film leaving only the bond pads exposed. On the other hand, Multi-Corder chip has three different sensors, thus the Ta_2O_5 film was patterned and only deposited on top of the ISFET sensors.

Table 5.4 – Lift-off process using S1818 and LOR10A

Step	Details
Coat	1. Static dispense – covers approximately 80% of the surface with LOR10A. 2. Spin cycle – ramp up from 0 to 9000 rpm at 2000 rpm/s and hold for 60 seconds.
Soft bake	Bake at 150^{o}C for 2 minutes on a hotplate.
Coat	1. Static dispense – covers approximately 80% of the surface with S1818. 2. Spread cycle – ramp up from 0 to 1000 rpm at 250 rpm/s and hold for 5 seconds. 3. Spin cycle – ramp up from 1000 to 4000 rpm at 2000 rpm/s and hold for 30 seconds. 4. Edge bead removal cycle – ramp up from 4000 to 9000 rpm at 20000 rpm/s and hold for 2 seconds.
Soft bake	Bake at 115^{o}C for 3 minutes on a hotplate.
Photolithography	Expose on a standard mask aligner for 6 seconds.
Develop	2 minute and 30 seconds in MF-319 developer with continuous agitation.
Rinse and dry	Rinse in DI water for at least 30 seconds and blow dry with a nitrogen gun.
Ash	40 W and 3 minutes in barrel asher to remove smaller residuals.
Metallisation	Deposit Ta_2O_5 with RF non-reactive sputtering.
Lift-off	Immerse the sample in hot 1165 resist stripper after deposition that allows the stripper to attack the resist and lift-off the resist with Ta_2O_5, leaving the desired pattern on top of the CMOS chip.

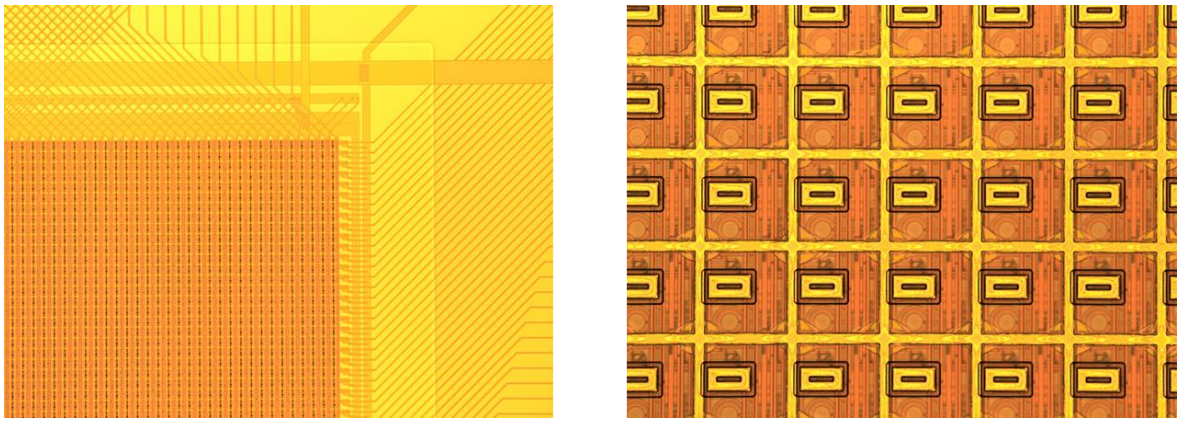

a) ISFET array chip b) Multi-Corder chip

Figure 5.7 – Photo micrograph of the patterning of Ta_2O_5 sensing layer on top of the CMOS chips.

5.2.1.2 Characteristics

The functionalities and pH response of the Ta_2O_5 film on top of the CMOS ISFET were characterised with the instrumentation system mentioned in Chapter 4 to demonstrate the ability and sensitivity to hydrogen ions. This was done with test solutions ranging from pH 1 – 14. These solutions were prepared from 1 M hydrochloric acid (pH 0) and 1 M sodium hydroxide (pH 14). Both the acid and alkali solution were diluted with DI water to make up pH 1 – 6 (0.1 M to 0.001 mM hydrochloric acid) and pH 8 – 14 (0.001 mM to 1 M sodium hydroxide), respectively. The pH sensitivity was tested by introducing different prepared pH solution on top of the ISFET sensor array of a packaged chip. The experiments were conducted by adding first alkali or acid and followed by a predefined order for consistency. Each pH solution was measured on top of the chip for approximately 2 minutes to obtain a stable result. The measurements were taken as indicated in Figure 5.8. Between each pH measurement, the chip was cleaned with DI water and blown dry with nitrogen gun. To ensure correct interpretation, the ISFET sensor array was measured with descending and ascending order of pH solution.

As can be seen from Figure 5.9, the sensitivity of the Ta_2O_5 film on top of the CMOS ISFET was about 45 mV/pH and yields a near linear voltage response between pH 2 – 12. The pH sensitivity of the Ta_2O_5 was less than the potential pH sensitivity of 58 mV/pH. There are two reasons that could cause the signal loss, which are the non-stoichiometric deposited Ta_2O_5 film from sputtering and

also the attenuation in the voltage-follower circuit in each pixel. Nevertheless, this was also termed as an improvement from the pH sensitivity measurement previously done in the MST group, using CMOS ISFET with the default Si_3N_4 passivation from the foundry, which was only 20 mV/pH [145]. In addition, the standard error of the data population from Figure 5.8 can be analysed to give 2.6 mV. This was calculated using the standard deviation of each pH trace over the three independent measurements that were made with the ISFET array chip. Then, the limit of detection of the ISFET sensor can be determined from 3 × standard error that was obtained and divided by the pH sensitivity [146], which is approximately 0.2 pH.

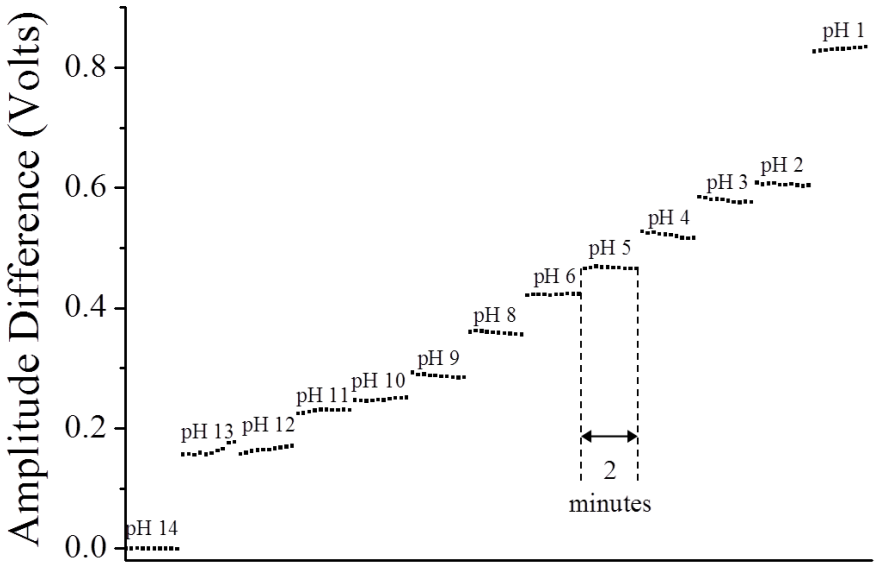

Figure 5.8 – A representation of differential voltage response of pH test measurements.

Besides pH sensitivity and wide working pH range, the Ta_2O_5 sensing film has an extra advantage over Si_3N_4 passivation from the foundry [147], which is the long term drift. The drift measurement was done by immersing the chip in triethanolamine buffered solution at pH 7.4 for a period of up to 6 hours. The drift measurements were taken using an average across the whole ISFET sensor array. Figure 5.10 shows the constant signal drift from the Ta_2O_5 sensing layer on one chip. Furthermore, two more chips with Ta_2O_5 sensing layer were also used to measure the drift in the same way, in order to investigate the chip-to-chip variation. Each chip was measured three times to take account into the variability between different experiments, such as the reference electrode position, cleanliness of the chip surface, buffer solutions concentration and volume. The deposited Ta_2O_5 sensing layer on all three chips was from three

separate batches of sputtering process, thus this will ensure that the film on top of all three chips is not identical. As can be seen from Figure 5.11, the drift of three different chips from the same wafer run and different sputtering runs are 3.1 ± 1.1 mV/hour, 0.1 ± 0.1 mV/hour and 16.3 ± 5.9 mV/ hour respectively. The drift from three different chips has an average of 6.5 mV/hour with a standard deviation of 8.6 mV/hour. The chip-to-chip variation may not completely be affected by the separate sputtering runs, as the multi-project wafer run from Europractice also had an effect to the variation. This is because each of these chips may locate in different areas on the wafer that leads to the chip-to-chip variation, which is uncontrollable. Nevertheless, this has still show that Ta_2O_5 sensing film can produce a stable enzyme assay measurement, unlike default Si_3N_4 passivation sensing layers from the foundry that suffer from drift issues. In addition, the enzyme assay measurements that were done in this work only takes 15 minutes to obtain sufficient data, thus the drift was not a major concern.

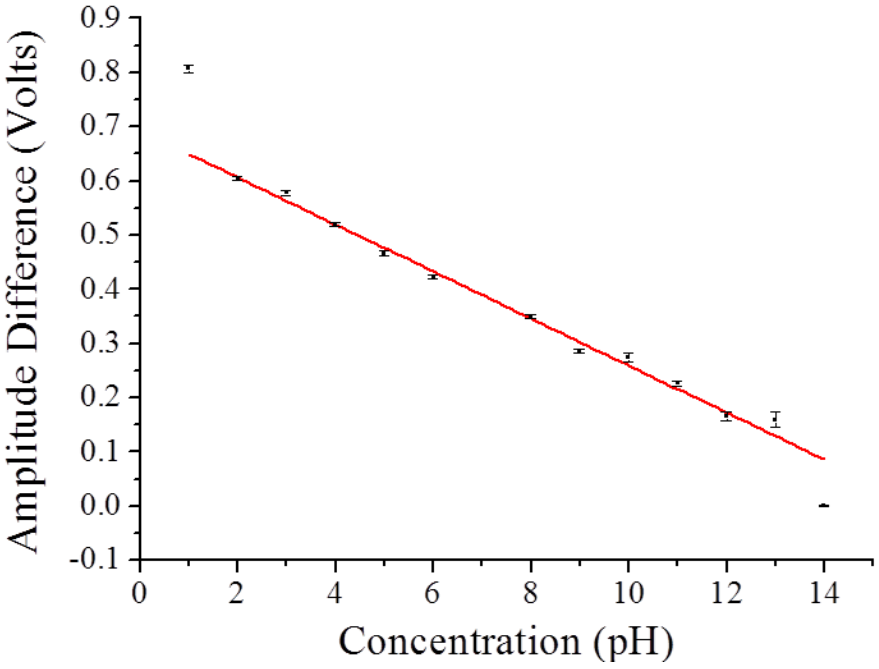

Figure 5.9 – pH sensitivity of Ta_2O_5 on top of the ISFET sensors.

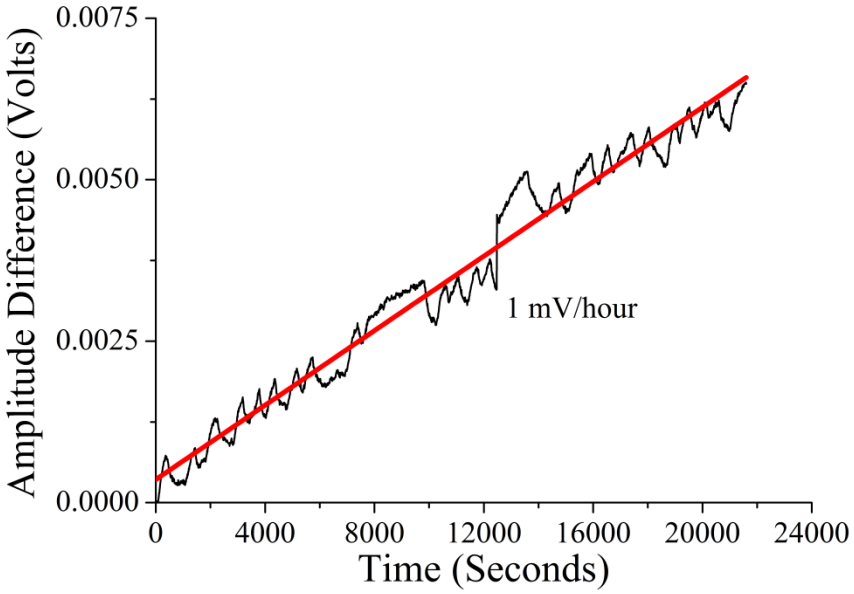

Figure 5.10 – A representation of drift measurement of Ta_2O_5 film on top of the CMOS ISFET sensors from one of the three chips.

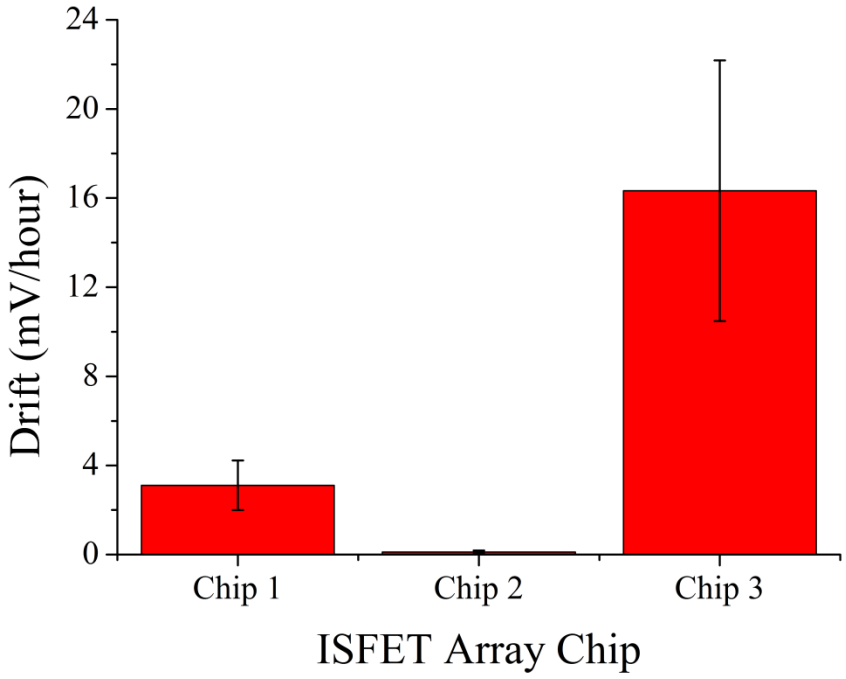

Figure 5.11 – The drift measurements from three different chips with different Ta_2O_5 sensing layer.

5.2.2 Polyoxometalates

After the introduction of ISFET and the presentation of pH sensitivity similar to a glass electrode, Bergveld believed that by introducing impurities to the sensing layer on top of the ISFET, would render the device ion selective. Moss *et al*. [74] demonstrated a potassium selective ISFET, using a chemical membrane made of valinomycin/plasticizer/poly(vinylchloride), which was solution casted and cured

on top of the Si_3N_4/SiO_2 passivation of the ISFET. However, valinomycin sensing membrane is an organic material that is not compatible with current CMOS technology, such as finite thermal stability [135] and poor adhesion [148]. Therefore, a potassium sensing membrane that is compatible with CMOS process is required. To investigate on CMOS compatible potassium selective ISFET sensing membranes, MST group, School of Engineering and Cronin group, School of Chemistry, from University of Glasgow join forces to make this a reality.

Polyoxometalates (POMs) [149], [150] are particularly interesting group of molecules which possess an unmatched range of physical and chemical properties. They consist of early transition-metal atoms (W, Mo, etc.) in their highest oxidation states that link together by oxygen bridges to form a cluster of well-defined size and shape. Since they are metal oxide based compounds, this makes them more compatible to metal oxide based electronics and holds an advantage over pure organic compounds. Moreover, they have high thermal stability of around 600^{o}C, which makes them an ideal candidate to be used in CMOS process. Another great benefit of POMs is their ability to self-assemble on surface without any chemical treatments required. Recently, Busche *et al.* [151] demonstrated that POMs are a candidate to act as storage node for MOS flash memory.

One of the POMs structure is particularly attractive to this work as a potassium sensing film for ISFET, which is $Li_{17}(NH_4)_{21}H_2[P_8W_{48}O_{184}]\cdot 85H_2O$ (abbreviated as $\{P_8W_{48}\}$ throughout this work). The $\{P_8W_{48}\}$ anion was first reported by Contant and Tézé [152] as a mixed lithium/potassium salt. Boyd *et al.* [153] from School of Chemistry at the University of Glasgow later synthesised a $\{P_8W_{48}\}$ anion with lithium and ammonium counter ions, which was used in this work. Figure 5.12 illustrates the structure of the $\{P_8W_{48}\}$ used in this work.

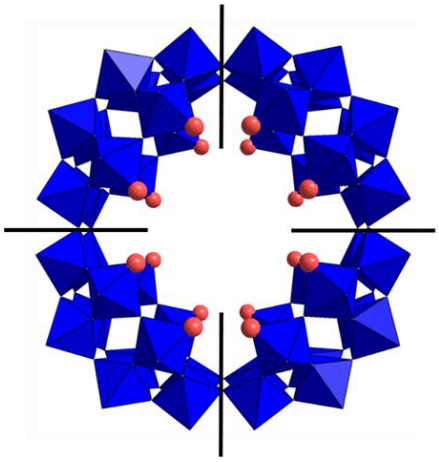

Figure 5.12 – Schematic diagram of $\{P_8W_{48}\}$ anion with four lacunary subunits and the respective oxygen atom binding sites [153].

The $\{P_8W_{48}\}$ anion comprises four $\{P_2W_{12}\}$ lacunary subunits bridged together to form a ring, with all the lacunary sites facing the centre of the ring, creating a nucleophilic environment. This exposed, nucleophilic, oxygen surface of the inner ring allows specific ions with the right size to bind to the inner surface of the ring structure, which in this case are potassium ions. Figure 5.13 shows all the binding sites for potassium ions. As can be seen from Figure 5.13a, there are eight half-occupied binding sites, located at the bridges of each $\{P_2W_{12}\}$ subunits and they are marked as red circles. From these eight possible binding sites, potassium ions can only bind to either the one above or below the symmetry plane of the molecules, as can be noticed in Figure 5.13b. Other potassium binding sites are located in between the nucleophilic faces of the $\{P_2W_{12}\}$ subunits, which are marked as yellow. These sites are fully-occupied and located in the equatorial belt of the molecules, with four terminal oxygen atoms of the exposed lacunary sites coordinate with one potassium ion. Hence, in total $\{P_8W_{48}\}$ has eight possible binding sites contain in the cavity of the ring, making it selective to potassium ions.

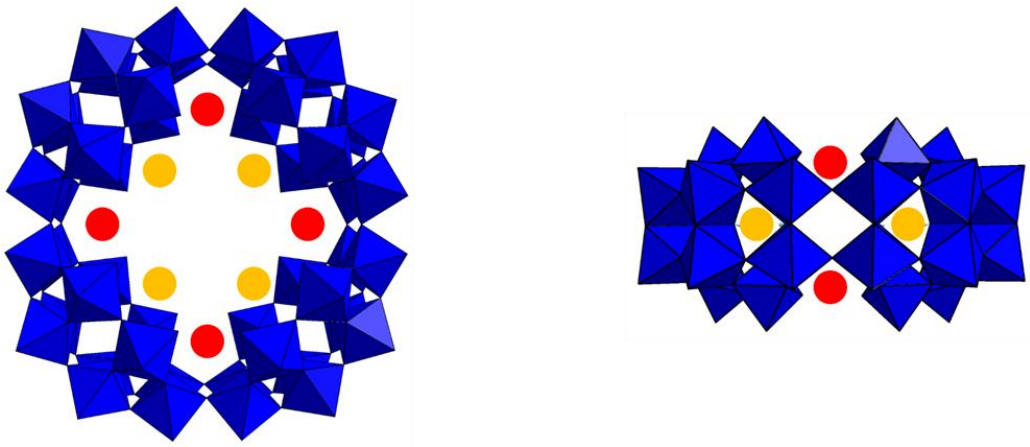

a) Top view b) Side view

Figure 5.13 – Cross-sectional view of all the binding sites of the $\{P_8W_{48}\}$ anion [153].

5.2.2.1 Process

The tetrabutylammonium (TBA) salt of the $\{P_8W_{48}\}$ ion was prepared in advance by our collaborator, Cronin Group at the School of Chemistry. In order to make the surface of ISFET sensitive towards potassium ions, $\{P_8W_{48}\}$ had to be functionalised on top of the passivation layer of the ISFET. The surface functionalisation process is similar to valinomycin membrane but it is simpler and quicker because it does not required a curing step of 24 hours at 50°C. The ISFET passivation surface was functionalised with $\{P_8W_{48}\}$ by drop casting. 10 μl of 1g/10ml (TBA)$\{P_8W_{48}\}$ in acetonitrile was applied with a Gilson pipette and left to evaporate for 10 minutes. This led to a formation of a stable and well-ordered $\{P_8W_{48}\}$ film on top of a CMOS ISFET chip.

5.2.2.2 Characteristics

Similar to characterising the Ta_2O_5 pH sensing capability on top of ISFET, the functionalities and pK responses of the $\{P_8W_{48}\}$ film on top of the ISFET were measured with the instrumentation system to demonstrate the potassium ions sensing capability. The pK measurements were done with test solutions ranging from pK 1 – 3. These solutions were prepared from 0.1 M potassium chloride (pK 1) and diluted several times to obtain pK 1 – 3 with a step size of pK 0.5. All the solutions were kept at pH 7.4 to ensure that any changes to ISFET signals would be corresponded to the concentration of potassium ions. Hence, the concentrations of the potassium chloride solutions were 100 mM, 31 mM, 10 mM, 3.1 mM and 1 mM. The different pK solutions were introduced on top of the

packaged CMOS ISFET chip in a predefined order for consistency. The experiments were conducted by first introducing DI water, which has no potassium ions and followed by pK 3 to pK 1 with a step size of pK 0.5. Each of the pK solutions was measured for 1 minute to obtain a stable result.

In order to determine that the $\{P_8W_{48}\}$ film is sensitive to potassium ions, control experiments had to be conducted. Moreover, it is very important to validate how sensitive Ta_2O_5 ISFET sensors towards potassium ions, as the sensors will be used for enzyme assays in blood serum which contains various ions such as potassium, sodium, calcium, magnesium and etc. These ions will be a factor in interfering with quantification of metabolites in an enzyme assay that relies on hydrogen ions consumption or production. Before any surface functionalisation with a $\{P_8W_{48}\}$ film on top of a CMOS ISFET chip, the chip was characterised with the whole range of pK solutions, in order to provide as a control measurement. After the surface functionalisation, the same pK solutions were introduced again in the same way. Figure 5.14 illustrates the pK measurements using a CMOS ISFET chip, without and with $\{P_8W_{48}\}$ film from one experiment as an example.

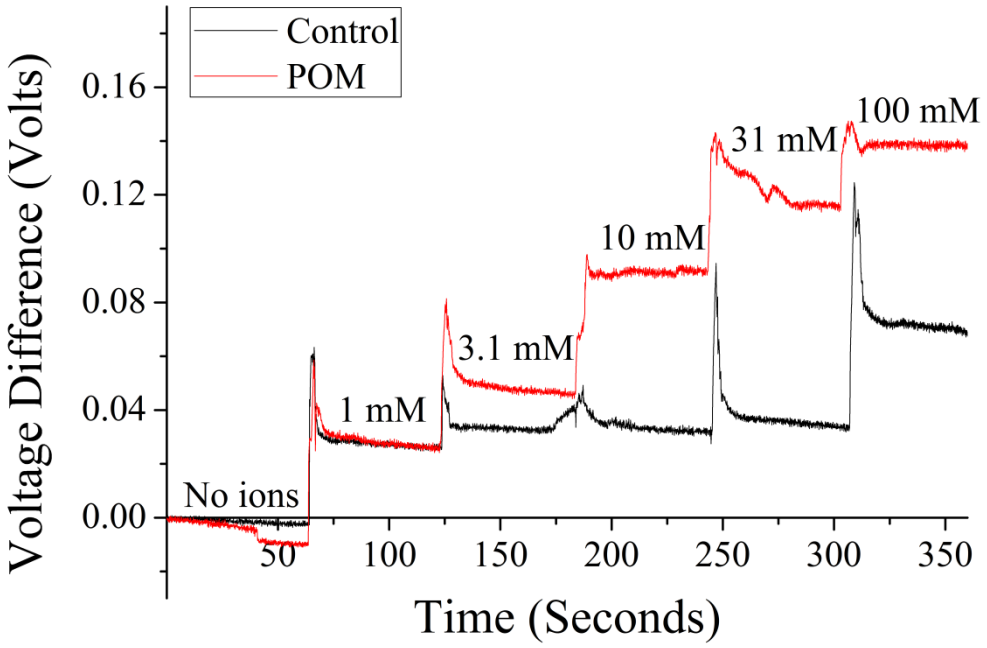

Figure 5.14 – Potassium ion concentration (pK) measurements without and with POMs layer.

From Figure 5.14, the control measurement (the plot in black) can be plotted as voltage difference versus potassium ion concentration, as shown in Figure 5.15. As mentioned previously, Ta_2O_5 film is selective towards hydrogen ions but the Ta_2O_5 film deposited in our cleanroom had a pK sensitivity of approximately

5 mV/pK in the range of pK 1.5 to pK 3, which can be observed in Figure 5.15. The slight potassium ion sensitivity that is presented by Ta_2O_5 film may due to the fact that the Ta_2O_5 film is non-stoichiometric as described previously, as opposed to the Ta_2O_5 film in the literature that exhibits almost zero potassium ion sensitivity. Moreover, it can also be seen that the error bars for each potassium ion concentrations is quite large, which are approximately in the range between 3 mV to 5 mV. These error bars were taken from three separate chips in the same wafer run but different Ta_2O_5 film sputtering runs. With such poor pK sensitivity together with the chip-to-chip variation had made each pK levels barely distinguishable, hence this level of pK sensitivity is not sufficient to be used for potassium sensing and therefore required an extra layer, in this case POMs, to boost the pK sensitivity.

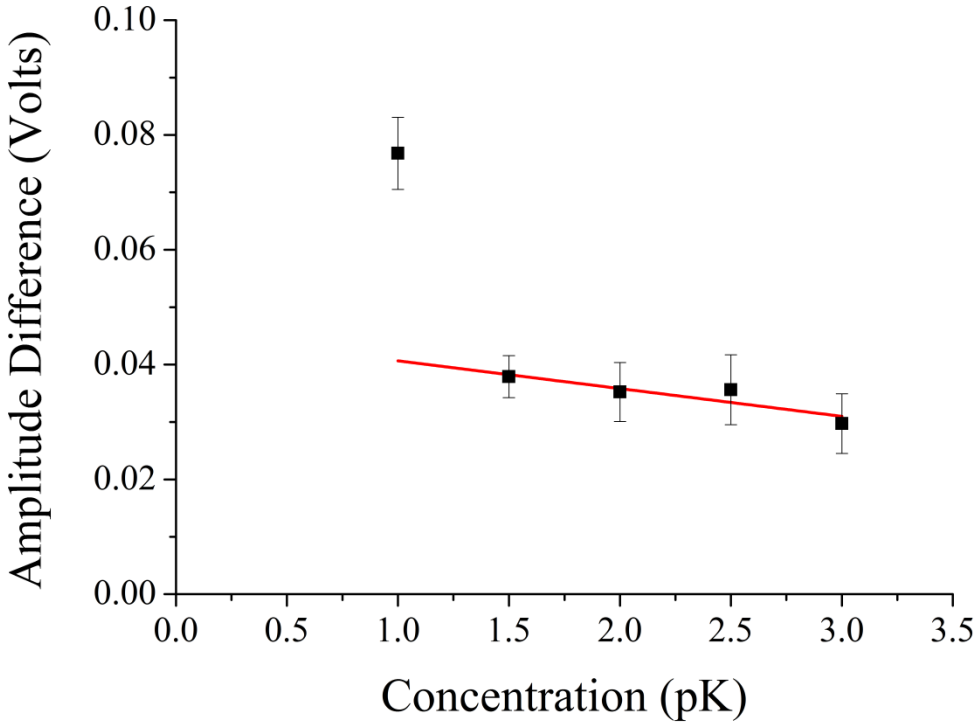

Figure 5.15 – Potassium ion concentration (pK) sensitivity on pure Ta_2O_5 sensing layer.

It is important to note that pure Ta_2O_5 sensing layer on top of ISFET sensor can be used to perform enzyme assay in blood serum, which will be explained in Chapter 6. Even though the potassium sensitivity is very small but it still had to be taken into account when doing measurements with enzyme assays in blood serum that involve hydrogen ions sensing. In human blood, most of the potassium ions contain in red blood cell (approximately 110 mM or above) and blood serum only contains about 1 mM or lower in potassium ions [154]. In spite of the low pK

sensitivity, the potassium ions concentration still have to be considered as a background analyte that will interfere with the enzyme assay results. There are a few important points to be taken into consideration when doing enzyme assays with blood serum using pure Ta_2O_5 film. Firstly, all the dilutions of blood serum had to be consistent to make sure that all the enzyme assays had the same concentration of potassium ions throughout as a background analyte, which can be treated as noise. Furthermore, blood serum are normally diluted to perform enzyme assays, where the factor of dilution is 1:100 or higher, thus this will reduce the potassium ion sensitivity below 1 mM (pK 3) that is 0.01 mM (pK 5) or above. Using the data from Figure 5.15, the linear line showing the sensitivity of potassium ions can be extrapolated to pK 5 and above, where the voltage difference (y-axis) is approximately 20 ± 4 mV or lower. Moreover, the standard error from the data population, which is 2.4 mV, had to be taken into account. With 3 × standard error and chip-to-chip variation, any potassium ion concentration from 0.01 mM and below is nearly at the noise floor of the ISFET sensor. Therefore, this made the potassium ion concentration in the blood serum almost negligible when doing enzyme assays using ISFET sensors with Ta_2O_5 layer.

In the same way, the pK measurements with a $\{P_8W_{48}\}$ film on top of CMOS ISFET chip was repeated, which can be seen in Figure 5.14 as the plot in red. Using the same three chips as mentioned before, they were drop casted with POMs from three different preparations to take account into both chip-to-chip variation and the tolerance of POMs preparations. Using these data, they can be plotted as voltage difference versus potassium ion concentrations, as shown in Figure 5.16. Using an average linear fitting through the data in Figure 5.16, it can be found that the pK sensitivity of ISFET with $\{P_8W_{48}\}$ layer improves to 80 mV/pK in the range between pK 1 to pK 3.This pK sensitivity had shown to extend beyond Nernstian response, which is named as super-Nernstian. To date, there is still no satisfactory explanation for this behaviour. A recent investigation by Wildi *et al.* had shown that super-Nernstian shift will occur if the plane of proton-electron transfer event does not coincide with electrode surface [155]. By separating the plane of hydrogenation and the OHP, the magnitude of the super-Nernstian shift will be affected. In this case, it was believed that the POMs layer is acting as a

plane to provoke such an additional voltage shift and provided an increment of sensitivity towards potassium ions.

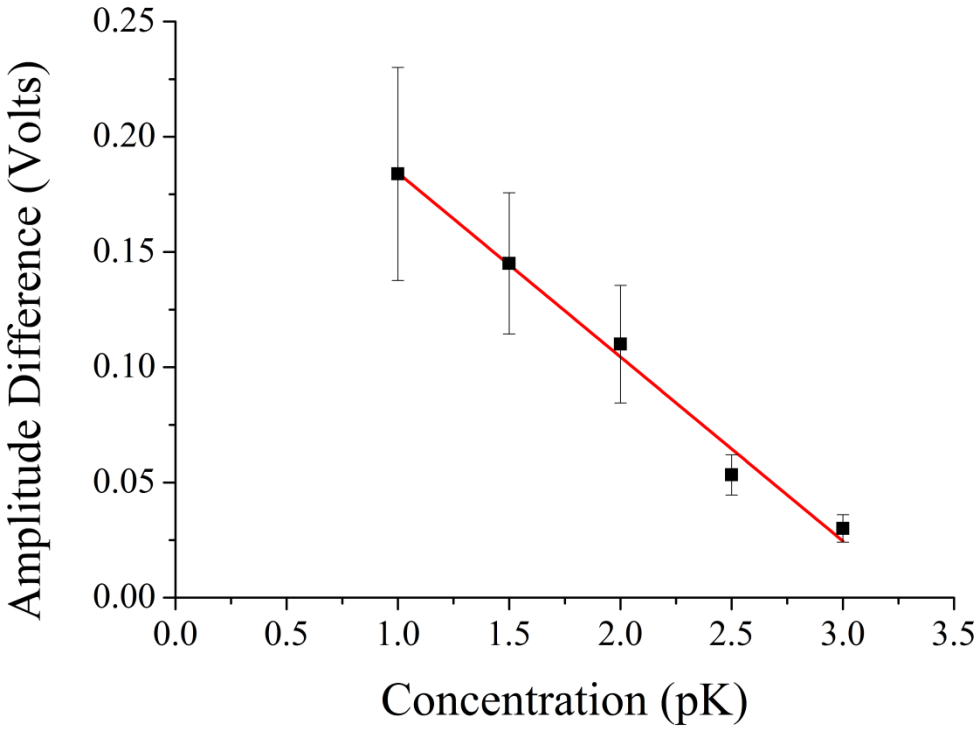

Figure 5.16 – Potassium ion concentration sensitivity using Ta_2O_5 ISFET sensor with POMs.

However, the pK sensitivity from Figure 5.16 is the summation of both pure Ta_2O_5 film and $\{P_8W_{48}\}$ layer. Therefore, using a simple equation below will give a new sensitivity calculation that is contributed to only $\{P_8W_{48}\}$ layer:

$$\underbrace{\Delta V/pK}_{net\ sensitivity} = V/pK_{POM} - V/pK_{control} \qquad 5.1$$

Hence, the net sensitivity of $\{P_8W_{48}\}$ towards potassium ions was obtained, which was calculated to be 75 mV/pK, with a range in between 1 mM (pK 3) to 100 mM (pK 1). This had provided a demonstration that a $\{P_8W_{48}\}$ film can be used as an alternative to valinomycin membranes as a potassium sensing membrane on top of a CMOS ISFET chip. In addition to pK sensitivity, the limit of detection of Ta_2O_5 ISFET with POMs layer was also extracted from the data. Using the trace from each pK concentration, a standard error was calculated and it was found to be 2.1 mV. Taking 3 × standard error and multiply by the sensitivity, it was determined to be 0.1 pK, which means that the Ta_2O_5 ISFET with $\{P_8W_{48}\}$ layer could resolve a step of 0.1 pK. Furthermore, it is also important to note that the voltage shift at low concentration of potassium ions between pure Ta_2O_5 layer

and $\{P_8W_{48}\}$ film is almost identical (refer to Figure 5.14). As mentioned previously, any low concentration of potassium ions will be reaching the noise floor of the ISFET sensor and render them undetectable and negligible. Since the physiological level of potassium ions is around 110 mM in red blood cells, thus diagnosis of potassium ions level in red-blood-cell level is a better indication than commonly used blood serum [154]. Therefore, this will take advantage of the increment pK sensitivity that $\{P_8W_{48}\}$ film could provide if the diagnosis of potassium ions level is using red blood cells with minimal dilution.

In addition to demonstrating $\{P_8W_{48}\}$ film is super sensitive to potassium ions level, it is also very important to investigate what effect it would give to hydrogen ions. The three chips that were used for potassium ions detection were cleaned with acetonitrile to dissolve $\{P_8W_{48}\}$ film and tested for hydrogen ions sensing for consistency. All these chips were then cleaned with methanol, IPA, DI water and finally blown dry with nitrogen gun, to be reused for the subsequent experiments. As described previously, solutions with pH 4, pH 3, pH 2.5 and pH 2 were prepared using HCl titration, where the potassium ions concentration was kept constant. Each of the pH solutions were introduced on top of ISFET with pure Ta_2O_5 film in a descending order, then followed by drop casting a layer of $\{P_8W_{48}\}$ on top and introduced the same pH solutions in the same order. Each pH solution was measured for 1 minute to give a stable result. These pH measurements (without and with POMs layer) can be seen in Figure 5.17 as a representation from one of the chips.

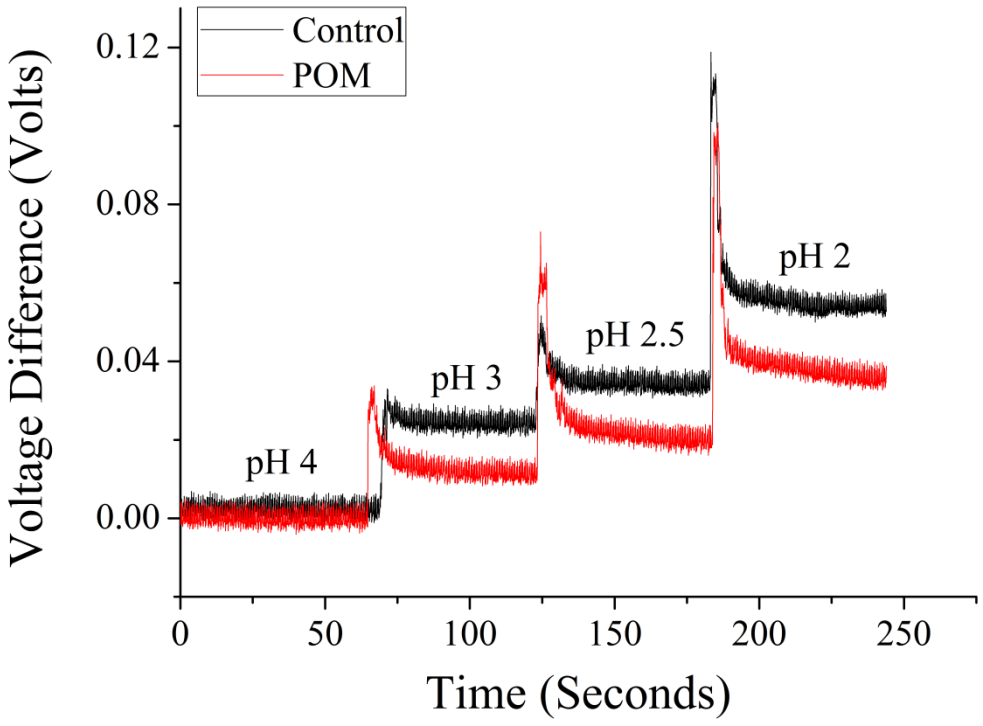

Figure 5.17 – pH measurements on top of ISFET sensors without and with POMs layer from one chip.

From Figure 5.17, the control experiment (plotted in black) can be plotted as voltage difference versus pH levels, which can be observed in Figure 5.18. As can be noticed, after the treatment of $\{P_8W_{48}\}$ film on top of the ISFET sensors, it deteriorated the pH sensitivity of the Ta_2O_5 film surface. The pH sensitivity of Ta_2O_5 ISFET sensor was approximately 25 mV/pH in the range between pH 2 to pH 4. The reason of the low pH sensitivity may be due to the fact that $\{P_8W_{48}\}$ changes the surface properties of Ta_2O_5 to be less oxygen rich, which in turn reduces the sensitivity. However, this pH sensitivity was sufficient to evaluate the behaviour of ISFET sensor on sensitivity towards hydrogen ions when POMs film was added on top of Ta_2O_5. In the same way, the plot in red from Figure 5.17 is plotted for voltage difference versus pH levels as well, which is shown in Figure 5.19. It can be noted that the pH sensitivity of Ta_2O_5 ISFET sensor with $\{P_8W_{48}\}$ layer on top is around 20 mV/pH in the range between pH 2 to pH 4. Using the Equation 5.1, the net sensitivity of the sensor with POMs is -5 mV/pH. There was a slight decrement in pH sensitivity when $\{P_8W_{48}\}$ layer was added on top of the sensor. From this observation, there are four aspects to be considered. First and foremost, $\{P_8W_{48}\}$ layer may prevent some hydrogen ions from getting to the plane of hydrogenation and impede the proton-electron transfer, which explains the slight pH sensitivity lost after the introduction of

POMs film. Second, the fact that the pH sensitivity from CMOS ISFET sensor is deteriorating with prolonged usage, which can also be used to explain the sensitivity lost after POMs film. Furthermore, the POMs layer did not suppress the ISFET sensitivity to hydrogen ions and completely selective to potassium ions, thus it is very important to always have a reference of pure Ta_2O_5 ISFET to be used with Equation 5.1 to determine the net change of potassium ions. Lastly, since human blood from different individuals ranges from pH 7.35 to pH 7.45 and the POMs ISFET sensor cannot cancel of pH sensitivity, thus a background pH will always be present. Therefore, control is required to be next to the POMs layer to be taken as reference, when taking measurement with any sample. In conclusion, these experiments had shown that $\{P_8W_{48}\}$ film does not give rise to any increment in pH sensitivity or potentially reduce the pH sensitivity, at the same time increases the sensitivity towards potassium ions.

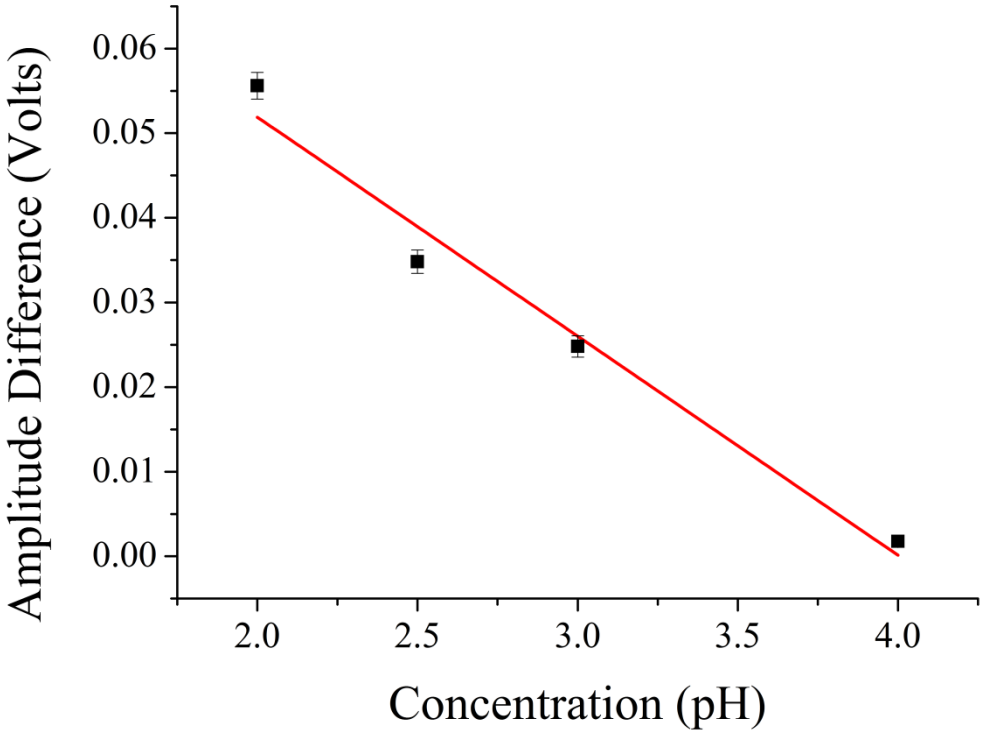

Figure 5.18 – pH sensitivity of Ta_2O_5 ISFET sensor.

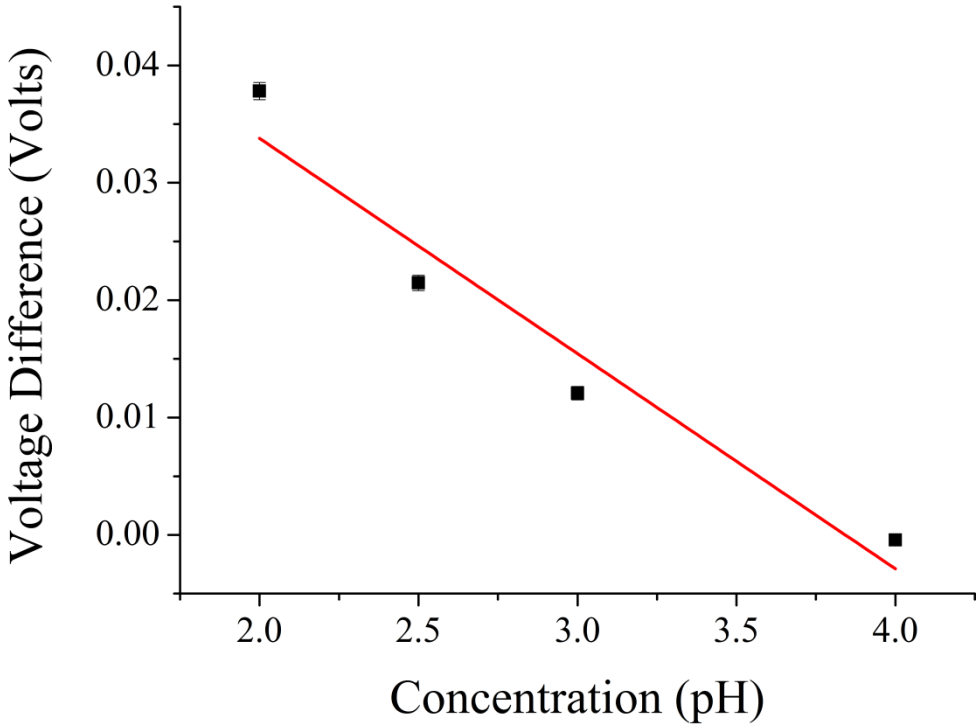

Figure 5.19 – pH sensitivity of Ta_2O_5 ISFET sensor with POMs layer.

Apart from hydrogen ions, there are a lot of other ions to be considered that are freely available in human blood, before it can be concluded that POMs layer has selectivity towards potassium ions only. One of the most dominant electrolytes in human blood is sodium ions, which stands about 85% in human body. The physiological concentration of sodium ions in human blood serum is around 140 mM, whereas the concentration of sodium ions in red blood cells is only about 40 mM [156]. With low sodium concentration in red blood cells further indicated that red-blood-cell potassium level is the proper approach, due to its high in potassium ions and low in interfering sodium ions. However, since blood serum measurement is the most common method of inspecting physiology of an individual, it would be great if potassium ions sensing and metabolites detection can be integrated into one blood serum sample measurement. Therefore, it is important to inspect the effect of POMs layer towards high concentration of sodium ions as interfering ions. In order to do this, the same pK dilution was prepared in a 140 mM NaCl solution as a constant background and maintains all the dilutions at pH 7.4. In the same way that was described previously, the different pK dilutions were introduced on top of the Ta_2O_5 ISFET sensors as control and POMs coated Ta_2O_5 ISFET sensors, as can be seen in Figure 5.20. All of the measurements were repeated in three different chips from the same wafer run with different Ta_2O_5 sputtering run.

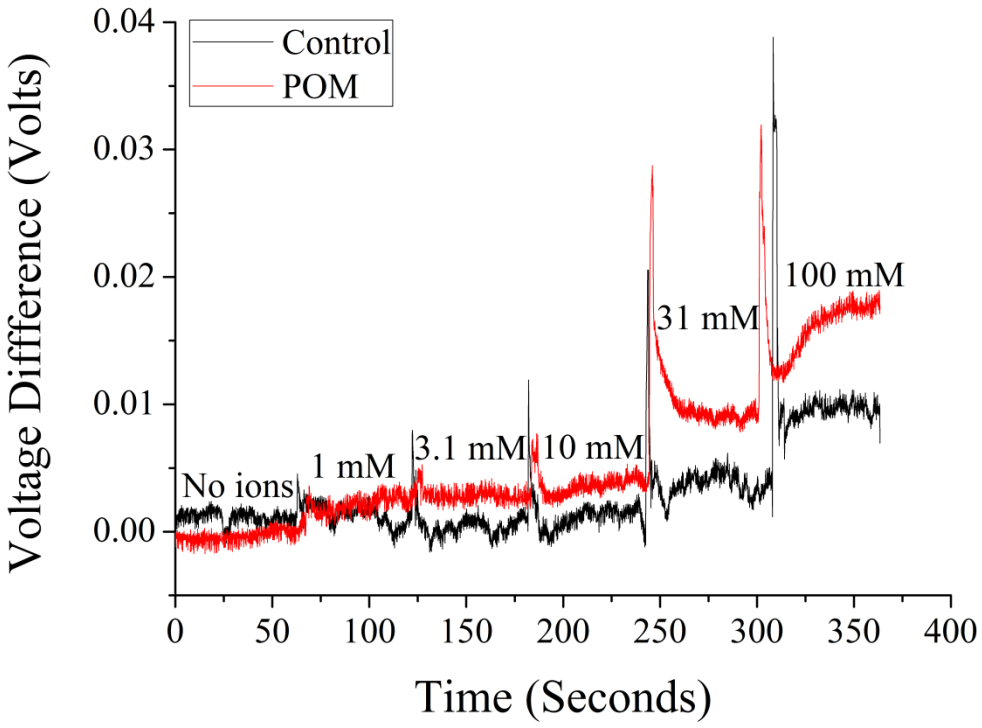

Figure 5.20 – pk measurements with the presence of 140 mM NaCl on top of ISFET sensors with Ta_2O_5 film

By observing the experimental curves from Figure 5.20, it can be deduced that high concentration of NaCl interferes and reduces the voltage signal of the ISFET sensors significantly for all pK solutions. At low potassium ion concentration, the ISFET voltage signal was not detectable. Whereas, at high potassium ion concentration, ISFET voltage signal manage to give a slight observable shift. Furthermore, the noise level of the ISFET sensors was taken as standard error across the data population, which was 1.8 mV. This agrees well with the standard error that was extracted from the previous experiments, which means that high concentration of NaCl did not increase the noise level of the device. Follow by that, data from Figure 5.20 is further plotted as voltage difference versus potassium ion concentrations for both control and POMs experiments, as shown in Figure 5.21 and Figure 5.22 respectively. From Figure 5.21, it can be seen that the potassium ions sensitivity of pure Ta_2O_5 ISFET sensors was only 8 mV/pH. This sensitivity is as expected from Ta_2O_5 surface that was fabricated from our cleanroom and it agrees well with previous experiments. However, this level of sensitivity can only be observed between pK 1 to pK 2, which is very high potassium ions concentration. Due to high NaCl concentration as interfering ions, voltage signal from ISFET was quenched. On the other hand, potassium ions sensitivity was increased to 15 mV/pH, when a layer of POMs was drop casted on

top of Ta_2O_5 ISFET sensors. However, this sensitivity is only observable in the range between pK 1 to pK 2 as well. Furthermore, the pK sensitivity that POMs layer offered to ISFET sensors was significantly reduced, in the presence of high concentration of NaCl.

The significant ISFET voltage drop may due to a layer of salt forming on top of the surface of the sensor (without or with POMs film), when a high sodium ion concentration is present. From these finding, it can be concluded that the $\{P_8W_{48}\}$ layer was not sufficient to present the required selectivity and sensitivity of potassium ions to be used in blood serum measurements. Further studies into the modification of $\{P_8W_{48}\}$ can be investigated to increase the sensitivity and selectivity of potassium ions, in order to demonstrate a single platform measurement that could extract a lot of physiology information from one type of sample.

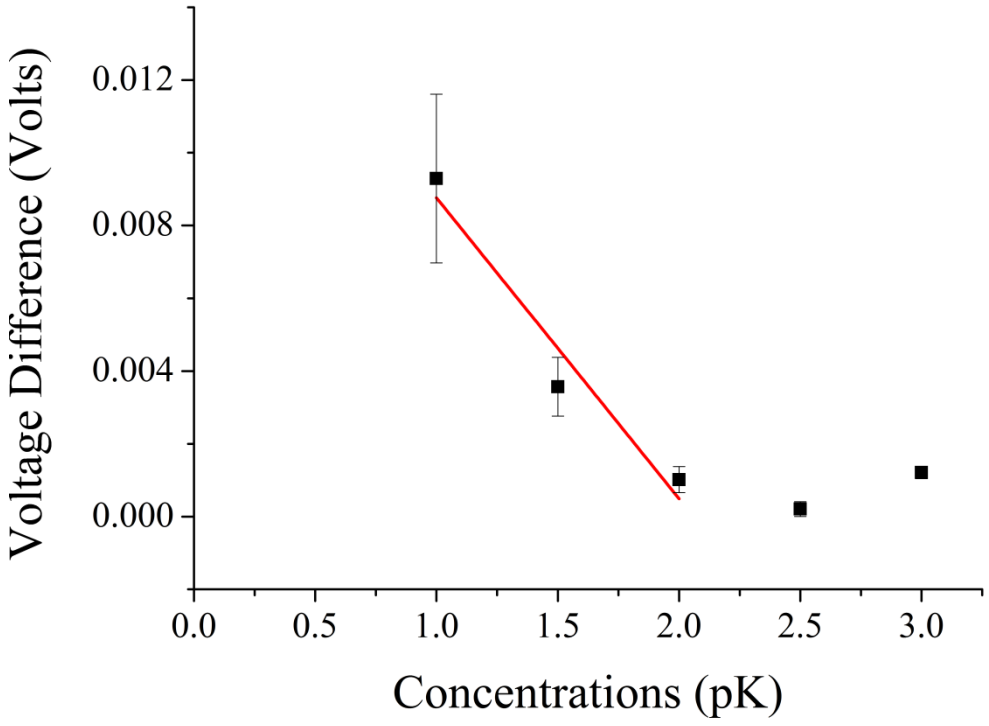

Figure 5.21 – pK sensitivity in the presence of 140 mM NaCl on top of pure Ta_2O_5 ISFET sensors.

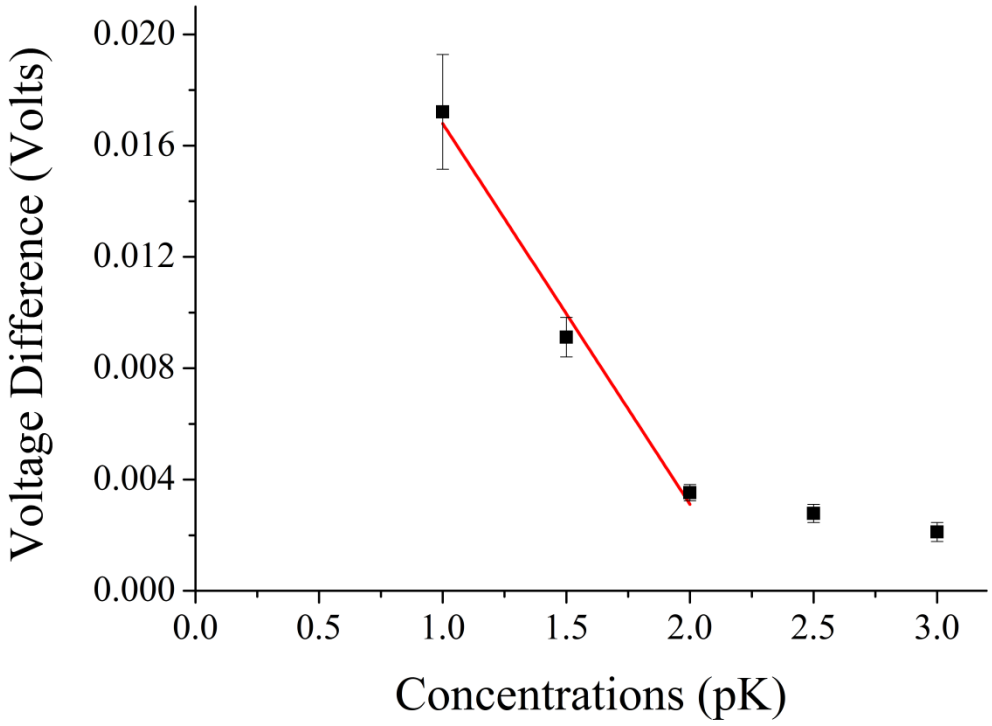

Figure 5.22 – pK sensitivity in the presence of 140 mM NaCl for POMs treated Ta_2O_5 ISFET sensors.

5.3 Microfluidics

In order to provide multiple metabolites measurements on chip that will lead to metabolome, microfluidics offers such capability to do so. Microfluidics is a technological system that could manipulate small amount of fluids in channels with dimensions of tens of micrometres [157]. It offers a low cost method to provide separation of each metabolite measurements on top of a CMOS chip without any cross-contamination and high throughput metabolites detection. Furthermore, microfluidics is also required to direct the fluids to the location of the enzymes to perform enzymatic reaction for metabolites quantification using the sensors. In order to fulfil such requirements in this work, the epoxy-based photoresist SU-8 was used to fabricate micro-channels on top of the CMOS chips.

5.3.1 SU-8

SU-8 is an epoxy-based, negative photoresist with thick and high aspect ratio resist structure, which is originally developed by IBM [158]. It is a very popular structural material in the field of MEMS [159] and microfluidics [160]. Its most distinctive characteristic is the ability to use a conventional spin coater to

obtain a film thickness from the range of 750 nm to 450 μm in a single coat. Normally SU-8 is exposed with a near ultraviolent (350 – 400 nm) radiation. This resist has a very high optical transmission in the ultraviolent region, which is very important in obtaining an outstanding high aspect ratio feature and vertical sidewall.

SU-8 is a multifunctional molecule that consists of 8 epoxy groups (the "8" in SU-8) in a hydrocarbon (ether), together with a photoacid generator (triarylium-sufonium salts) [161]. During the ultraviolent illumination, the photoacid is photochemically generated in the photoresist film. A post exposure bake is then used for the cross-linking mechanism in SU-8 and the produced photoacid acts as a catalyst for the process. During the cross-linking, the epoxy groups form a highly cross-linked three-dimensional network and shrink the film to make it denser. In addition, the hydrocarbon compound provided the cross-linked SU-8 a high resistance towards many solvents and thermal stability. This makes SU-8 well-suited for the fabrication of microfluidics in this work, where the material has to be chemically stable and resistant, which is non-reactive to the any enzymatic reactions.

In this work, SU-8 3000 series was selected to fabricate microfluidic channels on top of a CMOS chip. The 3000 series has been formulated to be the improvement from SU-8 and SU-8 2000 series, which has better adhesion and reduced coating stress. The key criteria for fabricating microfluidic channels on top of a CMOS chip is to have good isolation from each channels to avoid cross-contamination.

5.3.2 Micro-Fabrication Process

The SU-8 microfluidic channels fabrication process is shown in Figure 5.23. The fabrication of SU-8 microfluidic channels on top of a CMOS chip was according to the recommended guidelines from the datasheet [162]. In order to obtain maximum process reliability, CMOS chips were cleaned (with acetone, isopropanol and DI water) and blown dry with nitrogen gun. For even better performance, it is recommended to clean with piranha wet etch (using H_2SO_4 and H_2O_2) but the aluminium bond pads on the CMOS chips would be damaged by this wet etch cleaning. Hence, piranha etching was avoided. After cleaning, the surface of the CMOS chip was dehydrated by baking in an oven at 180^{o}C for 5

minutes and followed by cleaning with barrel asher supplied with O_2 plasma for 5 minutes at maximum power (Figure 5.23a).

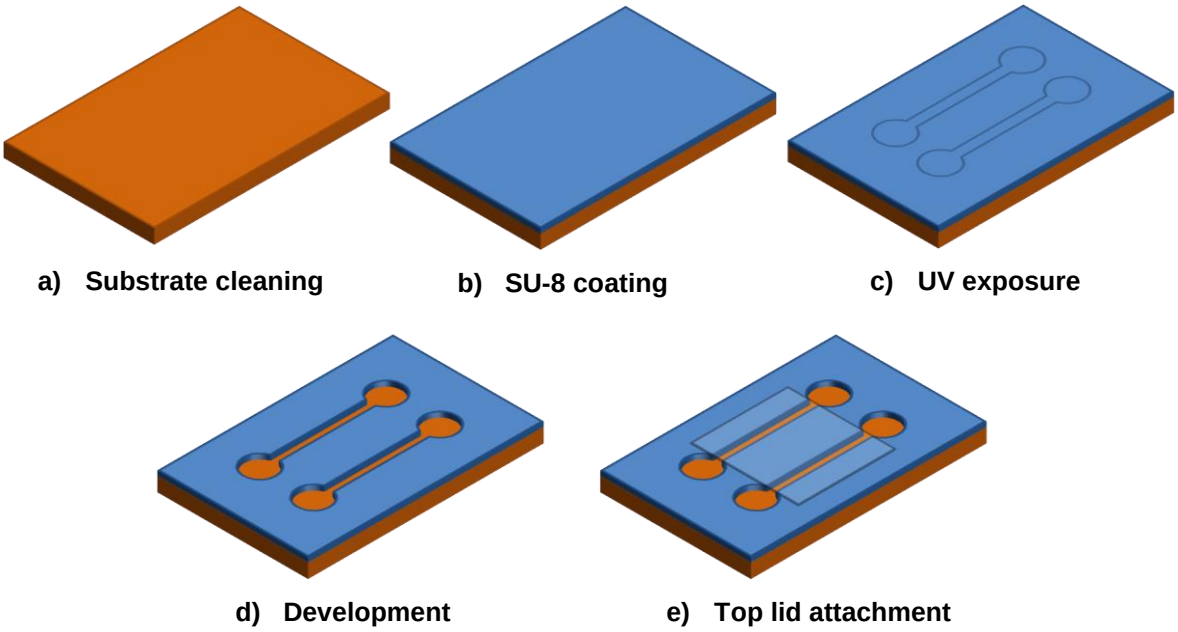

Figure 5.23 – Schematic diagram of SU-8 microfluidic channels fabrication process.

After O_2 ashing, a thick layer of SU-8 3025 was dispensed on to the CMOS chip and spin-coated at 2000 rpm for 30 seconds with a ramp up acceleration of 1000 rpm/s. Before the spin cycle, the CMOS chip went through a spread cycle where it was spun at 1000 rpm for 5 seconds with a ramp up acceleration of 250 rpm/s. Furthermore, before the end of the spin cycle, the CMOS chip was spun at 9000 rpm for 2 seconds with a ramp up acceleration of 20000 rpm/s, in order to reduce the edge bead size at the corners of the chip. Then the CMOS chip was baked on a hotplate at 65°C for one minute and then transferred to another hotplate at 95°C to carry out a soft bake for approximately two hours. The soft baking time depends on the size of the sample, where the smaller the sample, the longer the baking time or vice versa. The lower temperature bake before the actual soft bake is to prevent internal stress that can lead to cracked features and also to allow the solvent to evaporate in a more controllable way to have better resist adhesion. After the soft baking, the sample was transferred back to a 65°C hotplate for a minute before removing it and was left to cool down at room temperature (Figure 5.23b).

The SU-8 resist on top of the CMOS chip was exposed with ultraviolent light for 75 seconds using a standard mask aligner. The long soft baking step is crucial

when the mask and the sample come in contact (Figure 5.23c). If the solvent was not properly evaporated, the mask will stick to the resist and make the alignment impossible. After the exposure, the CMOS chip was again baked on a hotplate at 65°C for one minute, followed by a 95°C bake for 5 minutes and finally back to 65°C for another minute. This is the same technique used for the soft bake. The CMOS chip was then developed with Microposit EC solvent for 9 to 10 minutes, depending on the resist thickness and edge beads, with continue agitation (Figure 5.23d). Then the CMOS chip was rinsed with isopropanol. When the development was done and produced good microfluidic channels, the CMOS chip was hard baked in an 180°C oven for two hours. The final hard bake step will make the microfluidic channels very robust and extremely difficult to remove.

5.3.3 Evaluation

The fabricated SU-8 microfluidic channels on top of the CMOS chips were not completely seal. This is to allow immobilisation of enzyme in each channel before a top lid was used to cover the channels, providing isolation from each channel (Figure 5.23e). Figure 5.24 shows the SU-8 microfluidic channels fabricated on top of the CMOS chips.

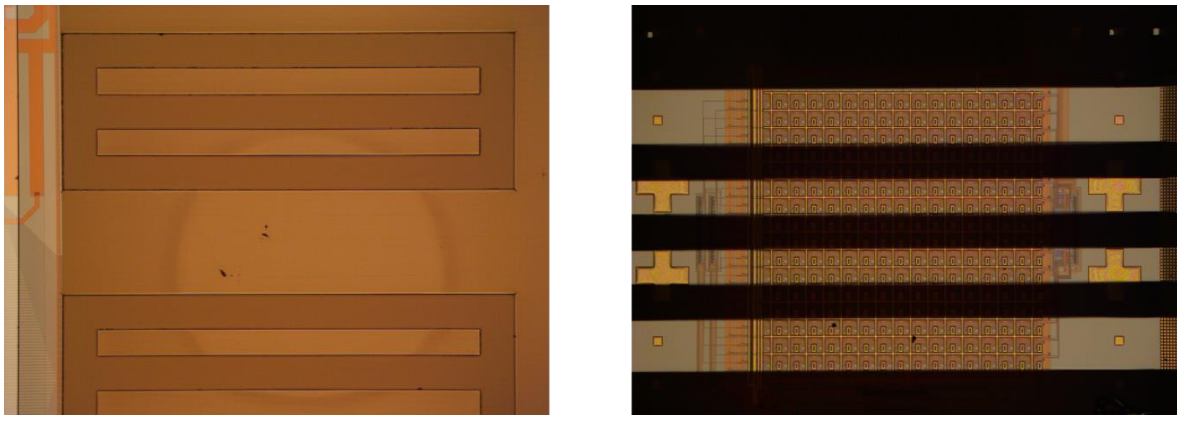

a) ISFET array chip **b) Multi-Corder Chip**

Figure 5.24 – Photo micrograph of SU-8 microfluidic channels on top of the CMOS chips.

After the packaging and encapsulation of the CMOS chip, the microfluidic channels are ready to be tested. To test the isolation of liquids from each channel, a surfactant free hydrophilic fluid transport film with transfer adhesive tape was used to bond the top lid on top of the SU-8 channels. The transport

film is optically clear, insoluble in water and non-leaching inert hydrophilic coating for capillary fluids transport. Using a pipette, a tiny amount of DI water was introduced at one of the open end of the channels and let the fluids to flow through the channels. Figure 5.25 illustrates the video images taken using a microscope showing the functionalities of the SU-8 channels. As can be seen, the top lid and the SU-8 channels have a good seal, which provided a capillary force and dragged the liquids into the channels. Moreover, each of the channels had no liquids in it until the channels opening were introduced with liquids. Hence, this had demonstrated that the SU-8 microfluidic channels on top of a CMOS chip can provide good channel isolation and fluids manipulation for the enzymatic work, which will be discussed in later Chapters.

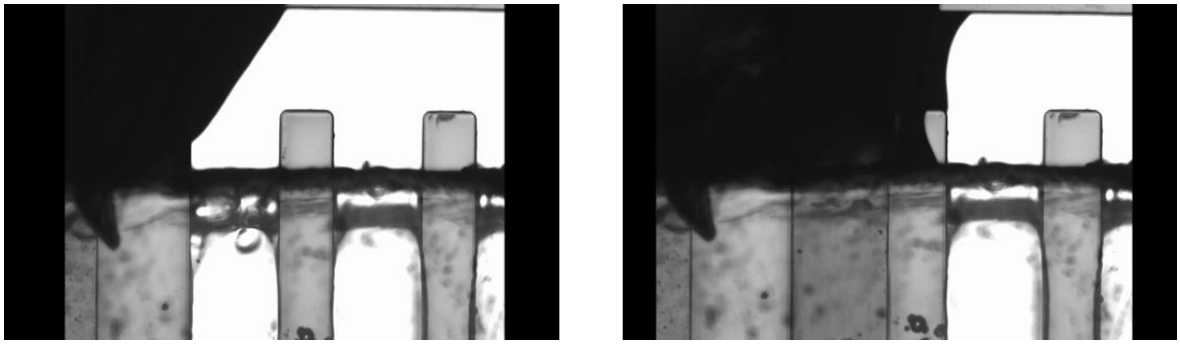

a) Introduction of liquids at the open inlet **b) Liquids flow into the channel**

Figure 5.25 – Photo micrograph of the fluids flow into the SU-8 microfluidics channel after the bonding of a top lid.

5.4 Packaging

All the CMOS chips that returned from the foundry and after post-fabrication had to be packaged onto a chip carrier to enable access to the bond pads. Moreover, all the metabolites and enzymes are in aqueous solution, which requires all the electrical connections of the CMOS chip to be well-insulated while leaving the surface of the sensors area expose to wet environment. These are the main criteria for packaging. The following discussions will explain the chip carrier used to house the CMOS chip and also various encapsulation methods to provide a waterproof CMOS chip.

5.4.1 Housing

All the CMOS chips, both ISFET array and Multi-Corder, were packaged in Ceramic Pin Grid Array (CPGA) packages from the Company Spectrum Semiconductor Materials Inc [163]. They are the largest independent World Wide Distributor of packages and lids for IC assembly. The CPGA through-hole mount package has a ceramic substrate to enhance thermal heat dissipation. The packages offer excellent electrical performance with the gold-plated pins brazed in a matrix pattern underneath the package, in order to insert the package into a socket. More importantly, the enzymatic reaction is very sensitive towards temperature change, thus this package offers a good heat dissipation capability to prevent the heat from the CMOS chip to build up and ruin the measurements. Since the number of bond pads for ISFET array chip and Multi-Corder chip is different, thus two different chip packages were obtained from the company. For ISFET array chip, the package contains 144 pins, a cavity of 10.8×10.8 mm, a pitch size of 2.54 mm and brazed in a 15×15 matrix. For Multi-Corder chip, the package contains 120 pins, a cavity of 8.3×8.3 mm, a pitch size of 2.54 mm and brazed in a 13×13 matrix. Figure 5.26a and b shows the top and bottom view of the ISFET array chip package, while Figure 5.26c and d shows the top and bottom view of the Multi-Corder chip package. As can be seen from Figure 5.26b and Figure 5.26d, there is an extra pin in both packages, which allows orientation guidance for the placement of the package into a socket. To mount the bare CMOS chips on to the chip carrier, EPO-TEK H74 epoxy [164] from Epoxy Technology Inc. was used on the back-side of the chip and glued on top of the chip carrier. This epoxy has a good thermal conductivity that allows heat to be transferred to the chip carrier easily. Then the CMOS chips were wire bonded following the specifically designed bonding diagrams. The wire bonding of the bond pads to the chip package was done using the Hesse and Knipps 710 ultrasonic wire bonder, which is located in the School of Physics and Astronomy at the University of Glasgow.

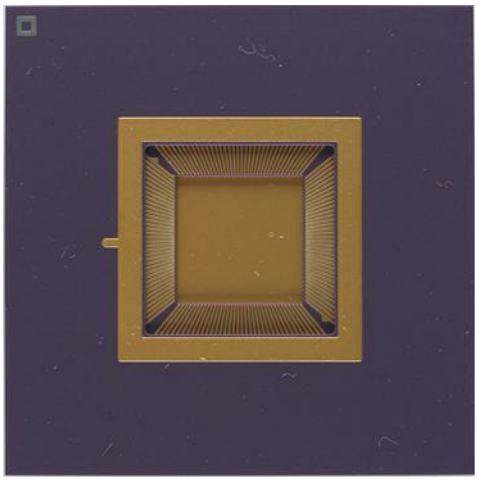

a) ISFET array package top view

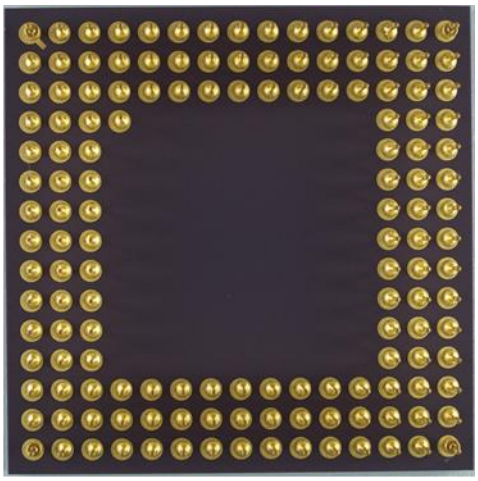

b) ISFET array package bottom view

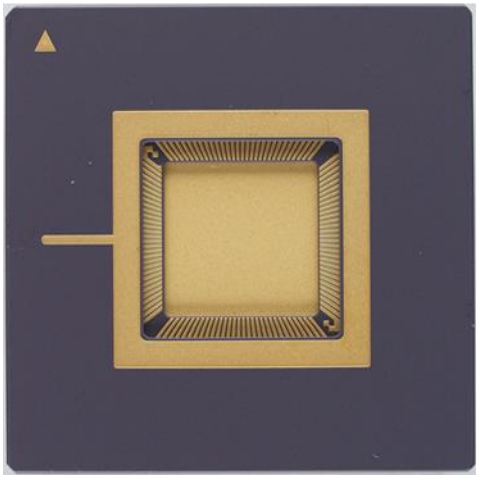

c) Multi-Corder package top view

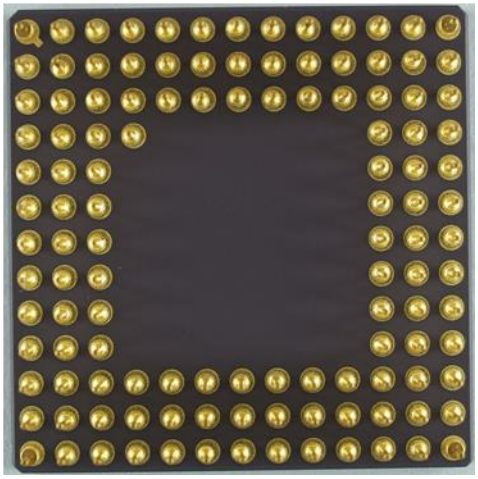

d) Multi-Corder package bottom view

Figure 5.26 – CPGA chip carrier for both ISFET array and Multi-Corder chips.

5.4.2 Encapsulation

In order to ensure an electrically well-insulated and waterproof CMOS chip for experiments with aqueous solution, a few methods were used in this work. Figure 5.27 shows the different three methods that were explored in this work for encapsulation. The following will describe each of the methods.

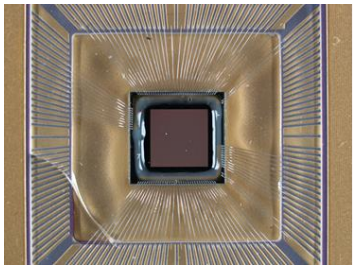

a) Dam and fill (glob top)

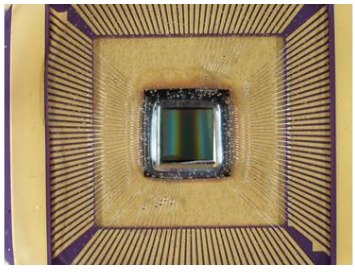

b) PDMS

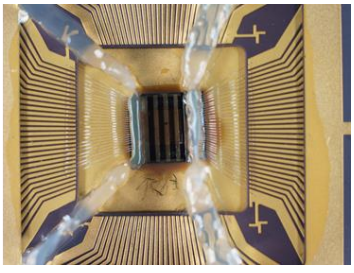

c) Manual dam and fill

Figure 5.27 – Three different encapsulation techniques.

Glob top based dam and fill

The packaging of the CMOS chips were initially outsourced to a company, Sencio, located in Nijmegen, the Netherlands [165]. They are an independent package design and assembly company. Using a dam and fill technique, a high viscosity fluid was dispense in between the sensor array and the bond pads, creating a wall that will prevent the filling material from entering into the dam. Then, a filling material with excellent chemical resistance was used to encapsulate the wire bonds and bond pads completely. This allows the CMOS chips to function without any disruption of the circuit operations. Figure 5.27a shows the packaging that was done by the Dutch company. In order for the company to provide good encapsulation, the die attachment and wire bonding were also done by them. 10 bare CMOS chips were packaged by the Dutch company and it turned out that the material they used to create the dam is porous, which allows liquids to flow pass the encapsulation and destroy the chips. In addition, the services from the company are quite expensive and also they do not handle CMOS chips that had already been post-processed. Hence, this method was abolished to investigate for a home-made method.

Polydimethylsiloxane (PDMS)

PDMS is an elastomeric material that was developed for the applications in microfluidics [166]. PDMS has an ability to make reversible van der Waals contact (conformal contact) to smooth surfaces. This makes PDMS demountable when it is bonded on to a surface. In this work, PDMS was used as a packaging material where a PDMS cube was placed on top of the sensor array. This provides a protection from any encapsulation material from the sensors area. Then EPO-TEK 302-3M epoxy [164] was used to encapsulate the bond pads and wire bonds. The epoxy was left to cure at room temperature for 24 hours. This long room temperature curing time is to eliminate the possibility of the epoxy to flow under the PDMS cube, where high temperature causes the viscosity of the epoxy to reduce. Finally, the PDMS was peeled off, leaving no markings on the sensors area and creating a cavity around the sensor array. This PDMS encapsulation technique is the best and simple method that was developed and it was used to package most of the CMOS chips throughout this work. Figure 5.27b illustrates the CMOS chip packaged with PDMS method.

Manual dam and fill

An alternative method was also used, which is a handmade dam and fill encapsulation. This method was mainly used to package CMOS chips that do not have smooth surface, such as CMOS chips with SU-8 microfluidic channels. A very viscous, short curing time, watertight seal and non-porous material, Aquaria transparent silicone sealant from Geocel, was used to create a dam around the sensor area. The silicone sealant was applied in between the sensor array and the bond pads, which was on top of the SU-8 wall. Then, EPO-TEK 302-3M epoxy was used to encapsulate all the wire bonds and bond pads, as described previously. Figure 5.27c shows the encapsulation technique that was done manually.

A final step in the packaging of the CMOS chips for wet chemistry experiments is to attach a ring surrounding the sensor array, two examples of the fully packaged CMOS chips are shown in Figure 5.28. Different sizes of rings were catered to different type of experiments. For example, 2D printing experiments required a short ring to fit under the printing nozzles, which will prevent the print head from crashing onto the ring. It was attached on the CMOS chip carriers using EPO-TEK-302-3M. These rings can be a cut Fisherbrand test tube or a 3D printed polylactic acid ring. These rings were used to contain all the liquids on top of the sensor array and prevent the liquid from leaking out of the chip carrier that will go on top of the underlying electronics on the PCB.

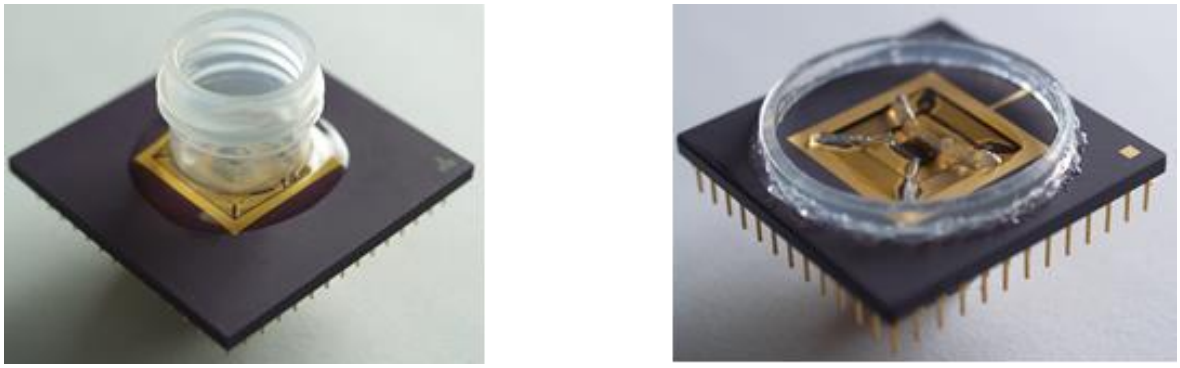

Figure 5.28 – Photographs of two chips that are fully packaged and ready for experiments.

5.5 Summary

A few post-processing techniques had been developed on CMOS ISFET to improve the sensitivity towards hydrogen and potassium ions. To improve the hydrogen ions sensing of CMOS ISFET, a Ta_2O_5 film was deposited on top of the sensor array. While the potassium ions sensing of CMOS ISFET was improved using an inorganic film called POMs to demonstrate the capability. Furthermore, microfluidic channels were used to segregate the sensor array to provide multiple metabolites measurements. This was done with SU-8 photoresist and an adhesive top lid, which had good isolation from each channel and well directional liquids flow on top of the sensors. Finally, several methods had been developed to package the CMOS chip for the use in metabolites experiments. This includes glob top based dam and fill, PDMS and manual dam and fill. After the post-processing of the CMOS chip, the next step will be to measure metabolites on top of the integrated sensor array chip.

Chapter 6 : Metabolite Quantification on Chip

6.1 Introduction

The previous chapter focused on chip post-processes for ultimately quantifying a number of metabolites produced by physiologically important enzyme assays. This chapter describes the experiments of several enzyme assays to be measured using the ISFET array chip including: the discovery of spatial noise reduction techniques using an array format; the design of a buffer system to maximise sensitivity and responsiveness on the ISFET; spectrophotometric enzyme assays are performed to verify the enzyme activity before transferring the assays to ISFET or PD devices; the demonstration of ISFET chip's ability to quantify four different metabolites (glucose, pyruvate, urea and triglyceride); and finally a description of the enzyme kinetics calculation used to quantify relative metabolite levels from the data obtained from ISFET. In addition, this chapter will also describe an optical quantification of one metabolite (cholesterol) measurement using the PD sensor array on Multi-Corder chip, together with its enzyme kinetics calculation.

6.2 Metabolite Sensing on ISFET

Both the ISFET array chip and the Multi-Corder chip contain the ISFET sensor, together with an enhanced capability from post-processing and a complete instrumentation system for each chip. The next step is to demonstrate the possibility to measure changes in hydrogen ion concentration as a result of an enzymatic reaction. This includes: using the average data from the array of sensors to reduce noise, enzyme buffer investigation, quantification of different metabolites and a derivation of enzyme kinetics.

The enzyme assays were mainly done on the ISFET array chip as it was the first chip to return from the foundry. In addition, the ISFET sensors on Multi-Corder

chip required further post-processing due to a thick passivation layer (approximately 7 μm) on top of all the ISFET sensors, which was not specified in the foundry's datasheet. With such a thick passivation layer, the sensitivity of the ISFET sensors would be reduced (refer to Section 3.4). Hence, all the data that will be presented in the following discussions were from 256×256-pixel ISFET array chip.

6.2.1 Averaging Noise Reduction

Ensemble averaging is a potent method to improve signals if measurements are taken for several times and averaged. Using this method, the signals will accumulate while the noise will cancel itself. A criterion for ensemble averaging to function correctly is that each measurement has to be repeated with same experimental conditions, in order to obtain a consistent signal. An advantage of using a sensor array is that it allows a set of identical independent biological or chemical reactions to be analysed from a single sensor and also from an average of several sensors. Using the ISFET array chip, all the data sets that were collected from each sensor pixel were independent from each other. Hence, the obtained data from the chip could be taken from just one pixel or from an average of 2 to 2^{16} pixels. Using this spatial averaging technique for an array of ISFET sensors reduced the mean square (MS) noise of the combined enzyme assay signal. Figure 6.1 illustrates a typical signal obtained from the chip for a small concentration of glucose as a function of time. As evident, the data obtained from one single ISFET sensor, gives an extremely high background noise (data in black colour). On the other hand, if the ensemble data obtained from all 2^{16} ISFET sensors was averaged, there was a significant noise reduction (data in red colour).

In order to understand the characteristic of the spatial averaging effect that reduces the noise, the voltage signal from any single sensor pixel in the array including its noise component, V_i can be calculated for its MS voltage noise e_i^2 using the equation below:

$$e_i^2 = \frac{1}{t_2 - t_1} \int_{t_1}^{t_2} V_i^2(t) dt \qquad 6.1$$

The voltage signal was taken in the interval from time t_1 to t_2, which is the region in the data where the voltage signal is not changing. When a number of independent sensor pixels, N, is taken as an average, the average voltage signal can be calculated using:

$$V_N = \frac{1}{N} \sum_{i=1}^{N} V_i(t) \qquad 6.2$$

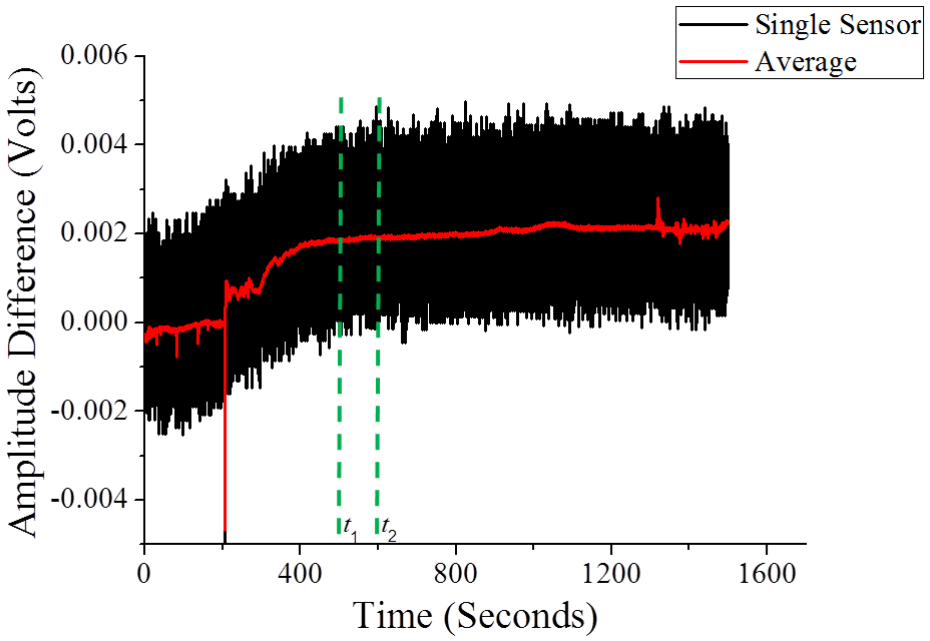

Figure 6.1 – The comparison of voltage signals obtained from one typical ISFET sensor and the average of all ISFET sensors.

Hence, the noise for the average voltage signal, $V_N(t)$ can be calculated using Equation 6.1. Using both Equation 6.1 and 6.2, the MS voltage noise was calculated for 1, 5, 25, 125, 625, 3125, 15625 and 65536 number of sensor pixels. The obtained results from these calculations were plotted as a function of $1/\sqrt{N}$, which is shown in Figure 6.2.

As can be seen from Figure 6.2, signal averaging from the array reduces the noise by a factor of $\sqrt{N}$ and the graph is quite linear. From this analysis, it was noticed that a determination on the number of sensor pixels required to perform

good measurements for the chosen assay conditions could be made. This is crucial when using microfluidic channels, in which several sensor pixels will be averaged to obtain a reliable data.

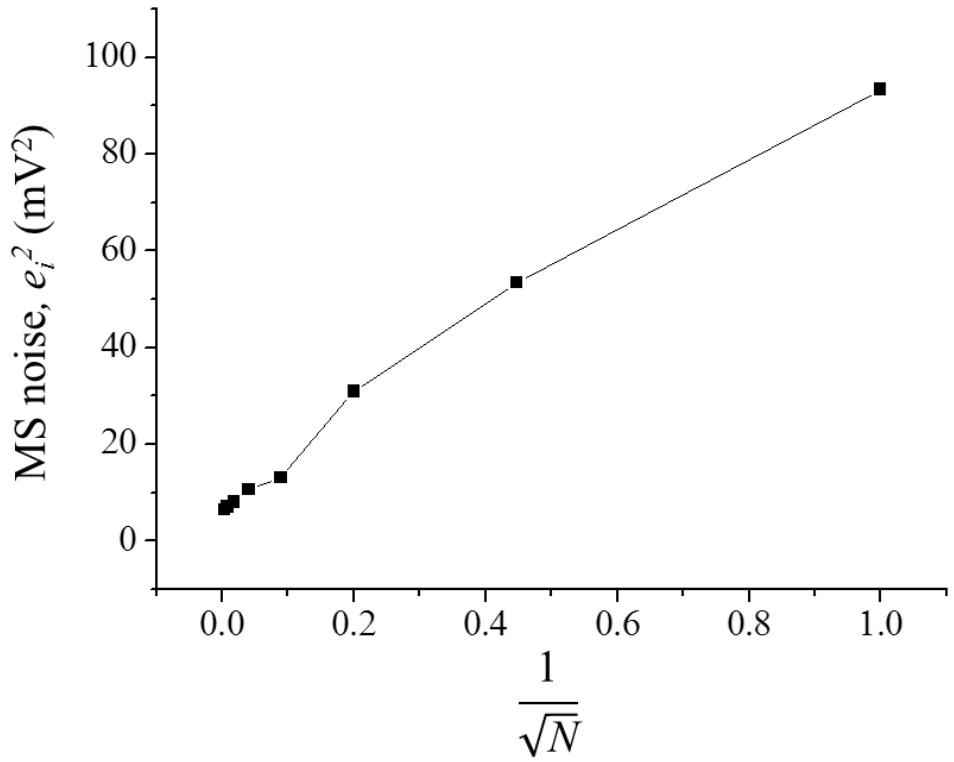

Figure 6.2 – The relationship between the MS noise, e_i^2 and $1/\sqrt{N}$, where *N* is the number of sensors.

Furthermore, it is possible to program a number of sensor pixels used to target different metabolite concentrations. If a targeted metabolite concentration is too low, more sensor pixels can be used to reduce the noise further so as to obtain an observable signal shift.

Table 6.1 – Physiological range of glucose levels in different body fluids

Body Fluids	Glucose Levels (mM)		References
	Normal	Diabetic	
Blood	3.89 – 5.56	7 and higher	[167], [168]
Tears	0.06 – 0.34	0.4 – 1.44	[168]
Saliva	0.33 – 0.35	0.59 – 0.63 and higher	[169]
Urine	0.1 – 0.5	2.78 – 5.55	[170]
Sweat	0.28 - 1.11	-	[171], [172]

Sometimes a metabolite is found at different physiological concentrations in different body fluids. Table 6.1 shows an example of the physiological range of glucose concentration in different biofluids. Therefore, an array chip offers a mean to improve the signal for measuring the metabolite concentration in different body fluids.

6.2.2 Buffer Systems

It is vital for an enzymatic reaction to proceed at an optimal pH. Enzymes work within different optimal pH ranges and this has to be maintained to allow the enzymes to remain catalytically active. Enzyme assays routinely employ a buffer system to sequester proton fluxes in order to maintain a steady pH. Since the ISFET is a device that measures the change in hydrogen ions production or consumption, a high concentration buffer system could inherently limit the biosensor sensitivity. This is a particular challenging problem when measuring enzymes whose reactions produce or consume protons. Therefore, the optimal concentration of the buffer employed is vital in maintaining a balance between optimal pH and sensitivity of protons detection.

Before testing the ability of the ISFET chip to detect proton changes from enzymatic reactions, the ISFET was used to understand how buffer concentration affected the ISFET sensitivity. A buffer system can be classified into an acid buffer or an alkali buffer. An acid buffer commonly consists of a mixture of a weak acid (HA) and its conjugated base (A^-), which has both acidic and basic species to neutralise OH^- and H^+ respectively, thus maintaining a steady pH. For example, if a strong base is added to a buffer, the weak acid will give up its H^+ to counteract with the OH^- to transform into H_2O and maintain the pH:

$$OH^- + HA \rightarrow A^- + H_2O \qquad 6.3$$

On the other hand, if a strong acid is added to a buffer, the weak base will react with the acid to transform into weak acid (HA) and maintain the pH:

$$HCl + A^- \rightarrow HA + Cl^- \qquad 6.4$$

When either the HA or A^- has been used up, then the buffer system will lose its capability to maintain a steady pH. Hence, the effectiveness of a buffer depends on the concentration of HA and A^-.

To test this on the ISFET, 50 mM sodium phosphate buffer, 5 mM of sodium phosphate buffer and DI water were tested in a 1 ml volume, together with an injection of 1 M HCl acid solution, as shown in Figure 6.3.

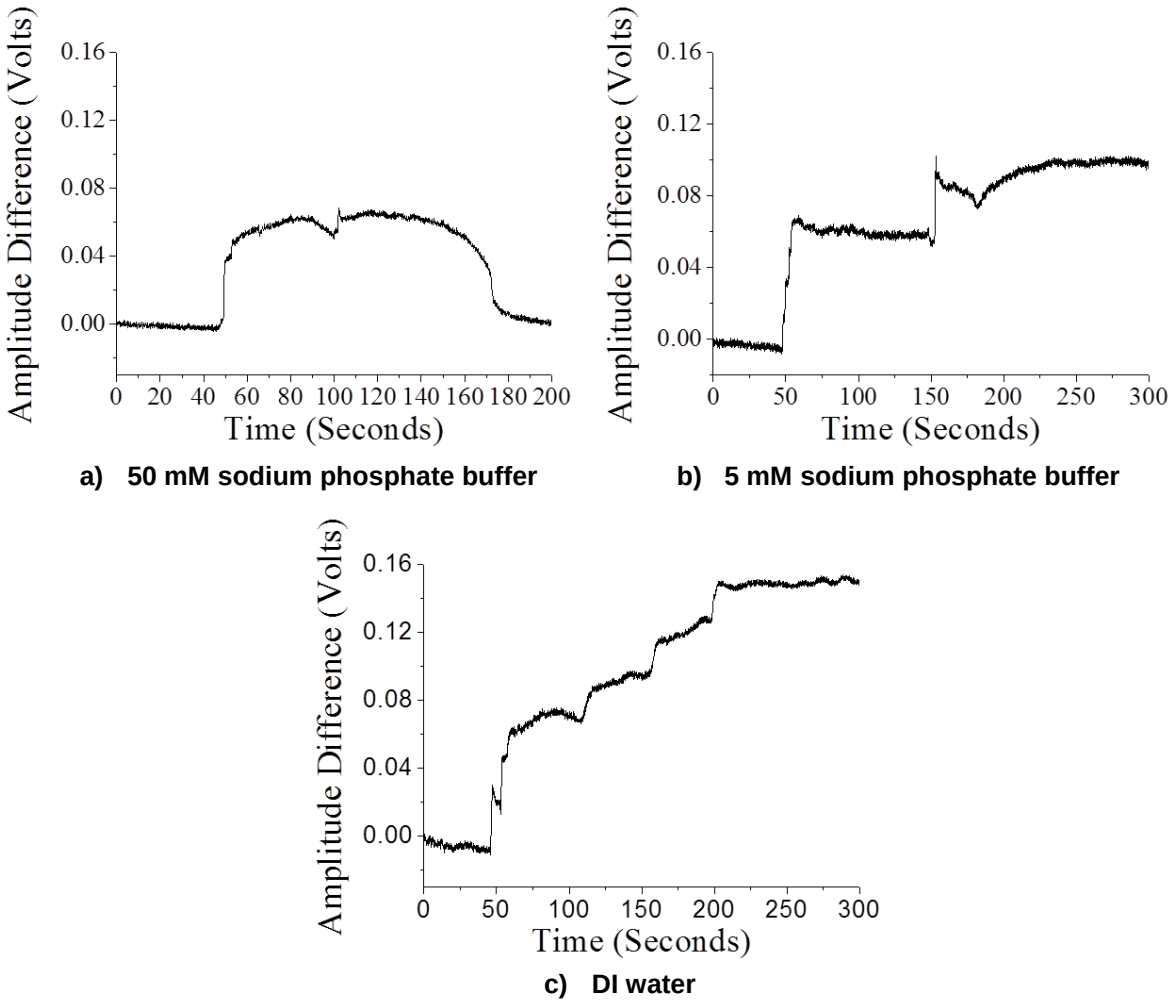

a) 50 mM sodium phosphate buffer **b) 5 mM sodium phosphate buffer**

c) DI water

Figure 6.3 – Effectiveness of buffering capacity for different solutions.

The addition of 5 μl of HCl did not exceed the buffering capacity of 50 mM sodium phosphate buffer, as a result of the ability of the buffer to sequester the excess protons produced by the complete dissociation of HCl in water. The buffer was again treated with another 5 μl of HCl and with a continued sequestration of the protons. Hence, the rise in signal from ISFET is transient before dropping back to the original pH (Figure 6.3a). However at the lower 5 mM sodium phosphate buffer, an addition of 20 μl of HCl was all that was

required to break the buffering capacity and reduce the pH. Therefore, the signal from the ISFET remains at a higher voltage (Figure 6.3b). DI water does not have any buffering capacity: an addition of 10 μl of HCl will release more protons and drop the pH dramatically. Hence, the signal from the ISFET rises and maintains at an even higher level compared to low buffer concentration (Figure 6.3c). These experiments show that a lower buffer concentration would be less effective in sequestering protons, leading to a higher signal from enzyme reactions to be measured on ISFET. However, if the pH changes from the enzyme reactions go beyond the optimal pH at a lower buffer concentration, then enzyme activities would be reduced. Therefore, the enzyme assays had to be well developed in a suitable buffer concentration.

As ISFET detection sensitivity could potentially be augmented at reduced buffer concentration, a stepwise approach was taken to understand each enzyme assay. Hexokinase was first chosen to illustrate this effect. Before measuring hexokinase assay on ISFET, a spectrophotometer was first used to investigate the reaction. In order to measure glucose using hexokinase spectrophotometrically, a coupled reaction with glucose-6-phosphate-dehydrogenase (G6PDH) enzyme was adopted (see Section 3.2.2.2). A product of the reaction, ß-NADPH, can be measured by spectrophotometry at a defined wavelength (340 nm). The reactions are given below:

$$D-Glucose+ATP \xrightarrow{Hexokinase} D-Glucose-6-P+ADP+H^{+}$$

$$D-Glucose-6-P+\beta-NADP \xrightarrow{G6PDH} 6-PG+\beta-NADPH+H^{+} \qquad 6.5$$

where ATP is adenosine 5'-triphosphate, D-Glucose-6-P is d-glucose-6-phosphate, ADP is adenosine 5'-diphosphate, ß-NADP is ß-nicotinamide adenine dinucleotide phosphate and 6-PG is 6-phospho-d-gluconate.

ATP and ß-NADP are essential components for hexokinase assay and both are acidic (below pH 5). If the buffering capacity has been exceeded, as for the case of low buffer concentration or DI water, the addition of ATP or ß-NADP would reduce the pH below the optimal pH for hexokinase, rendering the enzyme inactive. It was found that this problem was circumvented by adjusting the pH of

ATP and β-NADP solutions to physiological pH prior to being used in the hexokinase assay. Figure 6.4 shows a spectrophotometric hexokinase assay at different buffer concentrations, and ATP and β-NADP at different pHs. As evident, a marked improvement in hexokinase activity at low buffer concentration was observed when ATP and β-NADP solutions were prepared at the optimal pH for hexokinase assay. When the buffer concentration was high, the pH of ATP and β-NADP solutions had no effect on the activity, as the higher buffer concentration is resistant to pH changes caused by the addition of ATP and β-NADP. No change was seen when hexokinase was omitted. Crucially, these conditions could be translated to ISFET devices and would greatly enhance its sensitivity on the platform. However, a coupled reaction was not required to be used on the ISFET for hexokinase assay to produce β-NADPH, which can be measured by spectrophotometry. Therefore, only the pH of ATP solution was important for hexokinase assay on ISFET.

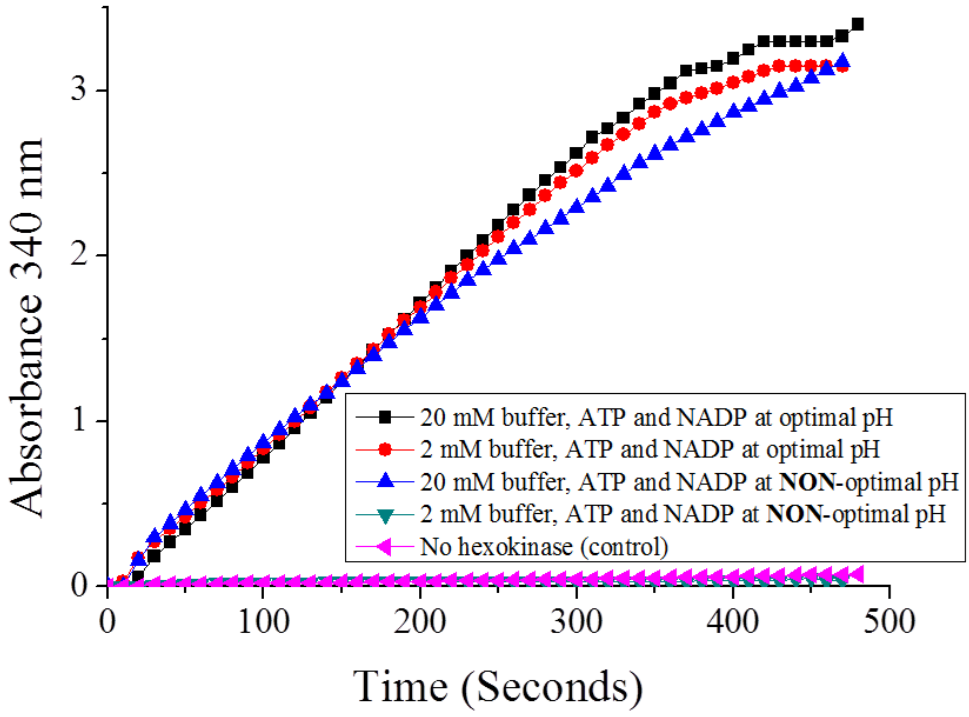

Figure 6.4 – Spectrophotometric hexokinase assay, using two different buffer concentrations with ATP and β-NADP solutions at different pHs. [Spectrophotometric measurements were done by Dr. Alasdair MacDonald].

Before testing the hexokinase assay on the ISFET, the enzyme reaction was also tested using a S220 SevenCompact pH/Ion meter (Mettler-Toledo, USA) to detect protons produced by hexokinase reaction, without the G6PDH coupled reaction.

Figure 6.5 shows that the pH was decreased when all hexokinase assay components were present at optimal buffer concentration.

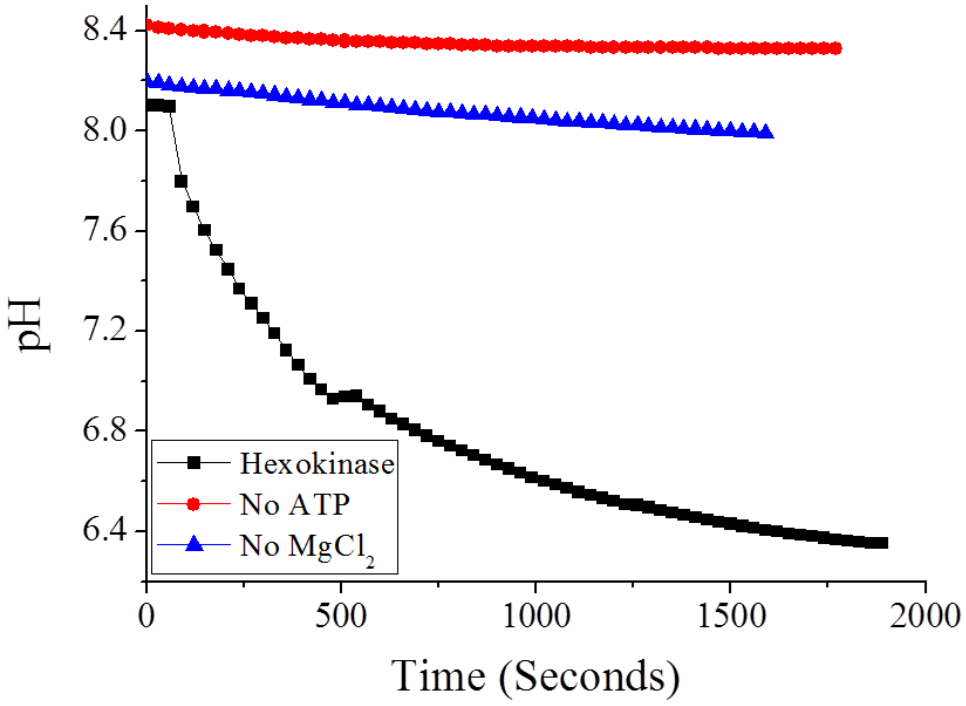

Figure 6.5 – Results obtained from pH meter with and without all the required components for hexokinase reaction. [pH meter measurements were done by Dr. Alasdair MacDonald].

These reactions were then performed on a CMOS ISFET chip to see if the hexokinase reaction could be recapitulated. In order to demonstrate that a lower buffer concentration could maximise the sensitivity of the measurement of hexokinase activity, 2.2 mM of triethanolamine buffer was used instead of 22 mM. Triethanolamine buffer has a wide buffering capacity between pH 5 to 9 (in the optimal pH range of hexokinase), in conjunction with its low cost, its ease of preparation and its compatibility with sodium alginate (will be discussed in Section 7.2). All these properties made it a suitable buffer of choice for further experiments. This buffer is sufficient to maintain the optimal pH range of the hexokinase enzyme (pH 7.5 – 9.0), while still allowing a detectable voltage signal from the ISFET sensor. The starting pH of this reaction was selected to be 8.5, which is at the higher end of the working pH range of hexokinase, allowing for subsequent pH drops to still be within the optimal pH range. The pH of the ATP solution had to be adjusted from pH 3.5 to pH 8.5 to prevent a pH reduction below the working range of the enzyme. This was done by titrating 1 M of sodium hydroxide. Figure 6.6 illustrates the comparison of voltage signal obtained from the ISFET sensor with 22 mM and 2.2 mM

triethanolamine buffer. Hexokinase activity on the chip was demonstrated by using different ATP concentrations and pHs together with a negative control for both buffer concentrations. Bovine serum albumin (BSA) was additionally used to substitute hexokinase enzyme to show that the voltage observed was hexokinase specific. As evident from Figure 6.6, the results of these experiments demonstrated that lower buffer concentration gave a higher signal change. There was no response from the ISFET when BSA was used instead of hexokinase.

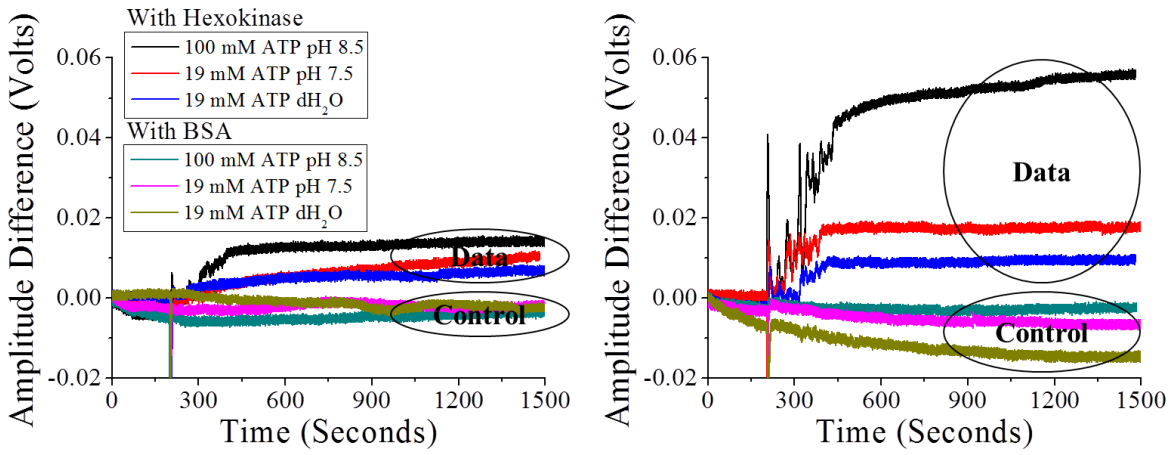

a) 22 mM buffer **b) 2 mM buffer**

Figure 6.6 – Enzymatic and control experiments on chip with different concentrations and pHs for ATP solution, at different buffer strengths.

6.2.3 Enzyme Assays

After determining the importance of ensemble averaging and buffer, the next step is to show the capability of ISFET to quantify different metabolites using a variety of different enzyme assays. To reiterate from Chapter 2 and 3, enzymes act as a biological catalysts and can be incorporated with biosensor technologies to detect a specific metabolite. The description below details the analysis of four different enzymes: hexokinase, lactate dehydrogenase, urease and lipase. Their biological significance and metabolite quantification will be discussed.

6.2.3.1 Hexokinase

The quantification of glucose concentration in various body fluids has been established as a valuable technique to monitor the symptoms of diabetes mellitus, a chronic metabolic disorder that is increasing in prevalence to an alarming degree [173]. This has placed a heavy burden on the social and medical

resources worldwide. Therefore, various biosensor technologies have been developed as an analytical tool to quantify glucose levels. Three enzyme reactions are commonly used for glucose measurement: hexokinase, glucose oxidase (GOx) and glucose-1-dehydrogenase (GDH) [174]. Commercial glucose biosensors are normally based on GOx and GDH to inform patients of their glycaemic status because these enzymes are cheap and easily obtainable. However, in this work we used hexokinase enzyme as the biological receptor to detect glucose levels. This assay was the first to be successfully applied on a CMOS platform in the research group and was investigated the most rigorously. Hexokinase is the first enzyme in glycolysis that converts glucose to glucose-6-phopsphate in the presence of ATP. Many clinical laboratories use hexokinase spectrophotometry as a reference method for glucose measurement [174], [175].

Spectrophotometric Measurement

Before performing the reaction on the ISFET chip, verification of hexokinase activity was tested by monitoring β-NADPH production, from the coupled enzyme reaction, using a UV-2550 Spectrophotometer (Shimadzu) at 340 nm and 25°C. The final concentrations of each reagent in a 1.26 ml volume solution were as follows: 20 mM triethanolamine buffer pH 8.5, 219 mM glucose, 7.9 mM $MgCl_2$, 1.1 mM β-NADP, 0.7 mM ATP, 1.25 Units G6PDH and 0.02 – 5 Units of hexokinase. The definition of a Unit of hexokinase activity is the amount of hexokinase required to phosphorylate 1 μmole of glucose per minute under standard conditions. Addition of different Units of hexokinase in the spectrophotometer allowed the determination of optimal amount to be used for subsequent experiments on the ISFET chip. By obtaining progress curves at different hexokinase concentrations, it was shown that between 0.125 and 5 Units gave a good response, with 2.5 Units being used for all subsequent experiments.

The following experiments were concerned with varying glucose concentration in the range of 0 – 220 mM using 2.5 Units hexokinase. This reaction was first tested on the spectrophotometer using a coupled enzyme reaction. Figure 6.7 presents the data obtained from the spectrophotometric hexokinase assay with different glucose concentrations. As evident, different glucose concentrations corresponded to different light absorbance levels. However, the signal was saturated at 0.7 mM glucose concentration, as a result of the depletion of ATP.

Nevertheless, this had demonstrated a working hexokinase assay to quantify different glucose levels.

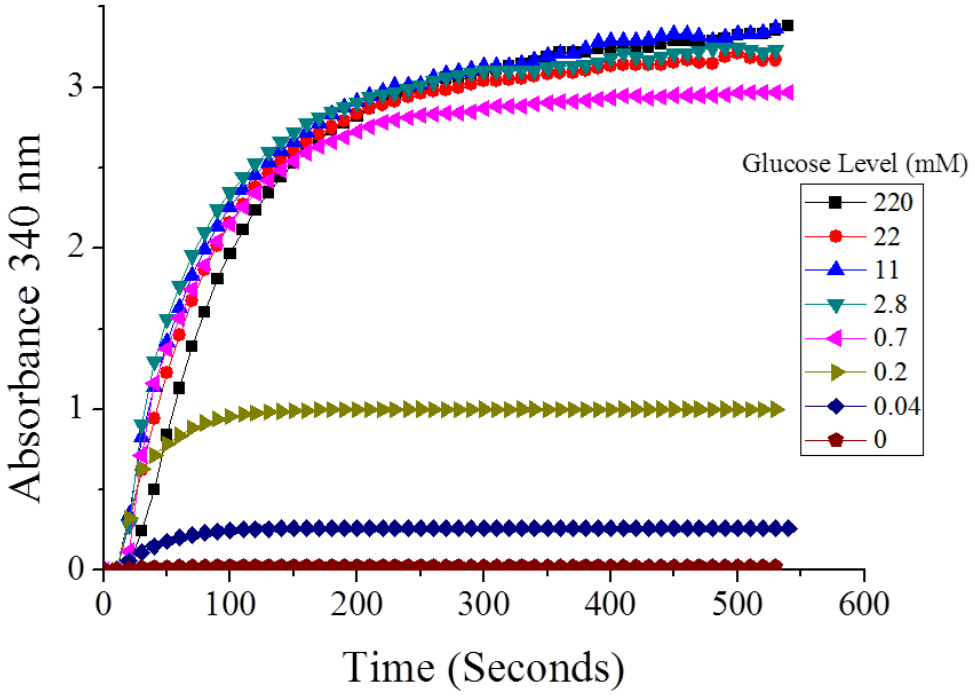

Figure 6.7 – The data obtained for different glucose concentrations using spectrophotometry. [Spectrophotometric measurements were done by Dr. Alasdair MacDonald].

ISFET Measurement

There was no need for a coupled reaction to produce β-NADPH, as the production of protons by hexokinase could be readily visualised by a decrease in pH. After determining the enzyme reaction conditions for hexokinase using spectrophotometry, the hexokinase assay without the coupled reaction was verified with a pH meter to see if protons produced by the hexokinase reaction resulted in a detectable change in pH (see Figure 6.4). Since ISFET measures hydrogen ion (proton) concentration, there is also no need for a coupled reaction, hence ISFET was used in replacement of the pH meter to provide a direct assay (preferred type of assay, refer to Section 3.2.2.1).

Hexokinase activity on the chip was tested with glucose concentration varying from 0.05 to 231 mM, which encompassed the physiological range of blood glucose, from 2.8 mM (hypoglycaemia) to 20 mM (extreme hyperglycaemia). The reaction was in a volume of 1.2 ml with final concentrations as follows: 2.2 mM

triethanolamine buffer pH 8.5, 8.6 mM $MgCl_2$, varied glucose concentrations, 4.17 mM ATP and 1 Unit of Hexokinase. A higher concentration of ATP was used so that it was stoichiometrically similar to glucose concentration. Furthermore, 43 μg/ml phenol red was added to the solution to provide a visual pH indicator, in order to help determine if the reaction was working properly on the chip rather than making a false measurement. To do hexokinase assay on chip, all the reagents were added on top of the chip and waited for roughly 3 minutes to get a baseline, then the reaction was initiated by adding hexokinase. After adding the hexokinase enzyme into the reaction cocktail, the solution was mixed with pipette to make sure that diffusion is not limiting the enzyme reaction. In addition, a negative control experiment is always a crucial part for biological measurements, BSA was used to initiate the reaction rather than hexokinase to make sure that the reaction was correct.

Figure 6.8 illustrates the quantification of glucose levels using ISFET. As can be seen in Figure 6.8a, the signal from a single typical ISFET sensor was obtained, which gave a rise in voltage signal until a fixed voltage plateau was reached. The voltage of the plateau varies as a function of glucose concentrations. Figure 6.8b shows the average of five different ISFET sensors. As expected, the noise was reduced and enabled the calculation of a standard deviation.

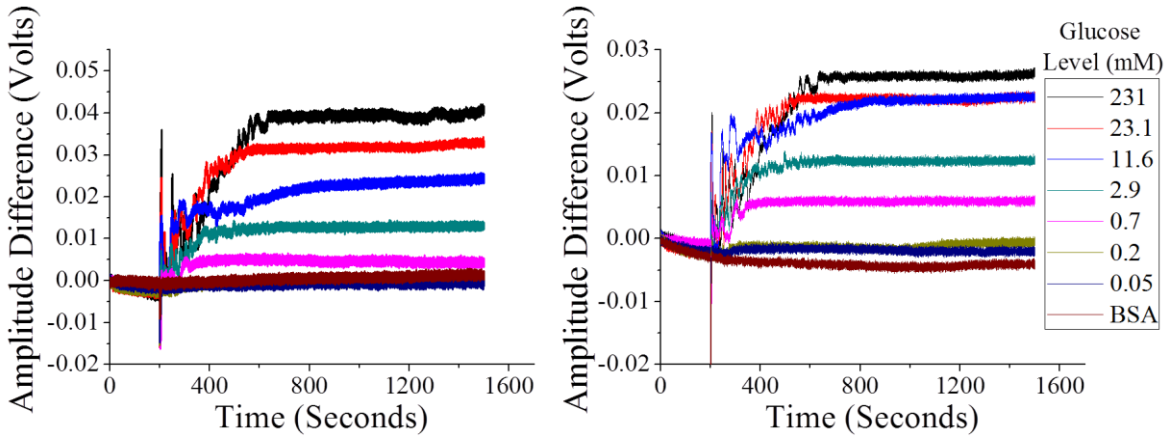

a) A typical single sensor **b) Average of five sensors**

Figure 6.8 – Data obtained from ISFET sensor for different glucose concentrations.

Since the turnover rate of glucose by hexokinase is constant at the voltage plateau and the concentration of glucose is directly related to voltage, hence the average of the plateau signal voltage was plotted against log [glucose] for a single sensor pixel and an average of five sensor pixels. Figure 6.9 shows that

there is a straight-line dependency through the central operating region for which the conditions of the assay is similar to the physiological range of blood glucose. As evident, the plot deviates from the Nernstian fit at both high and low end of the glucose concentrations. The assay that was performed in this work is not sensitive enough to measure such low glucose concentrations, whereas at very high glucose concentrations, the ATP was completely depleted after the reaction and led to a saturation of signal. More importantly, the sensitive region fell within the physiological range of blood glucose.

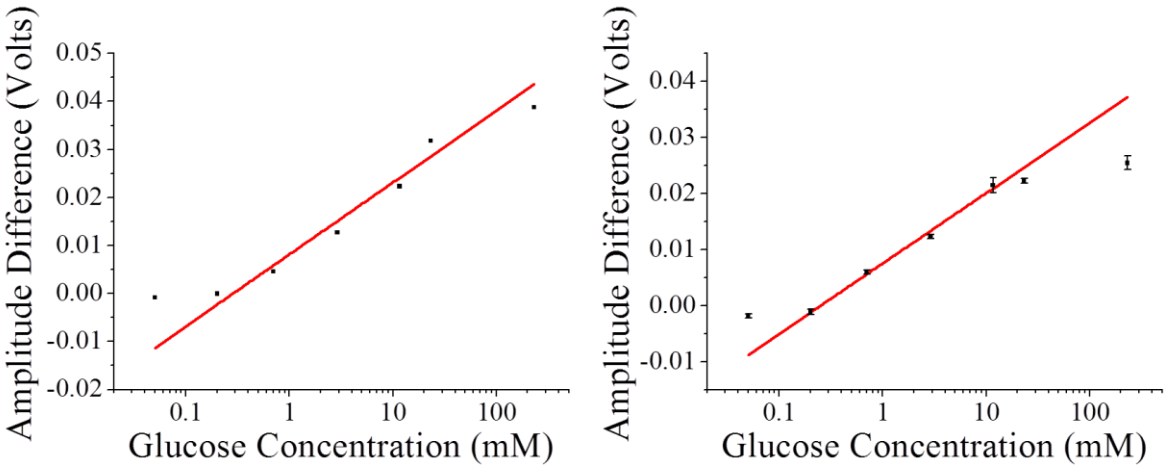

a) A typical single sensor **b) Average of five sensors**

Figure 6.9 – The voltage signal from ISFET sensor at the plateau as a function of glucose concentration.

6.2.3.2 Lactate Dehydrogenase

The next enzyme assay tested on the ISFET chip was lactate dehydrogenase (LDH). Pyruvate (pyruvic acid) is the final product of glycolysis and lies at the convergence point of multiple different metabolic pathways [176], [177]. A deviated amount of pyruvate in blood serum could be associated to several diseases, in particular for those who exhibit metabolic acidosis. These pathologies include: motor neuron disease, lactic acidosis and others. Hence, accurate measurement of pyruvate level could provide a valuable insight into a patient's clinical profile. There are several enzymes that involve in pyruvate metabolism and LDH was selected to be the biological recognition element in this work. LDH converts pyruvate to lactate by producing β-NADH and consuming hydrogen ions, which are measureable by spectrophotometry and the ISFET sensor respectively.

Spectrophotometric Measurement

Unlike hexokinase assay, LDH activity can be rapidly monitored by measuring the consumption of ß-NADH using a spectrophotometer, thus the reaction is very simple and does not require a coupled reaction. LDH catalyses the following reaction:

$$Pyruvate + \beta - NADH + H^+ \xrightarrow{LDH} Lactate + NAD^+ \qquad 6.6$$

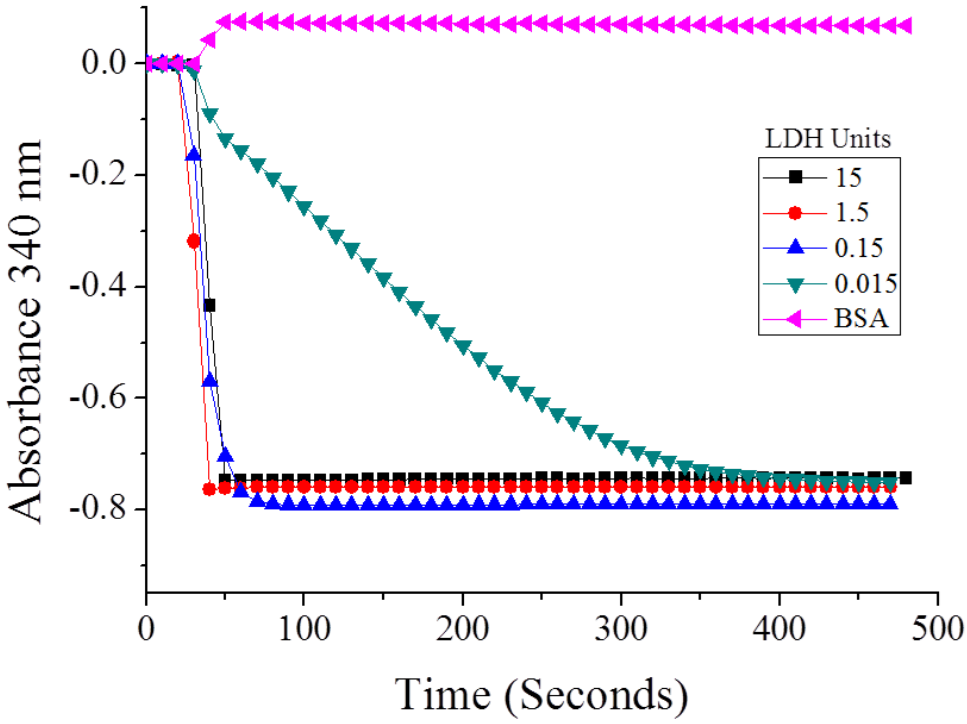

Figure 6.10 – Data obtained from spectrophotometry for different Units of LDH. [Spectrophotometric measurements were done by Dr. Alasdair MacDonald].

As hexokinase gave promising results with triethanolamine buffer, the same buffer was also tested with LDH. Ideally, the use of a 'universal buffer' would allow simultaneous measurements of the activities of a number of different enzymes. The final concentrations of each reagent in a 0.99 ml volume solution were as follows: 5 mM triethanolamine buffer pH 7.5, 0.12 mM ß-NADH, 1 mM sodium pyruvate and 0.015 – 15 Units of LDH. A pH of 7.5 was used because it is within the optimal pH for LDH enzyme. One Unit of LDH phosphorylates 1 μmole of pyruvate to L-lactate per minute at 37°C. Figure 6.10 shows the progress curves from spectrophotometer with different Units of LDH. These initial titration experiments of different Units of LDH had demonstrated the developed

LDH reaction to be used on ISFET chip and showed an optimal rate of reaction of 0.015 – 0.15 Unit of LDH, in solution.

ISFET Measurement

The reduction of pyruvate to lactate will result in the consumption of hydrogen ions. Therefore, the reaction functions as a hydrogen ion sink and should produce an increase in pH under developed conditions. LDH activity was also tested on a pH meter for further validation. A rise in pH was observed only at low buffer concentration when all reaction components were present. In addition, a higher Unit of LDH was required to obtain a detectable signal in pH meter, which was 1.5 Units. Hence, 1.5 Units LDH was used for all ISFET measurements. Subsequently, the enzyme reaction was transferred to the ISFET sensor to quantify pyruvate, which levels were proportional to hydrogen ion consumption.

The quantification capability of the ISFET sensor was then tested for pyruvate. This was done in 0.99 ml with all the required reagents corresponding at the final concentration: 5 mM triethanolamine pH 7.5, 1.65 – 6.6 mM ß-NADH, 3.5 – 14 mM sodium pyruvate and 1.5 Units of LDH. Again, 50 μg/ml phenol red was added to the solution to visualise the pH change. The LDH assay was done similarly to hexokinase with all the reagents added on top of ISFET sensor, waiting for approximately 3 minutes before initiating the reaction with LDH. Three negative controls were tested by omitting sodium pyruvate, ß-NADH and LDH from the solution, respectively. Figure 6.11 illustrates the results from the ISFET by changing the concentrations in sodium pyruvate and ß-NADH. As evident, the voltage signal from ISFET decreases as opposed to the hexokinase assay, a result of hexokinase assay decreases the pH while LDH assay increases the pH of the solution. It is clearly observed from Figure 6.11a that pyruvate levels can be quantified with the LDH assay, using 0 mM, 3.5 mM, 7 mM and 14 mM pyruvate. The highest concentrations of pyruvate gave saturation as a result of depletion of 6.6 mM ß-NADH, thus the maximum hydrogen ion change could only correspond to the concentration of ß-NADH. To prove that ß-NADH is the limiting factor, Figure 6.11b shows that by maintaining sodium pyruvate at 14 mM while varying ß-NADH (0 mM, 1.65 mM, 3.3 mM and 6.6 mM) had an effect on final pH/voltage change. All negative controls gave no change in voltage,

showing that the signal was a direct result of the LDH reaction. One point to note is that the physiological range of pyruvate levels is much lower than the one used here. In blood, the range is between 0.08 – 0.16 mM [178], which is lower than the lowest concentration used in this assay. Nevertheless, the experiments show that pyruvate can be quantified on the ISFET sensor. Further work can be done to reduce and investigate the buffer concentration and to improve the ISFET pH sensitivity so as to detect physiological concentration of pyruvate levels.

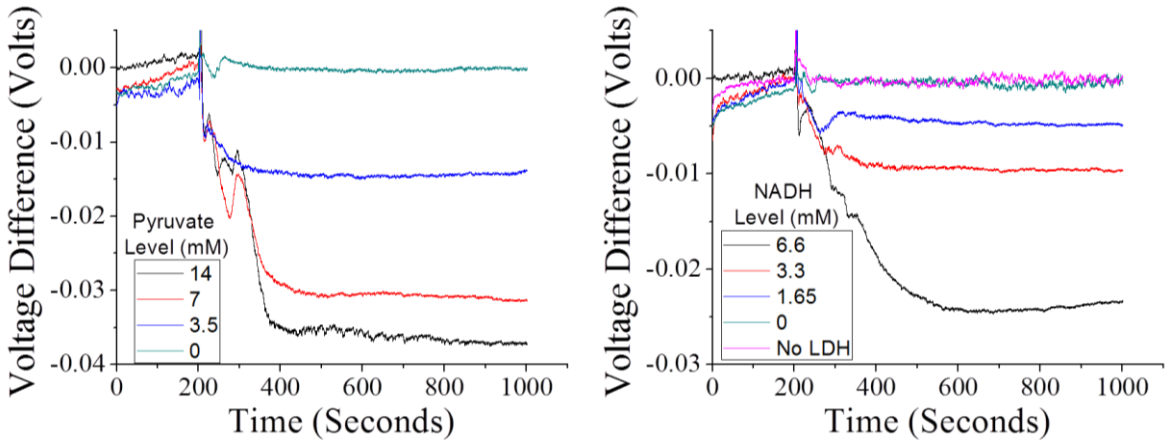

a) Pyruvate measurements **b) β-NADH measurements**

Figure 6.11 – Data obtained from ISFET sensors using different pyruvate and β-NADH concentrations.

6.2.3.3 Urease

The third enzyme assay used was urease, an enzyme which is used to determine urea concentration. Urea, $CO(NH_2)_2$ is one of the end products of protein metabolism and is produced by the liver [179]. By determining human urea levels, glomerular filtration rate of kidney and renal function can be analysed [180]. Hence, an elevated urea level in serum is important to determine if patients suffer from renal dysfunction. In addition, urea production can be blocked by liver disease. Therefore, the measurement of urea concentration is extremely useful for clinical diagnostic purposes, in terms of diagnosing liver and kidney disease. The urease reaction is a straightforward assay that can be readily done on the ISFET. The assay requires only urease and urea in a buffer to produce a pH change.

Urease does not produce a product that can be measured by spectrophotometry directly. The reaction of urease assay is given below:

$$CO(NH_2)_2 + 3H_2O \xrightarrow{Urease} CO_2 + 2NH_4^+ + 2OH^- \quad 6.7$$

The formation of ammonia by hydrolysis of urea (in the form of ammonium hydroxide) should result in a detectable rise in pH under suitable buffer conditions.

To verify that urease reaction produces a pH change, a pH meter was used. The buffer chosen was 4-morpholineethanesulfonic acid (MES) buffer at pH 6. This buffer was selected as urease has an optimal pH range from pH 4 to 9. A pH of 6 was chosen so that the increase in pH during reaction would still be within the optimal pH range of urease, allowing maximum detection. Figure 6.12 illustrates the urease assay using a pH meter. As shown, an increase in pH from 6 to 9.2 was observed at 5 mM MES buffer pH 6 when both 100 mM urea and 1.5 Units of urease were present. One Unit of urease will liberate 1 μmole of NH_3 from urea per minute at 30°C. No change was observed when either urease or urea was omitted.

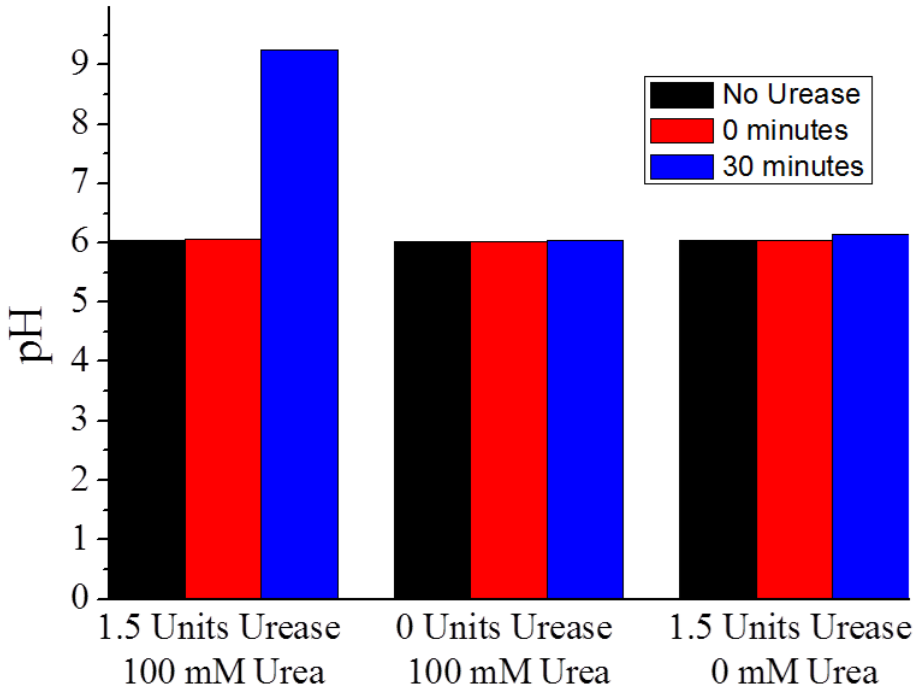

Figure 6.12 – Data obtained from pH meter for urease assay. [pH meter measurements were done by Dr. Alasdair MacDonald].

After validation from the pH meter, the quantification of urea was measured on an ISFET chip. This was done in 1007.5 μl volume of solution with the final concentrations of each reagent were as follows: 5 mM MES buffer pH 6, 12.5 – 100 mM urea, 3.75 Units of urease and 50 μg/ml of phenol red. A negative control without urea was also measured to show that the pH change was a direct result of the enzyme reaction. As with previous assays, a 3 minute baseline was recorded before addition of urease. Figure 6.13 shows the quantification of different urea levels using this assay. As shown, different urea concentrations gave different voltage signals. However, the physiological range of urea in blood is 2.9 – 8.9 mM [181]. The lowest concentration that was measured was 12.5 mM, so further work to measure physiological range of urea level has to be done to investigate the urease assay such as, lowering the starting pH value, reducing the buffer concentration or even increasing the pH sensitivity of the ISFET sensor. Nevertheless, the capability to quantify urea level using ISFET sensor had been demonstrated.

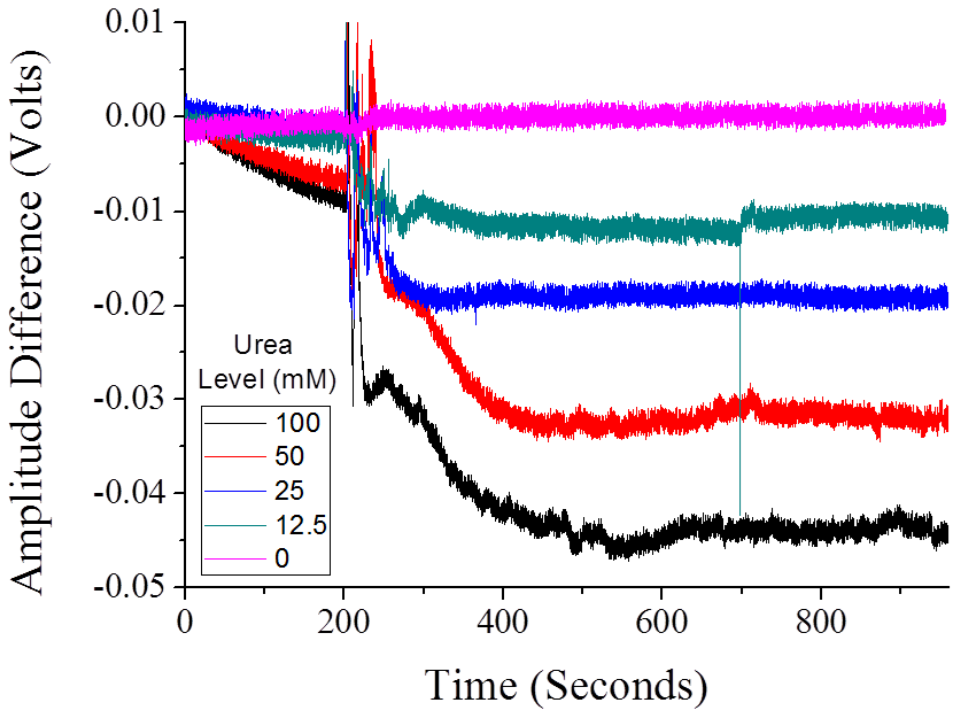

Figure 6.13 – Data obtained from a single ISFET sensor for different urea concentrations.

6.2.3.4 Lipase

The final enzyme assay tested on the ISFET chip was lipase. The lipase assay is a useful method to measure triglycerides, which are a type of fat (lipid) found in the blood. When an excess energy is required, triglycerides are metabolised as

an energy source in addition to glucose [182]. Triglycerides are not soluble in blood, thus can circulate in the blood with the help of proteins that transport the lipids (lipoprotein). Hence, an elevated amount of triglyceride in the blood can promote the thickening of artery wall, which increases the risk of stroke, heart attack and heart disease (coronary artery disease) [183]. Moreover, conditions such as obesity and metabolic syndrome, the latter using a collection of markers such as measurement of waist line, high blood pressure, high cholesterol and high blood glucose, are linked to elevated triglyceride levels. The lipase reaction is another relatively straightforward assay that can be done on the ISFET sensor.

The reaction below shows the reaction catalysed by lipase:

$$Triglyceride + H_2O \xrightarrow{Lipase} Diglyceride + Fatty\ acid \qquad 6.8$$

The formation of fatty acid by hydrolysis of triglyceride should result in a detectable lowering of pH under suitable reaction conditions. To test this assay, the reaction with a lipase substrate (trioleoyl glycerol) was first developed. The final concentrations of each reagent were as follows: 1.25 mM triethanolamine pH 8.5, 1.8 mM lipase substrate, 400 mM sodium chloride, 5 mM calcium chloride, 50 μg/ml phenol red and 80 Units of lipase in solution. One Unit of lipase will hydrolyse one microequivalent of fatty acid from a triglyceride per hour at pH 7.7 and 37^{o}C. As was done with previous assays, the reaction was initiated by addition of lipase. A pH meter was initially used to test the assay and found a decrease of one pH unit in the presence of lipase, and no observable change when either lipase or trioleoyl glycerol was omitted. This assay was next transferred to an ISFET chip. Figure 6.14 shows the ISFET voltage signal obtained from a lipase assay. As can be seen, 1.8 mM trioleoyl glycerol gave a response from the ISFET sensor while no response was observed when lipase or lipase substrate was omitted, recapitulating pH meter results. Healthy individuals should have around 1.7 mM triglyceride in the blood, which corresponds to the measurement obtainable from the ISFET. Even though, time had limited a number of different triglyceride levels to be measured, the assay suggested that higher levels of triglyceride could be detected by the ISFET sensor.

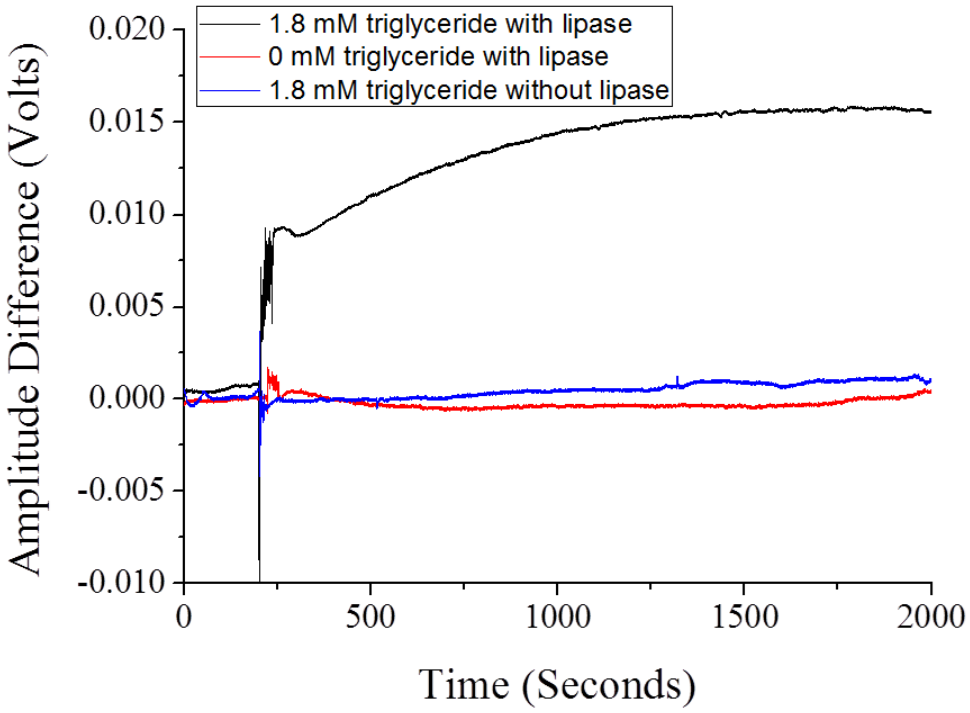

Figure 6.14 – Data obtained from ISFET sensors for lipase assay to detect triglyceride.

6.2.4 Enzyme Kinetics

As discussed in detail in Section 3.2.1, enzyme kinetics is an important field to understand the fundamentals of the catalytic mechanism of an enzyme. Since the hexokinase assay had been most rigorously tested on the ISFET, the plots from both spectrophotometer and ISFET were used to calculate the Michaelis-Menten constant of hexokinase enzyme for comparison. The Michaelis-Menten constant can be extracted from the initial rate of enzyme progress curves from different substrate concentrations. Usually an enzyme progress curve will have a rapidly rising linear signal before it slows down as substrate is being consumed. The progress curve from spectrophotometer and ISFET measures absorbance of product (ß-NADPH) or production of hydrogen ions versus time, respectively. As time increases, more ß-NADPH or hydrogen ions are formed in hexokinase assay, resulting in an increase in absorbance or ISFET voltage respectively, and then the absorbance or ISFET voltage plateaus are reached as the substrate is exhausted. The initial velocity at different substrate concentrations (i.e. by doing a number of progress curves) are then used to plot a graph of substrate concentration versus initial velocity. This gives a hyperbolic curve. At high substrate concentration, the enzyme is saturated and so the initial velocity remains constant, which is termed as the maximal velocity. At substrate

concentration where the initial velocity is half the maximal of velocity, it is defined as the Michaelis-Menten constant, K_m (see Section 3.2.1 for more details). Therefore, the initial velocity of each of the progress curve was taken and plotted against the substrate (glucose) concentrations. By using the software, GraFit, which has a built-in Michaelis-Menten algorithm, the value of K_m was calculated for both spectrophotometric and ISFET assays. By measuring the velocity during the first 60 seconds of the reaction, the reaction rate (absorbance for spectrophotometer or voltage for ISFET) was calculated for each substrate concentration. Using a linear fit at the slope of each concentration from the data obtained from spectrophotometric assay (refer to Section 6.2.3.1, Figure 6.7), the velocity of the first 60 seconds was then obtained and the K_m value was calculated to be 0.85 mM using GraFit.

With the data obtained from the ISFET for the hexokinase assay (refer to Section 6.2.3.1, Figure 6.8), the initial velocity (first 60 seconds) at each concentration was also plotted as a function of glucose concentration using GraFit to calculate the K_m. The reaction rate versus glucose concentration plot was then further plotted into Lineweaver-Burk double reciprocal plot for each concentration. Figure 6.15 shows the Lineweaver-Burk double reciprocal plots of 1/(dV/dt) versus 1/[glucose] for both typical single sensor pixel and average of five sensor pixels signals. As shown, the points fitted onto a line with the intercept 1/[glucose] axis being as $1/K_m$ using the equation below:

$$\frac{1}{v} = \frac{K_m}{v_{max}} \frac{1}{[S]} + \frac{1}{v_{max}} \qquad 6.9$$

Using this method, the value of K_m was calculated to be 0.58 ± 0.36 mM for the average of five sensor pixels for hexokinase assay on ISFET sensor. This K_m corresponded well with the one obtained from spectrophotometric assay for hexokinase. This had proven that CMOS ISFET with hexokinase as biological receptor has the capability to be used as a biosensor to monitor the symptoms of diabetes mellitus, with an accuracy that is comparable to a large-scale laboratory based spectrophotometer.

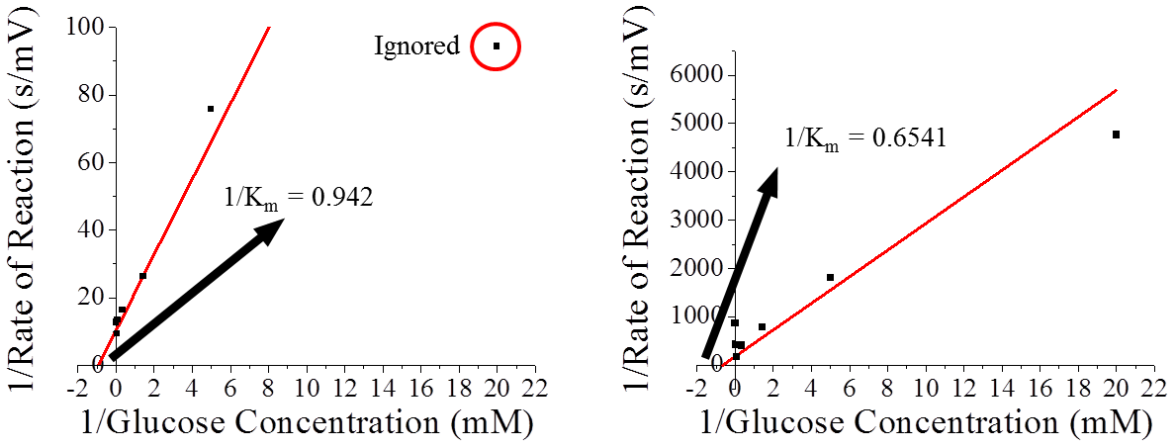

a) A typical single sensor

b) Average of 5 sensors

Figure 6.15 – Lineweaver-Burk double reciprocal plot for K_m value using the data obtained using ISFET.

6.3 Metabolite Sensing on PD

The Multi-Corder chip consisted of three different sensors, two optical sensors (PD and SPAD) and an electrochemical sensor (ISFET). 50 chips were delivered by the foundry, but only the PD and SPAD sensors could be used for testing as the ISFET sensors had some technical issues. A thick passivation layer on top of the ISFET reduced its sensitivity significantly. The Multi-Corder chip was also designed to allow microfluidic channels to be fabricated with ease for multiple metabolite quantification. In order to demonstrate that multiple metabolites could be tested on a single chip using microfluidic channels, one of the optical sensors had to be tested with at least one enzyme assay. Since some enzymatic reactions produce a colorimetric product, an optical sensor could be used to detect enzyme activity using a Multi-Corder chip. Therefore, PD was chosen to test cholesterol oxidase activity and to detect its corresponding metabolite, cholesterol. The following sections will explain how the cholesterol oxidase assay works in cholesterol solution and in serum, and finally the determination of the Michaelis-Menten constant from cholesterol oxidase will be described.

6.3.1 Cholesterol Oxidase and Cholesterol Esterase Assay

Cholesterol is a sterol lipid and is an essential constituent of animal cell membranes [184]. It is mainly produced by the liver and is also found in foods such as meat, milk, eggs and so on. As with triglyceride, cholesterol is insoluble

in blood, and is transported through the blood stream as a lipoprotein. There are three common lipoproteins: low-density lipoproteins (LDL), high-density lipoproteins (HDL) and very low-density lipoproteins (VLDL). Medical studies have shown that an elevated level of LDL cholesterol ("bad" cholesterol) could lead to a higher risk of coronary artery blockage, whereas an increased level of HDL cholesterol ("good" cholesterol) could lower the risk.

Even though cells require cholesterol for a number of metabolic processes and functions, an excess can lead to a thickening of arteries wall with a build-up of plaque deposits, a condition known as atherosclerosis (similar to elevated level of triglyceride). A blood clot can be formed on an exposed area when a piece of plaque breaks off from the surface. This will decrease blood flow and oxygen supply to other organs, leading to coronary heart diseases (heart attack or angina) [185], stroke or other cardiovascular diseases. These diseases pose a threat to society and a heavy burden towards healthcare resources in UK and worldwide. It is estimated that cardiovascular disease caused 160,000 deaths in 2011, which is the UK's biggest killer [186]. Normally, the best way to detect cholesterol is by a blood test. Normal serum cholesterol should be 5 mM or lower for a healthy individual.

Cholesterol oxidase is the most commonly used enzyme for cholesterol quantification in biosensors, and was thus used in this work. Only approximately 20% of cholesterol in serum is in 'free' form, while the remaining takes the form of cholesteryl esters [187]. To accurately determine total cholesterol in serum, the esterified form of cholesterol has to be hydrolysed to free cholesterol by addition of cholesterol esterase. Hence, in order to measure total cholesterol in human serum, two enzymes (cholesterol oxidase and cholesterol esterase) had to be applied together, in addition to a third enzyme (peroxidase) that yields an optical product to be measured by the spectrophotometer and the PD.

6.3.1.1 Spectrophotometric Measurement

Neither cholesterol esterase nor cholesterol oxidase produces a product that is measureable optically. Therefore, the enzymatic activity was evaluated using a coupled colorimetric assay to quantify the concentration of cholesterol in human serum, specifically human male AB plasma, USA origin, sterile-filtered and

sourced from Sigma Aldrich. The concentration range of cholesterol stated by Sigma Aldrich was 2800 – 5400 μM and it was later quantified by the NHS to be 3500 μM. The reaction involved three enzymatic steps. In the first step, the enzyme cholesterol esterase was used to hydrolyse cholesteryl esters to free cholesterol:

$$Cholesteryl\ ester + H_2O \xrightarrow{Cholesterol\ Esterase} Cholesterol + Fatty\ acid \qquad 6.10$$

The second step involved the addition of cholesterol oxidase, an oxidoreductase, which uses molecular oxygen as the electron acceptor and reduces it to hydrogen peroxide. In this reaction, the free cholesterol in the serum with the addition of free cholesterol produced by the esterase reaction, giving the 'total cholesterol' that could be quantified:

$$Cholesterol + O_2 \xrightarrow{Cholesterol\ Oxidase} 4 - Cholesten - 3 - one + H_2O_2 \qquad 6.11$$

However, cholesterol oxidase enzymatic reaction does not produce a measureable optical product for either spectrophotometry or PD. Thus, a coupled enzyme assay had to be used:

$$o - Dianisidine(reduced) + 2H_2O_2 \xrightarrow{Peroxidase} o - Dianisidine(oxidised) + 2H_2O \qquad 6.12$$

In the presence of peroxidase, hydrogen peroxide produced in Equation 6.11 is used to oxidise o-Dianisidine to a coloured product, which progressively changes into a deep orange colour. This change in colour depends on the concentration of hydrogen peroxide, which is itself proportional to the cholesterol concentration. Hence, the total amount of cholesterol in serum was quantified by measuring the absorbance at 500 nm wavelength of the oxidised o-Dianisidine. The reason for choosing 500 nm wavelength to perform the measurement will be explained later in the discussion.

The enzymatic activity of cholesterol oxidase was initially evaluated using a spectrophotometer. Initially, cholesterol oxidase activity was evaluated using cholesterol supplied in solution (refer to Equation 6.11 and 6.12). The

absorbance of oxidised o-Dianisidine was monitored at 500 nm and 25°C with a UV-2550 Spectrophotometer. The following final concentrations of each reagent in a 1 ml volume solution were used: 42 mM triethanolamine pH 7.5, 0.32 mM o-Dianisidine, 429 μM cholesterol in 0.33% Triton X-100, 3.3 Units of peroxidase and 0.067 - 0.67 Units of cholesterol oxidase. The definition of a Unit of cholesterol oxidase activity is the amount of cholesterol oxidase required to convert 1 μmole of cholesterol to 4-cholesten-3-one per minute at pH 7.5 and 25°C. The reaction was initiated with cholesterol oxidase. It was observed that 0.33 Units of cholesterol oxidase gave suitable kinetics, which was then used for all the subsequent experiments. The next experiment involved varying the concentration of cholesterol from 0 μM to 214 μM. Figure 6.16 illustrates the quantification of cholesterol in solution obtained from the spectrophotometer. As evident, as the concentration of cholesterol was higher, more o-Dianisidine was oxidised and formed a darker orange colour, resulting in more absorption at 500 nm wavelength (refer to Equation 6.11 and 6.12). By obtaining progress curves at different concentrations, it was shown that different concentrations of cholesterol corresponded to different endpoint absorbance. This had demonstrated a cholesterol oxidase assay that can quantify free cholesterol in solution.

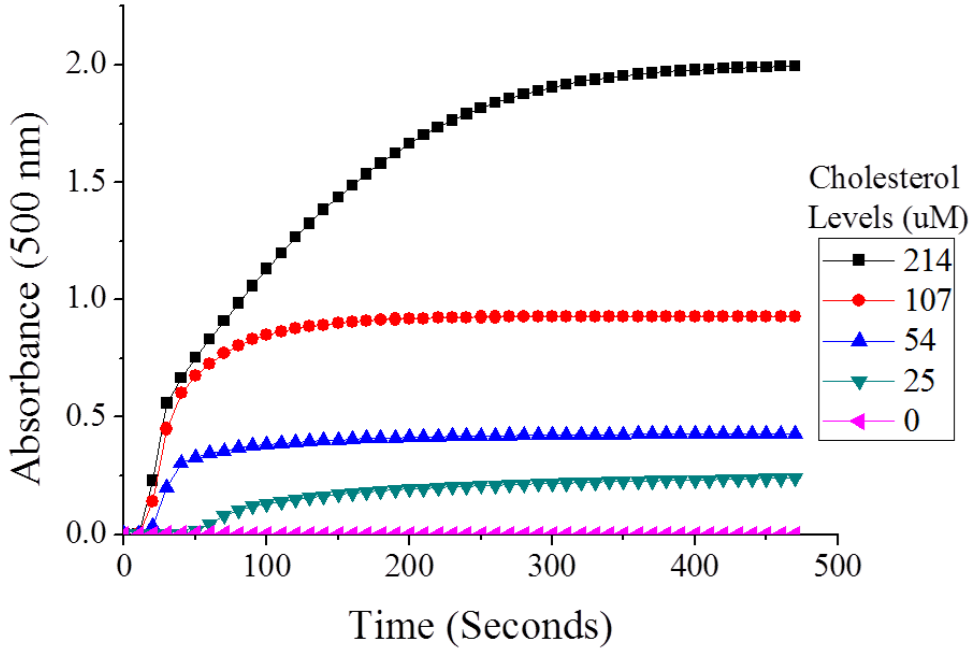

Figure 6.16 – Data obtained from the spectrophotometer for different cholesterol concentrations in solution. [Spectrophotometric measurements were done by Dr. Alasdair MacDonald].

The next step involved the evaluation of human serum using the developed cholesterol oxidase reaction conditions, together with the cholesterol esterase step to release free cholesterol from its esterified form (refer to Equation 6.8). To do this, an additional 15 minutes pre-incubation step at 37^{o}C with cholesterol esterase was required. The temperature 37^{o}C is the standard condition required for cholesterol esterase, thus it was used instead of 25^{o}C. The reaction mixture was at the following final concentrations for each reagent: 34.6 mM triethanolamine pH 7.5, 4.7 mM of taurocholic acid sodium salt hydrate, 5.9 mM sodium cholate hydrate, 25 mM sodium chloride, 0.14 Units of cholesterol esterase and diluted serum with final concentrations of cholesterol at 118 μM, 236 μM and 471 μM. Following the pre-incubation step, 0.32 mM o-Dianisidine and 3 Units of peroxidase were added, followed by initiation with 0.3 Units cholesterol oxidase. Figure 6.17 illustrates the results obtained from the spectrophotometer with serum cholesterol and cholesterol supplied in solution. The cholesterol in serum was diluted into 118 μM, 236 μM and 471 μM and was compared with cholesterol solution made up at 107 μM, 214 μM and 429 μM. As shown in Figure 6.17, when the cholesterol in serum was diluted to 236 μM or lower, the results corresponded quite well with the cholesterol supplied in solution. However, at higher concentration of cholesterol in serum, the result started to deviate from the result obtained from the cholesterol supplied in solution. This may be because of inhibitors present in the serum that may interfere with the reaction, or could be because at higher concentration the absorbance of the o-Dianisidine had reached saturation. Nevertheless, the results had demonstrated that by pre-treatment of human serum with cholesterol esterase, total amount of free cholesterol in serum could be determined.

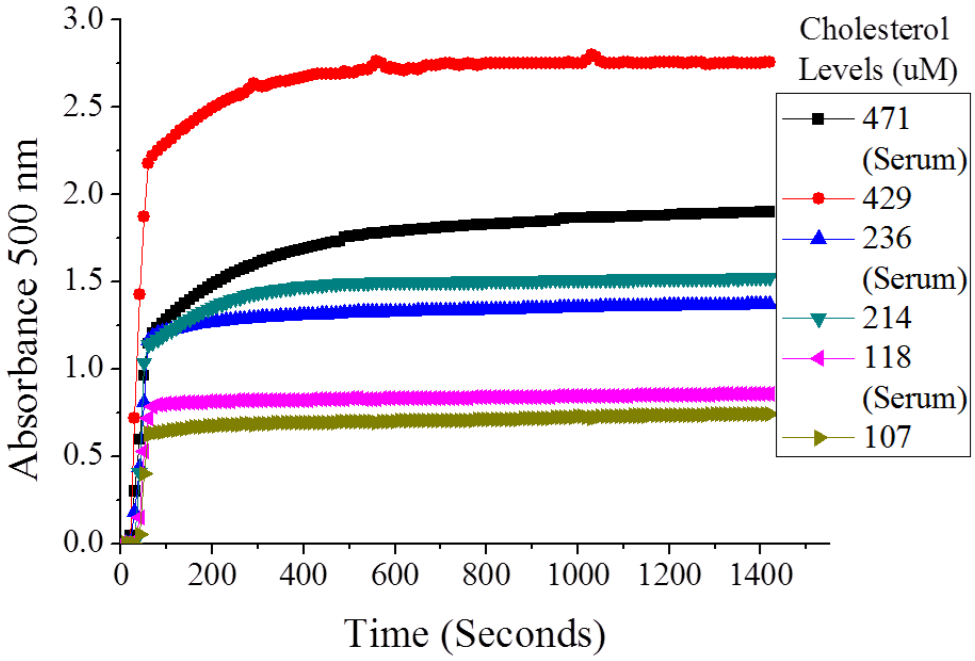

Figure 6.17 – Data obtained from the spectrophotometer for the comparison of cholesterol levels in serum and solution. [Spectrophotometric measurements were done by Dr. Alasdair MacDonald].

6.3.1.2 PD Measurement

In order to measure light absorbance of o-Dianisidine using PD, a light source was required. Since POC diagnostics aim to provide medical devices that can be available to a physician during medical investigation or patient for bedside treatment, biosensor technologies have to be low cost and amenable to miniaturisation. Therefore, a small and cheap off-the-shelf green light emitting diode (LED) was chosen as the light source. Figure 6.18 shows the experimental setup of a green LED with CMOS PD to measure light absorbance from an enzyme assay. For consistency, the optical light path between the LED and the chip was maintained at 5 cm for all experiments. Furthermore, the light path in the solution was also maintained the same by keeping the volume of the enzyme solution and also the size of the culture ring on top of the chip carrier (see Section 5.4.2) constant for all experiments. However, before commencing measurements of cholesterol levels on PD, the relationship between the optical characteristics of PD and the colorimetric product had to be determined and compared with commercially available green LED.

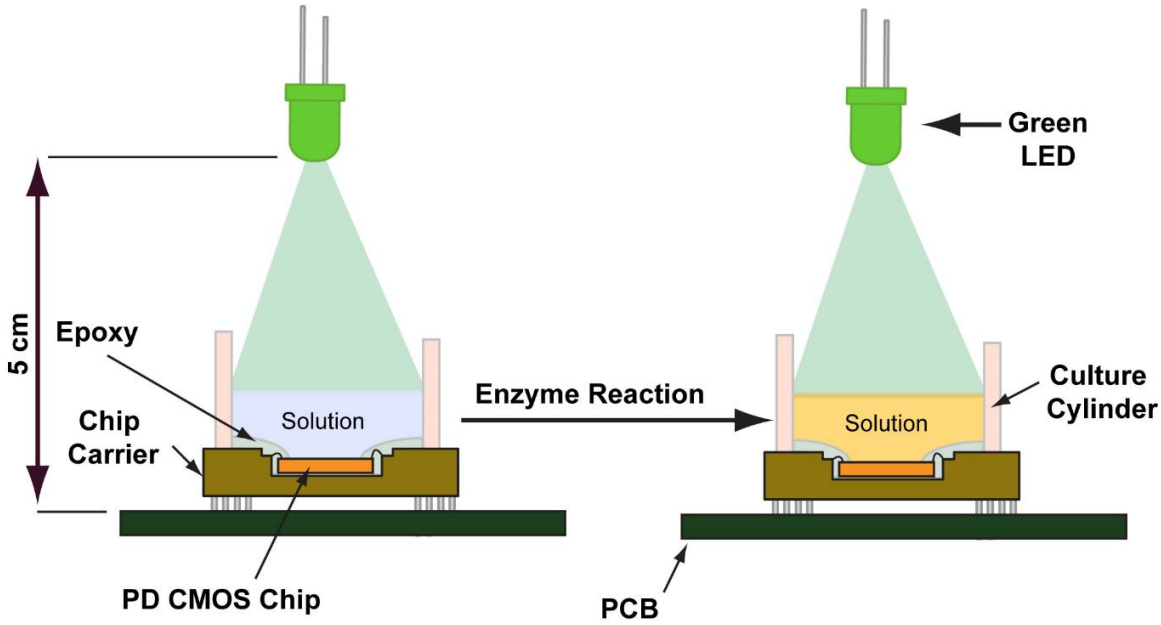

Figure 6.18 – Schematic diagram of the working principle of a colorimetric enzyme assay using PD on the Multi-Corder chip with LED illumination.

To evaluate the optical characteristics of the PD, a TMc300 monochromated light source (Benthem Instruments) was used and swept between 350 nm and 1000 nm in a dark environment. The output voltage of the light source was maintained at 11.5 V for every single wavelength. As can be seen in Figure 6.19, the spectral response produced from the PD (plot in black) has a maximum peak at 600 nm. This has shown that CMOS PD has varied sensitivity toward different wavelength of visible light. The next step was to investigate the spectrum of oxidised o-Dianisidine during cholesterol assay as a time course. A cholesterol reaction mix was prepared following the protocol as described above. Using a glass slide sample and attached with a cut test tube, all the reagents except the cholesterol oxidase was added and well mixed on top of the glass sample. A transmission measurement of the reaction mixture on top of the glass slide was performed using a TFProbe MSP300 spectrometer (Ångstrom Sun Technologies). The spectrometer was scanned between 350 nm and 1000 nm to obtain the absorbance spectrum of o-Dianisidine as a function of time. Using automated software, the spectrometer was obtaining the spectral response every five seconds. As can be seen in Figure 6.19, the first five traces of the o-Dianisidine maintained unchanged, which has zero adsorption at any wavelength. As soon as the cholesterol was added into the reaction cocktail and mixed it with a pipette for several times, the adsorption of the oxidised o-Dianisidine increases

monotonically with time until it reaches saturation. The oxidised o-Dianisidine absorbance spectrum was observed to have an absorption peak at 460 nm.

From both PD spectral response and oxidised o-Dianisidine absorbance spectrum when it comes to saturation, it can be seen that there is an overlap between these two traces, which is around 500 nm. Consequently based on this information, a green LED that has a peak spectrum close to 500 nm was chosen. Subsequently, a TFProbe MicroSpectrometer was used to measure the spectrum of the green LED to confirm its spectrum. As evident, the LED spectrum has a wavelength peak around 500 nm, which can be seen to coincide quite well at the overlap between the sensitivity of the PD and the absorbance spectrum of oxidised o-Dianisidine for the enzyme assay. Figure 6.19 illustrates the spectrums of o-Dianisidine, PD response and green LED, which are all plotted together.

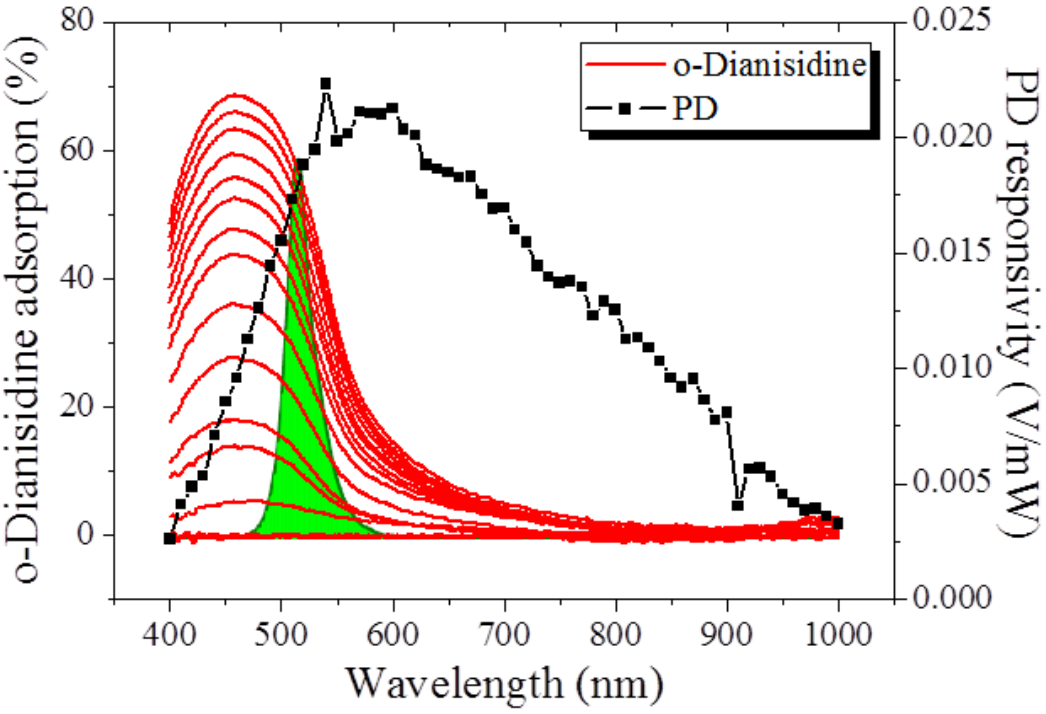

Figure 6.19 – The spectral response of the photodiode, the oxidised o-Dianisidine as a function of time during a cholesterol assay and a green LED.

In addition to optical evaluation, electrical evaluation of the photodiode array was also performed. As mentioned before, an increased in amount of ISFET sensors to be averaged is capable of reducing white noise and improve the output signal of the device. In the same way, the Multi-Corder chip also has an array of PD sensors, of which there are 256 sensors in total. The averaging

technique that was used in the ISFET array chip to reduce noise could be applied using the Multi-Corder chip as well. This could potentially be used to reduce noise as a function of $\sqrt{N}$, where N is the number of sensors. Figure 6.20 illustrates the data obtained from the PD using one single sensor and an average of all sensors for a low concentration of cholesterol. As evident, the signal obtained from one single sensor had a high level of noise which masked the signal, whereas the noise from an average of 256 sensors was much lower. Therefore, all the subsequent experiments were done and analysed using an average of the PD sensors with the same metabolite measurements.

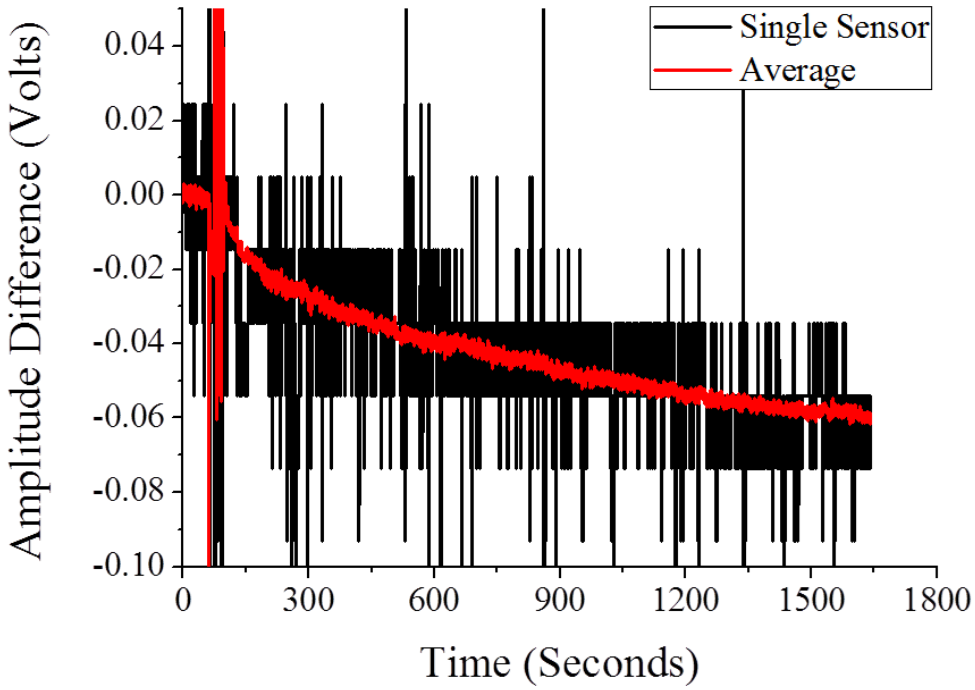

Figure 6.20 – The comparison of the absorbance levels obtained from the CMOS PD as voltage signal for one single sensor and an average of 256 sensors.

Using all the required reaction components and conditions that had been investigated using spectrophotometry, the reaction was tested on the Multi-Corder chip using the PD as the detector. The reagents were added to the chip in the same order as described above, with the serum being diluted to give four different cholesterol concentrations. This was followed by a pre-treatment with cholesterol esterase and then transferal of the reaction mix on top of PD with the addition of peroxidase and o-Dianisidine. The measurement was left for a base line of approximately 2 minutes before initiation with cholesterol oxidase. The serum supplied by Sigma Aldrich was evaluated by NHS to determine

cholesterol concentration and found to be 3500 μM. Hence, the final cholesterol concentrations in the diluted serum were 29 μM, 58 μM, 115 μM and 230 μM.

The initial measurement was done with the PD using a monochromated light source at 505 nm, with a linewidth of 5 nm. The reason of doing this was to replicate the exact same configuration of the spectrophotometer, which contains a charged coupled device (CCD) as a detector, diffraction gratings to obtain a monochromated light and a white light source. The intensity of the light source was adjusted, so that the voltage level from the PD was not too high to be saturated by the monochromated light or too low to be undetectable by the PD. This PD voltage level was chosen to be 1.8 V. The intensity of the light source was kept constant (11.5 V) throughout all the experiments for consistency. Three measurements for each cholesterol concentration were performed to check consistency and to extract the standard deviation of the measurements. A no-cholesterol oxidase negative control was also included.

The results obtained from the PD with a monochromated light source can be observed in Figure 6.21a. Subsequently, a green LED was used to replace the monochromated light source. The light intensity from the green LED was also adjusted to the same intensity level to give the same voltage signal on the PD as the monochromated light source, which was 1.8 V. The same cholesterol concentrations and negative control experiments were repeated. All the experiments were also repeated for three times for consistency and accuracy. Figure 6.21b illustrates the data obtained from PD with green LED illumination. In addition, the Figure 6.21 was further plotted into plateau PD voltage as a function of cholesterol concentration, since the reaction of cholesterol oxidase has come to saturation and remained constant at the voltage plateau, as shown in Figure 6.23 for both light sources. Hence, this plateau signal voltage is indirectly related to the concentration of cholesterol. As can be observed in Figure 6.22, both light sources could resolve a similar plateau PD voltage for the same cholesterol concentration and they have a straight-line dependency between 29 µM and 116 µM. Both plots deviate from the linear fitting at high concentration of cholesterol. This may due to the o-Dianisidine colour has come to a saturation point, where it can no longer change to a darker orange colour. Using the linear slope for both the plots, the sensitivity of the device was

determined to be 2.1 mV/μM and 2.2 mV/μM for both LED and monochromated light source, respectively.

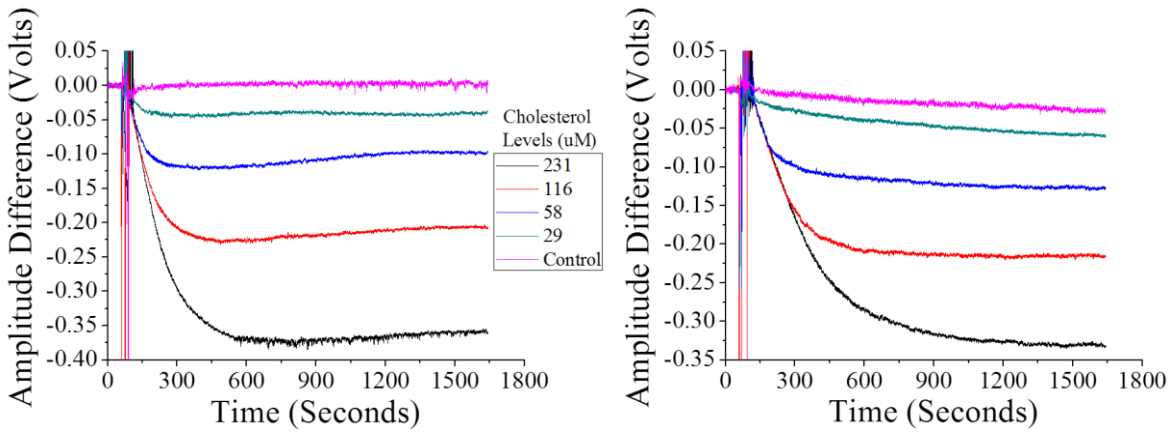

a) Monochromated light source **b) LED**

Figure 6.21 – Data obtained from the PD using Multi-Corder chip for different cholesterol serum dilutions.

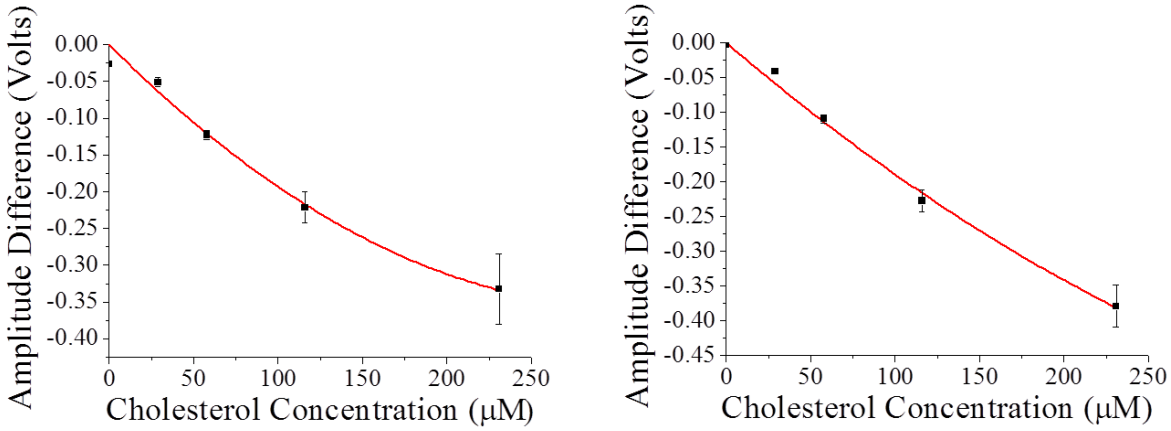

a) Monochromated light source **b) LED**

Figure 6.22 – The PD voltage plateau as a function of different cholesterol serum dilutions.

However, by observing the data from Figure 6.21, it was come to realise that the slope of the reaction is faster for the case of the monochromated light source compared to the slope of the reaction from the green LED and spectrophotometer, but the plateau from both was almost identical. The reason for this artefact was believed to due to the increment of temperature for the enzyme assay, as higher temperature increases enzyme reaction. Using an infrared camera, light spot of the LED and the monochromated light source shone on top of the PD array chip was evaluated. It was found that LED light spot has a temperature of 24.3°C while monochromated light source spot has a temperature of 29.2°C. Furthermore, the temperature condition of the

spectrophotometer was at 25°C. Hence, the monochromated light source that is available in our laboratory could produce a light spot that ultimately affects temperature, leading to a false reading. This has to be taken into account in the future experiments when doing enzyme assay that is sensitive to temperature changes. Regardless of this observation, monochromated light source measurement was not the main goal. The aim is to demonstrate the capability of using the above triple enzyme procedure to quantify the cholesterol levels in human serum using an inexpensive green LED and CMOS PD platform. From the experiments, it has shown that the inexpensive and miniaturised platform could replicate the measurements produced by a bench top spectrophotometer. Furthermore, the lowest concentration of cholesterol that was measured using this device configuration with LED light source is 150 times lower compare to the physiological range of cholesterol level in human serum, proving that this device has the capability for greater sensitivity applications. Moreover, using the data from Figure 6.22b, the limit of detection of the device can be calculated, by taking three times of the standard deviation of the blank control curve and divide by the sensitivity of the device [146], which equates to approximately 13 μM. Hence, a handheld diagnostic device based on this technology is proven to be feasible. This could ultimately be a miniaturised version of a spectrophotometer.

6.3.2 Enzyme Kinetics

As shown for ISFET enzyme kinetics, extracting the Michaelis-Menten constant could be calculated from the initial rate of a series of enzyme progress curves at different cholesterol concentrations with respect to time. Using the data obtained from the spectrophotometer, the PD with monochromated light source and the PD with LED illumination, a value of K_m for cholesterol oxidase was calculated and compared for each measurement technique. Hence, the extrapolated gradient during the first 60 seconds of the reaction was taken as the initial reaction rate, at different cholesterol concentration. Using GraphPad Prism, which has a built-in Michaelis-Menten algorithm, the initial velocity was plotted against each cholesterol concentration, using the data obtained from the spectrophotometer and PD sensors. Each of the plots was also plotted onto Lineweaver-Burk double reciprocal plot. The $1/K_m$ value can be obtained by

taking the interception of the line at the 1/[cholesterol] axis. Using this method, the K_m value for the spectrophotometer, the PD with monochromated light source and the PD with LED illumination, was obtained to be 40 ± 7 μM, 263 ± 95 μM and 80 ± 12 μM, respectively. Figure 6.23 shows all the initial velocity versus cholesterol concentration plots with its respectively Lineweaver-Burk double reciprocal plot for each measurement technique. The K_m value obtained from the spectrophotometer and the PD with LED illumination correlates well with each other. However, the PD with monochromated light source gave a higher K_m value, which may due to the sensitivity of colour change from o-Dianisidine towards such a narrowband light source. Nevertheless, this had further demonstrated that a low cost LED CMOS PD sensor array can be used as a POC diagnostic tool, with comparable results with conventional bench top spectrophotometer.

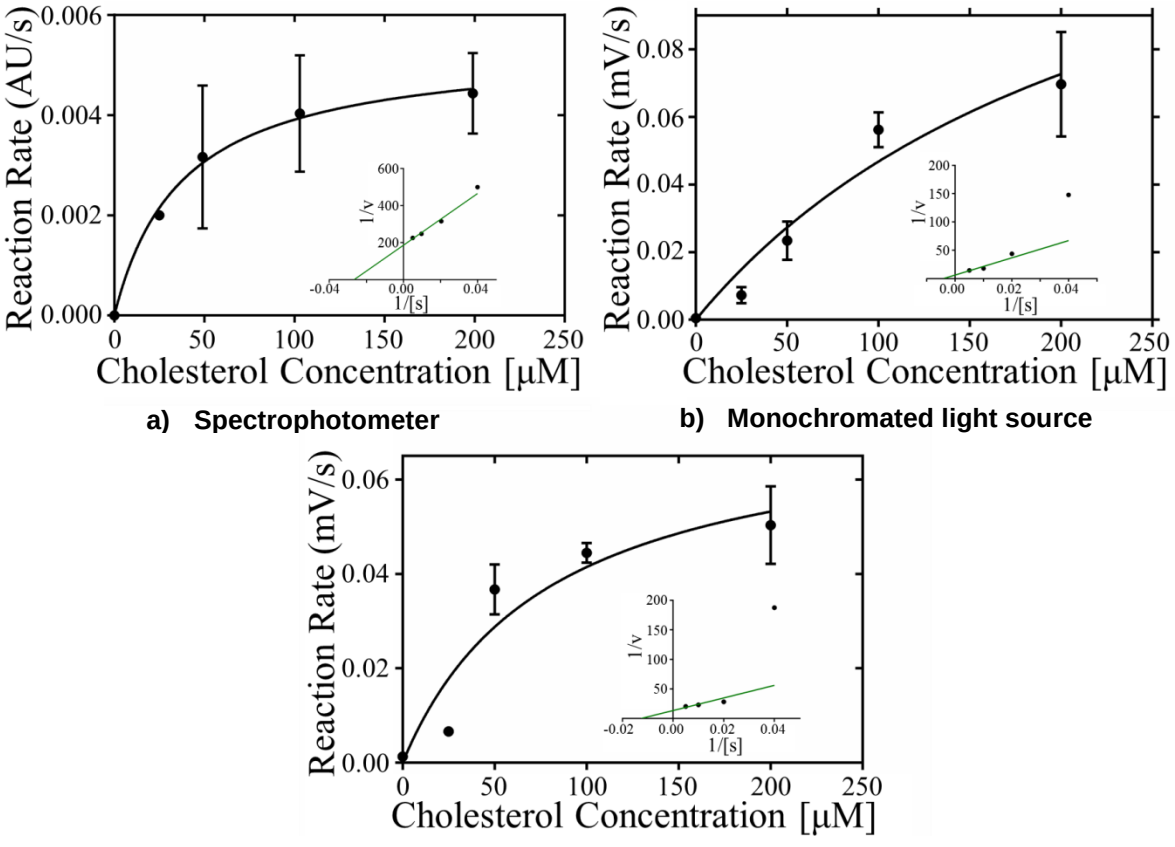

a) Spectrophotometer **b) Monochromated light source**

c) LED

Figure 6.23 – Data obtained from GraphPad Prism for K_m value extraction from all the individual techniques. [Results were analysed by Dr. ChunXiao Hu]

6.4 Summary

An example of a very minute amount of glucose was used to demonstrate that an array format can reduce the signal noise obtained from ISFET sensors. In addition, a buffer system was developed to improve the sensitivity of ISFET. This was then followed by the demonstration of ISFET sensors with the capability to quantify four different metabolites, those being glucose, pyruvate, urea and triglyceride. Each of these metabolites is linked to a number of different diseases. Moreover, the Michaelis-Menten constant was calculated using the data obtained from ISFET sensors for glucose and agreed very well with a conventional spectrophotometric method. Finally, the PD sensor array on the Multi-Corder chip was used to demonstrate cholesterol quantification in human serum. The quantification and Michaelis-Menten constant obtained from the PD sensor array was compared with spectrophotometric technique as well, and all the data agreed with each other. Since the CMOS chips had been demonstrated with the capability to quantify different metabolites, the next step will be integrating the CMOS sensor array with microfluidics and enzyme immobilisation techniques to demonstrate multiple metabolites measurement simultaneously, using one single chip.

Chapter 7 : Enzyme Immobilisation with Microfluidics Integration for Metabolite Sensing on Chip

7.1 Introduction

The previous chapter focused on the development of enzyme assays to quantify different metabolites on a CMOS ISFET and PD. This chapter describes the enzyme immobilisation technique used on top of a CMOS chip and also demonstrates working microfluidic channels fabricated on top of a CMOS chip. Finally, the complete system is then used to measure a metabolite with a specific enzyme assay.

7.2 Enzyme Immobilisation

As discussed in Section 2.3, a 2D microarray is important to allow simultaneous metabolite measurements on chip. Immobilisation of the enzyme onto the solid surface of the CMOS chip is a critical step. The matrix support used in immobilisation should be affordable, stable, chemically inert, reusable and should not interfere with enzyme activity. In the first instance, the bead arrays immobilisation technique used in an Ion Torrent chip was replicated in this work. Initially, sepharose beads (45 - 165 μm in diameter) were first used to immobilise the enzyme, in conjunction with an etching step on the surface of the CMOS chip to form a microwell to accommodate an enzyme bead. However, it was found that the immobilisation protocol was very complicated and involving numerous steps. Moreover, it was also realised that the surface topography on top of the ISFET array chip has a few trenches (1 μm wide and 400 nm deep) for each sensor pixel, which could act as microwells to accommodate enzyme beads. The trenches formed from the topography of the

chip can be seen in Figure 7.1a. It was therefore thought to take advantage of these trenches to eliminate the need to etch the surface of the CMOS chip to create microwells. Regardless, measurements were made using hexokinase sepharose beads with glucose as illustrated in Figure 7.1b but the results were difficult to interpret. This was then followed by the use of silica mesoporous nanobeads (200 nm in diameter) that are small enough to be placed into the microwells formed from the topography of the chip. However, it was found that the enzyme beads did not produce an observable signal from the ISFET. Furthermore, after the enzyme beads were used to fill up the surface topography of the ISFET chip, the chip was also not responding to any hydrogen ion concentration changes. The reason may be due to the overcrowding of the nanobeads on top of the surface of the chip, creating a hydrophobic environment. This could stop any hydrogen ions from penetrating through the nanobeads layer and interact with the sensing layer on top of the ISFET gate to produce a voltage signal. Due to all the complications faced from microwell bead array, this idea was therefore abandoned.

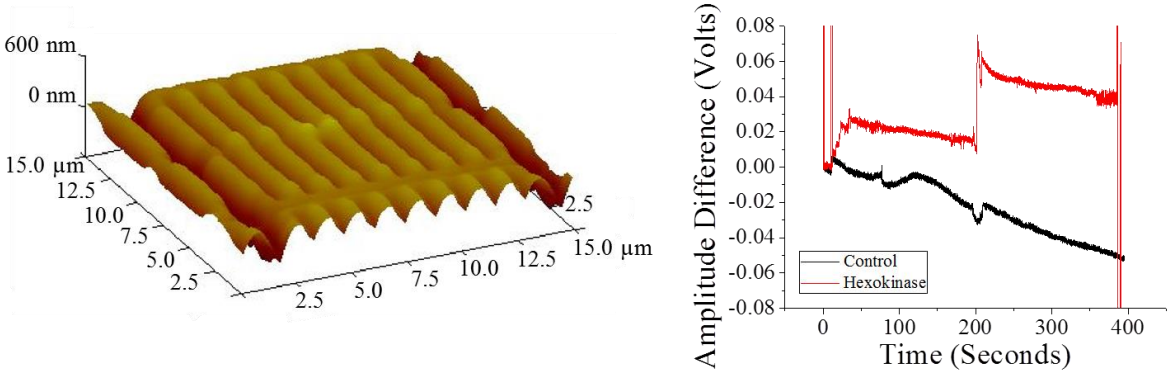

a) AFM image of a single ISFET pixel **b) Data obtained from an ISFET**

Figure 7.1 – AFM image showing trenches of a single ISFET pixel for nanobeads accommodation and also the data obtained from ISFET using sepharose bead hexokinase.

At a later stage, alginate gel immobilisation of enzymes using a 2D inkjet printing technique was used, as described in Section 2.3.1. Alginate, derived from brown algae, is a complex carbohydrate (polysaccharide) that polymerises in the presence of divalent cations such as calcium ions [188], [189]. Alginate is cheap to source and droplets can be easily prepared by dropping a defined volume of sodium alginate/enzyme solution into a $CaCl_2$ solution. In this process, sodium ions are displaced by calcium ions, rapidly forming a polymerised gel. Generally 10 μl droplets are added to $CaCl_2$ solution to form a single bead with a

defined number of enzyme units entrapped. Although easy to prepare, there are a number of caveats that must be addressed, most notably the possibility of enzyme leaching and the preclusion of the substrate into the gel. These conditions can be controlled by varying the gel percentage of the alginate. Alginate beads are stable and compatible with triethanolamine buffer, making them an attractive method for immobilisation.

In order to test the efficacy of enzymes entrapped in alginate before using the 2D inkjet printer, lactate dehydrogenase (LDH) and hexokinase were used to form alginate beads to be measured using the ISFET array chip. To do this, 1.5% sodium alginate solution was made up in the triethanolamine buffer and then mixed with a defined amount of enzyme to give a 1% final concentration of sodium alginate. The final amounts of enzyme in 1% sodium alginate were as follows: 0.05 U/μl LDH and 0.2 U/μl hexokinase. Sequentially, 10 μl drops of enzyme-alginate mix were then dropped from a height of approximately 5 cm into a vial of 0.2 M $CaCl_2$, upon which beads of enzyme entrapped in calcium alginate were rapidly formed. Beads were washed in triethanolamine buffer prior to assay. For each reaction, 5 Units of LDH and 10 Units of hexokinase were used respectively. Slightly different from the experiments explained in Chapter 6, the reaction was initiated with sodium pyruvate for the LDH assay and ATP solution for the hexokinase assay, rather than using the enzyme as initiation, since the enzyme was already immobilised in alginate beads. In addition, negative control beads were also made up without any enzyme entrapped in it, consisting of only buffer solution in alginate solution. Figure 7.2 illustrates the results obtained from an ISFET array chip for both a LDH and a hexokinase assay. As can be seen from Figure 7.2a, when there were LDH beads in the solution, the pH increased and decreased the voltage signal of ISFET, whereas when blank beads were used, there was no change in voltage signal from the ISFET. Similar to the LDH assay, Figure 7.2b shows that when there were hexokinase beads in the solution, the ISFET will detect a change in the voltage signal while the voltage signal stays unchanged if only blank beads were used. This demonstrated that the hexokinase or LDH in this concentration of alginate solution was sufficient to entrap the enzyme and also produce a measureable signal for the ISFET sensor.

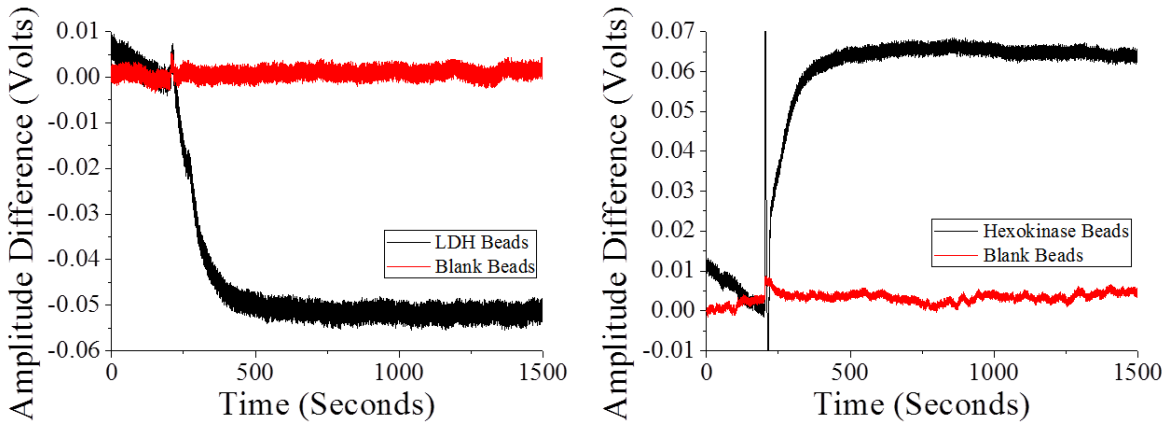

a) LDH assay **b) Hexokinase assay**

Figure 7.2 – Data obtained from ISFET for LDH and hexokinase alginate beads assay.

Instead of using a pipette to put down the droplet of enzyme alginate solution and form a bead in $CaCl_2$, a Jetlab II 2D inkjet printer was used, as shown in Figure 7.3. The 2D printer was used to print the $CaCl_2$ and then print the alginate containing enzyme to form a well-defined gel on top of the surface. As shown, the 2D printer is a very sophisticated tool which consists of a printing stage, a fluid reservoir, two cameras (vertical and horizontal), an air compressor, a vacuum pump and a dispenser print head [190]. The printing stage, controlled by a computer, can move in horizontal x and y directions. The fluid reservoir is used to contain the printing fluid with a maximum capacity of around 1.5 ml. The vertical camera is used to observe the printed droplets, whereas the horizontal camera is used to inspect the droplet formation at the tip of the print head. An air compressor is used as a pressure source (compressed air) to supply to the reservoir, in order to push the liquid through the tube that is connected to the dispenser print head. The air compressor is set to give a pressure of 4 bar. A control panel on the printer is used to change the pressure in between 0 to 400 in arbitrary units. The vacuum pump is required as a mean to switch between vacuum and pressure to the reservoir, in order to get the optimal pressure for printing. A control panel is also used to change the vacuum pressure in the range of 0 to -400 in arbitrary units. The optimal pressure required for printing (normally ranging from -14 to 20 in arbitrary units) is when the fluid is idled at the tip of the print head.

Figure 7.3 – A photograph showing the Jetlab II 2D inkjet printer [190].

The most important component of the 2D printer is the dispenser print head, which is made of glass. It consists of a ring-shaped piezoelectric actuator that is bonded to the glass capillary tube, which is connected to a fluid supply (reservoir) at one end, and an opening (30 – 60 μm) at the other end to dispense the fluid. By applying voltage to the actuator, the cross-section of the glass tube is reduced or increased, causing pressure variations of the fluid in the glass tube. These pressure variations are propagated in the glass capillary towards the opening of the glass tube. If a sudden change happens in the cross-section of the opening of the glass capillary tube, a droplet will be formed. In order to print multiple droplets, normally a sinusoidal voltage waveform is applied to the actuator.

In order to control the dispenser print head, the computer is used to drive the actuator with a waveform, as shown in Figure 7.4. The driving actuator parameters are t_{rise} = initial rise time, t_{dwell} = time at high voltage V_1 (dwell voltage), t_{fall} = transition time from high voltage to low voltage, t_{echo} = time at low voltage V_2 (echo voltage), and t_{frise} = final rise time. The voltage V_0 (idle voltage) generally is set to zero, while V_1 and V_2 have the same amplitude but with opposite phase. Normally, the rise and fall time is short, which is around 2 – 3 μs. The dwell time is typically in the range of 15 to 35 μs, and the echo time is normally twice the dwell time. The first half of the waveform (solid line) is used to form a droplet and dispense it, whereas the second half of the waveform (dotted line) is used to produce a clean break-off of the droplet from the tip of the print head. The droplet size is proportional to the dwell time t_{dwell} and voltages V_1 and V_2. Hence, in order to print a desired droplet size (normally ranging from 50 pl to 200 pl), all these parameters have to be well controlled.

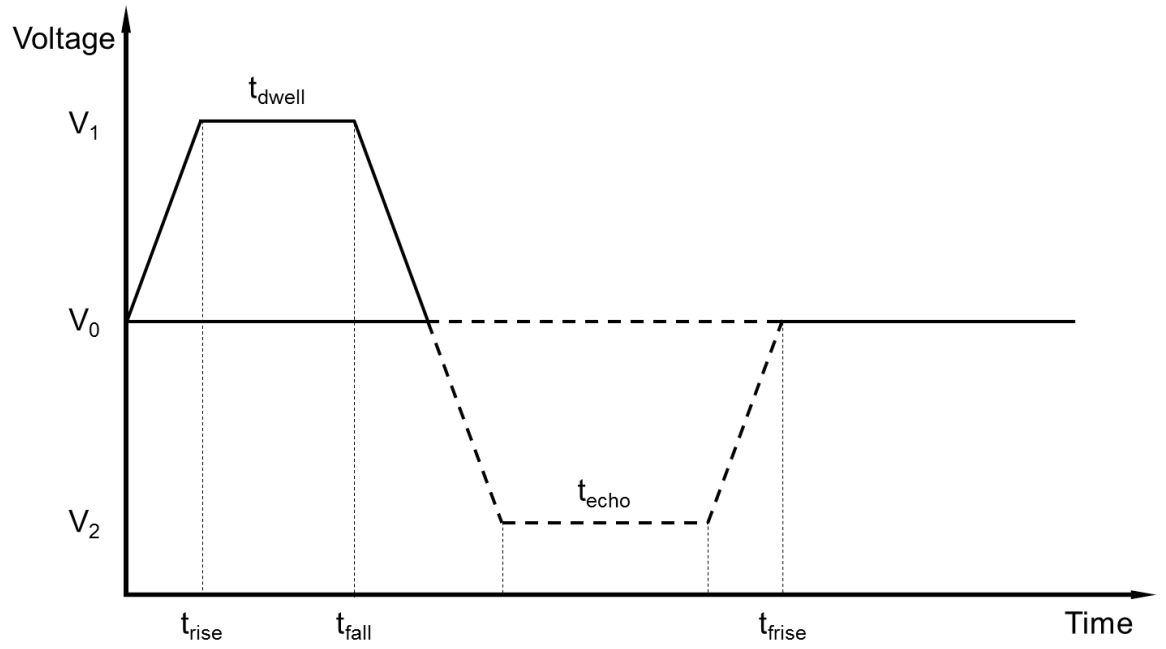

Figure 7.4 – The driving waveform for the piezoelectric actuator at the print head.

The process of printing was straightforward. First, 1.5 ml of the enzyme alginate solution or any fluid was filled into the reservoir connected to the printer. It was then followed by an investigation step to produce a desired droplet size. This was done by varying the actuator driving parameters (voltages and timings) and the required idle pressure (air compressor and vacuum pump), in order to form a nice droplet at the tip of the print head. One important thing to note was that the amount of solution that was required to be loaded into the reservoir must be greater or equal to 0.5 ml in volume, in order to obtain a good pressure for a decent droplet formation. The reason is because of the connection of the tube between the air compressor and the reservoir does not go all the way down to the bottom of the reservoir. When the desired droplet size and smooth printing are obtained, the solution can be readily printed onto the surface of the sample. Using this printer technique, multiple droplets can be printed in an array format on the surface of the chip in each microfluidic channels, leading to multiple enzyme assays. As can be seen from Figure 7.5a, an array of droplets with well-defined size and pitch size was successfully printed, demonstrating the technique's capability. Furthermore, the process of gelation of enzyme entrapped in alginate was also successfully printed on a silicon nitride coated substrate, demonstrating a good adhesion to the surface, this can be seen from Figure 7.5b. The droplet can be removed with ultra-sonication in a phosphate buffer solution.

The viscosity of the alginate solution, however, can increase the difficulty to perform a successful printing. The printer can only print fluids with a viscosity lower than 40 cP. The “thick” nature of the alginate solution clogged the printer nozzle very often, which required several hours of refinement to print a decent droplet. Therefore, a 1% final concentration of alginate enzyme solution (4 – 12 cP) was selected in order to create a successful printing and also to be able to entrap the enzyme. In addition, after the droplet was refined for a specific enzyme alginate solution, it had to be printed immediately before the alginate solution would accumulate and clog the printer nozzle.

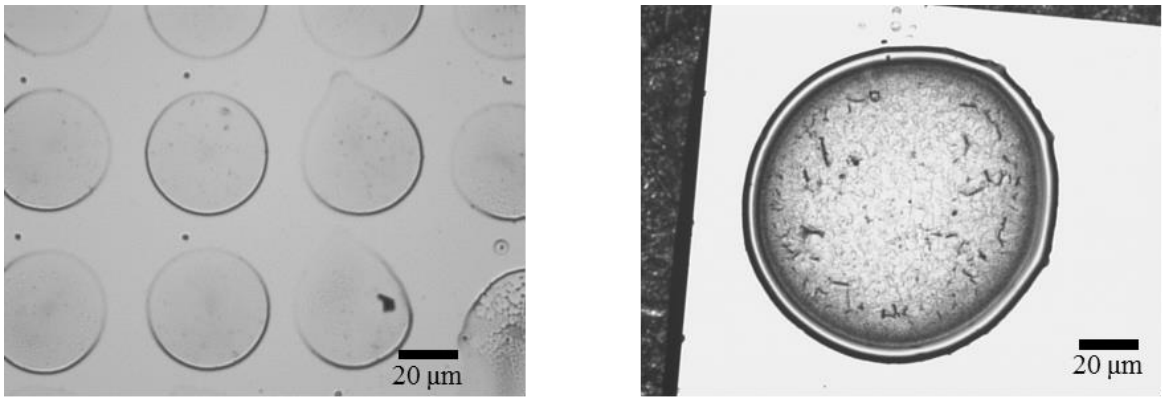

a) Array printing **b) Enzyme alginate printing**

Figure 7.5 – Optical microphotograph showing the printing of an array of droplets, and enzyme alginate gel printed on a silicon nitride coated substrate.

The printed alginate enzyme gel on the surface of the chip was tested and validated to make sure that the enzyme was still active after going through the printing procedure and also to make sure that it was detectable using the ISFET array chip. To do this, a small droplet of $CaCl_2$ solution was pipetted on top of the CMOS chip, enough to cover the whole surface of the sensor array. Refinement of both the $CaCl_2$ and enzyme alginate solution to be simultaneously printed normally takes a long time, thus $CaCl_2$ solution was pipetted to test the enzyme alginate immobilisation. The same enzyme alginate solution used to form the enzyme beads was used to print. The same amount of enzyme was printed in one go to reach the same concentration that was obtained using the enzyme alginate beads. After the printing, the excess $CaCl_2$ solution was cleaned with triethanolamine buffer and immediately all the substrate required for the enzyme assay was added to the chip except the initiation solution. As before,

the chip acquired a baseline of approximately 3 minutes and was followed by the initiation solution to trigger the enzyme assay.

As can be seen from Figure 7.6a, the printed droplet enzyme alginate gel was very big, covering the whole surface of the chip to produce the number of Units of enzyme similar to that obtained from enzyme alginate bead. This experiment was performed to determine if the printed enzyme was still active after the printing process, thus the droplet size was not a concern. However, a more concentrated enzyme alginate solution was later prepared for subsequent experiments to reduce the number of droplets required to print, with the downside that it is very expensive to prepare a highly concentrated enzyme alginate solution in 1.5 ml. Since there were no microfluidic channels on top of the chip, there was no segregation of the chip into multiple compartments to present multiple enzyme assays, all the sensors in the array therefore read the same assay. From Figure 7.6b, it can be seen that hexokinase was selected to be printed on top of the CMOS ISFET chip and the activity of hexokinase with glucose concentration of 23.1 mM was measured. It can be noticed that the signal obtained from the hexokinase assay from two separate prints was very alike, proving the repeatability of the printing process. A negative control with a triethanolamine buffer alginate solution was printed on the surface of the CMOS chip to form a blank gel. No signal was observed from the chip for the enzyme assays with the blank gel. Another negative control was done by removing glucose from the reaction with the result, as expected, of no change in ISFET response. These negative controls demonstrated that the assay was a direct result of the hexokinase reaction. Hence, this had proven that alginate gel immobilisation of enzymes using a 2D inkjet printing is a viable technique to perform enzyme assays.

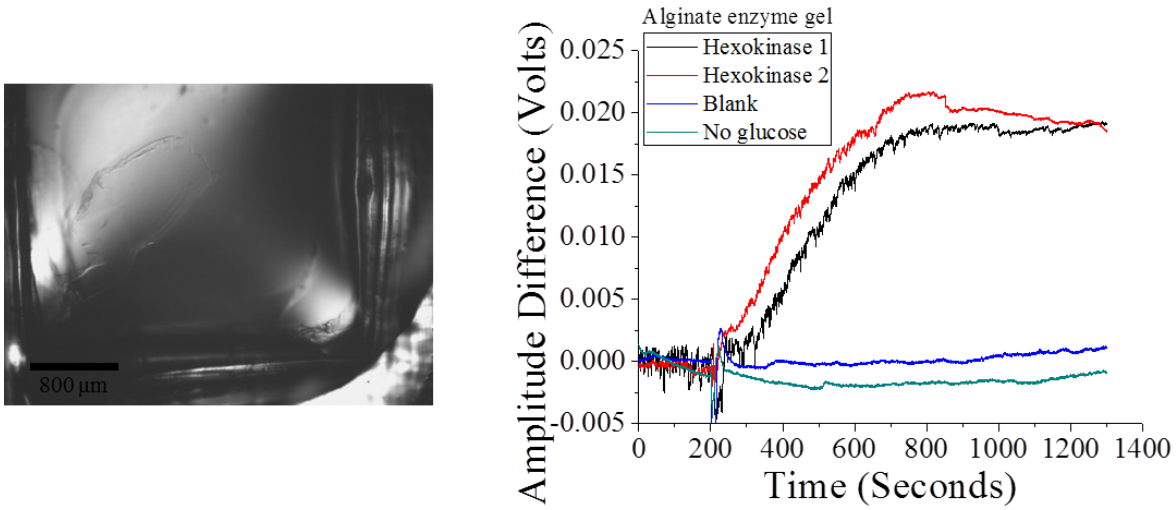

Figure 7.6 – Optical micrograph showing enzyme alginate gel printed on top of a CMOS chip and the data obtained from ISFET for enzyme alginate gel and control experiments.

7.3 Microfluidics

After demonstrating that the 2D inkjet printer can be used to immobilise enzymes on the surface of a CMOS chip, leading to a detection of substrate that is specific to the enzyme, the segregation of the chip into different compartments for multiple enzyme assays had to be validated. As discussed in Section 5.3, the microfluidic channels were fabricated using SU-8 negative photoresist on top of a CMOS chip. The CMOS chip was then wire bonded and encapsulated with epoxy, without compromising the channels, and finally the channels were covered with an adhesive film for complete isolation. In Section 5.3.3, the microfluidic channels were evaluated using an optical microscope to ensure that the liquid could flow into the channels without any obstruction and also verify the channels are well isolated from each other. However, this evaluation was done on a silicon substrate that has a different topography from a CMOS chip. In this section, the microfluidics will be evaluated again but using the sensor array in the CMOS chip as a "camera" and also having the SU-8 microfluidic channels on top of the sensor array.

As mentioned before in Section 4.3, the ISFET array chip has bond pads on each side of the chip, which does not leave any room for inlet and outlet ports for liquid to be injected or ejected. However, SU-8 microfluidic channels were still fabricated onto the ISFET array chip to be inspected. Since the resolution of the ISFET array chip (11.2 μm – the sensor pixel pitch size) is smaller compared to

the Multi-Corder chip (100 μm pitch size), the fluid flow in the channels can be observed using ISFET array chip. To be reminded of how the chip will look like after packaging and encapsulation, this is shown in Figure 7.7. The encapsulation epoxy formed a square cavity on top of the sensor array and there was no space to introduce the liquid. Several attempts had to be tried to inject some buffer solution at one end of the chip to allow the liquid to flow in. This was observed to be a major flaw due to the inconsistent flow of liquid into the channels. In spite of that, the buffer solution started to flow into the SU-8 channels after several attempts, proving that the SU-8 channels with the adhesive film is a viable technique to be used on a CMOS chip to separate the enzymes into different spatial locations, enabling simultaneous measurements of enzyme assays without cross-contamination. Using the high resolution ISFET array chip, images of the fluid flow in the SU-8 channels were taken, as shown in Figure 7.8.

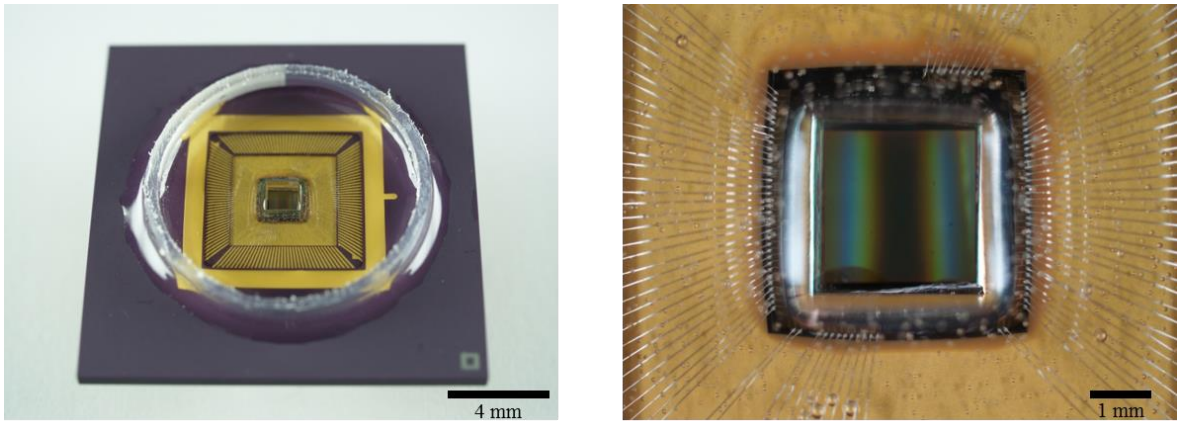

a) Side view **b) Top view**

Figure 7.7 – Optical image of the 256×256-pixel ISFET array chip with packaging and encapsulation.

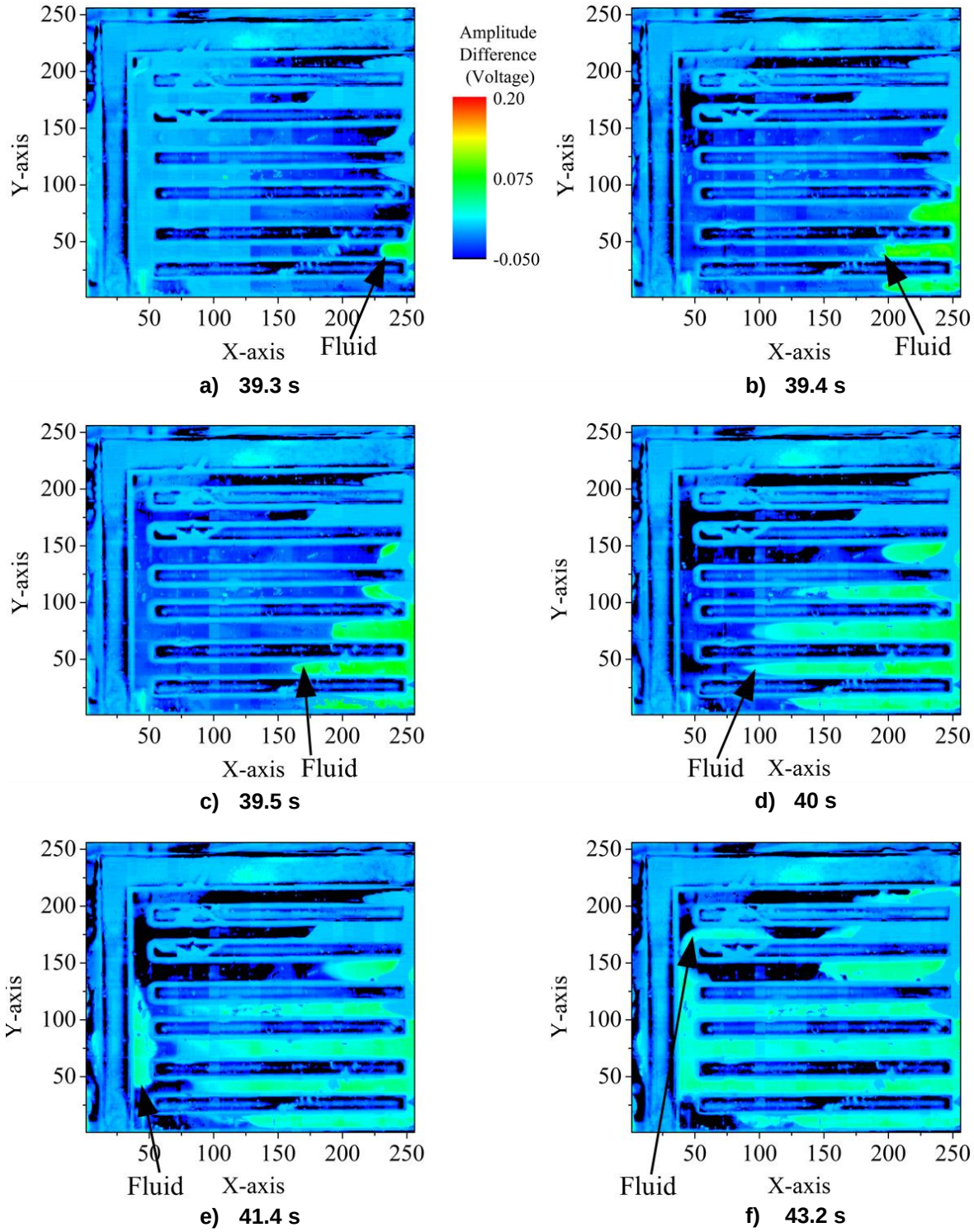

Figure 7.8 – 2D imaging of proton distributions over the 256×256-pixel ISFET array chip to visualise the fluid flow event across the SU-8 microfluidic channels.

7.4 Integration and Characterisation

Section 7.2 demonstrates that alginate enzyme immobilisation with 2D inkjet is a viable technique to perform enzyme assays, and Section 7.3 shows that SU-8 microfluidic channels on a CMOS chip provide good segregation and isolation. Hence, the final step is to integrate the immobilisation technique with microfluidics to perform multiple enzyme assays simultaneously, on one single chip. To integrate microfluidics and the immobilisation of the alginate enzyme gel, the adhesive film (top lid) was left out in the beginning to allow printing. After the printing, the top lid was immediately introduced on top of the channels, providing isolation. Since the ISFET array chip does not have any openings to introduce liquid with ease, the Multi-Corder chip was used because it only has two sides with bond pads and wire bonds. As can be seen from Figure 7.9, the encapsulation and packaging of the chip left two openings to allow liquid to be introduced easily into the channels. However, as mentioned in Section 6.3, the ISFET sensor did not work in the Multi-Corder chip, thus the PD sensor was used as the sensor to detect cholesterol oxidase assay, with microfluidics and alginate enzyme immobilisation. Since the ISFET sensor can be used to detect enzyme assays immobilised in alginate gel, it was believed that PD could also be used for enzyme assays entrapped in alginate gel. In addition, a cholesterol assay in solution had also been validated using the PD sensor (presented in Section 6.3), thus there were no reason to believe that it should not work in alginate.

In Section 6.3, a PD was used to demonstrate cholesterol quantification. Therefore, in this experiment, cholesterol oxidase with alginate solution was printed in the channel, followed by the introduction of $CaCl_2$ on top of the Multi-Corder chip for the gel formation. Then, the chip was gently cleaned with triethanolmine buffer to remove any excess $CaCl_2$ solution. This was then followed by the introduction of the adhesive film as the top lid of the SU-8 channels. The chip was inserted into the experimental setup and all the required reagents were introduced at one end of the SU-8 channels without any delay. The capillary force from the channels drags the reagents towards the sensor array, triggering the cholesterol oxidase assay. It is important to note that the top lid and reagents were introduced without delay (after the printing), in order

to preserve the enzyme activity. As the gel droplet was very small, evaporation may occur and hamper the enzyme activity.

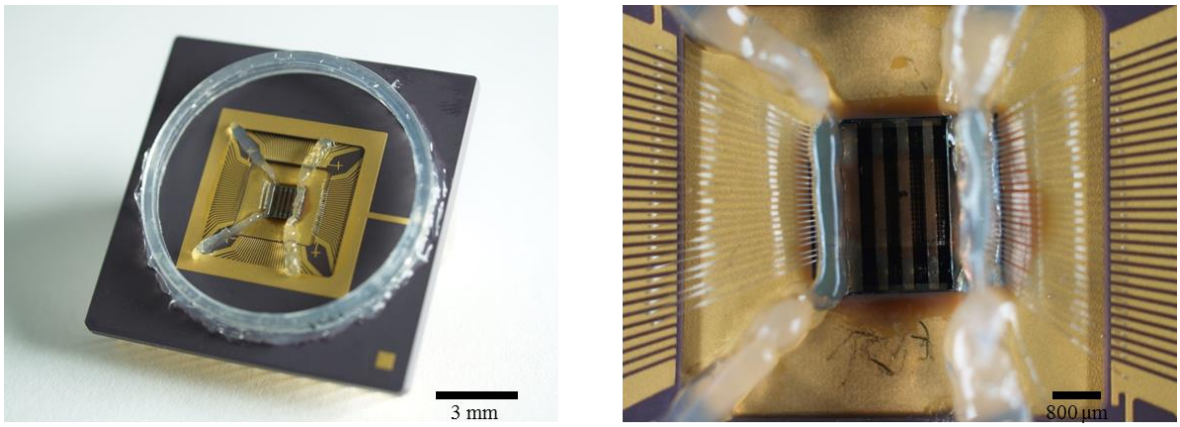

a) Side view **b) Top view**

Figure 7.9 – Optical image of Multi-Corder chip with packaging and encapsulation.

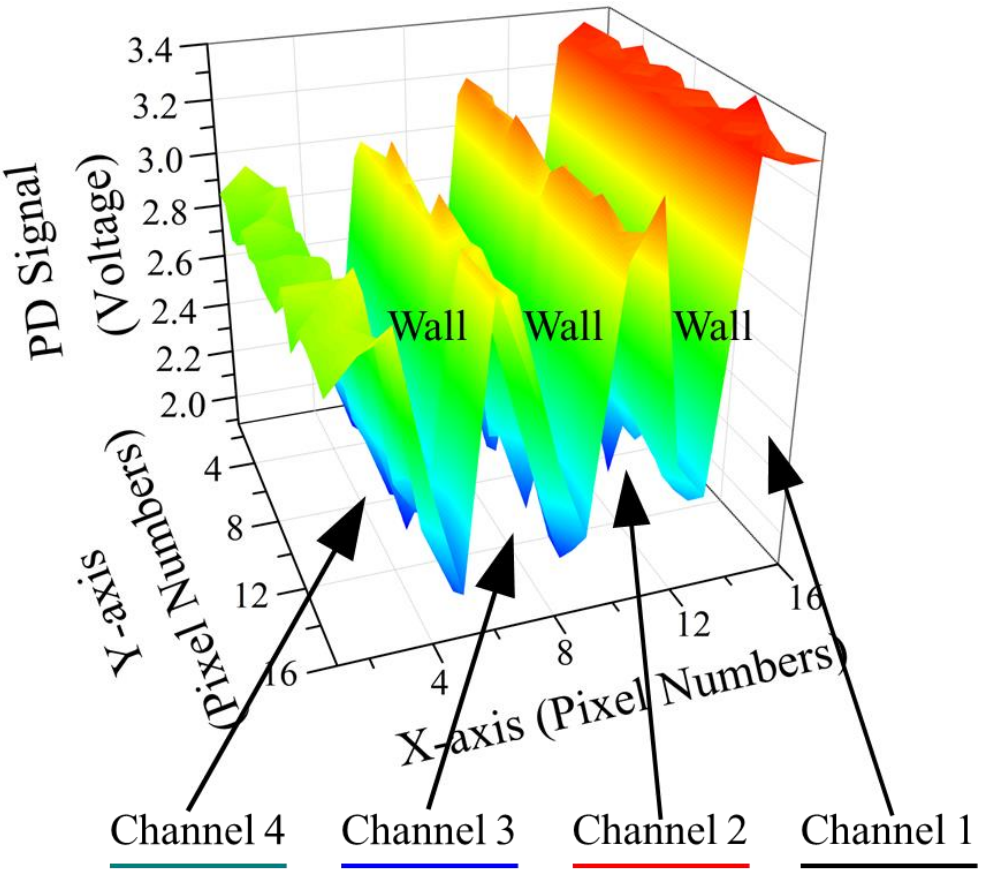

Figure 7.10 – 3D representative image of the SU-8 channels obtained from PD sensor array, with channel 1 to 4 is labelled as black, red, blue and cyan, respectively.

In Figure 7.10, the CMOS PD array was used to take a 3D representative image of the SU-8 channels fabricated on top of the chip. As can be seen, the PD signal is lower when the LED light is shining through the SU-8 resist wall on top of the

sensors, whereas the PD signal is higher when the LED light is shining straight on top of the sensor. It can be clearly observed that, there are three walls made up of SU-8 resist and four channels. A shadowing effect was occurring on top of the channels depending on how the LED light was shone on top of the PD. Some channels may have stronger PD signal than others due to this shadowing. Therefore, every time the enzyme assay was taken, a reference data was obtained in order to differentiate the change of PD signal. To better understand the following results, each of the channels was labelled from one to four with different colours, which were black, red, blue and cyan, respectively.

As can be seen from Figure 7.11a, 10k droplets and 5k droplets (ranging from 100 to 400 pl/droplet) of cholesterol oxidase alginate solution (0.0067 Units/μl) were printed on channel 1 and channel 2, respectively. Channels 3 and 4 were left blank to act as a negative control. A difference in magnitude of PD signal was observed when channels 1 and 2 were printed with different concentrations of cholesterol oxidase. In addition, channels 3 and 4 did not give rise to any signal, as was expected. A second experiment was performed in a reverse order to better interpret the results. This time, channel 1 was left blank as the negative control, whereas channels 2, 3 and 4 were printed with cholesterol oxidase alginate solution with 500 droplets, 1k droplets and 10k droplets, respectively. As can be seen from Figure 7.11b, the 10k droplets in channel 4 gave a signal change, with a similar response to the first experiment. At the same time, channel 1 gave no signal from the PD, which was expected from a negative control. However, channels 2 and 3 gave a small signal, which was barely distinguishable from the negative control. A lot more repeatable experiments have to be done to fully understand the working mechanism of the integration of microfluidics with alginate enzyme gel immobilisation on top of a CMOS chip to quantify metabolites. An optimised level of enzyme droplets to be printed has to be obtained and follow by doing measurements with different metabolites concentration in different channels to obtain variable electrical signals. By understanding having control experiments in one channel and varying different metabolites in other channels with the same printed enzyme, we can proceed to have more than one enzyme assay. Nevertheless, these preliminary experiments had demonstrated an important first step in understanding the integration of microfluidics and enzyme alginate gel immobilisation on a single

chip to run multiple enzyme assays for different metabolites quantification, leading towards a personal metabolome machine.

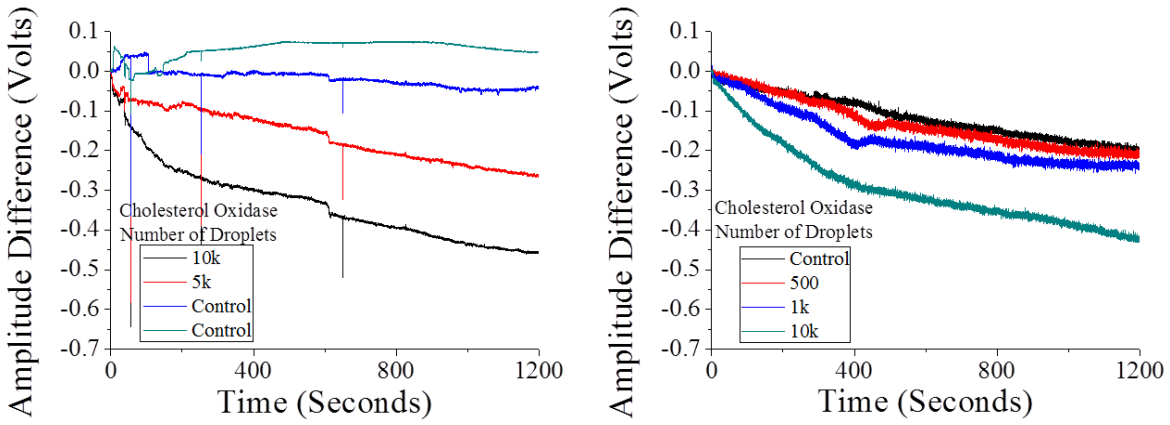

a) First attempt **b) Second attempt**

Figure 7.11 – Data obtained from PD sensor array with SU-8 channels for different cholesterol oxidase concentrations and control experiments. Channels 1 to 4 are labelled as black, red, blue and cyan, respectively.

7.5 Summary

In this chapter, a complete metabolome measurement system was realised by enzyme immobilisation and integrating microfluidic channels on top of a 16×16-pixel Multi-Corder chip. For enzyme immobilisation, alginate gel was used to entrap the enzyme and a state-of-the-art 2D inkjet printer was used to immobilise the enzyme alginate gel on the surface of the CMOS chip. SU-8 microfluidic channels were fabricated on top of a CMOS chip to image the flow of liquid, in order to prove good isolation of the channels. A cholesterol assay was then carried out with the immobilisation technique and microfluidic channels to demonstrate negative and positive control experiments, which were measured simultaneously. In the next and final chapter, a summary of the conclusions from the research will be given along with some future work.

Chapter 8 : Conclusion

8.1 Introduction

The previous chapter described how to integrate SU-8 microfluidic channels and entrapped alginate enzyme gel using a 2D inkjet printer into a complete system, in order to demonstrate metabolite detection and a control measurement simultaneously. This system has the potential to be used as a multi-enzyme platform for detection of different metabolites. This chapter concludes the research work and provides some potential suggestions for future work.

8.2 Final Analysis

Metabolites are the tiny molecules of life. Healthy metabolite levels are fundamental to our wellbeing and the collection of all these molecules makes up the metabolome. In the same way that pioneering technologies unravelled the personal genome for less than a thousand dollars and in just one day, it is also necessary to develop a technology to provide everyone their own metabolome. This technology will ultimately revolutionise diagnostics and delivery of precision healthcare worldwide. The purpose of this study focussed on developing an integrated CMOS sensor array technology as a single platform, while integrating microfluidics and bio-functionalisation techniques, to produce a portable multi-metabolite detection machine. The main achievements of this work are reported as follows:

- Two CMOS sensor array chips, a 256×256-pixel ISFET array chip and a 16×16-pixel Multi-Corder chip were fully understood. A high-speed instrumentation system was developed for the ISFET array chip. As the work progressed, a miniaturised version of the instrumentation system was developed for Multi-Corder chip, with the idea of making it portable and compatible with a portable electronic device such as a laptop.

- A lot of the work involves chemical and biological experiments, which have to be introduced in an aqueous solution. Therefore, a biocompatible,

robust and water-tight packaging technique was developed to encapsulate all the electrical connections from the aqueous environment.

- A fabrication process was developed using room temperature sputtering and a lift-off technique to deposit Ta_2O_5 film on top of a CMOS ISFET to improve sensitivity to hydrogen ion concentration, drift and robustness of the sensor performance.

- Several enzyme assays were investigated, measured and analysed using an ISFET array chip for hydrogen ion measurement and using PD array on the Muti-Corder chip for colorimetric light absorbance detection.

- SU-8 microfluidic channels were fabricated on top of the CMOS chips and the isolation of each channel and fluid flow in the channels demonstrated.

- Different enzyme immobilisation techniques were explored. The suitable technique was to entrap the enzyme in alginate and print it onto the surface of the CMOS chip using a 2D inkjet printer. This immobilisation technique had been demonstrated to be able to use on top of the CMOS chips and the enzyme assay signals were able to be detected by the CMOS sensor.

- A complete system was constructed by integrating SU-8 microfluidic channels and alginate enzyme entrapment using 2D inkjet printer on a CMOS platform. A first demonstration of a single enzyme assay and control experiments simultaneously performed on a single CMOS chip was presented. Further work still required to demonstrate multi-metabolite measurement on a single CMOS chip.

The following sections will summarise the major findings of the complete system and some significant problems that were encountered along the course of the research work.

8.2.1 Instrumentation Systems

The 256×256-pixel ISFET array chip was designed by Dr. Balazs Nemeth and provided to me. The sensor pixel design and readout architecture of the 256×256-pixel ISFET array chip was understood to begin with. Since the array size of the chip is very big, it was decided to construct a high-speed instrumentation system. It comprises a desktop computer, four PXI-Express-6538 X series acquisition cards in a PXI-Express-1073 chassis (National Instruments), a PCB and a fully packaged ISFET array chip. The whole system was controlled by a software package, LabVIEW, to acquire 64 analogue outputs from the chip and to provide 10-bit digital addresses to the chip. It has the capability to read one sensor pixel at a maximum speed of 2 µs/pixel. Hence, the maximum readout speed for the entire array (all 65,536 pixels) is 2.048 milliseconds for one frame, equating to approximately 500 frames per second. Using LabVIEW, 2D and 3D representation imaging can be obtained, as well as single pixel analysis.

Two thirds of the way through the research work, a second chip was designed by Dr. Mohammed Al-Rawhani, which was the 16×16-pixel Multi-Corder chip. Similar to ISFET array chip, the design and readout architecture of the chip was understood. This chip contains three different sensors, which are ISFET, PD and SPAD. The number of pixels on this chip is only 256, thus a high-speed acquisition system was not required. Moreover, the idea of creating a portable device and low cost diagnostic tool was in mind. Therefore, a low cost and miniaturised instrumentation system was constructed. This system comprised a laptop, one ARM mbed Integrated Development Environment STM32 Nucleo-F334R8 board (STMicroelectronics), a PCB, and a packaged Multi-Corder chip. LabVIEW was again used to control the whole system and to do 2D imaging and analysis of the data. Each of the sensors in the array could be addressed independently, thus any sensor can be selected using LabVIEW.

8.2.2 Post-Processing of CMOS Chips

The beginning of the research work concentrated solely on the ISFET, thus a lot of the post-processing of the CMOS chips was developed based on it. The first task was to improve the sensor performance on the ISFET array chip. Ta_2O_5 has

always been known to be an excellent material for pH sensing. Therefore, using a sputtering tool in JWNC, a room temperature sputtering process was developed to deposit Ta_2O_5 on chip. Various trials were performed followed by characterisation using AFM and XPS to determine the best approach to deposit Ta_2O_5, which is compatible for CMOS processing. Furthermore, a patterning method on top of the CMOS chip was also required. Since Ta_2O_5 is a difficult material to dry or wet etch, a lift-off process was chosen. Several photoresists were trialled to establish the most suitable lift-off process when sputtering Ta_2O_5. The best combination proved to be a LOR10A and S1818 bi-layer. After successful deposition of Ta_2O_5 on top of the ISFET sensor, the sensor performance was characterised with the instrumentation system. It was found that the pH sensitivity was 45 mV/pH, which is very close to Nernstian response of 58 mV/pH. In addition, the average drift of the sensor from chip-to-chip was around 6.5 ± 8.6 mV/hour and the working pH range was pH 2 – 12. Another material, polyoxometalates (POMs) was deposited by drop casting on top of the ISFET to improve its performance towards potassium sensing. Using POMs on an ISFET, a net potassium sensitivity of 75 mV/pK was obtained, with a linear range between pK 1.5 to 3. Moreover, the POMs ISFET had a pH sensitivity of -5 mV/pH, proving that POMs layer is selective towards potassium ions and not hydrogen ions. In addition, sodium ions as interfering background ions were investigated and found to reduce the POMs ISFET pK sensitivity to 15 mV/pK. Hence, POMs layer has to be investigated further to produce better sensitivity and selectivity.

Since the project required simultaneous quantification of different metabolites on a single chip, fabrication of microfluidic channels to segregate the sensor array was vital. Using SU-8 photoresist, microfluidic channels were developed. In addition, these channels had to have good channel isolation, a surfactant free hydrophilic fluid transport film was used to bond on top of the channels. The channels were then evaluated with an optical microscope and found to have good isolation and allow smooth liquid flow. The last processing step for the CMOS chips was packaging. Since all the biological and chemical experiments were done in aqueous solution, a good encapsulation technique to protect the electrical connections was developed using a PDMS method and a manual dam and fill method.

8.2.3 Enzyme Assays on Chip

Most of the research work was conducted with the ISFET array chip, thus many of the enzyme assays were performed using it. Using an array of sensors greatly reduces the noise as a function of $\sqrt{N}$, where N is the number of sensors used for averaging. This averaging spatial noise reduction was also found to obey Gaussian statistics. The work was then progressed to investigate different enzyme assays on the ISFET. This proved to be a major challenge since enzyme assays have to be measured in a buffer system to keep them in the optimised pH range, while the ISFET is a sensor that measures pH. To overcome this, the strength of the buffer system of each enzyme assay had to be altered, in order to work on the ISFET. Four different enzyme assays, hexokinase, lactate dehydrogenase, urease and lipase, were performed on the ISFET and showed quantification capability. In addition, enzyme kinetics calculations were performed using a hexokinase assay data to further demonstrate the capability of the device.

On receiving the Multi-Corder chip from the foundry, the ISFET sensor was not working correctly due to a 7 µm thick passivation on top of ISFET that impeded its operation. Therefore, one of the optical sensors had to be evaluated with an enzyme assay to achieve multi-enzyme platform quantification. The chosen sensor to be used was a PD. A colorimetric assay was demonstrated using cholesterol oxidase on a CMOS PD, with a green LED as a light source, to quantify cholesterol concentrations. It was then further demonstrated that this approach can be used to quantify cholesterol levels in pure human blood serum. Furthermore, the metabolite quantification results and enzyme kinetics obtained from this method were comparable to that obtained from a bench top spectrophotometer. This demonstrated a low cost and miniaturised version of spectrophotometer as a portable diagnostic device.

8.2.4 Integration of Microfluidics and Enzyme Immobilisation for Metabolite Detection on Chip

Last but not least, an enzyme immobilisation technique had to be developed to allow multiple metabolites to be quantified in a single chip format. A few

approaches for enzyme immobilisation were investigated. In the end, an alginate enzyme immobilisation was selected for the course of this study. The alginate enzyme entrapment technique was initially tested to demonstrate its capability. The work progressed onto using a 2D inkjet printer to deliver the alginate enzyme gel onto the desired location on the top surface of the CMOS chip. After showing that enzyme entrapped in alginate gel together with 2D inkjet printing was a viable immobilisation technique, the whole complete system was constructed, by integrating microfluidic channels as well. The complete system was then used to perform an enzyme assay with different enzyme concentrations in each channel together with control experiments simultaneously, proving that the system could be potentially used as a multiple metabolite quantification platform.

8.3 Future Work

The emphasis of this research work was placed on demonstrating a complete working system for multiple metabolite measurements. However, the system was not tested to its full potential. Moreover, there are still a lot of factors to be considered for every single component, in order to develop a future personal metabolome machine. Consequently, it is now possible to identify a few key criteria to improve on this technology.

8.3.1 Handheld Diagnostic Device

The instrumentation system that was constructed for the Multi-Corder chip has the capability to be further miniaturised to a complete handheld diagnostic device which can be connected to a mobile phone. Currently, the CMOS chip is powered by an Agilent power supply while a USB cable is connected to a laptop controlled by LabVIEW to power the mbed. The reason why ubiquitous USB connectors are such a popular interconnect for electronic devices is due to their battery free and plug-and-play capability. However, not all mobile phones offer USB as propriety power and analogue interfaces. Recently, the ubiquitous audio jack has been proven to be able to use for this functionality [191]. This can eliminate the need for a power supply and a laptop or a PC. As an alternative the electronic platform can be powered using a lithium battery while utilising

the standardised Bluetooth wireless communication to transfer data between mobile phone and the electronic system. Figure 8.1 shows how the multicorder chip is interfaced with the mobile phone in the future.

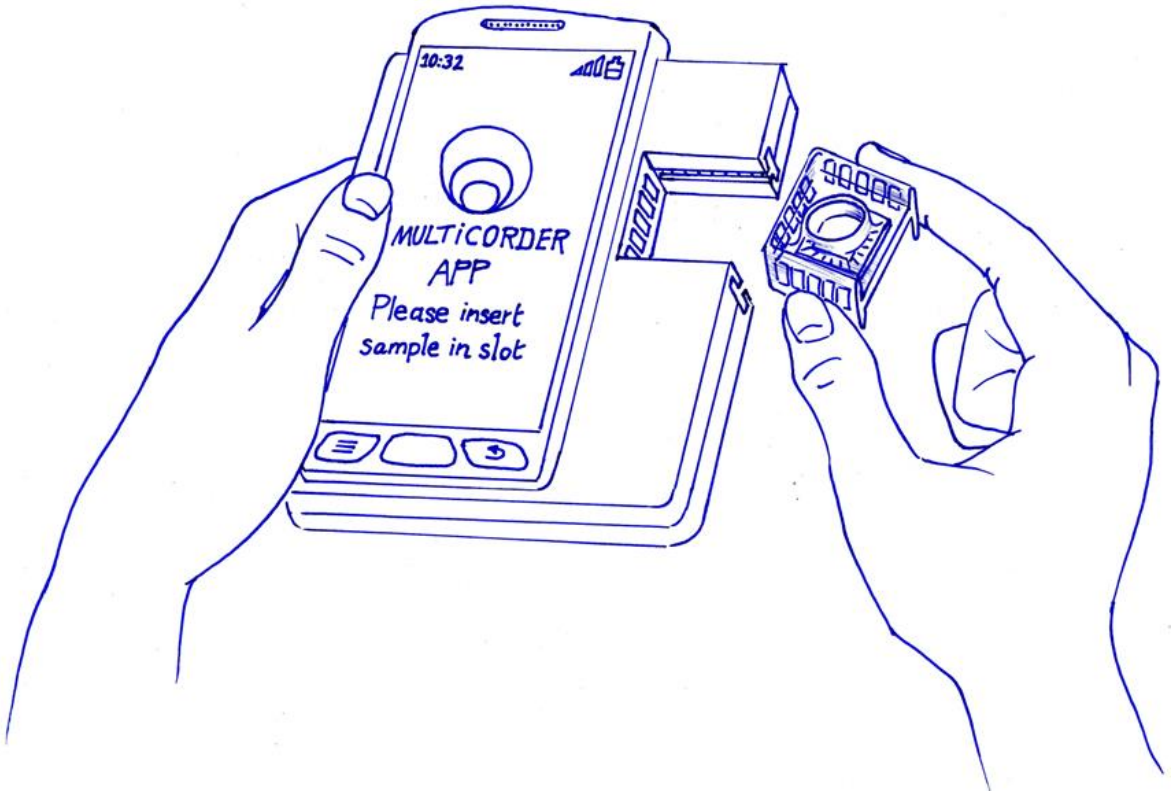

Figure 8.1 – The future of the Multi-Corder project – a handheld personal metabolome machine.

Secondly, the introduction of liquid to the device currently uses a pipette, which is not user friendly. Ideally, consumers will just need to prick their fingers and use a simple accessory to transfer the blood to the biosensor. A lot of the existing technology uses cyanoacrylate paper for home test kits to transfer blood into the biosensor [192], [193], which could be a good addition to the electronic platform that was developed in this study. Finally, the long term stability of alginate enzyme gel is very poor, which is not ideal to be used as a commercial product. There is also a lot of existing technology based on sol-gel film in dry format [194], which is used in commercialised glucose biosensors. They provide long term stability where the biosensor can be mass-produced and kept in store for a long period of time before it is actually being used. In a nutshell, in order to realise a handheld diagnostic device to produce a personal metabolome machine, all of these features have to be significantly improved. Figure 8.2 shows how the Multi-Corder platform would look like in the future.

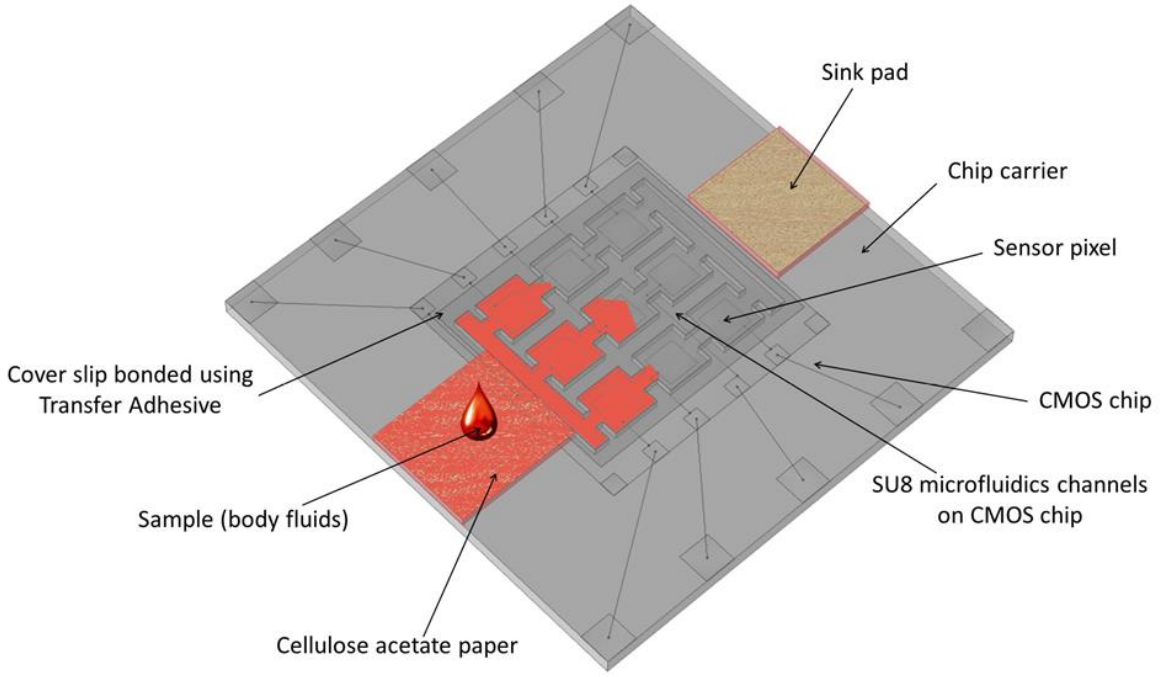

Figure 8.2– Schematic of a CMOS device with microfluidic channels for quantification of multiple metabolites of any body fluids.

8.3.2 Antibodies with Plasmonics Integration

Many of the currently available commercial biosensors exploit enzyme assays for the detection of specific metabolites. However, there are several serious limitations for using enzymes to quantify metabolites. For an enzyme reaction to function properly, the temperature, pH and other environmental factors have to be taken into consideration. Moreover, every single enzyme works in different conditions, which makes developing a multi-enzyme platform extremely difficult to match up one hundred or even thousands different enzymes. Furthermore, an enzyme reaction normally requires more than one substrate, where ideally a multiplexing platform would just require metabolite and a probing biomolecule to detect an output product change. Finally, the greatest weakness of enzymes is that they are very prone to various different kinds of inhibitors, for example a lot of drugs are inhibitors that stop enzyme reactions from occurring.

Recently, Hoshi *et al*. [195] had used a specific metabolite specific antibody to quantify metabolite trytophan for acute viral myocarditis in mice. Hence, a proposed suggestion to overcome enzymes' limitations is to use specialised antibodies that could accept specific metabolites into their binding ground. Antibodies are more robust structures than enzymes; they do not require a lot of

special conditions to be active. Furthermore, antibodies are very specific to only one specific target. Up until 7 to 10 years ago, antibodies were expensive and difficult to obtain, now they are a lot of antibodies that are widely available and are easily purchased. Hence, antibodies could be an alternative probing biomolecule to enzymes. However, antibodies and their specific antigen reaction do not release any biological product that is easily detected. Normally, an antibody and antigen reaction could use ELISA (enzyme-linked immunosorbent assay) detection to produce a colour change and quantify the antigen. This reaction requires a first antibody to bind to the antigen and a second antibody (containing an enzyme that could produce a colour product) to bind to the remaining binding sites of antigen to produce colour change, similar to a "sandwich". This approach will not work for antibodies and metabolites reaction because metabolites are a factor of 100 times smaller than an antigen, which do not provide a vast amount of binding sites for a second antibody.

More recently, Shakoor *et al*. [196] had developed a monolithic integration of nanophotonics structure on CMOS PD and demonstrated the capability to perform label-free immunoassay. Therefore, in order to detect this metabolite-antibody reaction, it is proposed to use localised plasmonics based on gold nanodisks, as can be seen in Figure 8.3. Since these nanodisks measure a shift in wavelength, which has no need of any detectable products from the biological reaction, thus this fits the bill perfectly. These gold nanodisks can be used to bind antibodies by exploiting straightforward thiol chemistry. Therefore, the quantification of metabolites will depend on how much wavelength shift. This can also be further integrated onto the CMOS PD platform to quantify the intensity of light based on the wavelength shift. As a concluding comment, specialised antibodies integrated on plasmonics and CMOS PD could be the future towards multiplexing platform for personal metabolome machine.

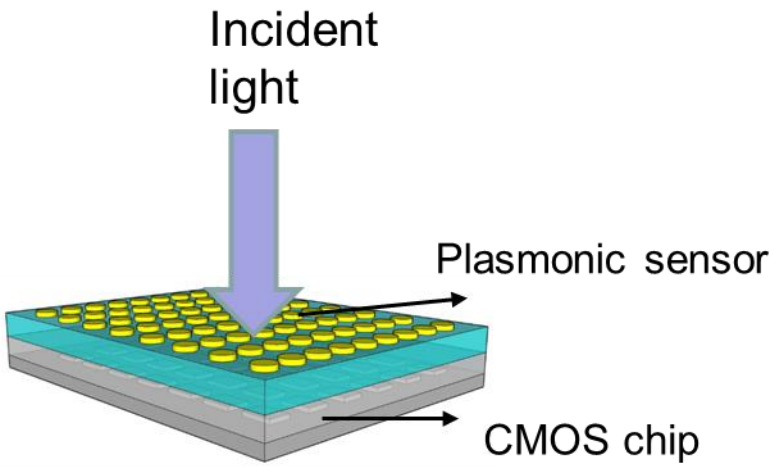

Figure 8.3 – Schematic showing the integration of plasmonic structures on top of a CMOS chip.

8.4 Summary

This research work has successfully achieved the main objective of developing an integrated CMOS sensor array with corresponding electronics platform that has the potential to be used to detect multiple metabolites simultaneously. This chapter has summarised the major findings and difficulties faced during the course of this study. Also, several suggestions to improve the current electronic and biological systems were given.

Appendix A : Graphical Programming Code

A.1 256×256-Pixel ISFET Array Platform

The software used for the instrumentation system to obtain analogue signals and provide digital addresses to the ISFET array chip, as well as data analysis, was based on the LabVIEW system-design platform and development environment, which is a visual programming language from National Instruments.

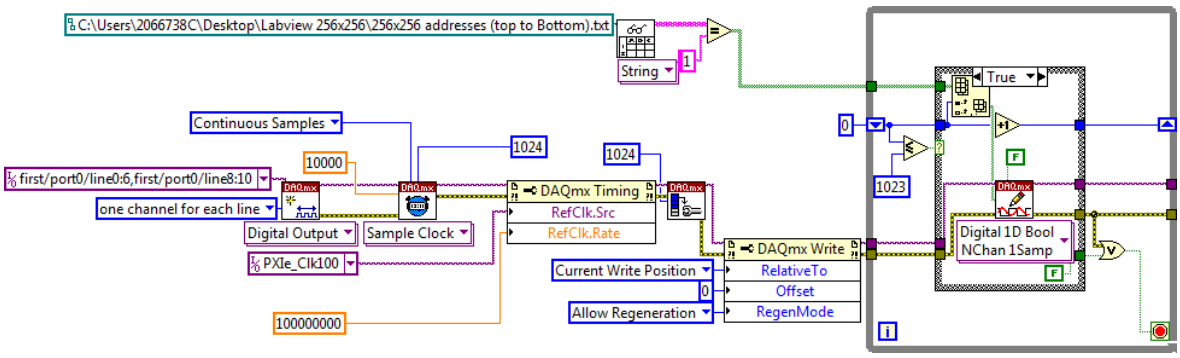

Figure A.1 – LabVIEW program used to send digital addresses to the memory and self-regenerate.

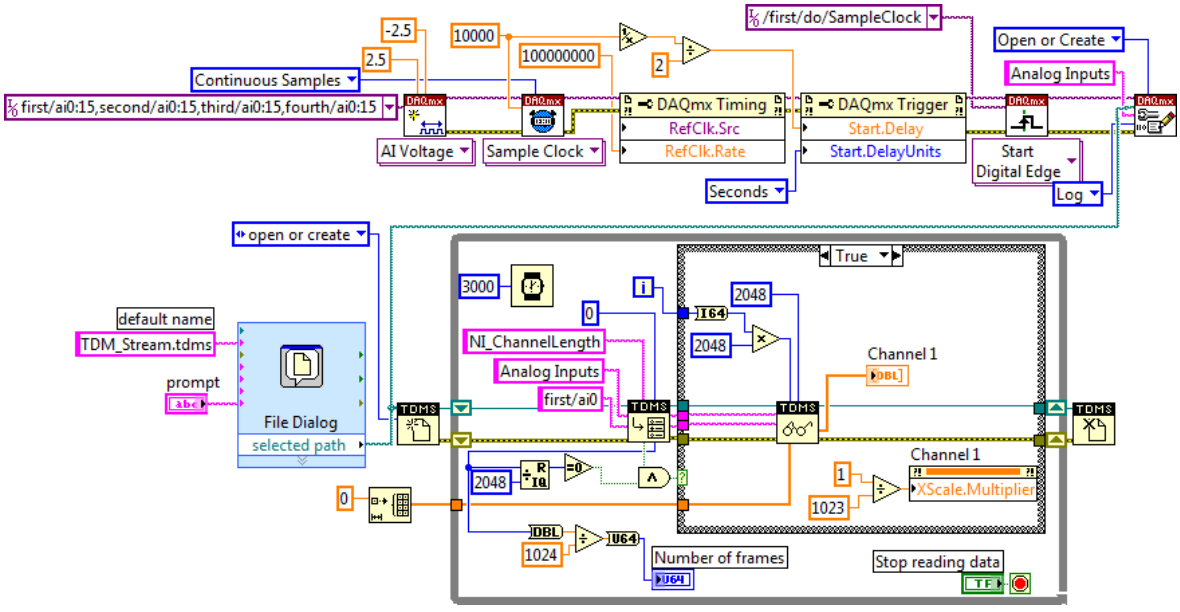

Figure A.2 – LabVIEW program used to acquire analogue signals which is synchronised with digital addresses. A partial of the analogue data was presented in real time and all the analogue data was logged into a TDMS file.

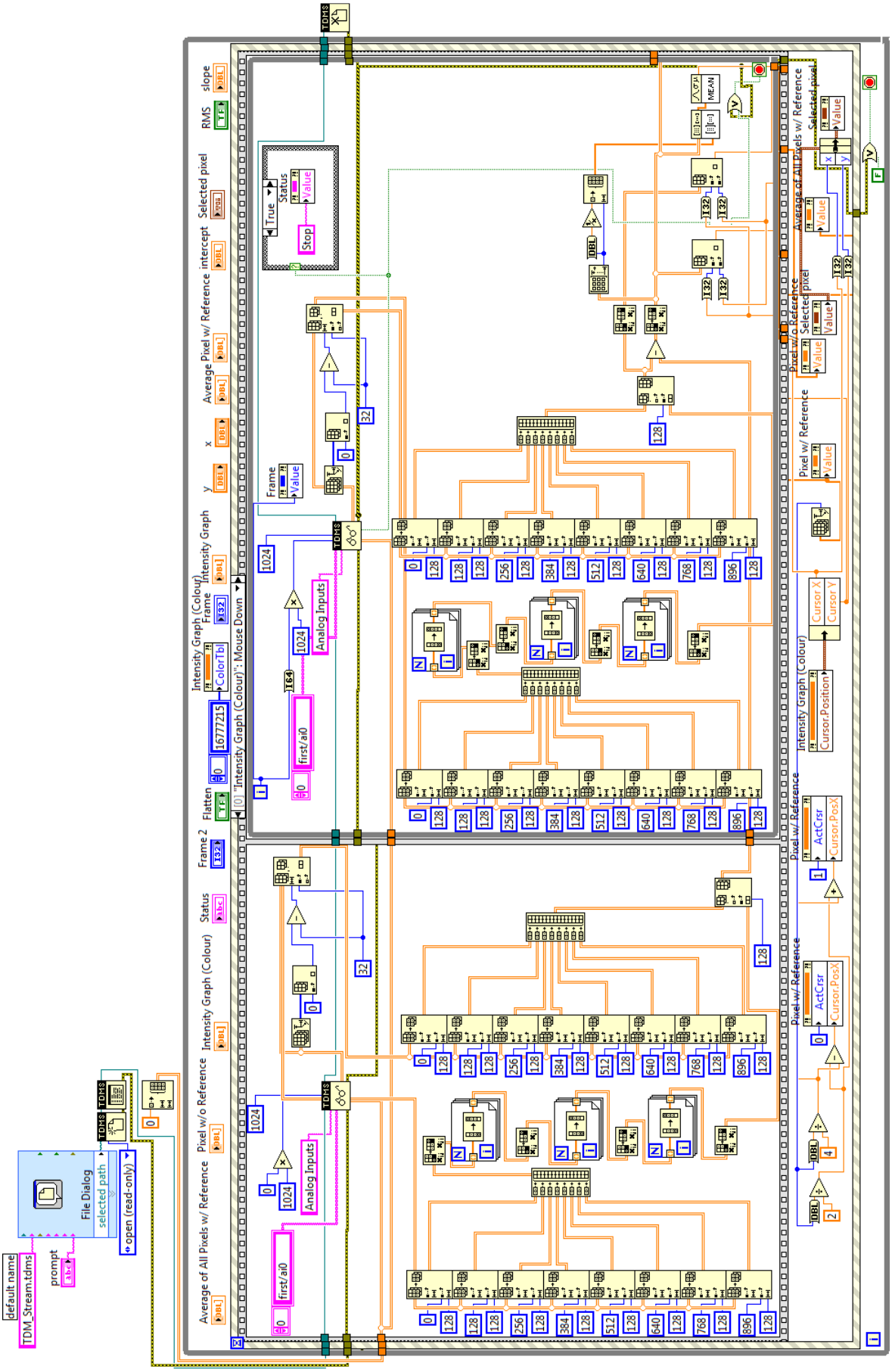

Figure A.3 – LabVIEW program for data analysis of a single pixel and an average of the entire array. The same program was also used for 2D and 3D imaging with slight alteration.

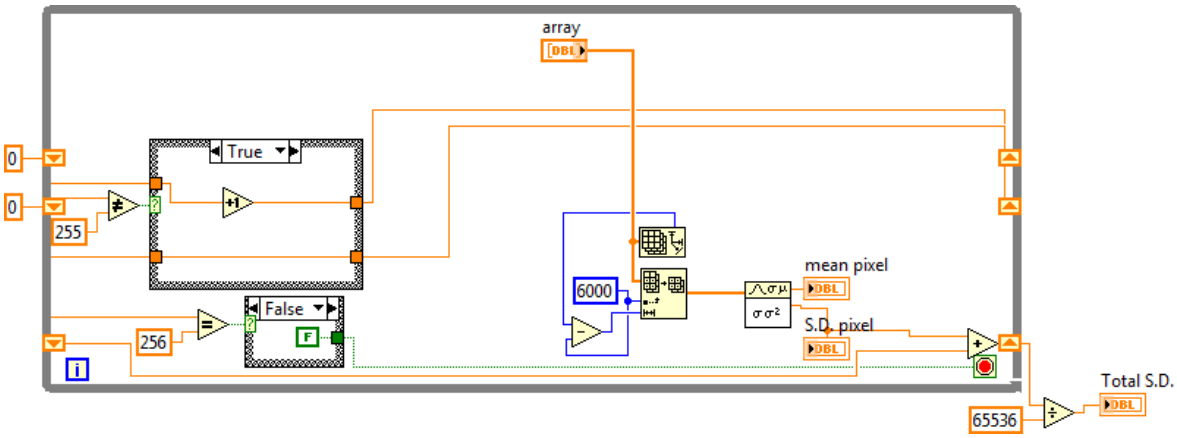

Figure A.4 – LabVIEW program to extract standard deviation and mean of the analogue signals.

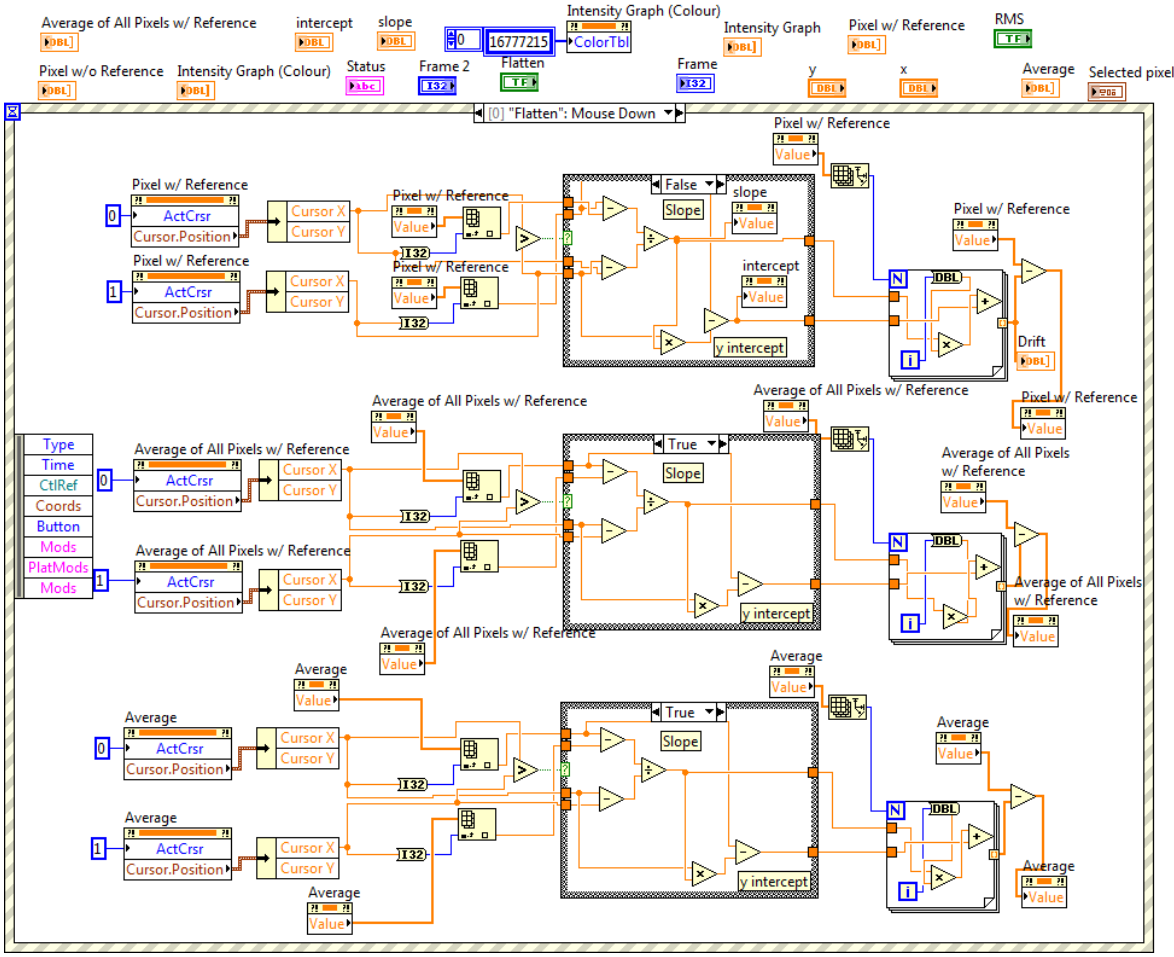

Figure A.5 – LabVIEW program for flattening of ISFET signal to cancel the drift.

A.2 16×16-Pixel Multi-Corder Array Platform

The same software LabVIEW was also used for instrumentation system to control Multi-Corder chip, in order to for the laptop to communicate with the microcontroller, mbed on the PCB and also data analysis.

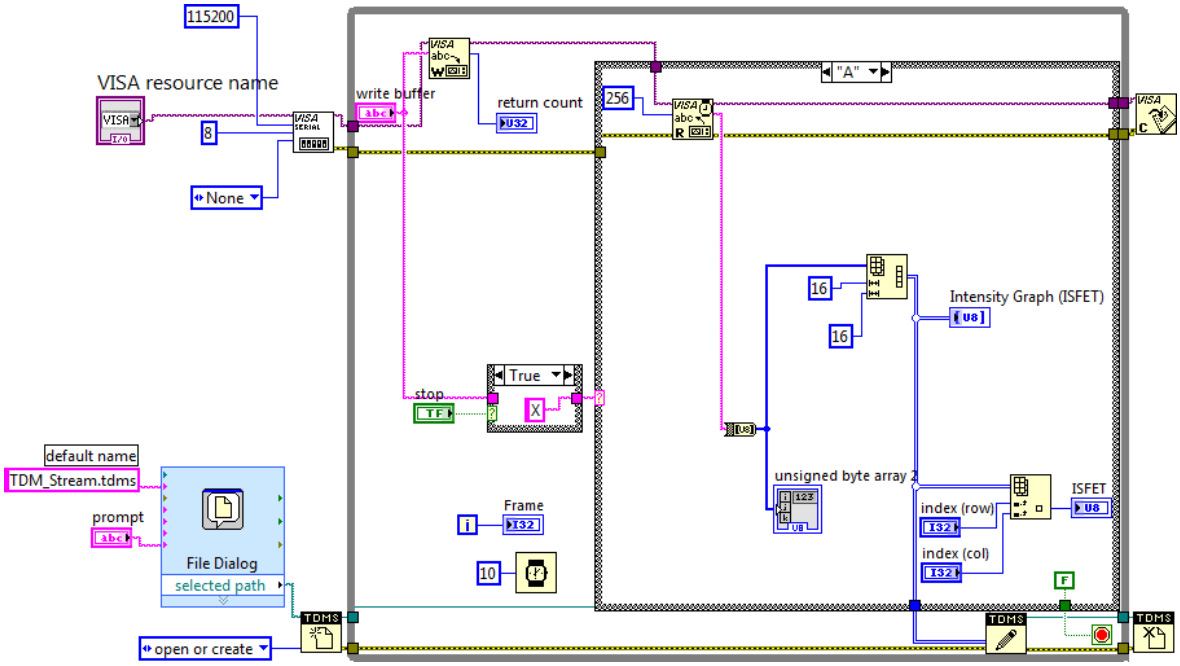

Figure A.6 – LabVIEW program to synchronise and obtain analogue signals for ISFET array on Multi-Corder chip. This program was also used to show real time 2D image and single pixel data, while storing as a TDMS file.

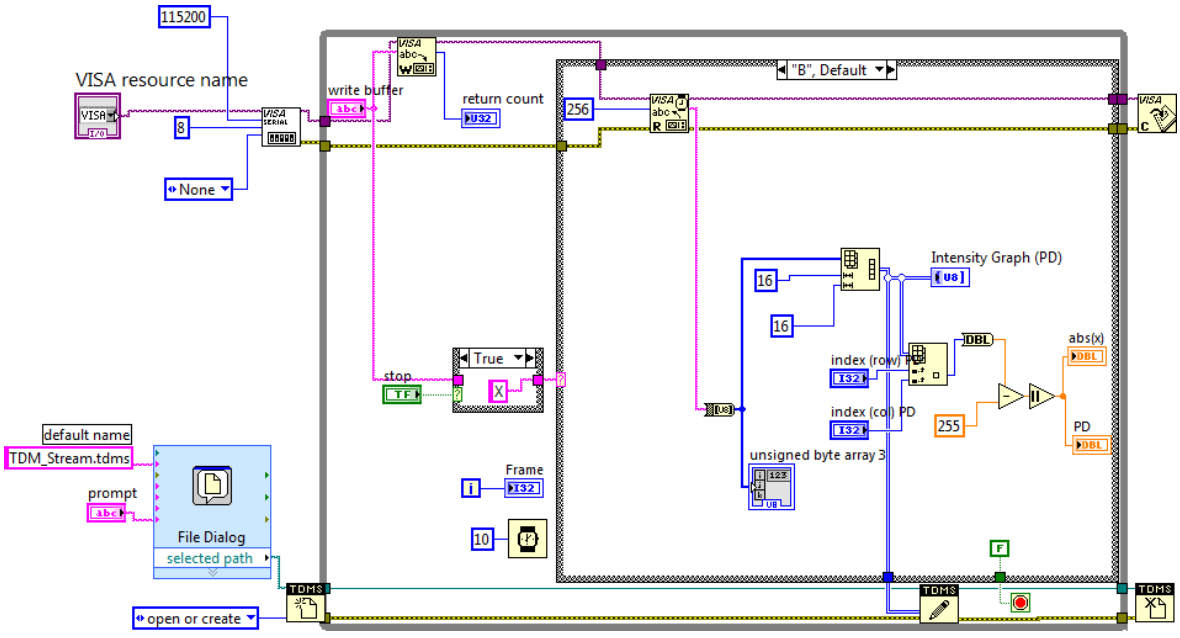

Figure A.7 – LabVIEW program for PD array of Multi-Corder with the same functionalities like ISFET array.

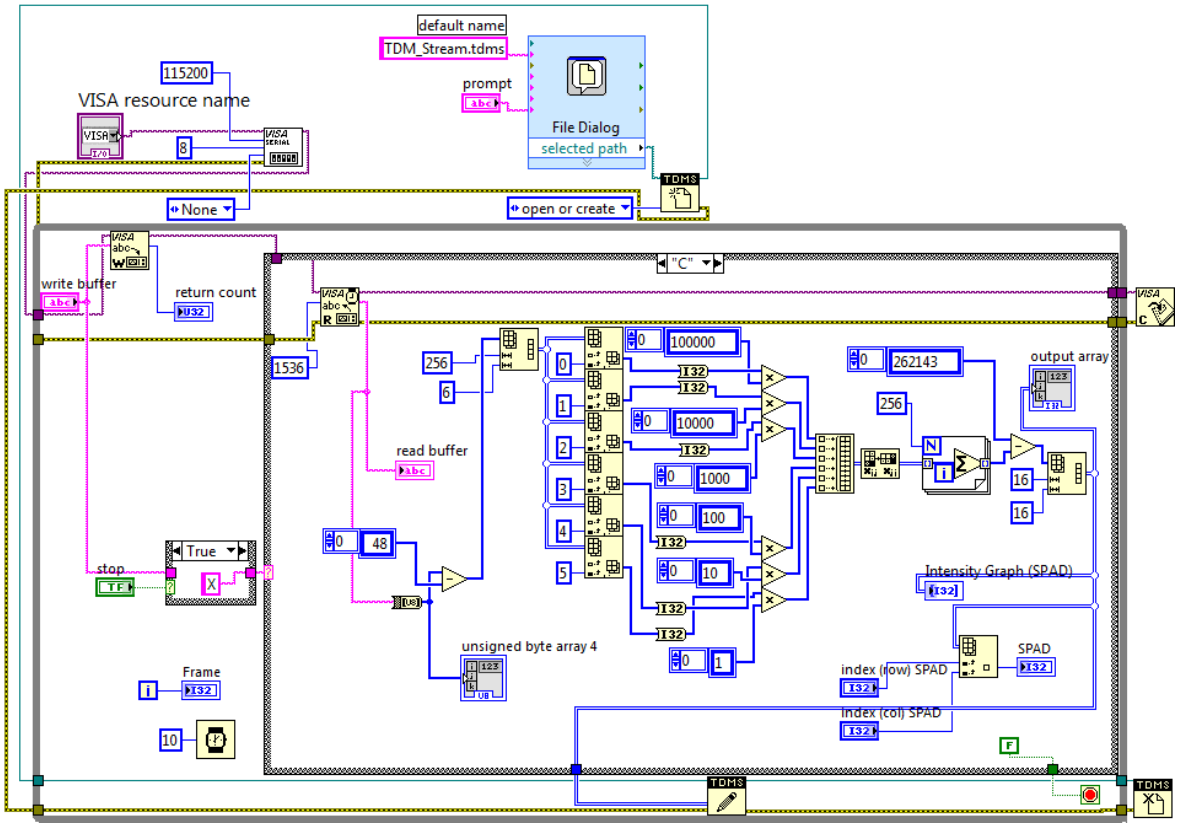

Figure A.8 – LabVIEW program for SPAD array of Multi-Corder with the same functionalities like ISFET and PD array.

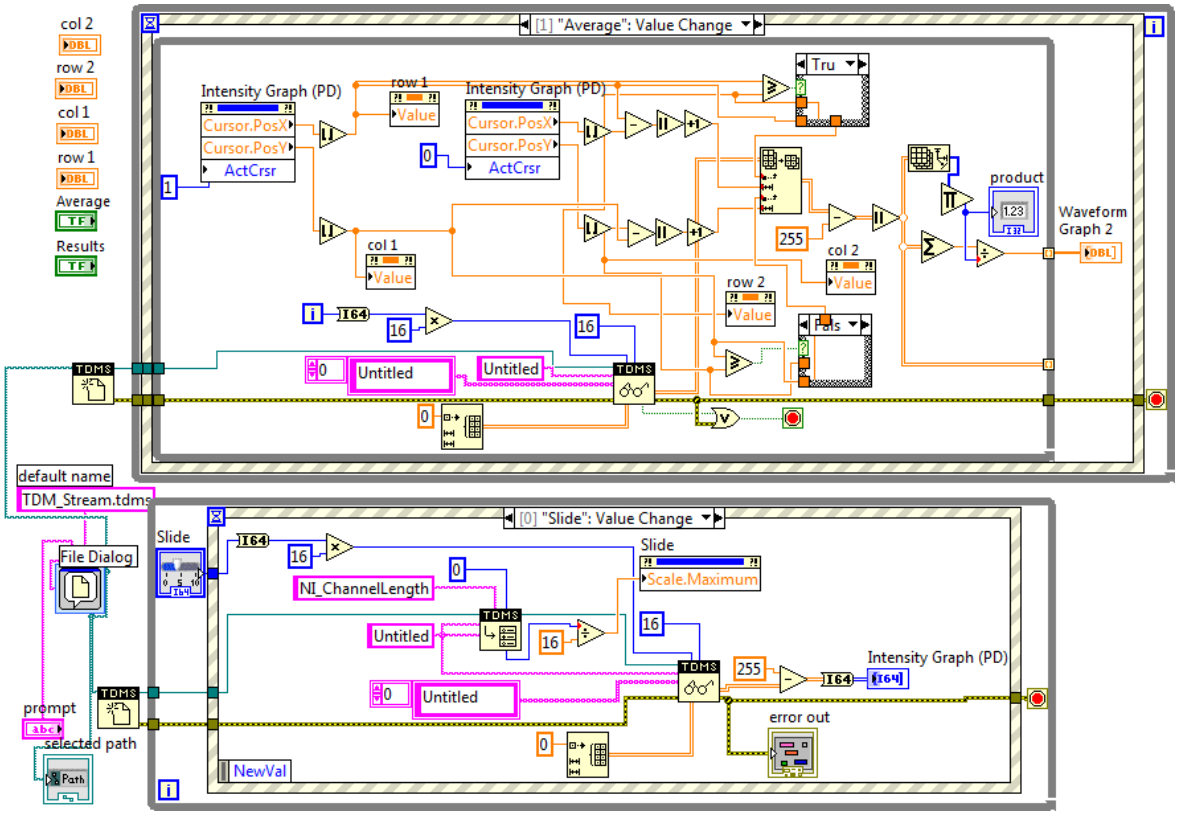

Figure A.9 – LabVIEW program for data analysis and 2D imaging, this is an example of PD array on Multi-Corder chip.

Appendix B : Source Code

The following C++ program enables the mbed platform to acquire signals and to provide digital addresses to the Multi-Corder chip.

```
#include "mbed.h"
PortOut ISFETcol(PortA, 0x03c0); //PA_6,7,8,9
PortOut ISFETrow(PortA, 0x1c00); //PA_10,11,12
PortOut PDcol(PortB, 0x0f00); //PB_8,9,10,11
PortOut PDrow(PortB, 0x00f0); //PB_4,5,6,7
PortOut SPADcol(PortC, 0x03c0); // PC_6,7,8,9
PortOut SPADrow(PortB, 0xf000); //PB_12,13,14,15

AnalogIn isfeta(PA_0);
AnalogIn isfetb(PA_1);
AnalogIn PD(PB_0);
DigitalOut PDrst(PD_2);
DigitalOut clear(PC_10);
DigitalOut gate(PC_11);
DigitalOut read(PC_12);
DigitalIn SPADout(PA_15);

Serial pc(USBTX, USBRX);

int main()
{
    int i,j,k;
    int isfetav, isfetbv, PDv, SPAD;
    pc.baud(115200);
    int a;
    uint32_t counter = 0;
    a=0;
    while(1) {
        a = pc.getc();
```

```
if (a==66) { //B
    a = 0;
    PDrst = 0;
    wait(0.001);
    PDrst = 1;
    wait(0.0005);
    PDrst = 0;
    wait(0.040);
    for (i=0; i<16; i++) {
        for(j=0; j<16; j++) {
            wait(0.00001);
            PDcol.write(i<<8);
            PDrow.write(j<<4);
            wait(0.00001);
            PDv = PD.read_u16();
            pc.putc(PDv>>8);
            wait(0.00001);
        }
    }
}else  if (a==69) { //E
    a = 0;
    PDrst = 0;
    wait(0.001);
    PDrst = 1;
    wait(0.0005);
    PDrst = 0;
    wait(0.040);
    for (i=0; i<16; i++) {
        for(j=0; j<16; j++) {
            wait(0.00001);
            PDcol.write(i<<8);
            PDrow.write(j<<4);
            wait(0.00001);
            PDv = PD.read_u16();
            pc.putc(PDv>>8);
```

```
            pc.putc(PDv&0xff);
            wait(0.00001);
        }
    }
} else if (a==65) { //A
    a = 0;
    for (i=0; i<16; i++) {
        for(j=0; j<8; j++) {
            wait(0.00001);
            ISFETcol.write(i<<6);
            ISFETrow.write(j<<10);
            wait(0.00001);
            isfetav = isfeta.read_u16();
            pc.putc(isfetav>>8);
            isfetbv = isfetb.read_u16();
            pc.putc(isfetbv>>8);
            wait(0.00001);
        }
    }
} else if (a==67) { //C
    a = 0;
    for(i=0; i<16; i++) {
        SPADcol.write(i<<6);
        clear = 1;
        gate = 0;
        read = 1;
        wait(0.000001);
        clear = 0;
        wait(0.000001);
        clear = 1;
        gate = 1;
        wait(0.01);
        gate = 0;
        for(j=0; j<16; j++) {
            SPADrow.write(j<<12);
```

```
                for(k=0; k<18; k++) {
                    read = 0;
                    wait(0.000001);
                    read = 1;
                    wait(0.000001);
                    SPAD = SPADout.read();
                    if (k==0 && SPAD == 1) {
                        counter++;
                    } else if(SPAD == 1) {
                        counter = counter << 1;
                        counter++;
                    } else {
                        counter = counter << 1;
                    }
                }
                pc.printf("%i", counter);
                counter = 0;
                wait(0.0001);
            }
        }
        wait(0.1);
    } else {
        ISFETcol.write(0);
        ISFETrow.write(0);
        PDcol.write(0);
        PDrow.write(0);
        SPADcol.write(0);
        SPADrow.write(0);
        PDrst = 0;
        clear = 0;
        gate = 0;
    }
    a = 0;
  }
}
```

References

[1] K. K. Jain, *Textbook of Personalized Medicine*, 1st ed. New York, United States of America: Springer, 2009.

[2] E. C. Hayden, "The $1,000 genome," *Nature*, vol. 507, pp. 294–295, 2014.

[3] M. L. Metzker, "Sequencing technologies - the next generation.," *Nat. Rev. Genet.*, vol. 11, no. 1, pp. 31–46, 2010.

[4] J. M. Rothberg, W. Hinz, T. M. Rearick, J. Schultz, W. Mileski, M. Davey, J. H. Leamon, K. Johnson, M. J. Milgrew, M. Edwards, J. Hoon, J. F. Simons, D. Marran, J. W. Myers, J. F. Davidson, A. Branting, J. R. Nobile, B. P. Puc, D. Light, T. A. Clark, M. Huber, J. T. Branciforte, I. B. Stoner, S. E. Cawley, M. Lyons, Y. Fu, N. Homer, M. Sedova, X. Miao, B. Reed, J. Sabina, E. Feierstein, M. Schorn, M. Alanjary, E. Dimalanta, D. Dressman, R. Kasinskas, T. Sokolsky, J. A. Fidanza, E. Namsaraev, K. J. McKernan, A. Williams, G. T. Roth, and J. Bustillo, "An integrated semiconductor device enabling non-optical genome sequencing," *Nature*, vol. 475, pp. 348–352, 2011.

[5] G. Novelli, "Personalized genomic medicine," *Intern. Emerg. Med.*, vol. 5, Suppl 1, pp. 81–90, Oct. 2010.

[6] R. Kaddurah-Daouk, B. S. Kristal, and R. M. Weinshilboum, "Metabolomics: A global biochemical approach to drug response and disease," *Annu. Rev. Pharmacol. Toxicol.*, vol. 48, pp. 653–683, 2008.

[7] A. A. Agyeman and R. Ofori-Asenso, "Perspective: Does personalized medicine hold the future for medicine?," *Journal of Pharmacy & Bioallied Sciences*, vol. 7, no. 3. India, pp. 239–244, 2015.

[8] "Personalised medicine." [Online]. Available: http://pharma.bayer.com/en/innovation-partnering/research-focus/oncology/personalized-medicine/.

[9] P. Bhushan, J. Kalpana, and C. Arvind, “Classification of human population based on HLA gene polymorphism and the concept of Prakriti in Ayurveda,” *J. Altern. Complement. Med.*, vol. 11, no. 2, pp. 349–53, Apr. 2005.

[10] S. Chen, F. Lv, J. Gao, J. Lin, Z. Liu, Y. Fu, Y. Liu, B. Lin, Y. Xie, X. Ren, Y. Xu, X. Fan, and A. Xu, “HLA class II polymorphisms associated with the physiologic characteristics defined by Traditional Chinese Medicine: Linking modern genetics with an ancient medicine,” *J. Aternative Complement. Med.*, vol. 13, no. 2, pp. 231–9, Mar. 2007.

[11] K. Sohn, A. Jeong, M. Yoon, S. Lee, S. Hwang, and H. Chae, “Genetic characteristics of Sasang typology: A systematic review,” *J. Acupunct. Meridian Stud.*, vol. 5, no. 6, pp. 271–89, Dec. 2012.

[12] C. R. Scriver, “The salience of Garrod’s `molecular groupings’ and `Inborn Factors in Disease’,” *J. Inherit. Metab. Dis.*, vol. 12, no. 1, pp. 9–24.

[13] E. S. Lander, L. M. Linton, B. Birren, C. Nusbaum, M. C. Zody, J. Baldwin, K. Devon, K. Dewar, M. Doyle, W. FitzHugh, R. Funke, D. Gage, K. Harris, A. Heaford, J. Howland, L. Kann, J. Lehoczky, R. LeVine, P. McEwan, K. McKernan, J. Meldrim, J. P. Mesirov, C. Miranda, W. Morris, J. Naylor, C. Raymond, M. Rosetti, R. Santos, A. Sheridan, C. Sougnez, N. Stange-Thomann, N. Stojanovic, A. Subramanian, D. Wyman, J. Rogers, J. Sulston, R. Ainscough, S. Beck, D. Bentley, J. Burton, C. Clee, N. Carter, A. Coulson, R. Deadman, P. Deloukas, A. Dunham, I. Dunham, R. Durbin, L. French, D. Grafham, S. Gregory, T. Hubbard, S. Humphray, A. Hunt, M. Jones, C. Lloyd, A. McMurray, L. Matthews, S. Mercer, S. Milne, J. C. Mullikin, A. Mungall, R. Plumb, M. Ross, R. Shownkeen, S. Sims, R. H. Waterston, R. K. Wilson, L. W. Hillier, J. D. McPherson, M. A. Marra, E. R. Mardis, L. A. Fulton, A. T. Chinwalla, K. H. Pepin, W. R. Gish, S. L. Chissoe, M. C. Wendl, K. D. Delehaunty, T. L. Miner, A. Delehaunty, J. B. Kramer, L. L. Cook, R. S. Fulton, D. L. Johnson, P. J. Minx, S. W. Clifton, T. Hawkins, E. Branscomb, P. Predki, P. Richardson, S. Wenning, T. Slezak, N. Doggett, J. F. Cheng, A. Olsen, S. Lucas, C. Elkin, E. Uberbacher, M. Frazier, R. A. Gibbs, D. M. Muzny, S. E. Scherer, J. B. Bouck, E. J. Sodergren, K. C. Worley, C. M. Rives, J. H. Gorrell, M. L. Metzker, S. L.

Naylor, R. S. Kucherlapati, D. L. Nelson, G. M. Weinstock, Y. Sakaki, A. Fujiyama, M. Hattori, T. Yada, A. Toyoda, T. Itoh, C. Kawagoe, H. Watanabe, Y. Totoki, T. Taylor, J. Weissenbach, R. Heilig, W. Saurin, F. Artiguenave, P. Brottier, T. Bruls, E. Pelletier, C. Robert, P. Wincker, D. R. Smith, L. Doucette-Stamm, M. Rubenfield, K. Weinstock, H. M. Lee, J. Dubois, A. Rosenthal, M. Platzer, G. Nyakatura, S. Taudien, A. Rump, H. Yang, J. Yu, J. Wang, G. Huang, J. Gu, L. Hood, L. Rowen, A. Madan, S. Qin, R. W. Davis, N. A. Federspiel, A. P. Abola, M. J. Proctor, R. M. Myers, J. Schmutz, M. Dickson, J. Grimwood, D. R. Cox, M. V Olson, R. Kaul, C. Raymond, N. Shimizu, K. Kawasaki, S. Minoshima, G. A. Evans, M. Athanasiou, R. Schultz, B. A. Roe, F. Chen, H. Pan, J. Ramser, H. Lehrach, R. Reinhardt, W. R. McCombie, M. de la Bastide, N. Dedhia, H. Blocker, K. Hornischer, G. Nordsiek, R. Agarwala, L. Aravind, J. A. Bailey, A. Bateman, S. Batzoglou, E. Birney, P. Bork, D. G. Brown, C. B. Burge, L. Cerutti, H. C. Chen, D. Church, M. Clamp, R. R. Copley, T. Doerks, S. R. Eddy, E. E. Eichler, T. S. Furey, J. Galagan, J. G. Gilbert, C. Harmon, Y. Hayashizaki, D. Haussler, H. Hermjakob, K. Hokamp, W. Jang, L. S. Johnson, T. A. Jones, S. Kasif, A. Kaspryzk, S. Kennedy, W. J. Kent, P. Kitts, E. V Koonin, I. Korf, D. Kulp, D. Lancet, T. M. Lowe, A. McLysaght, T. Mikkelsen, J. V Moran, N. Mulder, V. J. Pollara, C. P. Ponting, G. Schuler, J. Schultz, G. Slater, A. F. Smit, E. Stupka, J. Szustakowski, D. Thierry-Mieg, J. Thierry-Mieg, L. Wagner, J. Wallis, R. Wheeler, A. Williams, Y. I. Wolf, K. H. Wolfe, S. P. Yang, R. F. Yeh, F. Collins, M. S. Guyer, J. Peterson, A. Felsenfeld, K. A. Wetterstrand, A. Patrinos, M. J. Morgan, P. de Jong, J. J. Catanese, K. Osoegawa, H. Shizuya, S. Choi, Y. J. Chen, and C. International Human Genome Sequencing, “Initial sequencing and analysis of the human genome,” *Nature*, vol. 409, no. 6822, pp. 860–921, 2001.

[14] A.-C. Syvanen, “Toward genome-wide SNP genotyping,” *Nat. Genet.*, vol. 37, no. June, pp. S5–S10, 2005.

[15] D. N. Howbrook, A. M. Van Der Valk, M. C. O’Shaughnessy, D. K. Sarker, S. C. Baker, and A. W. Lloyd, “Developments in microarray technologies,” *Drug Discov. Today*, vol. 8, no. 14, pp. 642–651, 2003.

[16] “SNP.” [Online]. Available:

http://learn.genetics.utah.edu/content/pharma/snips/.

[17] “DNA Microarray.” [Online]. Available: https://thegenefactor.wordpress.com/final-paper/.

[18] A. J. F. Griffiths, S. R. Wessler, R. C. Lewontin, W. M. Gelbart, D. T. Suzuki, and J. H. Miller, *An introduction to genetic analysis*, 8th ed. W.H.Freeman & Co Ltd, 2005.

[19] “A brief guide to genomics.” [Online]. Available: https://www.genome.gov/18016863/.

[20] “An overview of the Human Genome Project.” [Online]. Available: https://www.genome.gov/12011238/.

[21] I. Miko, “Gregor Mendel and the principles of inheritance,” *Nat. Educ.*, vol. 1, no. 1, pp. 134–139, 2008.

[22] J. D. Watson and F. H. C. Crick, “Molecular structure of nucleic acids,” *Nature*, vol. 171, pp. 737–738, 1953.

[23] G. P. Bates, “The molecular genetics of Huntington disease - a history.,” *Nat. Rev. Genet.*, vol. 6, no. 10, pp. 766–773, 2005.

[24] “DNA to Genome.” [Online]. Available: http://www.broadinstitute.org/education/glossary/genome.

[25] F. Sanger, S. Nicklen, and a R. Coulson, “DNA sequencing with chain-terminating inhibitors,” *Proc. Natl. Acad. Sci. U. S. A.*, vol. 74, no. 12, pp. 5463–5467, 1977.

[26] J. Shendure and H. Ji, “Next-generation DNA sequencing,” *Nat. Biotechnol.*, vol. 26, no. 10, pp. 1135–1145, 2008.

[27] “History of DNA sequencing technologies.” [Online]. Available: http://dnasequencing.yolasite.com/timeline-and-history.php.

[28] K. B. Mullis and F. A. Faloona, “Specific synthesis of DNA in vitro via a polymerase-catalyzed chain reaction,” *Methods Enzymol.*, vol. 155, no. C, pp. 335–350, 1987.

[29] S. Kumar, T. W. Banks, and S. Cloutier, “SNP discovery through next-generation sequencing and its applications,” *Int. J. Plant Genomics*, vol. 2012, p. 15, 2012.

[30] J. Sun, R. D Berguer, and L. K Schackenberf, “Metabolomics as a tool for personalizing medicine : 2012 update,” *Futur. Med.*, vol. 10, pp. 149–161, 2013.

[31] H. F. Willard, M. Angrist, and G. S. Ginsburg, “Genomic medicine: genetic variation and its impact on the future of health care,” *Philos. Trans. R. Soc. B Biol. Sci.*, vol. 360, no. 1460, pp. 1543–1550, 2005.

[32] “Metabolomics.” [Online]. Available: http://www.omics.org/index.php/Metabolomics.

[33] D. S. Wishart, T. Jewison, A. C. Guo, M. Wilson, C. Knox, Y. Liu, Y. Djoumbou, R. Mandal, F. Aziat, E. Dong, S. Bouatra, I. Sinelnikov, D. Arndt, J. Xia, P. Liu, F. Yallou, T. Bjorndahl, R. Perez-Pineiro, R. Eisner, F. Allen, V. Neveu, R. Greiner, and A. Scalbert, “HMDB 3.0-The Human Metabolome Database in 2013,” *Nucleic Acids Res.*, vol. 41, no. D1, pp. 1–7, 2013.

[34] “Genotypic to Phenotypic Profile.” [Online]. Available: http://www.metabonews.ca/Oct2013/MetaboNews_Oct2013.htm.

[35] W. B. Dunn and D. I. Ellis, “Metabolomics: Current analytical platforms and methodologies,” *TrAC - Trends Anal. Chem.*, vol. 24, no. 4, pp. 285–294, 2005.

[36] M. F. Templin, D. Stoll, M. Schrenk, P. C. Traub, C. F. Vohringer, and T. O. Joos, “Protein microarray technology,” *Trends Biotechnol.*, vol. 20, no. 4, pp. 160–166, 2002.

[37] R. P. Ekins, “Multi-analyte immunoassay,” vol. 7, no. 2, pp. 155–168, 1989.

[38] D. Stoll, J. Bachmann, M. F. Templin, and T. O. Joos, “Microarray technology: An increasing variety of screening tools for proteomic research,” *Drug Discov. Today TARGETS*, vol. 3, no. 1, pp. 24–31, 2004.

[39] M. B. Miller and Y. W. Tang, “Basic concepts of microarrays and potential applications in clinical microbiology,” *Clin. Microbiol. Rev.*, vol. 22, no. 4, pp. 611–633, 2009.

[40] M. Schena, R. A. Heller, T. P. Theriault, K. Konrad, E. Lachenmeier, and R. W. Davis, “Microarrays: Biotechnology’s discovery platform for functional genomics,” *Trends Biotechnol.*, vol. 16, no. 7, pp. 301–306, 1998.

[41] G. Macbeath and S. S. L., “Printing proteins as microarrays for high-throughput function determination,” *Science (80-.).*, vol. 289, no. 5485, pp. 1760–1763, 2000.

[42] M.-Y. Lee, C. B. Park, J. S. Dordick, and D. S. Clark, “Metabolizing enzyme toxicology assay chip (MetaChip) for high-throughput microscale toxicity analyses,” *Proc. Natl. Acad. Sci.*, vol. 102, no. 4, pp. 983–987, 2005.

[43] S. V. Chittur, *Microarray Methods for Drug Discovery*, vol. 53, no. 9. New York: Springer, 2010.

[44] M. He and M. J. Taussig, “Single step generation of protein arrays from DNA by cell-free expression and in situ immobilisation (PISA method),” *Nucleic Acids Res.*, vol. 29, no. 15, pp. 73–78, 2001.

[45] M. He, O. Stoevesandt, and M. J. Taussig, “In situ synthesis of protein arrays,” *Curr. Opin. Biotechnol.*, vol. 19, no. 1, pp. 4–9, 2008.

[46] I. M. Ross, “The invention of the transistor,” *Proc. IEEE*, vol. 86, no. 1, pp. 7–28, 1998.

[47] J. Bardeen and W. H. Brattain, “The transistor, a semi-conductor triode,” *Phys. Rev.*, vol. 74, pp. 230–231, 1948.

[48] J. S. Kilby, “Invention of the integrated circuit,” *IEEE Trans. Electron Devices*, vol. 23, pp. 648–654, 1976.

[49] F. Wanlass and C. Sah, “Nanowatt logic using field-effect metal-oxide semiconductor triodes,” *Dig. IEEE Int. Solid-State Circuits Conf.*, pp. 32–33, 1963.

[50] A. Hierlemann and H. Baltes, “CMOS-based chemical microsensors,” *Analyst*, vol. 128, no. 1, pp. 15–28, 2003.

[51] G. T. A. Kovacs, N. I. Maluf, and K. E. Petersen, “Bulk micromachining of silicon,” *Proc. IEEE*, vol. 86, no. 8, pp. 1536–1551, 1998.

[52] J. Bustillo and M. Milgrew, “Methods for manufacturing microwell structures of chemically-sensitive sensor arrays,” US 20120329192 A1, 2012.

[53] T. C. W. Yeow, M. R. Haskard, D. E. Mulcahy, H. I. Seo, and D. H. Kwon, “A very large integrated pH-ISFET sensor array chip compatible with standard CMOS processes,” *Sensors Actuators B Chem.*, vol. 44, no. 1–3, pp. 434–440, 1997.

[54] C. Hagleitner, A. Hierlemann, D. Lange, A. Kummer, N. Kerness, O. Brand, and H. Baltes, “Smart single-chip gas sensor microsystem.,” *Nature*, vol. 414, pp. 293–296, 2001.

[55] P. A. Hammond, D. Ali, and D. R. S. Cumming, “A system-on-chip digital pH meter for use in a wireless diagnostic capsule,” *IEEE Trans. Biomed. Eng.*, vol. 52, no. 4, pp. 687–694, 2005.

[56] Y. Huang, T. Tzeng, T. Lin, C. Huang, P. Yen, P. Kuo, C. Lin, and S. Lu, “A self-powered CMOS reconfigurable multi-sensor SoC for biomedical applications,” *IEEE J. Solid-State Circuits*, vol. 49, no. 4, pp. 851–866, 2014.

[57] P. Bergveld, “Development of an ion-sensitive solid-state device for

neurophysiological measurements," *IEEE Trans. Biomed. Eng.*, vol. 17, no. 1, pp. 70–71, 1970.

[58] P. Bergveld, "Development, operation, and application of the ion-sensitive field-effect transistor as a tool for electrophysiology," *IEEE Trans. Biomed. Eng.*, vol. 19, no. 5, pp. 342–351, 1972.

[59] T. Matsuo and K. D. Wise, "An integrated field-effect electrode for biopotential recording," *IEEE Trans. Biomed. Eng.*, vol. 21, no. 6, pp. 485–487, 1974.

[60] T. Matsuo and M. Esashi, "Methods of ISFET fabrication," *Sensors and Actuators*, vol. 1, pp. 77–96, 1981.

[61] T. Akiyama, Y. Ujihira, and Y. Okabe, "Ion-sensitive field-effect transistors with inorganic gate oxide for pH sensing," *IEEE Trans. Electron Devices*, vol. 29, no. 12, pp. 1936–1941, 1982.

[62] H.-K. Liao, J.-C. Chou, W.-Y. Chung, T.-P. Sun, and S.-K. Hsiung, "Study of amorphous tin oxide thin films for ISFET applications," *Sensors Actuators B Chem.*, vol. 50, no. 2, pp. 104–109, 1998.

[63] V. Rocher, J. Chovelon, N. Jaffrezic-Renault, Y. Cros, and D. Birot, "An oxynitride ISFET modified for working in a differential mode for pH detection," *J. Electrochem. Soc.*, vol. 141, no. 2, pp. 535–539, 1994.

[64] W. D. Huang, H. Cao, S. Deb, M. Chiao, and J. C. Chiao, "A flexible pH sensor based on the iridium oxide sensing film," *Sensors Actuators A Phys.*, vol. 169, pp. 1–11, 2011.

[65] Y.-H. Y. Chang, Y. Y.-S. Lu, Y. Y.-L. Hong, S. Gwo, and J. A. Yeh, "Highly sensitive pH sensing using an indium nitride ion-sensitive field-effect transistor," *IEEE Sens. J.*, vol. 11, no. 5, pp. 1157–1161, 2011.

[66] L. T. Yin, J. C. Chou, W. Y. Chung, T. P. Sun, and S. K. Hsiung, "Study of indium tin oxide thin film for separative extended gate ISFET," *Mater.*

Chem. Phys., vol. 70, pp. 12–16, 2001.

[67] T. M. Pan and K. M. Liao, “Structural and sensing properties of high-k PrTiO3 sensing membranes for pH-ISFET applications,” *IEEE Trans. Biomed. Eng.*, vol. 56, no. 2, pp. 471–476, 2009.

[68] J. A. Mihell and J. K. Atkinson, “Planar thick-film pH electrodes based on ruthenium dioxide hydrate,” *Sensors Actuators B Chem.*, vol. 48, pp. 505–511, 1998.

[69] T. M. Pan and M. De Huang, “Structural properties and sensing characteristics of high-k Ho2O3 sensing film-based electrolyte-insulator-semiconductor,” *Mater. Chem. Phys.*, vol. 129, pp. 919–924, 2011.

[70] T. M. Pan, J. C. Lin, M. H. Wu, and C. S. Lai, “Study of high-k Er2O3 thin layers as ISFET sensitive insulator surface for pH detection,” *Sensors Actuators B Chem.*, vol. 138, pp. 619–624, 2009.

[71] W. W. A. Olszyna and W. T. D. Sobczyńska, “A study of borazon-gate pH-sensitive field effect transistors,” *J. Cryst. Growth*, vol. 82, pp. 757–760, 1987.

[72] K. Tsukada, T. Kiwa, T. Yamaguchi, S. Migitaka, Y. Goto, and K. Yokosawa, “A study of fast response characteristics for hydrogen sensing with platinum FET sensor,” *Sensors Actuators B Chem.*, vol. 114, pp. 158–163, 2006.

[73] S. Wakida, S. Mochizuki, R. Makabe, A. Kawahara, M. Yamane, S. Takasuka, and K. Higashi, “pH-sensitive ISFETs based on titanium nitride and their application to battery monitor,” in *Proceedings of IEEE International Conference on Solid-State Sensors and Actuators (TRANSDUCERS ’91)*, 1991, pp. 222–224.

[74] S. D. Moss, J. Janata, and C. C. Johnson, “Potassium ion-sensitive field effect transistor,” *Anal. Chem.*, vol. 47, no. 13, pp. 2238–2243, 1975.

[75] M. Wipf, R. L. Stoop, A. Tarasov, K. Bedner, W. Fu, I. a Wright, C. J. Martin, E. C. Constable, M. Calame, and C. Scho, “Selective sodium sensing with gold-coated silicon nanowire field-effect transistors in a differential setup,” *ACS Nano*, vol. 7, no. 7, pp. 5978–5983, 2013.

[76] S. Wakida, Y. Kohigashi, K. Higashi, and Y. Ujihira, “Chemically modified copper ion-selective field-effect transistor with 7,7,8,8-tetracyanoquinodimethane,” in *Proceedings of IEEE International Conference on Solid-State Sensors and Actuators (TRANSDUCERS ’91)*, 1995, pp. 925–927.

[77] L. Bousse, J. Shott, and J. D. Meindl, “A process for the combined fabrication of ion sensors and CMOS Circuits,” *IEEE Electron Device Lett.*, vol. 9, no. 1, pp. 44–46, 1988.

[78] H.-S. Wong and M. H. White, “A CMOS-integrated ‘ISFET-operational amplifier’ chemical sensor employing differential sensing,” *IEEE Trans. Electron Devices*, vol. 36, no. 3, pp. 479–487, 1989.

[79] J. Bausells, J. Carrabina, A. Errachid, and A. Merlos, “Ion-sensitive field-effect transistors fabricated in a commercial CMOS technology,” *Sensors Actuators B Chem.*, vol. 57, no. 1–3, pp. 56–62, 1999.

[80] M. J. Milgrew, M. O. Riehle, and D. R. S. Cumming, “A 16x16 CMOS proton camera array for direct extracellular imaging of hydrogen-ion activity,” in *2008 IEEE International Solid-State Circuits Conference - Digest of Technical Papers*, 2008, pp. 590–592.

[81] B. Nemeth, M. D. Symes, A. G. Boulay, C. Busche, G. J. T. Cooper, D. R. S. Cumming, and L. Cronin, “Real-time ion-flux imaging in the growth of micrometer-scale structures and membranes,” *Adv. Mater.*, vol. 24, no. 9, pp. 1238–1242, 2012.

[82] B. Nemeth, C. Busche, S. Tsuda, L. Cronin, and D. R. S. Cumming, “Imaging the Belousov-Zhabotinsky reaction in real time using an ion sensitive array,” *Chem. Commun.*, vol. 48, no. 42, pp. 5085–5087, 2012.

[83] P. Estrela, A. G. Stewart, F. Yan, and P. Migliorato, “Field effect detection of biomolecular interactions,” *Electrochim. Acta*, vol. 50, pp. 4995–5000, 2005.

[84] S. Purushothaman, C. Toumazou, and C. P. Ou, “Protons and single nucleotide polymorphism detection: A simple use for the Ion Sensitive Field Effect Transistor,” *Sensors Actuators B Chem.*, vol. 114, pp. 964–968, 2006.

[85] T. Sakurai and Y. Husimi, “Real-time monitoring of DNA polymerase reactions by a micro ISFET pH sensor,” *Anal. Chem.*, vol. 64, no. 17, pp. 1996–1997, 1992.

[86] S. Caras and J. Janata, “Field effect transistor sensitive to penicillin,” *Anal. Chem.*, vol. 52, no. 8, pp. 1935–1937, 1980.

[87] I. A. Koshets, Y. U. M. Shirshov, B. A. Snopok, A. L. Kukla, N. F. Starodub, N. Kanjuk, and R. Koehlr, “The ISFET-based system for glucose determination,” in *Proceedings of SPIE*, 2001, vol. 4425, pp. 163–169.

[88] O. A. Boubriak, A. P. Soldatkin, N. F. Starodub, A. K. Sandrovsky, and A. K. El’skaya, “Determination of urea in blood serum by a urease biosensor based on an ion-sensitive field-effect transistor,” *Sensors Actuators B Chem.*, vol. 26–27, pp. 429–431, 1995.

[89] A. P. Soldatkin, J. Montoriol, W. Sant, C. Martelet, and N. Jaffrezic-Renault, “Development of potentiometric creatinine-sensitive biosensor based on ISFET and creatinine deiminase immobilised in PVA/SbQ photopolymeric membrane,” *Mater. Sci. Eng.*, vol. 21, pp. 75–79, 2002.

[90] J. C. van Kerkhof, P. Bergveld, and R. B. M. Schasfoort, “The ISFET based heparin sensor with a monolayer of protamine as affinity ligand,” *Biosens. Bioelectron.*, vol. 10, pp. 269–282, 1995.

[91] A. Hai, D. Ben-Haim, N. Korbakov, A. Cohen, J. Shappir, R. Oren, M. E. Spira, and S. Yitzchaik, “Acetylcholinesterase-ISFET based system for the

detection of acetylcholine and acetylcholinesterase inhibitors," *Biosens. Bioelectron.*, vol. 22, pp. 605–612, 2006.

[92] D. Braeken, D. R. Rand, A. Andrei, R. Huys, M. E. Spira, S. Yitzchaik, J. Shappir, G. Borghs, G. Callewaert, and C. Bartic, "Glutamate sensing with enzyme-modified floating-gate field effect transistors," *Biosens. Bioelectron.*, vol. 24, pp. 2384–2389, 2009.

[93] Y. Hanazato, M. Nakako, and S. Shiono, "Multi-enzyme electrode using hydrogen-ion-sensitive field-effect transistors," *IEEE Trans. Electron Devices*, vol. 33, no. 1, pp. 47–51, 1986.

[94] R. A. Copeland, *Enzymes: A Practical Introduction to Structure, Mechanism, and Data Analysis*, 2nd ed. John Wiley & Sons, 2000.

[95] H. F. Gilbert, *Basic Concepts in Biochemistry*, 2nd ed. McGraw-Hill, 1992.

[96] R. A. Baker and L. Wicker, "Current and potential applications of enzyme infusion in the food industry," *Trends in Food Science and Technology*, vol. 7, no. 9. pp. 279–284, 1996.

[97] O. Kirk, T. V. Borchert, and C. C. Fuglsang, "Industrial enzyme applications," *Curr. Opin. Biotechnol.*, vol. 13, no. 4, pp. 345–351, 2002.

[98] F. Hasan, A. A. Shah, S. Javed, and A. Hameed, "Enzymes used in detergents : Lipases," *African J. Biotechnol.*, vol. 9, no. 31, pp. 4836–4844, 2010.

[99] T. Hemalatha, T. UmaMaheswari, G. Krithiga, P. Sankaranarayanan, and R. Puvanakrishnan, "Enzymes in clinical medicine: An overview," *Indian J. Exp. Biol.*, vol. 51, no. 10, pp. 777–788, 2013.

[100] E. Kopetzki, K. Lehnert, and P. Buckel, "Enzymes in diagnostics: Achievements and possibilities of recombinant DNA technology," *Clin. Chem.*, vol. 40, no. 5, pp. 688–704, 1994.

[101] R. Eisenthal and M. J. Danson, *Enzyme Assays: A Practical Approach*, 2nd

ed. Oxford University Press, 2002.

[102] S. R. Corrie, J. Coffey, J. Islam, K. A. Markey, and M. A. F. Kendall, “Blood, sweat, and tears: Developing clinically relevant protein biosensors for integrated body fluid analysis,” *Analyst*, vol. 140, pp. 4350–4364, 2015.

[103] C. A. Burtis, E. R. Ashwood, and D. E. Bruns, *Textbook of Clinical Chemistry and Molecular Diagnostics*, 4th ed. Elsevier, 2006.

[104] S. J. Charnock and B. V. McCleary, “Enzymes: Industrial and analytical applications.”

[105] T. D. H. Bugg, *Introduction to Enzyme and Coenzyme Chemistry*, 3rd ed. John Wiley & Sons, 2012.

[106] L. Michaelis and M. L. Menten, “The Kinetics of Invertase Action,” *Biochem Z*, vol. 49, no. February, pp. 333–369, 1913.

[107] H. Bisswanger, *Enzyme Kinetics: Principles and Methods*, 3rd ed. Wiley-VCH, 2002.

[108] C. M. A. Brett and M. O. Brett, *Electrochemistry: Principles, Methods, and Applications*. Oxford Univesity Press, 1993.

[109] G. Meisenberg and W. H. Simmons, *Principles of Mecial Biochemistry*, 3rd ed. Elsevier, 2012.

[110] G. E. Briggs and J. B. S. Haldane, “A Further Note on the Kinetics of Enzyme Action,” *Biochem. J.*, vol. 19, no. 6, pp. 1037–1038, 1925.

[111] P. R. Bergethon, *The Physical Basis of Biochemistry: The Foundations of Molecular Biophysics*. New York, United States of America: Springer, 2000.

[112] A. J. Bard and L. R. Faulkner, *Electrochemical Methods: Fundamentals and Applications*, 2nd ed. John Wiley & Sons, 2001.

[113] S. D. Collins, “Practical limits for solid-state reference electrodes,”

Sensors Actuators B Chem., vol. 10, no. 3, pp. 169–178, 1993.

[114] S. M. Sze and K. K. Ng, *Physics of Semiconductor Devices*, 3rd ed., vol. 1. John Wiley & Sons, 2007.

[115] D. C. Grahame, "The electrical double layer and the theory of electrocapillarity," *Chem. Rev.*, pp. 441–501, 1947.

[116] W. M. Siu and R. S. C. Cobbold, "Basic properties of the electrolyte-Si02-Si system: Physical and theorectical aspects," *IEEE Trans. Electron Devices*, no. 1, pp. 1805–1815, 1979.

[117] D. E. Yates, S. Levine, and T. W. Healy, "Site-binding model of the electrical double layer at the oxide/water interface," *J. Chem. Soc. Faraday Trans. 1 Phys. Chem. Condens. Phases*, vol. 70, pp. 1807–1818, 1974.

[118] D. L. Harame, L. J. Bousse, J. D. Shott, and J. D. Meindl, "Ion-sensing devices with silicon nitride and borosilicate glass insulators," *IEEE Trans. Electron Devices*, vol. 34, no. 8, pp. 1700–1707, 1987.

[119] L. Bousse, N. F. De Rooij, and P. Bergveld, "Operation of chemically sensitive field-effect sensors as a function of the insulator-electrolyte interface," *IEEE Trans. Electron Devices*, vol. 30, no. 10, pp. 1263–1270, 1983.

[120] D. F. Swinehart, "The Beer-Lambert Law," *J. Chem. Educ.*, vol. 39, no. 7, p. 333, 1962.

[121] B. Nemeth, C. Busche, S. Tsuda, L. Cronin, and D. R. S. Cumming, "Imaging the Belousov–Zhabotinsky reaction in real time using an ion sensitive array," *Chem. Commun.*, vol. 48, pp. 5085–5087, 2012.

[122] B. Nemeth, M. D. Symes, A. G. Boulay, C. Busche, G. J. T. Cooper, D. R. S. Cumming, and L. Cronin, "Real-time ion-flux imaging in the growth of micrometer-scale structures and membranes," *Adv. Mater.*, vol. 24, pp.

1238–1242, 2012.

[123] B. Nemeth, S. Tsuda, C. Busche, L. Cronin, and D. R. S. Cumming, “ISFET sensor system for real-time detection of extracellular pH oscillations in slime mould,” *Electron. Lett.*, vol. 48, no. 3, pp. 3–4, 2012.

[124] “austriamicrosystems AG.” 0.35 um CMOS C35 Process Parameters, 2013.

[125] “austriamicrosystems, AG.” [Online]. Available: http://ams.com/eng.

[126] “Europractice MPW Service.” [Online]. Available: http://www.europractice-ic.com/.

[127] D. A. Fiedler, M. Koppenol, and A. M. Bond, “An ESR-electrochemical cell which can be ssed in high and low dielectric solvents over wide ranges of temperature and time domain,” *J. Electrochem. Soc.*, vol. 142, no. 3, pp. 862–867, 1995.

[128] “austriamicrosystems AG.” 0.35 um 50 V CMOS Process Parameters, 2009.

[129] E. R. Fossum, “CMOS image sensors: Electronic camera-on-a-chip,” *IEEE Trans. Electron Devices*, vol. 44, no. 10, pp. 1689–1698, 1997.

[130] B. F. Aull, A. H. Loomis, D. J. Young, R. M. Heinrichs, B. J. Felton, P. J. Daniels, and D. J. Landers, “Geiger-mode avalanche photodiodes for three-dimensional imaging,” *Lincoln Lab. J.*, vol. 13, no. 2, pp. 335–350, 2002.

[131] M. A. Al-Rawhani, D. Chitnis, J. Beeley, S. Collins, and D. R. S. Cumming, “Design and implementation of a wireless capsule suitable for autofluorescence intensity detection in biological tissues,” *IEEE Trans. Biomed. Eng.*, vol. 60, no. 1, pp. 55–62, 2013.

[132] M. A. Al-Rawhani, J. Beeley, and D. R. S. Cumming, “Wireless fluorescence capsule for endoscopy using single photon-based detection,” *Sci. Rep.*, vol. 5, p. 18591, 2015.

[133] “ARM mbed.” [Online]. Available: https://developer.mbed.org/.

[134] T. Mikolajick, R. Kühnhold, and H. Ryssel, “The pH-sensing properties of tantalum pentoxide films fabricated by metal organic low pressure chemical vapor deposition,” *Sensors Actuators B Chem.*, vol. 44, pp. 262–267, 1997.

[135] M. Wipf, R. L. Stoop, A. Tarasov, K. Bedner, W. Fu, M. Calame, and C. Schonenberger, “Potassium sensing with membrane-coated silicon nanowire field-effect transistors,” *2013 Transducers Eurosensors XXVII 17th Int. Conf. Solid-State Sensors, Actuators Microsystems, TRANSDUCERS EUROSENSORS 2013*, no. June, pp. 1182–1185, 2013.

[136] M. J. Madou, *Fundamentals of Microfabrication and Nanotechnology*, 3rd ed. Taylor & Francis Group, 2011.

[137] J. C. Chou and C. N. Hsiao, “Comparison of the pH sensitivity of different surfaces on tantalum pentoxide,” *Sensors Actuators B Chem.*, vol. 65, pp. 237–238, 2000.

[138] D.-H. Kwon, B.-W. Cho, C.-S. Kim, and B.-K. Sohn, “Effects of heat treatment on Ta2O5 sensing membrane for low drift and high sensitivity pH-ISFET,” *Sensors Actuators B Chem.*, vol. 34, pp. 441–445, 1996.

[139] S.-J. J. Wu, B. Houng, and B.-S. Huang, “Effect of growth and annealing temperatures on crystallization of tantalum pentoxide thin film prepared by RF magnetron sputtering method,” *J. Alloys Compd.*, vol. 475, pp. 488–493, 2009.

[140] “Miscellaneous Etchants.” [Online]. Available: http://engineering.dartmouth.edu/microeng/processing/etching/Miscellaneous Etchants.pdf.

[141] “MicroChemicals lift-off processes.” [Online]. Available: http://www.microchemicals.com/technical_information/lift_off_photoresist.pdf.

[142] “MicroChemicals AZ2070 resist.” [Online]. Available:

http://www.microchemicals.com/products/photoresists/az_nlof_2070.html.

[143] “Shipley S1818 resist.” [Online]. Available: http://cmnst.ncku.edu.tw/ezfiles/23/1023/img/127/s1800seriesDataSheet.pdf.

[144] “MicroChemicals LOR10A resist.” [Online]. Available: http://microchem.com/pdf/PMGI-Resists-data-sheetV-rhcedit-102206.pdf.

[145] B. Nemeth, M. S. Piechocinski, and D. R. S. Cumming, “High-resolution real-time ion-camera system using a CMOS-based chemical sensor array for proton imaging,” *Sensors Actuators B Chem.*, vol. 171–172, pp. 747–752, 2012.

[146] C. Hu, I. Zeimpekis, K. Sun, S. Anderson, P. Ashburn, and H. Morgan, “Low-cost nanoribbon sensors for protein analysis in human serum using a miniature bead-based enzyme-linked immunosorbent assay,” *Anal. Chem.*, vol. 88, no. 9, pp. 4872–4878, 2016.

[147] N. Moser, T. S. Lande, C. Toumazou, and P. Georgiou, “ISFETs in CMOS and emergent trends in instrumentation: A review,” *IEEE Sens. J.*, vol. 16, no. 17, pp. 6496–6514, 2016.

[148] H. Yagi and T. Sakai, “Rear-gate ISFET with a membrane locking structure using an ultrahigh concentration selective boron diffusion technique,” *Sensors Actuators B Chem.*, vol. 13, no. 1–3, pp. 212–216, 1993.

[149] D.-L. Long, E. Burkholder, and L. Cronin, “Polyoxometalate clusters, nanostructures and materials: From self assembly to designer materials and devices.,” *Chem. Soc. Rev.*, vol. 36, no. 1, pp. 105–21, 2007.

[150] D. L. Long, R. Tsunashima, and L. Cronin, “Polyoxometalates: Building blocks for functional nanoscale systems,” *Angew. Chemie - Int. Ed.*, vol. 49, no. 10, pp. 1736–1758, 2010.

[151] C. Busche, L. Vilà-Nadal, J. Yan, H. N. Miras, D.-L. Long, V. P. Georgiev, A. Asenov, R. H. Pedersen, N. Gadegaard, M. M. Mirza, D. J. Paul, J. M. Poblet, and L. Cronin, "Design and fabrication of memory devices based on nanoscale polyoxometalate clusters," *Nature*, vol. 515, no. 7528, pp. 545–549, 2014.

[152] R. Contant and A. Teze, "A new crown heteropolyanion, K28Li5H7P8W48O184.92H2O: Synthesis, structure, and properties," *Inorg. Chem.*, vol. 24, no. 26, pp. 4610–4614, 1985.

[153] T. Boyd, S. G. Mitchell, D. Gabb, D.-L. Long, and L. Cronin, "Investigating cation binding in the polyoxometalate-super-crown [P 8 W 48 O 184] 40−," *Chem. - A Eur. J.*, vol. 17, no. 43, pp. 12010–12014, 2011.

[154] E. M. Haas, "Role of potassium in maintaining health," *Period. Paralys. Int.*, pp. 1–4, 2011.

[155] C. Wildi, G. Cabello, M. E. Zoloff Michoff, P. V??lez, E. P. M. Leiva, J. J. Calvente, R. Andreu, and A. Cuesta, "Super-Nernstian shifts of interfacial proton-coupled electron transfers: Origin and effect of noncovalent interactions," *J. Phys. Chem. C*, vol. 120, no. 29, pp. 15586–15592, 2016.

[156] H. G. Keitel, H. Berman, H. Jones, and E. MacLachlan, "The chemical composition of normal human red blood cells, including variability among centrifuged cells," *Blood*, vol. 10, pp. 370–376, 1955.

[157] G. M. Whitesides, "The origins and the future of microfluidics," *Nature*, vol. 442, no. 7101, pp. 368–373, 2006.

[158] H. Lorenz, M. Despont, N. Fahrni, N. LaBianca, P. Renaud, and P. Vettiger, "SU-8: A low-cost negative resist for MEMS," *J. Micromechanics Microengineering*, vol. 7, no. 3, pp. 121–124, 1997.

[159] E. H. Conradie and D. F. Moore, "SU-8 thick photoresist processing as a functional material for MEMS applications," *J. Micromechanics Microengineering*, vol. 12, no. 4, pp. 368–374, 2002.

[160] Y. J. Chuang, F. G. Tseng, J. H. Cheng, and W. K. Lin, “A novel fabrication method of embedded micro-channels by using SU-8 thick-film photoresists,” *Sensors Actuators A Phys.*, vol. 103, no. 1–2, pp. 64–69, 2003.

[161] D. M. Altpeter, “Description of SU-8,” 2005.

[162] “MicroChemicals SU-8 3000 series.” [Online]. Available: http://microchem.com/pdf/SU-8 3000 Data Sheet.pdf.

[163] “SPECTRUM Semiconductor Materials.” [Online]. Available: http://www.spectrum-semi.com/.

[164] “Epoxy Technology.” [Online]. Available: http://www.epotek.com/site/.

[165] “SENCIO Functional Packaging Center.” [Online]. Available: http://www.sencio.nl/.

[166] J. M. K. Ng, I. Gitlin, A. D. Stroock, and G. M. Whitesides, “Components for integrated poly(dimethylsiloxane) microfluidic systems,” *Electrophoresis*, vol. 23, no. 20, pp. 3461–3473, 2002.

[167] American Diabetes Association, “Standards of medical care in diabetes-2014,” *Diabetes Care*, vol. 37, pp. 14–80, 2014.

[168] R. Agrawal, N. Sharma, M. Rathore, V. Gupta, S. Jain, and S. Goyal, “Noninvasive method for glucose level estimation by saliva,” *J. Diabetes Metab.*, vol. 4, no. 5, pp. 266–270, 2013.

[169] D. K. Sen and G. S. Sarin, “Tear glucose levels in normal people and in diabetic patients,” *Br. J. Ophthalmol.*, vol. 64, pp. 693–695, 1980.

[170] L. Su, J. Feng, X. Zhou, C. Ren, H. Li, and X. Chen, “Colorimetric detection of urine glucose based ZnFe2O4 magnetic nanoparticles,” *Anal. Chem.*, vol. 84, no. 13, pp. 5753–5758, 2012.

[171] O. Olarte, J. Chilo, J. Pelegri-Sebastia, K. Barbe, and W. Van Moer,

"Glucose detection in human sweat using an electronic nose," *Proc. Annu. Int. Conf. IEEE Eng. Med. Biol. Soc. EMBS*, pp. 1462–1465, 2013.

[172] J. Moyer, D. Wilson, I. Finkelshtein, B. Wong, and R. Potts, "Correlation between sweat glucose and blood glucose in subjects with diabetes," *Diabetes Technol. Ther.*, vol. 14, no. 5, pp. 398–402, 2012.

[173] S. F. Clarke and J. R. Foster, "A history of blood glucose meters and their role in self-monitoring of diabetes mellitus," *British Journal of Biomedical Science*, vol. 69. pp. 83–93, 2012.

[174] E.-H. Yoo and S.-Y. Lee, "Glucose Biosensors: An Overview of Use in Clinical Practice," *Sensors*, vol. 10. pp. 4558–4576, 2010.

[175] R. A. Gatenby and R. J. Gillies, "Why do cancers have high aerobic glycolysis?," *Nat. Rev. Cancer*, vol. 4, no. 11, pp. 891–899, 2004.

[176] A. Zhu, R. Romero, and H. R. Petty, "A sensitive fluorimetric assay for pyruvate," *Anal. Biochem.*, vol. 396, pp. 146–151, 2010.

[177] L. R. Gray, S. C. Tompkins, and E. B. Taylor, "Regulation of pyruvate metabolism and human disease," *Cell. Mol. Life Sci.*, vol. 71, no. 14, pp. 2577–2604, 2014.

[178] "Pyruvic acid, blood." [Online]. Available: http://www.mayomedicallaboratories.com/test-catalog/Clinical+and+Interpretive/8657.

[179] "Kidney Disease." [Online]. Available: http://www.edren.org/pages/edreninfo/blood-tests-in-kidney-disease.php.

[180] K. Saeedfar, Y. H. Lee, L. L. Tan, and M. Rezayi, "Potentiometric urea biosensor based on an immobilised fullerene-urease bio-conjugate," *Sensors*, vol. 13, no. 12, pp. 16851–16866, 2013.

[181] "Urea, blood." [Online]. Available:

http://www.globalrph.com/labs_u.htm.

[182] “Triglycerides, blood.” [Online]. Available: http://www.mayoclinic.org/triglycerides/art-20048186?pg=1.

[183] S. G. Klotzsch and J. R. McNamara, “Triglyceride measurements: A review of methods and interferences,” *Clin. Chem.*, vol. 36, no. 9, pp. 1605–1613, 1990.

[184] K. K. Birtcher and C. M. Ballantyne, “Measurement of cholesterol: A patient perspective,” *Circulation*, vol. 110, no. 11, pp. 296–297, 2004.

[185] M. J. Martin, W. S. Browner, S. B. Hulley, L. H. Kuller, and D. Wentworth, “Serum cholesterol, blood pressure, and mortality: Implications from a cohort of 361 662 men,” *Lancet*, vol. 328, no. 8513, pp. 933–936, 1986.

[186] “Cardiovascular disease.” [Online]. Available: http://www.nhs.uk/conditions/cardiovascular-disease/Pages/Introduction.aspx.

[187] R. S. Dey and C. R. Raj, “Development of an amperometric cholesterol biosensor based on graphene-Pt nanoparticle hybrid material,” *J. Phys. Chem. C*, vol. 114, no. 49, pp. 21427–21433, 2010.

[188] “Sodium Alginate.” [Online]. Available: http://www.sigmaaldrich.com/catalog/substance/sodiumalginate12345900538311?lang=en&region=GB.

[189] M. Rinaudo, “Biomaterials based on a natural polysaccharide: Alginate,” *Tip*, vol. 17, no. 1, pp. 92–96, 2014.

[190] “Jetlab II Precision Printing Platform.” [Online]. Available: http://www.microfab.com/complete-systems/jetlab-ii-tabletop.

[191] Y.-S. Kuo, S. Verma, T. Schmid, and P. Dutta, “Hijacking power and bandwidth from the mobile phone’s audio interface,” *Proc. First ACM Symp. Comput. Dev. - ACM DEV ’10*, pp. 1–6, 2010.

[192] J. V Mei, J. R. Alexander, B. W. Adam, and W. H. Hannon, “Use of filter paper for the collection and analysis of human whole blood specimens,” *J. Nutr.*, vol. 131, pp. 1631–1636, 2001.

[193] P. W. Smit, I. Elliott, R. W. Peeling, D. Mabey, and P. N. Newton, “Review article: An overview of the clinical use of filter paper in the diagnosis of tropical diseases,” *Am. J. Trop. Med. Hyg.*, vol. 90, no. 2, pp. 195–210, 2014.

[194] U. Narang, P. N. Prasad, and F. V Bright, “Glucose biosensor based on a sol-gel- derived platform,” *Anal. Chem.*, vol. 66, no. 19, pp. 3139–3144, 1994.

[195] M. Hoshi, K. Matsumoto, H. Ito, H. Ohtaki, Y. Arioka, Y. Osawa, Y. Yamamoto, H. Matsunami, A. Hara, M. Seishima, and K. Saito, “L-tryptophan–kynurenine pathway metabolites regulate type I IFNs of acute viral myocarditis in mice,” *J Immunol*, vol. 188, pp. 3980–3987, 2012.

[196] A. Shakoor, B. C. Cheah, D. Hao, M. Al-Rawhani, B. Nagy, J. Grant, C. Dale, N. Keegan, C. McNeil, and D. R. S. Cumming, “Plasmonic sensor monolithically integrated with a CMOS photodiode,” *ACS Photonics*, vol. 3, no. 10, pp. 1926–1933, 2016.